THE DARK AND LUMINOUS STRUCTURE OF EARLY-TYPE GALAXIES: OBSERVATIONAL DYNAMICS AND STELLAR POPULATIONS

Nicholas Fraser Boardman

A Thesis Submitted for the Degree of PhD
at the
University of St Andrews

2018

Please use this identifier to cite or link to this item:
http://hdl.handle.net/10023/15979

The Dark and Luminous Structure of Early-Type Galaxies: Observational Dynamics and Stellar Populations

Nicholas Fraser Boardman

University of
St Andrews

This thesis is submitted in partial fulfilment for the degree of

Doctor of Philosophy (PhD)

at the University of St Andrews

August 2017

Candidate's declaration

I, Nicholas Fraser Boardman, do hereby certify that this thesis, submitted for the degree of PhD, which is approximately 37,240 words in length, has been written by me, and that it is the record of work carried out by me, or principally by myself in collaboration with others as acknowledged, and that it has not been submitted in any previous application for any degree.

I was admitted as a research student at the University of St Andrews in September 2013.

I received funding from an organisation or institution and have acknowledged the funder(s) in the full text of my thesis.

Date 12 February 2018 Signature of candidate

Supervisor's declaration

I hereby certify that the candidate has fulfilled the conditions of the Resolution and Regulations appropriate for the degree of PhD in the University of St Andrews and that the candidate is qualified to submit this thesis in application for that degree.

Date 12 February 2018 Signature of supervisor

Permission for publication

In submitting this thesis to the University of St Andrews we understand that we are giving permission for it to be made available for use in accordance with the regulations of the University Library for the time being in force, subject to any copyright vested in the work not being affected thereby. We also understand, unless exempt by an award of an embargo as requested below, that the title and the abstract will be published, and that a copy of the work may be made and supplied to any bona fide library or research worker, that this thesis will be electronically accessible for personal or research use and that the library has the right to migrate this thesis into new electronic forms as required to ensure continued access to the thesis.

I, Nicholas Fraser Boardman, confirm that my thesis does not contain any third-party material that requires copyright clearance.

The following is an agreed request by candidate and supervisor regarding the publication of this thesis:

Printed copy

No embargo on print copy.

Electronic copy

No embargo on electronic copy.

Date 12 February 2018 Signature of candidate

Date 12 February 2018 Signature of supervisor

Underpinning Research Data or Digital Outputs

Candidate's declaration

I, Nicholas Fraser Boardman, understand that by declaring that I have original research data or digital outputs, I should make every effort in meeting the University's and research funders' requirements on the deposit and sharing of research data or research digital outputs.

Date 12 February 2018 Signature of candidate

Permission for publication of underpinning research data or digital outputs

We understand that for any original research data or digital outputs which are deposited, we are giving permission for them to be made available for use in accordance with the requirements of the University and research funders, for the time being in force.

We also understand that the title and the description will be published, and that the underpinning research data or digital outputs will be electronically accessible for use in accordance with the license specified at the point of deposit, unless exempt by award of an embargo as requested below.

The following is an agreed request by candidate and supervisor regarding the publication of underpinning research data or digital outputs:

No embargo on underpinning research data or digital outputs.

Date 12 February 2018 Signature of candidate

Date 12 February 2018 Signature of supervisor

Abstract

Lenticular and elliptical galaxies, collectively referred to as "early-type galaxies" (ETGs), are commonly thought to represent the end-points of galaxy evolution. Lying in the red sequence of galaxies, these objects are defined by their mostly old stellar populations and by their "red and dead" appearance in optical observations. Much progress in understanding these objects has been made with integral-field spectroscopy in recent years, with results repeatedly pointing to a link between early-type galaxies and high-redshift spiral galaxies. However, the exact nature of this link remains unclear, with a wide variety of evolution scenarios likely required to fully explain the range of observed early-type galaxy properties.

In my study, I analysed observations of twelve early-type galaxies taken with the Mitchell Integral-Field Spectrograph at McDonald Observatory, Texas. These galaxies have previously been found to contain detectable quantities of neutral hydrogen gas, with ten out of the twelve displaying large-scale hydrogen disks. I extracted line-of-sight kinematics of the stellar and ionised gas components of these galaxies, and I used various modelling approaches to constrain their stellar population parameters as well as their three-dimensional mass structure in terms of both dark and visible components. An important feature of this study is the wide field of view of the spectroscopic observations, which reach beyond two half-light radii for almost all of the sample; this remains rare for integral-field unit (IFU) studies of ETGs, and so sets this study apart from most earlier works. The gas-rich nature of the sample is likewise novel. I find all aspects of my analysis to yield a consistent view of these galaxies' evolution, in which one or more gaseous interaction events served to shape them into their observed forms. I find these galaxies to contain low dark matter fractions on average within the inner half-light radius, and I also find mass modelling to favour near-isothermal total density profiles over much of the sample.

Acknowledgements

I would like to thank Anne-Marie Weijmans, my supervisor, for being nothing less than a role-model throughout my PhD studentship. Anne-Marie always made time for me when I needed assistance, no matter how numerous her other commitments. Her unwavering support and encouragement have been invaluable to the success of this project, as well as to my development into an independent scientist. My time at St Andrews has made me both a kinder and a more confident person, and I feel that I owe this to Anne-Marie more than anyone else. I could not have asked for a better supervisor.

I have received help and support from many people over the course of my work, without whom my research would not have nearly been so thorough. I would like to thank Remco van den Bosch, Glenn van de Ven, Ling Zhu and Akin Yildirim for the abundant help they provided towards my work and towards the Schwarzschild modelling of NGC 3998 in particular. I thank Harald Kuntschner and Richard McDermid for their invaluable support towards the stellar population modelling of my sample. I thank Michele Cappellari for the abundant advice and insight he has provided towards my work, which has greatly helped my development as a scientist. I thank Eric Emsellem, Thosten Naab, Tim de Zeeuw, Davor Krajnovic and Jesus Falcón-Barroso for their many helpful comments on my papers. I thank Marc Sarzi for his assistance in extracting galaxies' ionised gas contents, I thank Vivienne Wild for providing fruitful discussion regarding the extraction of stellar population parameters, and I thank Pierre-Alain Duc for his abundant assistance regarding the extraction of my galaxies' photometry. I thank Ronald Laesker for his assistance with the comparison between the Mitchell and Atlas^{3D} kinematics. I thank Anne Sansom for her thorough and constructive report on my 2nd paper, on which the 2nd and 3rd chapters of this thesis are based.

I thank Anne-Marie, Remco, Adam Atkinson, Phil Cigan, Carina Lagerholm, Kevin Luecke and Kristina Nyland for their roles in taking the Mitchell Spectrograph observations on which this thesis rests. I thank Josh Adams, Guillermo Blanc and Jeremy Murphy for their help with reducing the raw Mitchell data. I also thank Ian Taylor for assisting me with my numerous computer issues, along with the staff of the university's PC Clinic.

I have been fortunate to work alongside many fantastic people within the School of Physics and Astronomy at St Andrews, and I would like to thank all of them for making my PhD experience so memorable. I would especially like to thank Alistair Hodson and Alasdair Leggat, who were my office-mates for much of my studentship, and Graham Lee, with whom I have shared a flat for the last two years.

I would like to thank the many local people who made my St Andrews experience so special. I would especially like to thank Pat Dodds, who runs the wonderful St Andrews Harbour Cafe in which I have spent many a weekend morning.

Finally, I thank my parents, Ron and Marion, for all the love and support they have provided me over the years. I dedicate this thesis to them.

This work was supported by the STFC (grant number ST/K502339/1), and by the University of St Andrews.

Contents

List of Figures

List of Tables

1

Early-type galaxies - an overview

Today, early-type galaxies (ETGs) are believed to be amongst the most highly-evolved structures in the Universe. When viewed through imaging, these seemingly "red and dead" objects look far less spectacular than spiral galaxies; however, the rise of integral-field spectroscopy in recent years has revealed the true range of properties that ETGs have. Integral-field spectroscopy of ETGs is therefore vital to understanding the nature of these objects and, in turn, to understanding how the modern Universe came to be.

1.1 Spectroscopy of galaxies and the inference of dark matter - a history

The power of spectroscopy for studying the galaxies in our Universe did not begin to be recognised until 1800, when William Herschel used a prism to measure the temperature of the Sun's light over various colours (Herschel, 1800b). In the process, Herschel noted a spike in temperature just beyond the red end of the Sun's spectrum, thus discovering the presence of infra-red

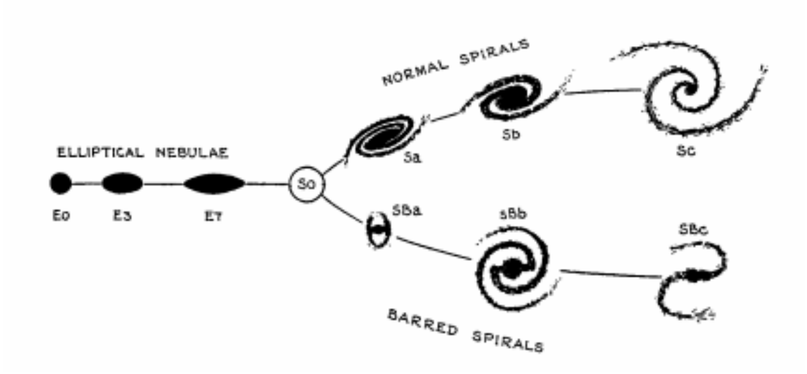

Figure 1.1: "Tuning fork" galaxy classification diagram, from Hubble (1936). Galaxies are classified based on their visual appearance in the sky. A range of structures are noted for spiral galaxies, while elliptical galaxies are essentially classified on ellipticity alone.

radiation within the Sun's spectrum (Herschel, 1800a).

Soon afterwards, the existence of dark features in the solar spectrum was established (e.g. Wollaston, 1802); these were subsequently linked to the presence of chemical elements in the Sun's atmosphere (Kirchhoff, 1860). The foundations of spectroscopy continued to be laid over the remainder of that century: Henry Draper began to photograph the spectrum of Vega in 1872 and published his findings a few years later (e.g. Draper, 1877), while Julius Scheiner photographed the absorption spectrum of the Andromeda galaxy in 1899 (Scheiner, 1899).

At the time of Scheiner's photograph, the true nature of "nebulae" such as Andromeda remained unknown. Scheiner demonstrated Andromeda's spectrum to be solar-like in appearance, and subsequently announced that Andromeda must be a star system in its own right, similar to our own Milky Way. Debate to this end continued until the 1920s, when Hubble discovered Cepheid variable stars in the Andromeda Galaxy. Hubble used the Cepheids to demonstrate Andromeda's vast distance from the Milky Way and, in turn, to demonstrate Andromeda to be a galaxy in its own right (Hubble, 1929). Hubble followed this up with his now-famous tuning fork diagram (Figure 1.1; Hubble, 1936), proposing the lenticular galaxy (or "S0") classification in the process.

It was over this period that dark matter also first began to enter discourse within the field of astronomy, with stellar spectroscopy again playing an important role. Jacobus Kapteyn coined the term "dark matter" in a 1922 spectroscopic study of the Milky Way's stellar kinematics, though he went on to conclude that dark matter was *not* needed in large quantities in the solar neighbourhood to explain the motion of stars in the Milky Way (Kapteyn, 1922), based on the apparent similarity between the Milky Way's visible and total mass. Kapteyn parametrised the Milky Way's stellar configuration as a series of spheroidal shells of constant density, based on the work of Kapteyn & van Rhijn (1920) on the Milky Way's stellar configuration, and assumed the stars to be a dynamical steady state. Another key assumption of Kapteyn's 1922 dynamical study was that the Milky Way's density distribution out of the plane of its disc resembled that of a gas in isothermal equilibrium; Jeans (1922) repeated Kapteyn's calculations without this assumption, assuming instead that the Milky Way's total density distribution mirrored its stellar density distribution, and found that dark matter needed to be added to the visible mass in a roughly 3:1 ratio in order to explain the Milky Way's dynamics. Oort (1932) meanwhile obtained a similar result to Kapteyn, concluding that "the total mass of nebulous or meteoric matter near the sun...is probably less than the total mass of visible stars, possibly much less." Fritz Zwicky calculated radial velocities of galaxies within the Coma Cluster, meanwhile, and then inferred their radial velocity dispersion. Zwicky then used the Virial Theorem to infer a mass-to-light ratio M/L of approximately 500, suggesting the need for much dark matter (Zwicky, 1933, 1937).

The need for dark matter ultimately became widely accepted, with studies of spiral galaxy rotation curves repeatedly finding the need for large amounts of dark material (Rubin & Ford, 1970; Bosma, 1978; Rubin et al., 1980). Such findings stimulated the development of the first "cold dark matter" (CDM) models of the Universe (e.g. Blumenthal et al., 1984), in which baryonic material makes up only a small proportion of the Universe's total mass.

While CDM models were successful on the scale of individual galaxies, various problems remained on greater scales; in particular, the level of observed large-scale structure in the Universe was higher than what simple CDM models predicted (e.g. Maddox et al., 1990). Such findings led to the development of a revised model that included both cold dark matter and a cosmological constant (ΛCDM; e.g. Efstathiou et al., 1990). Subsequent observations have provided further support for ΛCDM, including the measurement of the Cosmic Microwave Background (CMB) anisotropy by the COBE satellite (Smoot et al., 1992). ΛCDM has also been shown to provide good agreements with estimations of the Hubble parameter as well as with estimates of the Universe's age from the ages of old globular cluster stars. A review of this topic can be found in Frieman et al. (2008), and I direct the interested reader to that article for a fuller account of ΛCDM's development.

I note however that a number of outstanding problems exist for ΛCDM on the scales of galaxies and galaxy clusters. The first of these is the so-called "missing sattelites problem", in which ΛCDM models predict far more subhalos around a Milky Way-sized halo than the number of observed Milky Way satellites (Klypin et al., 1999; Moore et al., 1999). A related problem is the "too big to fail problem", in which dissipationless ΛCDM simulation predict Milky Way subhalos that are too dense to be hosts of any observed satellite galaxies (Boylan-Kolchin et al., 2011). Another problem in ΛCDM is the "core-cusp" problem: cosmological N-body simulations predict dark matter halos with cusped density profiles (e.g. Navarro et al., 1996), while observations of luminous dwarf galaxies instead support cored dark matter distributions (e.g. Kormendy & Freeman, 2004). Accurate modelling of baryonic processes is a potential solution to the core-cusp problem: Governato et al. (2012), for instance, find gas outflows to be capable of flattening dark matter cusps for model galaxies with stellar mass $M_* \geq 10^5 M_\odot$.

1.2 Early-type galaxies: an observational perspective

Even as great strides were being made in various aspects of astronomy, the full nature of the so-called "early-type" galaxies remained frustratingly elusive. These galaxies, consisting of the "elliptical" and "lenticular" galaxies from Hubble's tuning fork diagram, were commonly noted for their "red and dead" appearance as well as for their relative dearth of gas. By the beginning of 1980s, there were two broad types of theory concerning how such galaxies developed: either such galaxies evolved from spiral galaxies(e.g. Gunn & Gott, 1972; Larson et al., 1980), or else were formed parallel to spiral galaxies in some alternative manner (e.g. Sandage et al., 1970; Gott & Thuan, 1976).

Dressler (1980) presented an optical study of 55 rich galaxy clusters, and noted a trend in which the proportion of lenticulars and ellipticals in the clusters increases with the galaxy population density. A naive interpretation of this result would be that infalling spirals are stripped of gas by the cluster environment to become ETGs. However, Dressler himself urged caution towards such an interpretation, pointing out previous findings that lenticular galaxies have lowered disk-to-bulge ratios compared to spirals (Faber & Jackson, 1976; Sandage & Visvanathan, 1978; Burstein, 1979), which is difficult to explain by spiral gas stripping alone;

indeed, this result also holds for the galaxies in the Dressler (1980) sample.

Dressler noted that angular momentum was ignored in his 1980 study, and suggested that including angular momentum would be highly important for understanding galaxy evolution. Dressler was not the first to suggest this; indeed, a similar sentiment was expressed by Sandage et al. (1970) a decade earlier. Such sentiments would prove to be prophetic, with various attempts made in subsequent years to incorporate galaxy dynamics into ETG classification schemes. For instance, Kormendy & Bender (1996) proposed a classification system based on ETG isophote shapes, with the shapes serving as proxies for galaxies' underlying stellar dynamics. Subsequently, Emsellem et al. (2007) proposed a scheme based directly on ETGs' kinematics, with ETGs classified as "fast rotators" (FRs) or "slow rotators" (SRs); this scheme was later refined in Emsellem et al. (2011) in order to take both ETG kinematics and observed ETG ellipticities into account.

Emsellem et al. (2007) and Emsellem et al. (2011) both used ETG kinematics from the SAURON integral-field-unit (IFU) instrument (Bacon et al., 2001), with data from the SAURON (de Zeeuw et al., 2002) and ATLAS^{3D} (Cappellari et al., 2011a) surveys respectively. The ATLAS^{3D} survey in particular was notable for containing data of 260 nearby ETGs, representing a significant step up from previous studies of its kind. Analysis of the SAURON and ATLAS^{3D} stellar kinematics led to a much-improved understanding of ETG kinematics with almost all lenticulars as well as most ellipticals being classified as FRs (Emsellem et al., 2007, 2011); a minority of ETGs, which includes the most massive objects, show little ordered motion in their kinematics and are instead classified as SRs. Stellar kinematics have also shown a range of kinematic substructures within individual ETGs, including kinematics twists and kinematically-decoupled cores (Krajnović et al., 2011). Fast-rotating ATLAS^{3D} ETGs were also shown with these data to have a wide range of bulge fractions, similar to spiral galaxies (Cappellari et al., 2011b); this led to a proposed revision to the Hubble diagram, making use of both mophological and kinematic ETG properties as shown in Figure 1.2.

Dynamical modelling of the ATLAS^{3D} sample galaxies has yielded further insight. In Cappellari et al. (2013b) and Cappellari et al. (2013a), dynamical models of the ATLAS^{3D} sample galaxies were constructed using the Jeans Anisotropic Modelling (JAM) method (Cappellari, 2008), which is based on the work of Jeans (1922). JAM modelling of the ATLAS^{3D} sample galaxies demonstrated that the bulge mass fraction of nearby fast-rotating ETGs, which dom-

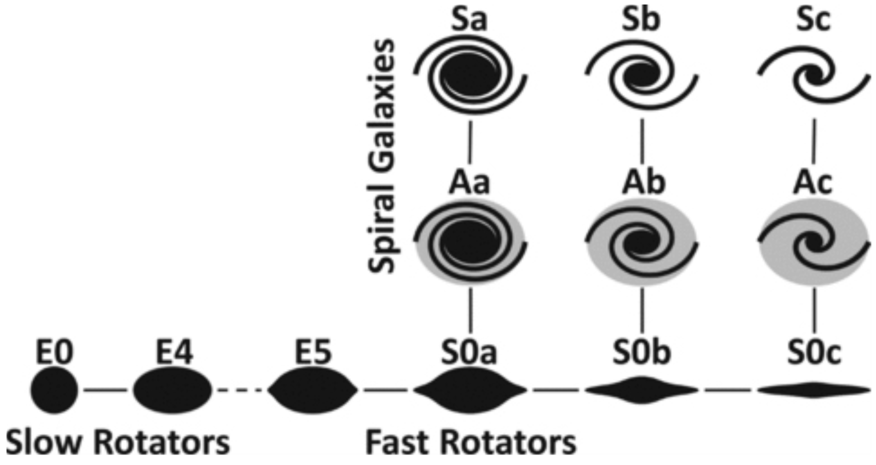

Figure 1.2: "Comb" galaxy classification diagram, from Cappellari et al. (2011b). This classification scheme takes into account galaxies' stellar kinematics as well as their morphological appearance, and so captures a much wider range of ETG properties than the earlier "tuning fork" diagram.

inate the local ETG stellar population for masses below $M_{\rm crit} \sim 2 \times 10^{11} M_\odot$, is correlated with many other properties such as stellar age, colour and the stellar initial mass function (IMF) (Cappellari et al., 2013a). This implies that the evolution of FRs is tied closely with their central bulge, wheras SRs (which dominate for stellar masses above $M_{\rm crit}$) must evolve in such a way as to "wash out" such relations. ETGs were also shown to lie near-parallel with spirals on the mass-size plane, with ETGs systematically more concentrated at a given mass (Cappellari et al., 2013b). These results imply that ETG formation is linked to bulge-growth in progenitor spiral galaxies, with the most massive SRs then evolving from repeated merging events.

Additional information has been obtained in recent years by deep imaging of high-redshift galaxies, which enables one to probe the progenitors of local ETGs directly. Such studies have repeatedly found evidence of significant size evolution in the progenitors of high-mass ellipticals since redshift $z \simeq 2$, with ETGs appearing significantly smaller and more compact in the past than in the present day (e.g. Trujillo et al., 2006; Cimatti et al., 2012; van Dokkum et al., 2010). Lower-mass disk galaxies, meanwhile, have been shown to assemble their mass in a far more uniform way (e.g. van Dokkum et al., 2013). The resulting picture is therefore in very good agreement with that obtained from spectroscopy of nearby systems, and so demonstrates the complimentary nature of these approaches.

Various other findings provide challenges for explaining the evolution of FRs, however. In particular, results from the CALIFA IFU survey have shown that ETGs on average have less angular momentum at a given concentration with respect to spiral galaxies, which is consistent with simulations of galaxy mergers (Querejeta et al., 2015). Sa-type spiral galaxies appear to overlap with S0s on the mass-concentration plane, however, which is consistent with Sa galaxies passively fading into S0s; such a scenario is also consistent with measurements of of total luminosity and disk scale length, which are larger for Sa galaxies than S0s (Vaghmare et al., 2015).

ETGs have also been shown to contain neutral hydrogen gas (hereafter H I) far more commonly than once thought, based on radio data. Early radio studies of ETGs consisted of single-dish observations and typically made firm detections of H I in only a minority of objects. Knapp et al. (1985) detect H I in around 15% out of ≈150 ellipticals, for instance, while Wardle & Knapp (1986) detect H I in ≈30% of lenticular galaxies out of sample of around 300. Wardle & Knapp (1986) made a distinction between S0/a galaxies and S0 galaxies, noting that the relative H I content resembled that of spirals for the former and resembled that of ellipticals for the latter; this provided an early hint that H I could have an external origin for many ETGs, while also implying that at least some lenticular galaxies could be quenched spirals.

More sensitive single-dish observations have since revealed H I in many additional ETGs (e.g. Grossi et al., 2009), while radio interferometry as allowed H I morphology to be studied for ETGs in far greater detail. Recent observations with the Westerbork Synthesis Radio Telescope (WSRT) provide a good example of the information that interferometry can provide. WSRT observations have yielded H I detections in nearly half of local ETGs studied (Serra et al., 2012). In addition, of the ETGs with regular H I disks, roughly half display significant kinematic misalignments with respect to the galaxies' stars, while the neutral and ionised gas components are typically well-aligned (Serra et al., 2014). Any complete picture of ETG evolution must be able to explain the range of gas properties detected, in addition to the observed breadth of properties of ETGs' stellar components.

An additional question in the context of ETG evolution concerns the role of dark matter. Under the cold dark matter view of the Universe, all massive galaxies have formed within massive dark halos; as a result, it is expected that all such galaxies will have evolved alongside these halos, and vice-versa. Is is important therefore to understand the dark matter contents of ETGs, both to understand ETGs' evolution as well as to understand the development of the Universe as a whole.

1.3 Dark matter in early-type galaxies

The need for dark matter in spiral galaxies has been established for several decades, thanks largely to the significant extended neutral H I disks that they typically contain; these disks allow the mass content of these galaxies to be explored out to several half-light radii (or effective radii, R_e). Dark matter work on ETGs, by contrast, has lagged behind significantly. ETGs typically contain relatively little H I as explained in the previous section, meaning that firm H I detections were few and far between until quite recently. Stellar kinematics of ETG outskirts were likewise difficult to extract via traditional long-slit spectroscopy, due to the faintness of these outskirts.

Alternative kinematic tracers have therefore been used to trace ETG dynamics out to large radii; these include planetary nebulae (PNe) and globular clusters (GCs). PNe are easily detectable from their bright [OIII] emission lines, and spectroscopic follow-up work can then be used to extract their kinematics out to many effective radii (e.g. de Lorenzi et al., 2008; Napolitano, 2012, and references therein). Likewise, GCs are discrete, bright objects that can be detected out to several effective radii, enabling one to trace the potential of ETGs well beyond the region in which stars can be detected; of particular note in this regard is the SAGES Legacy Unifying Globulars and GalaxieS Survey (SLUGGS; Brodie et al., 2014), in which two-dimensional spectroscopy was obtained for ETG stars and GCs simultaneously for 25 nearby ETGs.

A recurring challenge for ETG dark matter work is that their dynamics are often non-rotational in nature, which complicates the interpretation of data due to the possibility of severe projection effects. A good example of this difficulty can be seen in study of Romanowsky et al. (2003) who found that little dark matter is needed to explain the PNe kinematics of the elliptical galaxies NGC 821, NGC 3379 and NGC 4494. Dekel et al. (2005) subsequently used numerical simulations to argue that the Romanowsky galaxies could potentially have much dark matter if more radial anisotropies were assumed for the PNe kinematics; in other words, Dekel et al. (2005) argued that Romanowsky et al. (2003) had fallen prey to the mass-anisotropy degeneracy, in which more radial stellar orbits may serve to "hide" galaxy mass from an observer. Douglas et al. (2007) subsequently provided a counter-argument, pointing out that this degeneracy had specifically been discussed in the original Romanowsky study; based on new PNe observations of NGC 3379, Douglas et al. (2007) found the required dark matter fraction to be less than 40% for that galaxy within $5R_\mathrm{e}$. However, de Lorenzi et al. (2009) subsequently showed that much larger dark matter fractions could be calculated from the Douglas et al. (2007) if radial anisotropies were assumed, and concluded that kinematic data out to even larger radii would be needed to firmly deduce the size of the dark matter halo.

With the advent of IFU spectroscopy, it has become significantly more feasible to use ETGs' stellar kinematics to investigate their dark matter contents. Weijmans et al. (2009), for instance, construct dynamical models of NGC 821 and NGC 3379 using a series of SAURON observations out to $4R_\mathrm{e}$, with all SAURON lenslets binned into a single spectrum for each observation in order to obtain sufficient signal-to-noise; they find best-fit dark matter fractions of 49 percent (18 percent) and 34 percent (8 percent) for the two galaxies within $4R_\mathrm{e}$ ($1R_\mathrm{e}$) respectively. JAM modelling of the ATLAS^{3D} survey data, meanwhile, has yielded a median dark matter fraction of 13% within $1R_\mathrm{e}$ (Cappellari et al., 2013a). Stellar kinematics may also be used in conjunction with other kinematic data to probe a galaxy in further detail; for instance Zhu et al. (2016) combine SAURON and SLUGGS stellar kinematics with PNe and GC kinematics in order to model the dark halo of the giant elliptical galaxy NGC 5846 out to $6R_\mathrm{e}$.

It is interesting to note that ETGs have repeatedly been found to have near-isothermal total density profiles, based on both dynamical modelling of ETG kinematics and lensing data. Bolton et al. (2006) reported this result from a strong lensing analysis of Sloan Lenses ACS galaxies - a trend confirmed by various subsequent re-analyses (e.g. Auger et al., 2010; Barnabè et al., 2011). Cappellari et al. (2015) obtain near-isothermal total density distributions from dynamical modelling of combined ATLAS^{3D} and SLUGGS kinematic data, while Poci et al. (2017) obtain a similar result from dynamical models of selected ATLAS^{3D} galaxies. Barnabè et al. (2010) likewise obtains a near-isothermal density distribution on the early-type galaxy SDSSJ0728+3835 from a combination of integral-field spectroscopy, lensing and stellar mass estimates from multiband imaging. This apparent "bulge-halo conspiracy" mirrors the "disk-halo conspiracy" previously noted in spiral galaxies (Bahcall & Casertano, 1985; van Albada & Sancisi, 1986), and is not a generic prediction of ΛCDM cosmology; indeed, the existence of such a "disk-halo conspiracy" is key motivator of alternative theories of gravity such as Modified Newtonian Dynamics (MOND; Milgrom, 1983), which aim to explain the dynamics of galaxies without invoking the presence of dark matter.

Such a "bulge-halo conspiracy" places challenging constraints on galaxy formation models in the context of ΛCDM. Such challenges could never be overcome from observational work alone. For this reason as well as others, detailed simulations are a necessary part of understanding how ETGs evolve.

1.4 ETG evolution and cosmological simulations

Cosmological simulations may be used in order to study a wide variety of topics relevant to evolution of ETGs; such topics include the growth of large-scale structure, the effects of minor and major galaxy mergers and the kinematics of individual systems. By performing simulations over various spatial scales and resolutions and by then comparing these to results of observations, one can gain much information on how ETGs form.

As an example of the power of cosmological simulations, I provide here a discussion of the study of Oser et al. (2010) and the various studies that follow up on it. A complete review of this topic may be found in Somerville & Davé (2015). Oser et al. (2010) make use of the GADGET-2 code (Springel et al., 2005) to investigate the relative importance of star formation and stellar accretion in the build-up of galaxies' stellar mass, by first performing a large-scale GADGET-2 dark matter simulation and then performing high-resolution resimulations of 39 individual dark halos. They find stellar accretion to be important across all galaxy masses, with lower mass galaxies accreting around 60% of their present-day stellar mass and higher mass galaxies accreting around 80% . This work was followed up in Oser et al. (2012) with 40 further resimulations of Oser et al. (2010) galaxies, which showed good agreement with the observed size evolution and velocity dispersion evolution of ETGs. Such results compare well with observations of high-redshift ETGs, and so are in good agreement with the "two-phase" formation model discussed previously.

A series of studies have since investigated the original Oser et al. (2010) simulations in more detail. Naab et al. (2014) present 44 "zoom-in" resimulations of 44 galaxy halos selected from the Oser et al. (2010) simulation data in order to construct two-dimensional dynamics maps. They demonstrate that a wide variety of merger histories can produce similar-looking final galaxies, while also demonstrating some key differences between galaxies with gas-rich and gas-poor histories. Röttgers et al. (2014) use the same re-simulations to study the three-dimensional dynamics of the galaxies; they find that most ETGs have radially anisotropic orbits in the outskirts, with only ETGs that have experienced gas-rich mergers having significant tangential anisotropy. Wu et al. (2014) likewise find that tangential anisotropy only occurs for galaxies that have had a high fraction of in-situ star formation.

Hydrodynamical merger simulations are another area of interest. Such simulations have shown that merger remnants may have a wide variety of properties, bases on the relative masses of the merging galaxies as well as their individual kinematics and orientation (e.g. Hoffman et al., 2010). Of particular interest with respect to ETG evolution is that major mergers have been shown to produce fast-rotating remnants in certain cases (Querejeta et al., 2015), providing the possibility that even fast-rotating ETGs could be the result of major mergers rather than of direct evolution from high-redshift spirals.

Simulations have also been used to investigate the origin of the "bulge-halo conspiracy" described in the preceding section. Remus et al. (2013) perform cosmological and binary merger simulations of ETGs in order to study ETGs' total density slopes; they report that binary major mergers produce remnants with total density slopes dependent on the amount of gas involved in the merger, with subsequent minor mergers serving to evolve the density slope closer to isothermal. Dutton & Treu (2014) likewise find that their cold dark matter cosmological simulations may reproduce the near-isothermal profiles computed from observations, so long as the relative importances of processes serving to expand and contract dark matter halos are finely turned.

1.5 The power of wide-field integral-field spectroscopy

The state of our knowledge of ETGs has improved immeasurably within the last few years, with great progress achieved both from observational studies and from detailed simulations. With regards to ETGs, the growth of IFU spectroscopy has been of particular importance. IFU observations have provided invaluable information on ETGs' structures, in terms of such things as stellar kinematics, stellar populations and galaxy masses; however, most large surveys of nearby ETGs to date have been largely confined to the inner effective radius, leaving much of these galaxies' stellar contents unexplored.

One way to study ETGs further is to measure their stellar kinematics to 2 R_e and beyond, in order to verify that the kinematics are consistent with currently proposed formation scenarios as well as with those seen in simulations. Naab et al. (2014), for instance, find from their simulations that almost all centrally fast-rotating galaxies remain fast-rotating out to several effective radii. Observed FR stellar kinematics should therefore likewise show regular rotation out to several effective radii, provided that current understanding of ETG evolution is sound. This is something that cannot generally be explored using current large IFU datasets such as those from ATLAS^{3D} or MaNGA (Bundy et al., 2015); however, wider-field IFU data hold the potential to study such topics in detail.

Arnold et al. (2014) present slitlet stellar kinematics for 22 ETGs from the SLUGGs survey out to $2-4\ R_e$ and find kinematic transitions in a few of their objects, with abrupt drops in the angular momentum beyond 1 R_e; Arnold et al. (2014) argue this to be evidence of two-phase formation in these objects, with the momentum drops signifying a transition to accretion-dominated stellar halos. By contrast, Raskutti et al. (2014) do not report finding such transitions from Mitchell Spectrograph IFU observations of their massive ETGs out to $2-5\ R_e$, though they caution that such transitions could yet occur beyond their available field of view (FOV).

In addition, wide-field IFU stellar kinematics provide useful inputs for dynamical models. Cappellari et al. (2015) construct JAM models of combined ATLAS^{3D} and SLUGGs data, as discussed in Section 1.3. Yıldırım et al. (2015) construct dynamical orbit-based models of two compact ETGs, MRK 1216 and NGC 1277 out to 3-4 R_e; they find a dark halo to be a necessary component to models of MRK 1216, while finding dark matter free models to be sufficient for fitting the kinematics of NGC 1277. Yıldırım et al. (2016) model the compact ETG NGC 1286 out to 5 R_e, meanwhile, and find their modelling to favour a significant dark matter component for that system.

Wide-field IFU data may also be used to study the properties of ETGs' stellar populations. To date, ETGs have been found to typically contain negative metallicity gradients (e.g. Davies et al., 1993; Rawle et al., 2008; Greene et al., 2013, 2015; Wilkinson et al., 2015) in their stellar populations, with the ages typically being flat or close to flat. The stellar populations of massive ETGs have also been found to show flattening of their metallicity beyond $\approx 1R_e$, suggesting repeated dry accretion events which served to "wash out" the initially-steep gradients (Coccato et al., 2010; Greene et al., 2013; Pastorello et al., 2014, e.g.); less massive ETGs, by contrast, display no such feature(Weijmans et al., 2009; Pastorello et al., 2014). It is also possible to use IFU data in order to map the expected gradient of a galaxy's stellar mass-to-light ratio;

Mitzkus et al. (2017) use this approach to include a stellar mass-to-light gradient in their JAM models of NGC 5102.

One instrument that offers particular promise for outer ETG IFU spectroscopy is the Mitchell Spectrograph, which is currently mounted on the Harlan J. Smith Telescope at McDonald Observatory, Texas. Formerly named VIRUS-P, the Mitchell Spectrograph is a fibre-fed integral-field spectrograph with a $1.7' \times 1.7'$ FOV and a one-third filling factor (Hill et al., 2008).

This instrument was originally designed as a prototype for a series of industrially-replicated IFUs for the Hobby-Eberly Dark Energy Experiment (HETDEX; Hill et al., 2004), and so was originally designed for observing distant lyman-α emitting galaxies (LAEs). However, its unusually large fibres have also proven very useful in the study of nearby galaxies' outskirts, as they reduce the need for spatial binning of data in galaxies' outer regions. To date, the Mitchell has been used to study stellar kinematics in the context of dark matter (e.g. Murphy et al., 2011; Adams et al., 2012), stellar populations (e.g. Yoachim et al., 2010; Greene et al., 2012, 2013) and star formation (e.g. Blanc et al., 2009). A detailed review of Mitchell Spectrograph science can be found in Blanc et al. (2013).

1.6 This thesis

In this thesis, I present results from integral-field spectroscopy of a sample of twelve nearby ETGs, obtained with the Mitchell Spectrograph. The aim of this thesis is to analyse the properties of both the luminous and dark components of these ETGs in a detailed way, in order to further our understanding of how such ETGs form. To this end, I analysed the IFU data using a number of complimentary approaches. I extracted stellar kinematics and ionised gas kinematics for the ETGs, and I investigated their stellar population contents via spectral modelling. I also investigated the galaxies' three dimensional mass distributions using both Jeans and Schwarzschild dynamical modelling methods.

This thesis is structured as follows:

- Chapter 2 contains a description of the methodology used for analysing the stellar and ionised gas contents of the ETGs. I describe the reduction of raw IFU data (Section 2.1) and I then explain the spatial binning of the data in order to obtain sufficient signal-to-noise (Section 2.2). I explain the extraction of stellar kinematics (Section 2.3), using the galaxy NGC 3626 as an example, and I then use the kinematics to investigate the angular momentum of the galaxy's stars (Section 2.4). I also explain the extraction of ionised gas kinematics (Section 2.5) as well as methods for analysing galaxies' stellar populations (Sections 2.6, 2.7), again using NGC 3626 to demonstrate.

- Chapter 3 presents results for the full ETG sample, using the methods described in the previous chapter. I first describe the sample and summarise previous observations of the sample galaxies (Section 3.1), before providing details of the Mitchell Spectrograph observations of these objects (Section 3.2). I then describe my procedure for flux-calibrating the observed galaxy spectra (Section 3.3). I present stellar kinematics maps along with various tests of their robustness (Section 3.4). I then also present maps of the galaxies' ionised gas (Section 3.5), before presenting the results of absorption line strength measurements (Section 3.6) and stellar population modelling (Section 3.7). I end this chapter by discussing the possible evolution histories of these galaxies, with reference to cosmological simulations (Section 3.8).

- Chapter 4 presents results from Jeans dynamical modelling of the ETG sample. I present my modelling of the galaxies' surface brightness, which I parametrise using the Multi-Gaussian Expansion (MGE; Emsellem et al., 1994) method as implemented by Cappellari (2002) (Section 4.1) . I then explain my Jeans modelling procedure, which I carry out using the JAM modelling method (Section 4.2). I present the results of this modelling in terms of the galaxies' dark and visible mass contents and in terms of their overall mass distributions (Section 4.3), before discussion my findings in the context of ΛCDM cosmology and in terms of past ETG studies (Section 4.4).

- Chapter 5 presents a Schwarzschild modelling study of the galaxy NGC 3998, carried out using the method and code of van den Bosch et al. (2008). I first present all data that were used, which include IFU data from both the Mitchell Spectrograph and SAURON instruments (Section 5.1). I then present my modelling method and results (Section 5.2), in terms of NGC 3998's mass distribution as well as in terms of its three-dimensional dynamics. Afterwards, I discuss my results with respect to NGC 3998's possible formation histories (Section 5.3)

- I present a summary of my conclusions in Chapter 6, highlighting the key results of my study (Sections 6.1, 6.2, 6.3). I give a brief outline of my future aims in Section 6.4.

2

Methods

In this chapter, I showcase observations of the early-type galaxy NGC 3626, demonstrating how wide-field IFU observations can be used to study the properties of its stars and ionised gas. I begin by describing the reduction of the raw IFU data. I then discuss the extraction and analysis of this galaxy's stellar kinematics, before describing the extraction of the ionised gas component. Lastly, I explain how the stellar populations of this galaxy may be analysed using multiple approaches. In the following chapter, I will apply the methods described here to a sample of 12 nearby ETGs including NGC 3626.

2.1 Observations and data reduction

12 exposures of NGC 3626 were taken with the Mitchell Spectrograph (Hill et al., 2008) over five nights between the 26th and 30th of April, 2011, using the VP2 grating. I give an overview of the Mitchell Spectrograph's characteristics in Table 2.1. Each exposure has an exposure time of 1800s, producing a total time on source of 6 hours. The galaxy was observed at three dither positions in order to fully sample the field of view; this is illustrated in Figure 2.1. Since

Field of view	1.68'×1.68'
Fibre size	4.08"
Wavelength range	≈ 4770—5430 Å
Primary mirror diameter	2.72 m
Filling factor	≈ 1/3
Spectral resolution FWHM	≈ 1.4 Å

Table 2.1: Summary of characteristics of the Mitchell Spectrograph when using the VP2 grating. I also give the primary mirror diameter of the Harlan J. Smith telescope on which the Mitchell is mounted.

the spectrograph lacks dedicated sky fibres, sky exposures of 900s each were taken so as to bracket pairs of science observations. Bias frames, flat frames and arc frames were taken at the beginning and end of each night. I selected either the dawn or dusk arcs and flats for each night to minimise the temperature differences between those and the observations. I used Ne+Cd comparison lamps for all arc frames.

I carried out most of the data reduction using the VACCINE pipeline (Adams et al., 2011). The primary goal of VACCINE is to avoid resampling of data, which can result in propagated errors; this was achieved using similar techniques to Kelson (2003), who addressed the same problem for long-slit spectra. Below, I summarise VACCINE's key steps.

First, I subtract all frames - bias, flat, arc, sky and science - of virtual overscan and then combine all bias frames into a single master frame. Here, I used 140 bias frames. In all cases, VACCINE combines frames using the biweight estimator (Beers et al., 1990), chosen for its robustness in dealing with outliers (Adams et al., 2011).

Next, I combined the arc and flat frames for each night. Shifts in fibre positions on the CCD of approximately 0.1 pixels have been observed to occur during large shifts in temperature (Blanc et al., 2013); to minimise such shifts, I picked dawn or dusk arcs and flats so as to minimise the temperature difference between these frames and the sky/galaxy frames.

I then combined flat frames to trace fibre solutions for each night; like many IFU instruments, the fibres are typically parallel to neither the CCD rows nor to each other (Adams et al., 2011), and this must be corrected to accurately extract the spectra. During this step, I found that seven fibres were not wholly on the CCD chip, which confused the tracing algorithm; to get around this problem, I excluded these fibres from all future steps. These fibres make up only a small minority of the Mitchell Spectrograph's 246 optical fibres, and so removing them has a minimal effect on my analysis. Once tracing solutions are obtained, VACCINE uses the

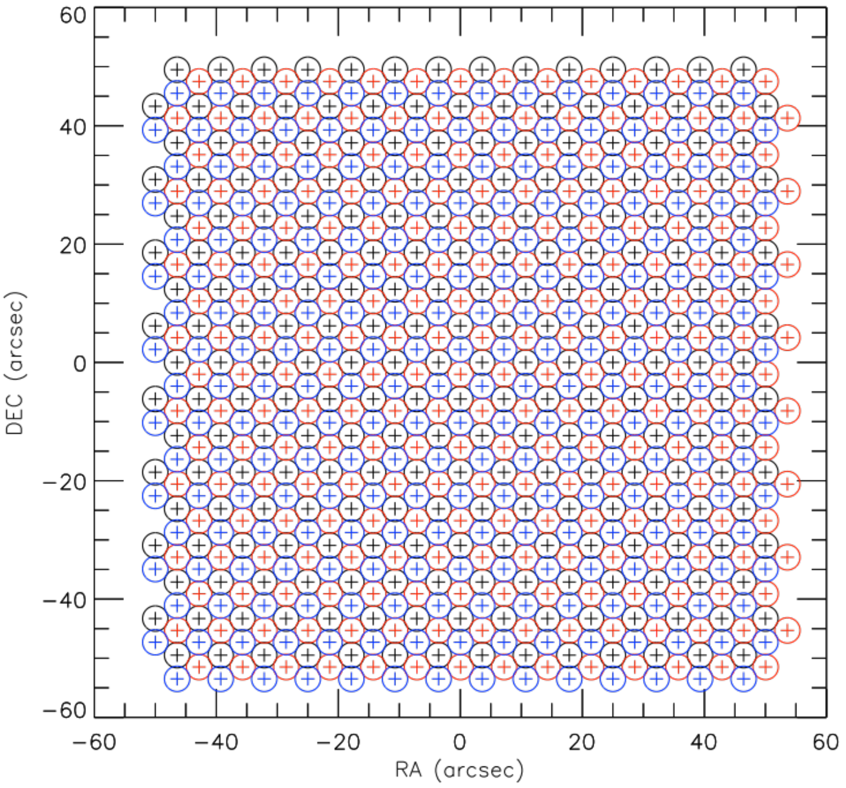

Figure 2.1: Mitchell Spectrograph first (black crosses), second (red crosses) and third (blue crosses) dither positions. The circles around each cross represent the fibre cross sections. I achieve close to 100% sky coverage by combining all three dithers

arc frames to obtain wavelength solutions for all fibres on each night: Gaussians are fitted to the arc lines and are then themselves fitted with a 4th order polynomial (e.g. Greene et al., 2012).

At this point, VACCINE flat-fields the science frames. It removes the solar spectrum from the master flat and then runs a smoothing kernel along the flat's spatial direction to create a smoothed version. For each fibre in the master flat, the solar spectrum is derived and then removed as follows: a B-spline is fitted to the twilight spectra of a subset of neighbouring fibres in order to create a template solar spectrum, with the fibre spectrum then normalised according to the created template. VACCINE then divides the original flat by the smoothed one, resulting in a "pixel-to-pixel" twilight flat (Blanc et al., 2013). VACCINE subsequently flat-fields images by dividing them by this flat.

I perform sky-subtraction at this point by averaging spectra over bracketing sky observations, as described in Blanc et al. (2009). I perform this step in order to estimate the signal-to-noise ratio (S/N) of galaxy spectra, which is necessary for performing Voronoi binning as discussed below. After calculating the S/N, I re-add the sky to the galaxy spectra. Final sky substraction is carried out while extracting stellar kinematics, as discussed in section 2.3.

I combined all science frames for NGC 3626 into a single datacube, with all spectra interpolated onto a common linear scale with steps of size 0.4 Å. I calculated the instrumental resolutions of the galaxy spectra by fitting Gaussians to the 5154.660 and 5400.56 Å emission lines in the master arc frames, weighting the frames in accordance with that galaxy's observation dates. I found the spectral resolution to vary smoothly as a function of fibre position, viewed in both 2 dimensions and 1 dimension (I.E by order of fibre placement on the CCD camera); I therefore chose to fit a fifth-order polynomial to the resolution as a function of fibre position in 1 dimension to eliminate the noise inherent in this calculation. The highest spectral full-width at half-maximum (FWHM) that I found from this process is 1.53Å and the lowest I found is 1.26Å; these correspond to instrumental velocity dispersions of approximately 31 and 38 km/s respectively. I broadened all spectra to the maximum obtained spectral FWHM.

Due to a lack of suitable flux standard star observations, I was not able to flux-calibrate the galaxy spectra in the standard manner. I therefore performed flux calibration by comparing spectra for my full galaxy sample to archival flux-calibrated spectral datasets; I discuss my implementation of this in the following chapter, in which I introduce the full ETG sample.

I quantify the achieved level of coverage of NGC 3626 using the $R_{\max}$ parameter, defined as the maximum radius of a circular aperture with area equal to an ellipse that is at least 85% filled with spectra. I symmetrized the fibre positions of NGC 3626 when performing this calculation, due to NGC 3626 not being centred on the Mitchell Spectrograph's FOV. I find a $R_{\max}$ of 73.3″, or $2.9R_{\mathrm{e}}$. Using the galaxy distance of 19.5 Mpc provided in Cappellari et al. (2011a), this corresponds to a physical $R_{\max}$ value of 6.9 kpc.

2.2 Voronoi binning

To reliably extract the galaxy kinematics in the outermost areas, it was first necessary to bin together spectra from individual spaxels so as to improve the obtained S/N. Binning was carried out using the publicly available Voronoi Binning algorithm of Cappellari & Copin (2003). For a given spaxel, I calculated the average S/N across all pixels using

$$S = \frac{\sum_{i=1}^{M} S_i}{M} \tag{2.1}$$

$$N = \sqrt{\frac{\sum_{i=1}^{M} \sigma_i^2}{M}} \tag{2.2}$$

where S_i represents the sky-subtracted data spectra, σ_i^2 the corresponding variance arrays and M the number of pixels in a single spectrum.

At the start, all spaxels in the datacube are unbinned. The first bin is started at the spaxel with the highest S/N value; provided that this spaxel is not already beyond the target S/N, the nearest neighbouring spaxel is selected for potential inclusion into the bin. To be included, this candidate spaxel must satisfy three requirements: there must not be any other bins between the spaxel and the current bin, it must enable the current bin to remain sufficiently round, and it must bring the S/N of the bin closer to the target value.

If the candidate spaxel is accepted, then the bin centroid is recomputed and a new candidate selected; this continues until a candidate is rejected. The centroid of this bin is calculated one last time. The centroid of all current bins is computed, and a new bin is then started at the closest unbinned spaxel. This process is then repeated until all spaxels have been binned.

At this point, any bin with a S/N value greater than 80% of the desired S/N threshold is

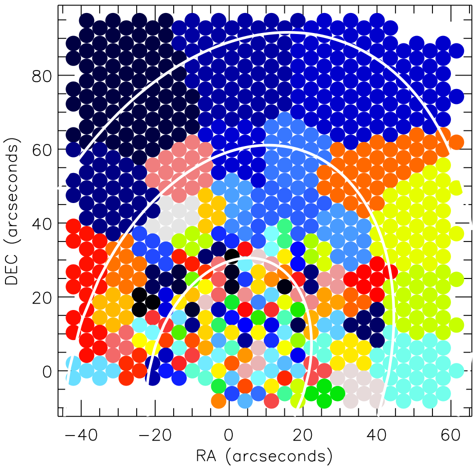

Figure 2.2: Voronoi bin regions of NGC 3626, with fibres binned to a target S/N of 20 per spectral pixel. Each coloured region represents a single Voronoi bin. The white contours are spaced in integer steps of half-light radii. I find that no binning is required within the inner effective radius, due to the large optical fibres of the Mitchell Spectrograph; further out, neighbouring fibres are binned together so as to achieve sufficient S/N out to $\sim 3R_{\mathrm{e}}$

deemed "successful"; bins with S/N values lower than this are instead deemed "unsuccessful", and their spaxels are individually reassigned to the "successful" bin closest to them. The centroids of affected bins are then recalculated once more, enabling the final bin regions to be generated.

I chose a target S/N value of 20 per spectral pixel for all galaxies in my sample, which is roughly equivalent to an S/N of 30 per angstrom. In Figure 2.2, I present the Voronoi map of NGC 3626. I achieve a S/N of ∼20 throughout the Mitchell Spectrograph FOV, ensuring sufficient data quality for the work to come.

2.3 Stellar kinematics

I extracted stellar kinematics using the publicly available penalised PiXel Fitting (pPXF) software of Cappellari & Emsellem (2004), including the upgrade described in Cappellari (2017). The pPXF routine recovers the line-of-sight velocity distribution (LOSVD) by fitting an optimised template $G_{mod}(x)$ to an observed galaxy spectrum directly in pixel space after logarithmically rebinning the spectrum in the wavelength direction such that $x = \ln \lambda$. I added the derived sky spectra back into the galaxy spectra prior to running pPXF, and then performed a second sky subtraction as part of the pPXF fit; this serves to improve the quality of sky subtraction in the sky-dominated outskirts of the Mitchell FOV (e.g. Weijmans et al., 2009). The model spectra therefore take the form

$$G_{\mathrm{mod}}(x) = \sum_{k=1}^{K} w_k [\mathscr{L}(cx) * T_k](x) + \sum_{l=0}^{L} b_l \mathscr{P}_l(x) + \sum_{n=1}^{N} s_n S_n(x), \tag{2.3}$$

where T_k is a set of distinct stellar templates and w_k the optimal weight of each of those templates, with $*$ describing convolution. S_n represents a set of sky templates while s_n is their corresponding weight in the pPXF fit; for a given galaxy, the sky templates consist of all sky observations taken as part of that galaxy's observing run, summed over all unmasked Mitchell fibres. $\mathscr{P}_l(x)$ is a Legendre polynomial of order l, with b_l the corresponding weight; these are used to adjust for low-frequency differences between model and data. Here, I allow for a tenth-degree additive Legendre polynomial correction; such a correction has previously been used for fitting certain galaxies of the ATLAS$^{\mathrm{3D}}$ survey (Cappellari et al., 2011a) and appears to be well-suited to performing pPXF fits to the Mitchell spectra.

$\mathscr{L}(cx)$ describes the broadening function, with c the speed of light; it is given by

$$\mathscr{L}(cx) = \frac{e^{-\frac{y^2}{2}}}{\sigma\sqrt{2\pi}} \left[1 + \sum_{m=3}^{M} h_m H_m(y) \right], \tag{2.4}$$

where $y = (cx - V)/\sigma$ and H_m is the Hermite polynomial of order m with weight h_m.

Here, I wished to use pPXF to fit stellar kinematics up to the 4th Gauss-Hermite moment; in other words, I wished to fit for h_3 and h_4 as well as mean velocity V and velocity dispersion σ. These four parameters may be understood as follows. When h_3 and h_4 are equal to zero, the LOSVD can be represented as a Gaussian with mean V and standard deviation σ; h_4 parametrises the symmetric deviation of the LOSVD from a Gaussian distribution (kurtosis), whereas h_3 parametrises the asymmetric deviation from a Gaussian (skewness). The impact of h_3 and h_4 on the appearance of the LOSVD is summarised in Figure 2.3.

To better understand the broadening function $\mathscr{L}(cx)$, one can consider the meaning of cx. Since $x = \ln\lambda$, one can show from the Doppler formula that

$$\Delta(x) \simeq \frac{\Delta v}{c}, \tag{2.5}$$

which means that one can immediately obtain the line-of-sight velocity from the observed offset, in pixels, between the galaxy spectrum and the stellar templates. Similar arguments

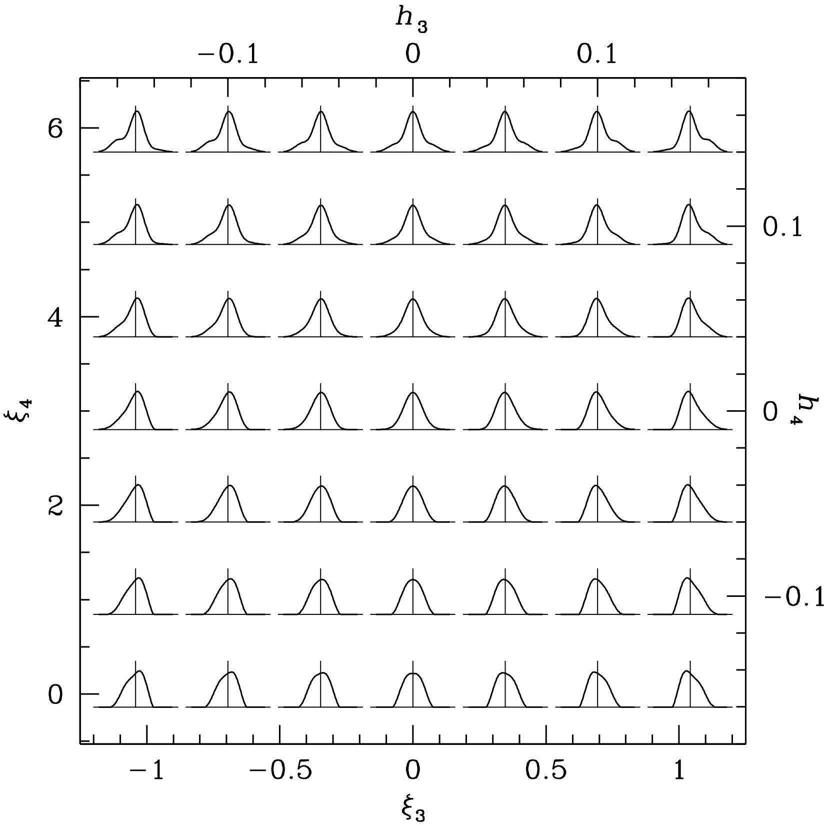

Figure 2.3: LOSVDs of fixed velocity dispersion, plotted with various combinations of h_3 and h_4. A positive (negative) h_3 value signifies a long tail on the positive (negative) side of the distribution, while a positive (negative) h_4 value signifies a distribution that is peaky-er (boxier) than a Gaussian. From Figure 11.5 of Binney & Merrifield (1998)

can be made for the higher-order LOSVD terms. Thus, by optimising $G_{\mathrm{mod}}(x)$ as given by (2.3), the optimal set of LOSVD parameters can be determined.

If one wishes only to obtain the first two kinematic moments (V,σ), then the pPXF method reduces to a χ^2 minimisation procedure, with χ^2 given by

$$\chi^2 = \sum_{n=1}^{N} \left(\frac{G_{\mathrm{mod}}(x_n) - G(x_n)}{\Delta G(x_n)} \right)^2 \tag{2.6}$$

where $G(x_n)$ is an observed galaxy spectrum and $\Delta G(x_n)$ the associated uncertainty. However, if one also wishes to measure higher-order moments (h_3, h_4), then this prescription will cause problems if the signal quality is insufficiently high or if the velocity dispersion is insufficiently large, with large errors in (h_3, h_4) leading to correspondingly large errors in (V, σ). To account for this, pPXF is designed to bias the derived LOSVD towards a perfect Gaussian when (h_3, h_4) are ill-defined, by instead minimising a "biased" χ^2 of the approximate form

$$\chi_{\mathrm{b}}^2 = \chi^2(1 + \lambda'^2 \mathscr{D}^2), \tag{2.7}$$

where λ' is the so-called bias parameter and $\mathscr{D}$ denotes the deviation from a perfect Gaussian. The latter term is well-approximated by

$$\mathscr{D}^2 \simeq h_3^2 + h_4^2. \tag{2.8}$$

This means that when the data quality is poor, a minimum χ_{b}^2 will likely be achieved when $\mathscr{D}$ is low, rather than when χ^2 itself is minimised. The result will be an accurate estimate of (V, σ) at the expense of higher-order terms.

For stellar templates, I used the full medium-resolution (FHWM = 0.51Å) ELODIE library (Prugniel & Soubiran, 2001) of observed stars. However, it is computationally expensive to fit the full library to each individual spectral bin; as such, it was necessary to pre-select the templates in some manner. I therefore selected templates from the library by binning each galaxy into a series of elliptical annuli using the global ellipticities and position angles derived in Krajnović et al. (2011) from Sloan Digital Sky Survey (SDSS) and Isaac Newton Telescope (INT) imaging data; I performed pPXF fits on these annuli using the full ELODIE library, and I

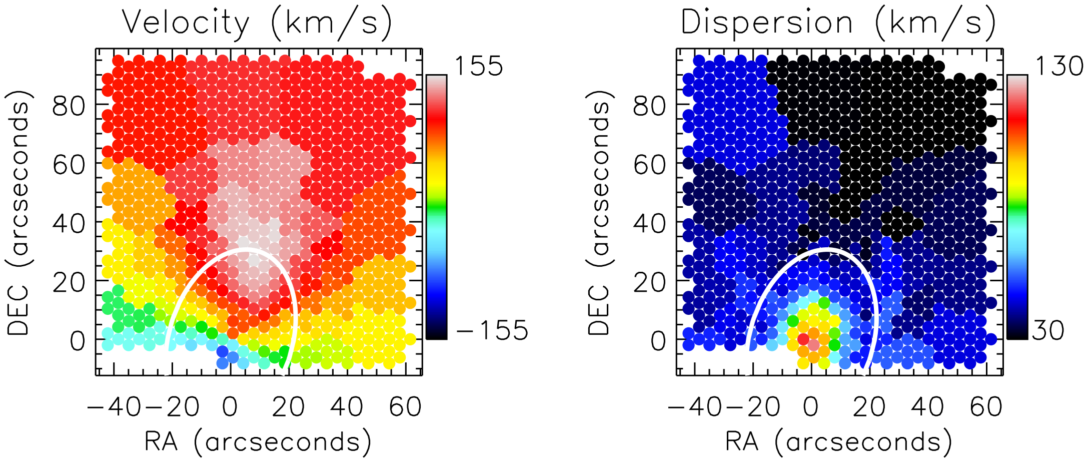

Figure 2.4: LOSVD maps of NGC 3626, obtained with pPXF when fitting for mean velocity and velocity dispersion only. The white contour marks the central effective radius. The galaxy appears to be rotation-dominated throughout the field of view, with velocity dispersion rapidly declining away from the centre.

selected any star which was given a non-zero weight. I then ran pPXF over all galaxy spectra, while iteratively detecting and masking bad pixels; for each spectrum I used as stellar templates all ELODIE stars selected from the corresponding annulus as well as any star selected from annuli at smaller radii. I masked out the emission line regions (Hβ, [O III] and [N I]) for all pPXF fits, while also masking out the red and blue edges of the spectra to avoid any potential flat-fielding problems.

In Figure 2.4 I present stellar kinematics calculated for the first two kinematic moments (V and σ) only. In this case, the value of the penalisation parameter is irrelevant as the LOSVD is assumed to be a perfect Gaussian. My velocity map extends beyond this galaxy's velocity maximum. I find evidence of ordered rotation throughout, with the velocity dispersion continuously falling with distance from the galaxy centre.

In Figure 2.5 I present kinematics calculated to include the higher-order moments h_3 and h_4 in the case where the penalty parameter λ' is set to zero. Here, the higher-order moments become poorly constrained in the outskirts of the galaxy due to the lack of appropriate penalisation, leading to large amounts of noise in the h_3 and h_4 maps as well as to increased noise in σ. As such, I show why some degree of penalisation is useful for extracting kinematics.

In Figure 2.6, I present 4-moment kinematics in the case where λ' is set to 1. Here, the LOSVD becomes biased towards a perfect Gaussian even when the data are sufficient to constrain h_3 and h_4 accurately, which limits the amount of information provided by the higher-order moments; consequently, the obtained values of V and σ here are virtually indistinguish-

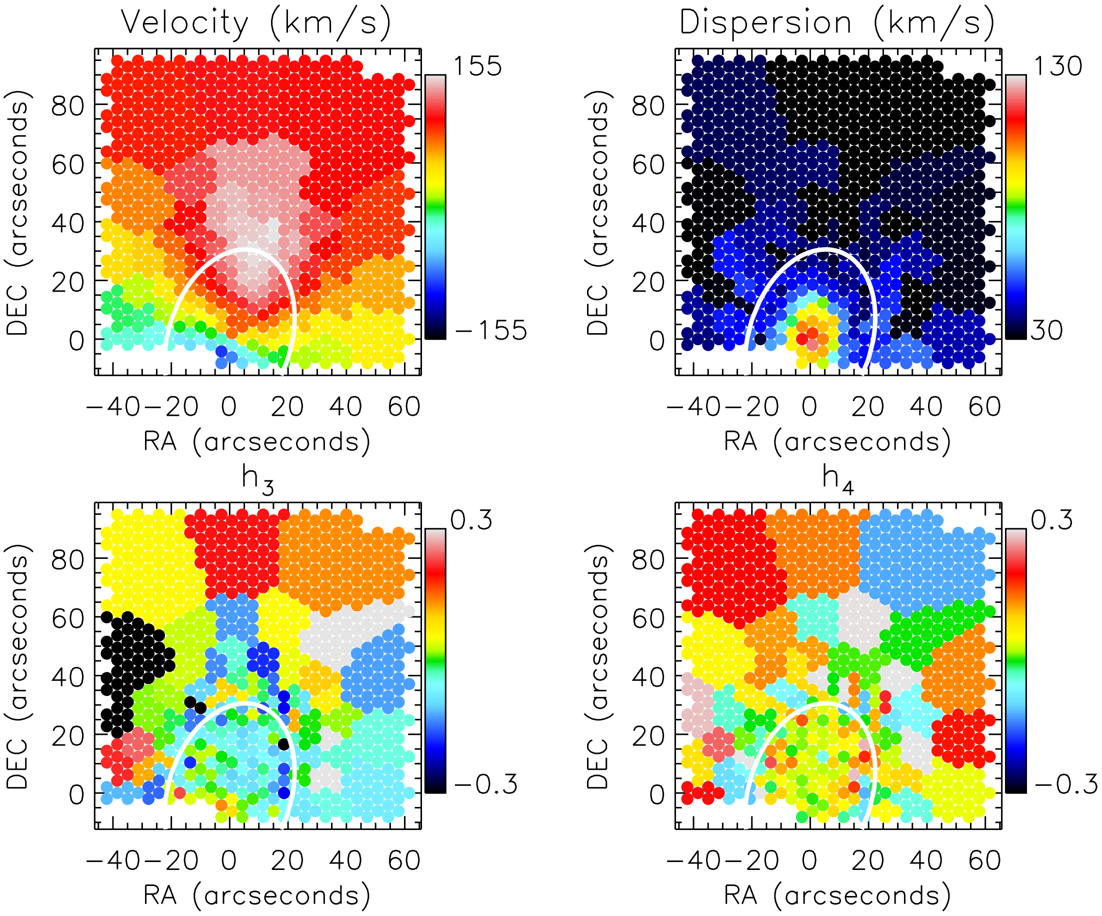

Figure 2.5: LOSVD maps of NGC 3626, obtained with pPXF when fitting 4-order kinematics with zero penalisation. The white contour marks the central effective radius. The higher-order moments h_3 and h_4 appear noisy due to the lack of penalisation, and lead to increased noise in the velocity dispersion map as well.

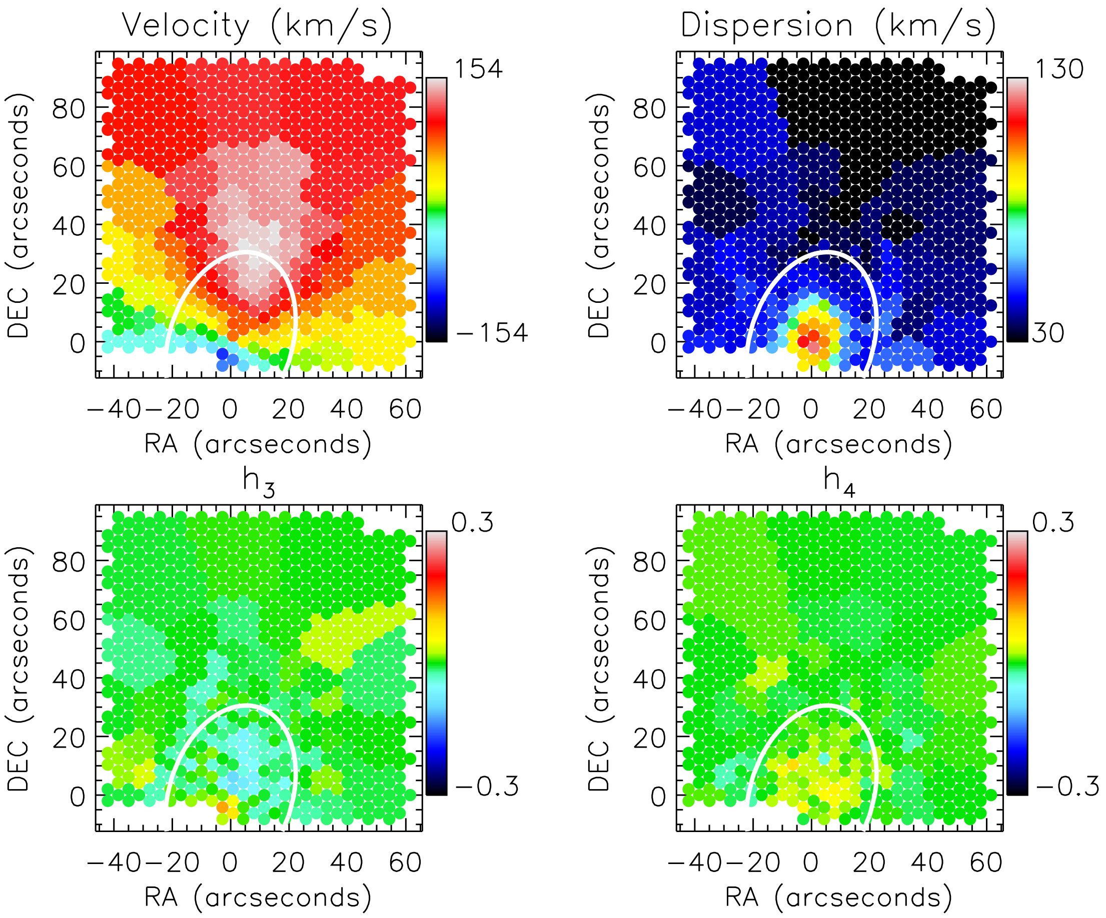

Figure 2.6: LOSVD maps of NGC 3626, obtained with pPXF when fitting 4-order kinematics with the penalty parameter λ' set to 1. The white contour marks the central effective radius. The higher-order moments h_3 and h_4 are excessively penalised in this case, and are forced to near-zero values in almost all cases.

able here from those in Figure 2.4. We see, therefore, that the value of λ' must be chosen carefully: too high a value will bias the kinematics towards a Gaussian distribution even when h_3 and h_4 could be determined accurately, while too low a value risks over-fitting of noisy data.

I optimised the bias parameter λ' as follows, using the simulation code provided with the pPXF package. First, I performed a pPXF fit with zero bias on a galaxy spectrum with high S/N, in order to obtain an unbiased optimal template. I then performed a series of Monte-Carlo simulations, using the prescription from the documentation supplied with the pPXF code that the average deviation between input and output h_3 and h_4 should be less than one third of the root-mean-square scatter of the deviation for values of σ greater than three times the velocity scale; the velocity scale is set by the wavelength step-size of the galaxy spectra in log-space, $\Delta v = \Delta(\ln \lambda)$. This led to an optimal bias of 0.2 for my target S/N of 20. In Figure 2.7, I present 4-moment kinematics obtained after optimising the pPXF penalty parameter.

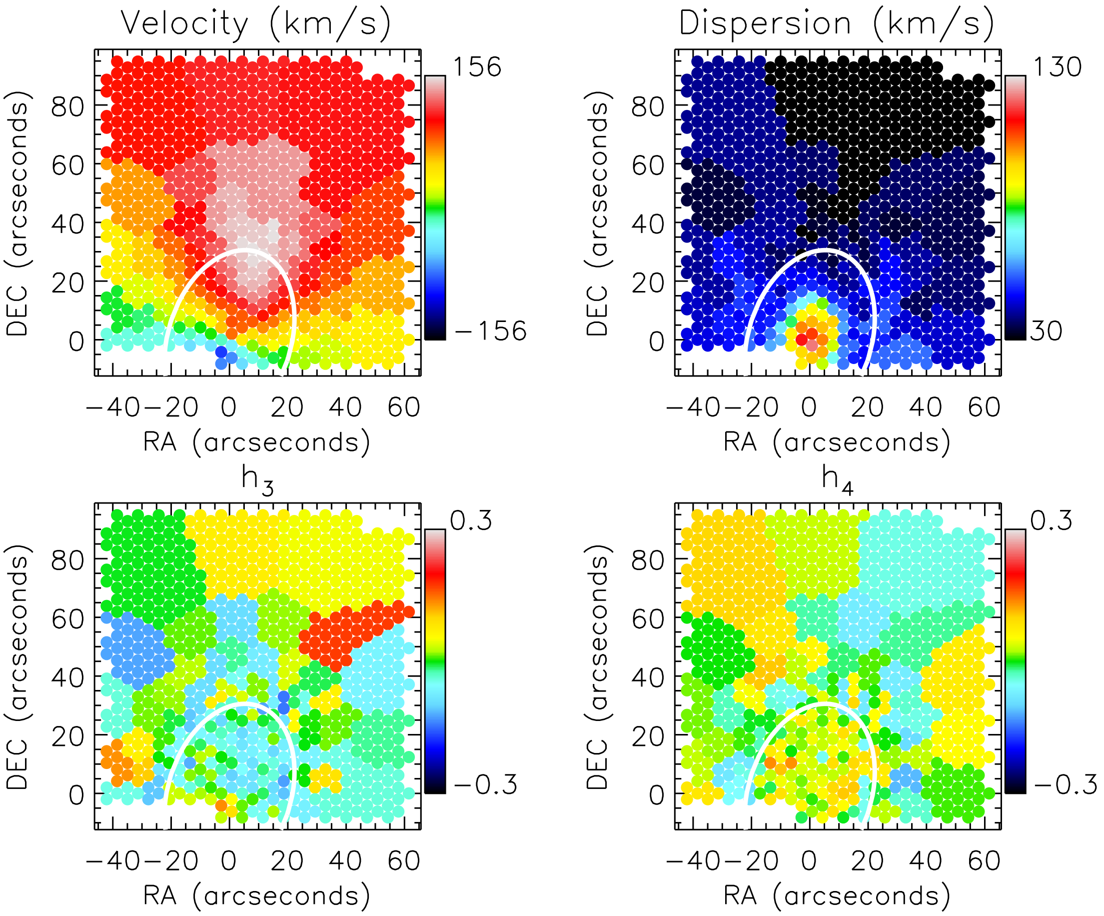

Figure 2.7: LOSVD maps of NGC 3626, obtained with pPXF when fitting 4-order kinematics with the penalty parameter λ' optimised to 0.2. The white contour marks the central effective radius. h_3 and h_4 are recovered accurately for high S/N Voronoi bins, while receiving a degree of penalisation in lower S/N bins.

I calculated the random errors on the kinematics by adding Gaussian noise to the sky-subtracted spectra and then re-running the pPXF fits one hundred times apiece. This produces mean error values of 2.8 km/s, 3.9 km/s, 0.058 and 0.068 for velocity, velocity dispersion, h_3 and h_4 in turn. Unsurprisingly, the obtained error values depend significantly on the S/N of a spectrum. For spectra with S/N $\geq$ 50, the mean error values are 1.1 km/s, 1.5 km/s, 0.009 and 0.010 for velocity, dispersion, h_3 and h_4; by contrast, the mean error values for spectra with S/N $\leq$ 25 are 3.6 km/s, 4.8 km/s, 0.080 and 0.092 for velocity, velocity dispersion, h_3 and h_4.

In Figure 2.8, I show a pair of example pPXF fits of NGC 3626, with the penalty parameter optimised as described above. I demonstrate that my procedure produces good fits to high S/N spectra for which the sky is sub-dominant; in addition, I demonstrate that the sky may be accurately subtracted in cases where it is significant.

2.4 Stellar angular momentum

I quantified the level of rotational support by considering the galaxy angular momentum as a function of radius. I used velocities and dispersions from the pPXF fits to V and σ only. I quantify the angular momentum using a pair of proxy parameters, λ_{R} (Emsellem et al., 2007) and Λ_{R} (Arnold et al., 2014; Raskutti et al., 2014). λ_{R} is a quantity that is integrated out from a galaxy's centre, and in the case of two-dimensional spectroscopy takes the form

$$\lambda_{\mathrm{R}} = \frac{\langle \sum_{i=1}^{N_{\mathrm{P}}} F_i R_i |V_i| \rangle}{\langle \sum_{i=1}^{N_P} F_i R_i \sqrt{V_i^2 + \sigma_i^2} \rangle}, \tag{2.9}$$

where R signifies the circularized radius of an ellipse and F represents the flux. I calculate λ_{R} by summing over all fibres for which the centre falls within a given ellipse, after applying to each fibre the kinematics of its corresponding Voronoi bin. I do not attempt to calculate the profiles beyond $R = R_{\mathrm{max}}$, to ensure that the ellipse is always well-filled with spectra. I symmetrized the kinematics and fibre positions for NGC 3626, due to the galaxy not being centred on the FOV.

Λ_{R} is defined similarly to the above, except that it is integrated over an annulus rather than over a filled aperture. Λ_{R} is designed to be sensitive to changes in levels of rotational support in the outskirts of galaxies, which only contribute little to calculated values of λ_{R}. I calculate

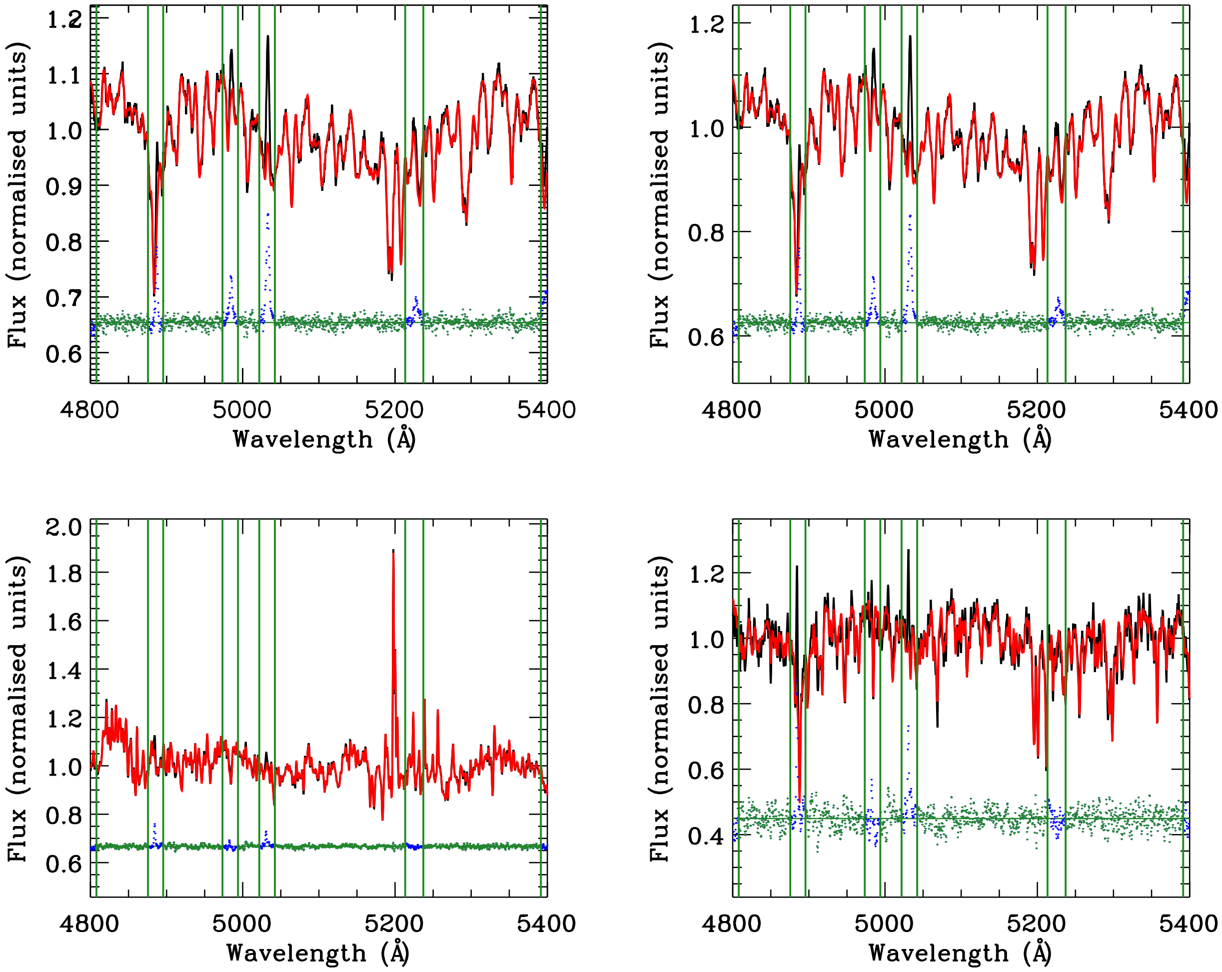

Figure 2.8: Example pPXF fits of high S/N (top) and sky-dominated (bottom) spectra from NGC 3626, before (left) and after (right) pPXF has been used to subtract the sky. Black lines show the observed spectra and red lines show the best-fit superposition of templates. Vertical green lines indicate masked regions of the spectra, which include the positions of emission lines as well as the edges of the spectra, while the blue and green dots show the fit residuals. I obtain good fits to the galaxy spectra, and I find that the pPXF method is sufficient to fit and extract the sky component as well.

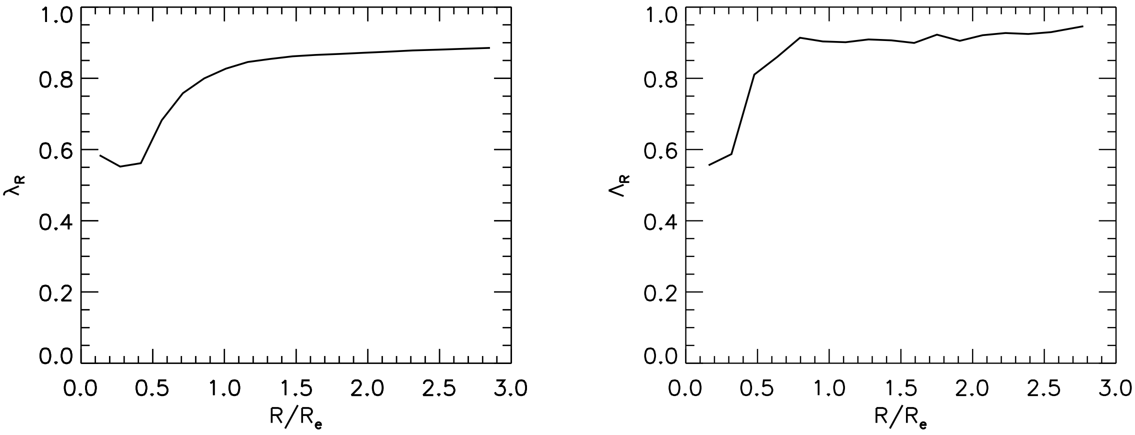

Figure 2.9: λ_{R} and Λ_{R} profiles for NGC 3626. The profiles show evidence of strong rotational support throughout the FOV, with no significant change in behaviour beyond the central half-light radius.

Λ_{R} over a series of 5" annuli with the final annulus boundary at radius $R = R_{\mathrm{max}}$, moving the annulus centre by 1" at a time.

In Figure 2.9, I present the resulting λ_{R} and Λ_{R} profiles of NGC 3626. I find the profiles to show high levels of rotational support, as expected from the kinematics maps. As such, I find NGC 3626 to be rotation-dominated throughout the Mitchell Spectrograph FOV.

2.5 Ionised gas kinematics

I extracted ionised gas fluxes and kinematics using the GANDALF code of (Sarzi et al., 2006). I use GANDALF to obtain the ionised gas distribution and kinematics of NGC 3626, as well as to clean the galaxy's spectra of emission lines.

Previously, I ran pPXF allowing for an *additive* Legendre polynomial correction. Such a correction is degenerate with respect to individual absorption and emission line strengths, making it ill-suited for extracting ionised gas emission lines. I therefore reran pPXF and instead allowed for a 10th degree *multiplicative* Legendre polynomial instead, which accounts for residual continuum variation while avoiding degeneracies between the ionised gas components and stellar absorption components of spectra. I used pPXF to fit and subtract the sky as before, therefore obtaining model galaxy spectra of the form

$$G_{\mathrm{mod}}(x) = \sum_{k=1}^{K} w_k[\mathscr{L}(cx) * T_k](x) \times \sum_{l=1}^{L} b_l \mathscr{P}_l(x) + \sum_{n=1}^{N} s_n S_n(x), \tag{2.10}$$

where all symbols are as in Equation 2.3, with the superposition of stellar templates $\sum_{k=1}^{K} w_k[\mathscr{L}(cx)*$

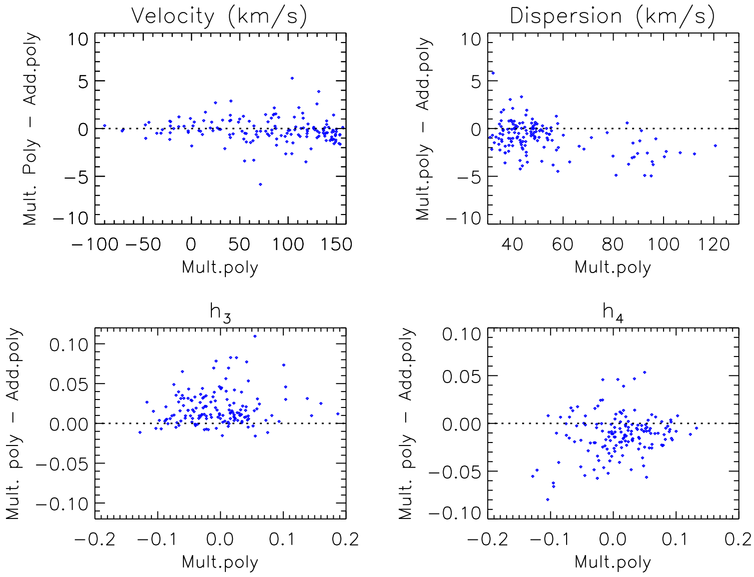

Figure 2.10: Comparison between pPXF kinematics of NGC 3626 extracted using an additive polynomial correction and a multiplicative polynomial correction. The blue points represent measurements from individual Voronoi bins, with the dashed lines representing the 1-1 relations. Good agreement is obtained between the two approaches, indicating that the choice of polynomial does not significantly affect the outcome of the pPXF fits.

$T_k](x)$ now multiplied though by Legendre polynomial correction $\sum_{l=1}^{L} b_l \mathscr{P}_l(x)$. In Figure 2.10, I compare the stellar kinematics obtained this way with the stellar kinematics obtained using an additive polynomial correction as described above. I find a near 1-1 agreement between the kinematics produced by the two polynomial corrections. I parametrise the level of scatter in each kinematic moment by calculating the 1-σ dispersion with respect to zero between the kinematics derived using additive and multiplicative polynomials; this yields values of 1.1 km/s,1.9 km/s, 0.025 and 0.024 for velocity, dispersion, h_3 and h_4 in turn. I also note some systematic differences between the two sets of kinematics: the multiplicative polynomial produces velocity dispersions and h_4 values that are lower on average, as well as h_3 values that are higher on average. However, these systematic effects are generally small compared to the errors I derived previously from Monte-Carlo simulations.

The GANDALF code uses the pPXF-derived stellar kinematics as inputs in order to derive a new optimal stellar template along with an accompanying optimal emission template. Flux values are calculated for each emission line, along with the first two kinematic moments (V, σ).

I implemented GANDALF as follows. I again allowed for a tenth-order multiplicative Legendre polynomial correction, to account for continuum variation. I searched for three ionised

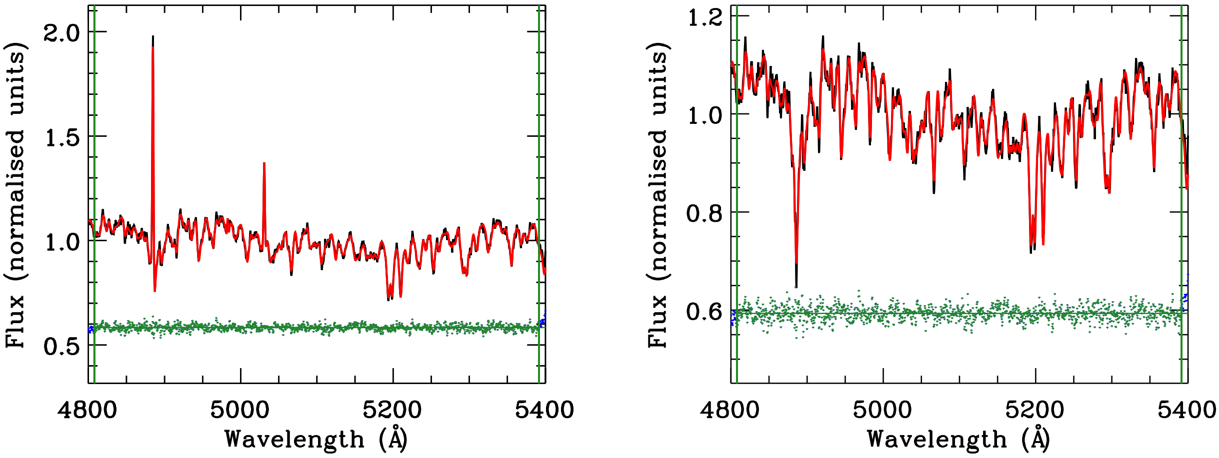

Figure 2.11: Example GANDALF fit of a sky-subtracted galaxy spectrum from NGC 3626, before (top) and after (bottom) subtracting the GANDALF-derived emission component. All lines are as in Figure 2.8

gas emission features in each of the spectra: the Hβ line, the [O III] doublet and the [N I] doublet. I performed an initial GANDALF fit for each binned spectrum in which the Hβ and [NI] emission regions were masked, to derive kinematics for the [O III] emission; afterwards, I fitted for all expected emission features with the gas kinematics fixed that of [O III], in order to minimise the impact of template mismatch on the measurement of Hβ and [N I] lines (Sarzi et al., 2006). I calculated for each spectrum the amplitude-over-noise ratio (A/N) of all detected features in the GANDALF fit. I then extracted all [O III] features with $A/N > 4$ and I extracted all Hβ and [N I] features with $A/N > 3$, following the procedure in Sarzi et al. (2006). I present an example GANDALF fit in Figure 2.11. I applied the GANDALF-derived continuum correction to each spectrum in turn before proceeding, in order to account for any residual continuum contamination.

I estimated the equivalent widths (EWs) of emission lines using Equation 1 from Sarzi et al. (2006):

$$EW = \frac{A/N \times \sqrt{2\pi}\sigma_{gas}}{S/N} \tag{2.11}$$

where S and N are the continuum and noise levels of the spectra and σ_{gas} the observed Gaussian width of the emission lines in Angstroms. I observe a median EW value of 0.75Å for the

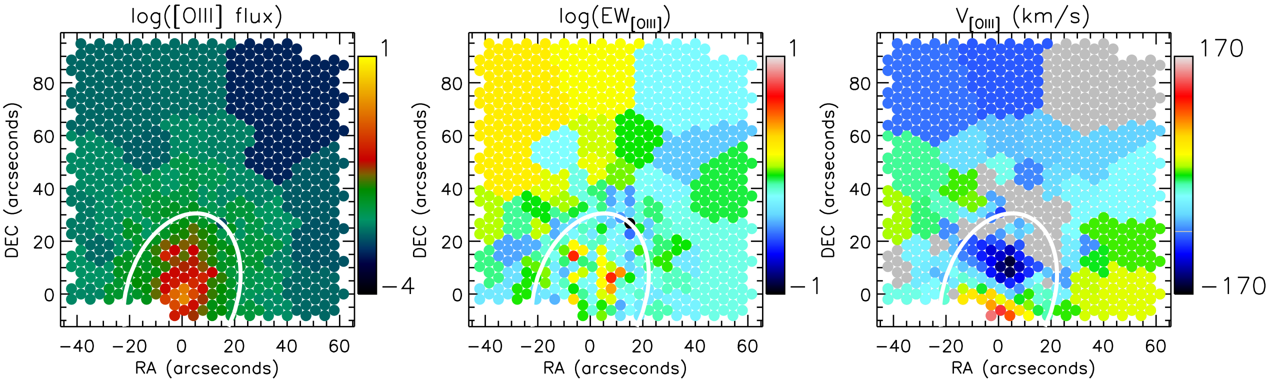

Figure 2.12: [O III] flux (arbitrary units), equivalent width and velocity maps of NGC 3626, extracted using the GANDALF procedure. The white contour marks the central effective radius. Ionised gas is detected well beyond the central half-light radius, and is counter-rotating with respect to the stellar component.

[O III] lines of NGC 3626.

In Figure 2.12, I show the [O III] flux, EW and mean velocity maps derived for NGC 3626 with GANDALF. I show that NGC 3626 contains regularly-rotating gas that is counter-rotating with respect to its stellar component. This is not a new result for this galaxy, being already apparent from ATLAS^{3D} spectroscopy; however, it will nonetheless be valuable to consider with respect to this galaxy's evolution.

Typically, it is ill-advised to attempt to fit Hβ emission independently in a galaxy, due to degeneracies between the Hβ emission line and the underlying Hβ absorption feature. This is demonstrated for instance in Figure 2 of Sarzi et al. (2006), who show an example Hβ velocity map for the S0 galaxy NGC 3489; this Hβ map is extracted independently of [O III], and strongly resembles the galaxy's stellar velocity map with a constant added.

However, given the high flux of Hβ in NGC 3626, it is worthwhile to attempt fitting Hβ independently. I therefore performed a similar fitting procedure to that described before, except with Hβ fit independently in the second step instead of being tied to the [O III] kinematics. I show the results of this process in Figure 2.13; I find the Hβ to strongly resembly the [O III] kinematics and, crucially, to *not* resemble the stellar kinematics presented previously. As such, I find that Hβ can indeed be extracted independently in the case of NGC 3626. I obtain a median Hβ emission EW of 0.73 Å.

In Figure 2.14, I compare the mean velocities and velocity dispersions extracted for the Hβ and [O III] emission regions in the case where the former is fit independently. I find the

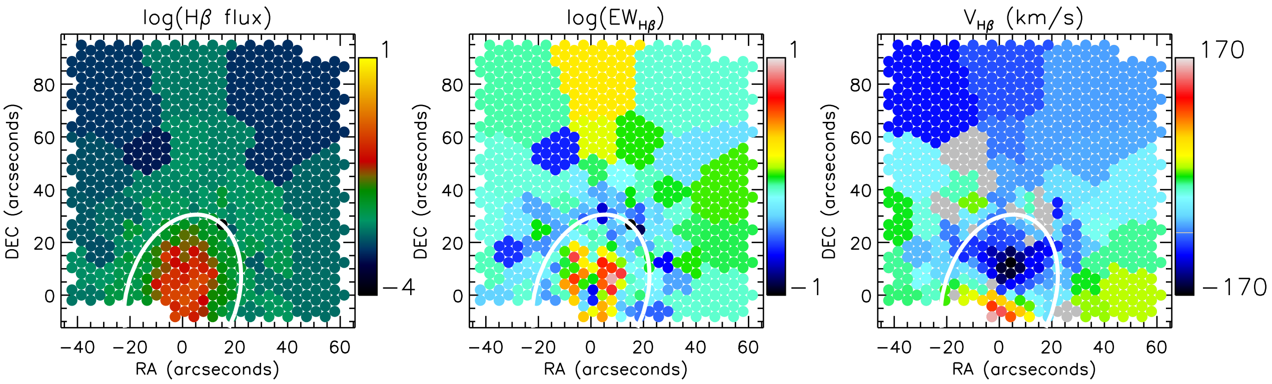

Figure 2.13: Hβ flux (arbitrary units), equivalent width and velocity maps of NGC 3626, extracted using the GANDALF procedure. The white contour marks the central effective radius. The velocity map strongly resembles that derived for the [O III] and does *not* resemble the stellar velocity, indicating that Hβ emission kinematics can be reliably extracted for this galaxy

velocities of the two components to show near 1-1 agreement, as expected from the maps, though the Hβ component appears to have a slightly larger velocity maximum. I also find that the [O III] emission component generally has a larger velocity dispersion. Sarzi et al. (2006) have previously noted that Hβ emission lines tend to have narrower widths than the [O III] lines and have also suggested Hβ to be a better tracer of the circular velocity across galaxies' equatorial planes, and my findings are consistent with this general picture.

2.6 Line strengths

In this section I describe the extraction of absorption line indices in NGC 3626. Each index consists of a central bandpass, where the absorption feature is located, along with a pair of blue and red pseudo-continua. An index is measured by determining the mean of each pseudo-continuum and then drawing a straight line between the two midpoints; the index is then given by the difference in flux between the central bandpass and the line (e.g. Worthey et al., 1994).

I begin by broadening all binned spectra to the 14Å line-index system (LIS) proposed in Vazdekis et al. (2010), in which spectra are broadened to a spectral resolution FWHM of 14Å independent of wavelength, after subtracting the emission features detected when fixing gas kinematics to [O III]. I take both the instrumental dispersion and stellar velocity dispersion into account when broadening. I then calculate line indices for each of our spectra, using the pPXF-derived stellar velocities to determine the required amount of redshifting. I calculate the Hβ, Fe5015, Mg *b*, Fe5270 and Fe5335 indices, the wavelength definitions for which are given in Table 2.2.

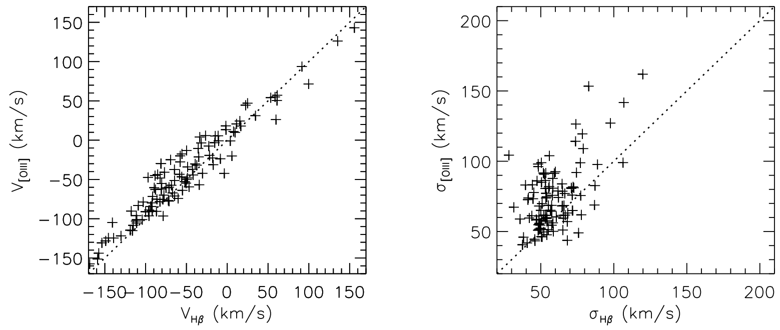

Figure 2.14: Comparison between mean velocities (left) and velocity dispersions (right) derived for the Hβ and [O III] emission lines of NGC 3626. The velocities show near 1-1 agreement, though the Hβ component appears to have a slightly higher velocity maximum (see lower left of left panel). The [O III] line has a higher velocity dispersion overall.

Index	Blue pseudo-continuum (Å)	Central bandpass(Å)	Red pseudo-continuum(Å)
Hβ	4827.875	4847.875	4876.625
	4847.875	4876.625	4891.625
Fe5015	4946.500	4977.750	5054.000
	4977.750	5054.000	5065.250
Mg *b*	5142.625	5160.125	5191.375
	5161.375	5192.625	5206.375
Fe5270	5233.150	5245.650	5285.650
	5248.150	5285.650	5318.150
Fe5335	5304.625	5312.125	5353.375
	5315.875	5352.125	5363.375

Table 2.2: Bandpass definitions of measured line strength indices. All values from Worthey et al. (1994)

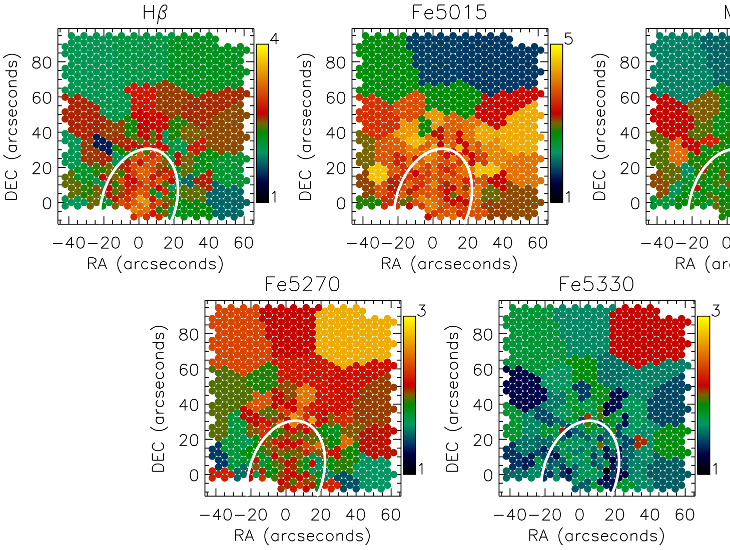

Figure 2.15: Maps of absorption line indices Hβ, Fe5015, Mgb, Fe5270 and Fe5335 in NGC 3626, in units of Å. All indices are calculated on the 14 Å line index system of Vazdekis et al. (2010). The white contour marks the central effective radius.

I calculate errors by performing 500 Monte-Carlo re-simulations, with Gaussian noise added to the spectra and to the input pPXF line-of-sight velocities. In this case, I set the noise levels of the spectra using the spectra's variance arrays. I set lower limits on the errors by calculating the differences between the indices from a given spectrum and those from the associated optimal template, in order to estimate how stronger the indices are affected by over- or under-subtraction of emission features (McDermid et al., 2015); in practice, however, the errors from the Monte-Carlo re-simulations are typically larger than these lower limits.

In Figure 2.15, I present absorption line index maps calculated for NGC 3626. I find that Hβ declines with radius, and that Mg b is roughly constant over much of the FOV. The Fe features also appear approximately flat in the inner parts, though they become increasingly noisy further out.

Given the large ionised gas content of this galaxy, it is important to consider what effect errors in the gas subtraction process could have on the results. In particular, imperfect Hβ subtraction could have significant effects on the derived Hβ absorption line strength, owing to the large Hβ emission flux over much of the FOV. In Figure 2.16, I compare the Hβ absorption line strengths from the presented maps with the Hβ absorption line strengths derived when the Hβ emission component is fitted independently of [O III]. I find good agreement between the absorption line strengths derived from the two methods, with the level of scatter small

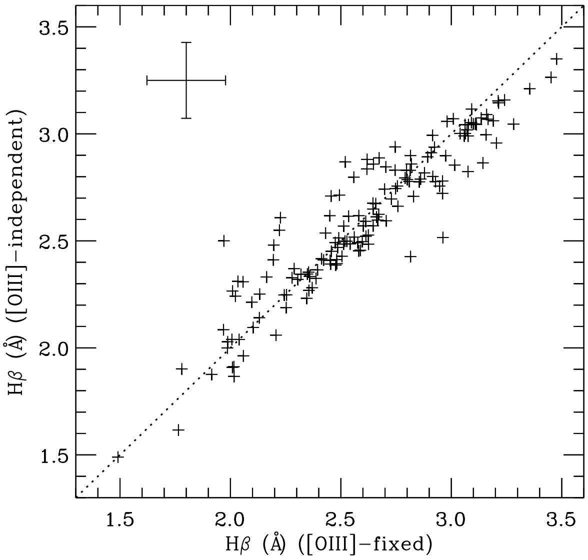

Figure 2.16: Comparison of Hβ absorption line indices in NGC 3626, in the cases where the Hβ emission kinematics are fixed to that of [O III] and where the Hβ kinematics are fit independently. Mean errors are shown in the upper left corner. I find near 1-1 agreement, with the scatter small compared to the sources of error already considered.

compared to the calculated errors; this implies that the impact of fitting Hβ independently is *insignificant* compared to the errors due to noise in the spectra and/or kinematics, and so indicates that the choice of method is *not* important for this particular galaxy. As such, I allow the Hβ component to be fixed to the [O III] component for the remainder of this analysis.

For visualisation purposes, I construct smoothed profiles of Hβ and Mg *b* in the following manner. I place a central elliptical aperture around NGC 3626 along with three elliptical annuli; the central aperture has a major axis radius of $0.5R_e$, while the annuli have major-axis boundaries at 0.5, 1, 1.5 and $2.5R_e$. I obtain the associated line index value across all of the resulting regions by taking the flux-weighted mean of all Voronoi bins whose light-weighted centres fall within each annulus, with errors propagated accordingly. I present the resulting profiles in Figure 2.17, in which radii are given as flux-weighted average radii for a given aperture or annulus position. The profiles emphasise the behaviour seen in the absorption line index maps discussed previously: I observe a fall in the Hβ absorption strength with radius along with a near-flat Mg *b* gradient.

At this point, I consider what absorption line strengths may tell us about a given galaxy using simple stellar population models (SSPs). These models provide predicted spectra for a given initial mass function (IMF) and for a given stellar age, metallicity and elemental abun-

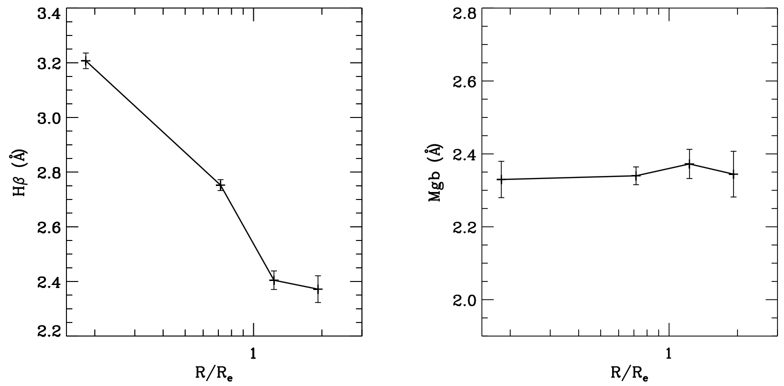

Figure 2.17: Radial Hβ and Mg *b* profiles NGC 3626. I find a near-flat Mg *b* profile and a declining Hβ profile.

dance ratio. By comparing observed spectra to those from SSP models, one can therefore constrain the stellar population properties of a given galaxy as well as detect spatial gradients in these properties.

In Figure 2.18, I present a grid of SSP models in terms of Hβ and Mg *b*, showing the corresponding age and metallicity for each location on the grid. I use models from the MILES SSP library (Vazdekis et al., 2010) with solar elemental abundance ratios, after broadening their spectra to the 14 Å LIS. It can be seen that the Hβ absorption feature is mostly sensitive to the age of a galaxy's stars, whereas the Mg *b* feature chiefly constrains the metallicity. Given my finding of falling Hβ and flat Mg *b* indices, I find that NGC 3626 has a positive radial age gradient and a negative radial metallicity gradient; due to the falling Hβ, we see from Figure 2.18 that a positive Mg *b* gradient would be required to maintain constant metallicity with radius in this galaxy.

One way to quantify the stellar population properties of NGC 3626 would be to compare the calculated absorption line strengths directly to those of the SSP modelling. This approach typically involves oversampling the SSP model grids and then performing a χ^2 fit to calculated line strengths, after correcting the line strengths for systematic errors in some manner (e.g. Kelson et al., 2006; McDermid et al., 2015). However, the high-resolution spectra offered by the Mitchell Spectrograph provide an alternative: instead of using only the few adopted absorption features, one may instead make use the full range of information offered by the data, by fitting SSP spectra directly to gas-cleaned galaxy spectra.

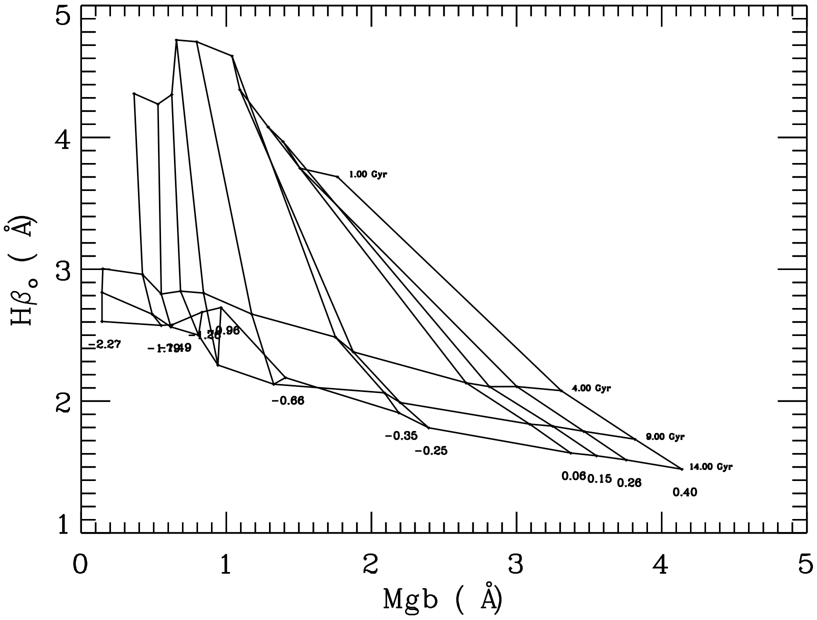

Figure 2.18: Solar-scaled MILES SSP model grid, shown in terms of the Hβ and Mg b absorption line strength indices. Metallicities ($[Z/H]$) are shown at the bottom of the grid, while ages are shown on the right hand side. This demonstrates that Hβ is mostly sensitive to the age of a galaxy's stars, while Mg b is sensitive mainly to the metallicity.

2.7 Stellar population modelling

In this subsection, I describe the process of stellar population modelling using the pPXF procedure. I use pPXF to fit linear combinations of SSP models to the spectra of NGC 3626, rather than using the ELODIE library of observed stars like before. By tracking the properties of the individual SSP models within the pPXF fits, I investigate the stellar population properties of NGC 3626.

A detailed description of stellar population modelling methodology with pPXF can be found in Cappellari (2017). I apply pPXF to the gas-cleaned spectra, using a 10th-degree multiplicative polynomial like before. The fitted model spectra take the form

$$G_{\mathrm{mod}}(x) = \sum_{k=1}^{K} w_k [\mathscr{L}(cx) * T_k](x) \times \sum_{l=1}^{L} b_l \mathscr{P}_l(x), \tag{2.12}$$

where all symbols are as in Equation 2.3, with template T_k drawn from a library of SSP model spectra. This, in practice, serves to discretize the fundamental integral equation

$$G_{\mathrm{mod}}(\lambda) = \int_{t=0}^{t=T} \mathrm{SSP}_{\lambda}(\mathrm{t}, \mathrm{Z})\mathrm{SFR}(\mathrm{T}-\mathrm{t})\mathrm{dt} \tag{2.13}$$

where SSP_{λ} describes an SSP spectrum per unit mass with age t and metallicity Z, SFR the star formation rate, and T the age of the Universe at the redshift of the observed galaxy. This equation is highly degenerate by construction, with a wide combination of SSP models capable of producing acceptable fits to an observed galaxy spectrum; this makes modelling results difficult to interpret unless additional assumptions are made.

One way to solve this degeneracy is to employ regularization - that is, to chose the smoothest combination of SSP models allowed by the data. This means that a stellar population fit will only yield multiple bursts of star formation if such bursts are actually *needed* to fit to the observational data.

I de-redshifted all Voronoi-binned spectra for NGC 3626 and then combined them into a series of central apertures and elliptical annuli, in order to ensure sufficiently high S/N when performing the SSP fit. I used ellipticities equal to the global ellipticity for each galaxy, with aperture/annulus boundaries at 0.5, 1, 1.5 and 2.5 R_{e}; for each aperture or annulus, I then combine all Voronoi-binned spectra for which the luminosity-weighted centre falls within the annulus. I cleaned the combined spectra of *all* detected gas emission rather than using the A/N limits discussed previously. This is because the detected emission often went below the conventional A/N limits at the edges of the FOV, resulting in significant under-subtraction of the emission (and so notable residuals in the pPXF fits) when the spectra were combined.

I performed spectral fitting on the combined spectra by using pPXF to fit linear combinations of SSP models from the MILES SSP library (Vazdekis et al., 2010). I used solar-scaled ($[\alpha/Fe] = 0$) and alpha-enhanced ($[\alpha/Fe] = 0.4$) MILES models, spaced approximately logarithmically in age and metallicity. I used model ages from 0.5 to 14 Gyr, and I used model metalicities $[Z/H]$ from -2.27 to 0.4. I did not use exact log-spacing for age and metallicity, due to the models themselves not being available with such spacing. I used model ages of 0.5, 0.7, 1, 1.5, 2.25, 3.25, 4.5, 6.5, 9.5 and 14 Gyr; I used model metalicity $[Z/H]$ values of -2.27, -1.79, -1.49, -1.26, -0.96, -0.66, -0.35, 0.06 and 0.4. I also tracked the stellar mass M_* and luminosity L_V of each model, where M_* includes the mass of stellar remnants, in order to derive a mass-to-light ratio (M_*/L_V) for each combined spectrum.

I allowed for four kinematic moments in the fit, as well as a 10th-degree multiplicative polynomial. I used a pPXF penalty parameter of 0.2, as before. I did not broaden the spectra to match the MILES spectral resolution: my Mitchell spectra are already broad enough to be fit by the MILES SSP templates due to the stellar velocity dispersions, and so I did not wish to degrade the galaxy's spectra unnecessarily.

The pPXF SSP fits enables me to detect multiple stellar population components, which in turn allows me to investigate the star-formation history (SFH) of NGC 3626. I impose a regularisation constraint using the "regul" keyword in pPXF, in order to force the pPXF solution towards the maximum smoothness allowed by high S/N data. The amount of regularisation is controlled by a single regularisation parameter; I optimise this parameter for each combined spectrum by first performing a pPXF fit on the spectrum with no regularisation and scaling the errors on that spectrum such that $\chi^2 = N$, where N is the number of good pixels across the spectrum. I then choose the regularisation parameter such that $\Delta\chi^2 \simeq \sqrt{2N}$, where $\Delta\chi^2$ indicates the difference in χ^2 values for the regularised and non-regularised fits. I derived errors by performing 100 Monte-Carlo re-simulations with added Gaussian noise, using zero regularisation and zero penalty. I present the pPXF fits to the four combined spectra in Figure 2.19

I calculated light-weighted and mass-weighted values for the age, metallicity and abundance ratio of each fitted model. The light- and mass-weighted value of a given stellar population parameter is respectively given by:

$$X_{\text{mass}} = \frac{\sum_{k=1}^{K} w_k x_k}{\sum_{k=1}^{K} w_k} \tag{2.14}$$

$$X_{\text{light}} = \frac{\sum_{k=1}^{K} w_k x_k F_k}{\sum_{k=1}^{K} w_k F_k} \tag{2.15}$$

where x represents the parameter value of a given template, X the final weighted value of that parameter, w_k the template weights and F_k the flux of each template. I use logarithms of the model ages when applying these equations along with the previously-stated values of $[Z/H]$ and $[\alpha/Fe]$, due to the logarithmic spacing employed for the SSP models (e.g. McDermid et al., 2015). I calculated M_*/L_V using

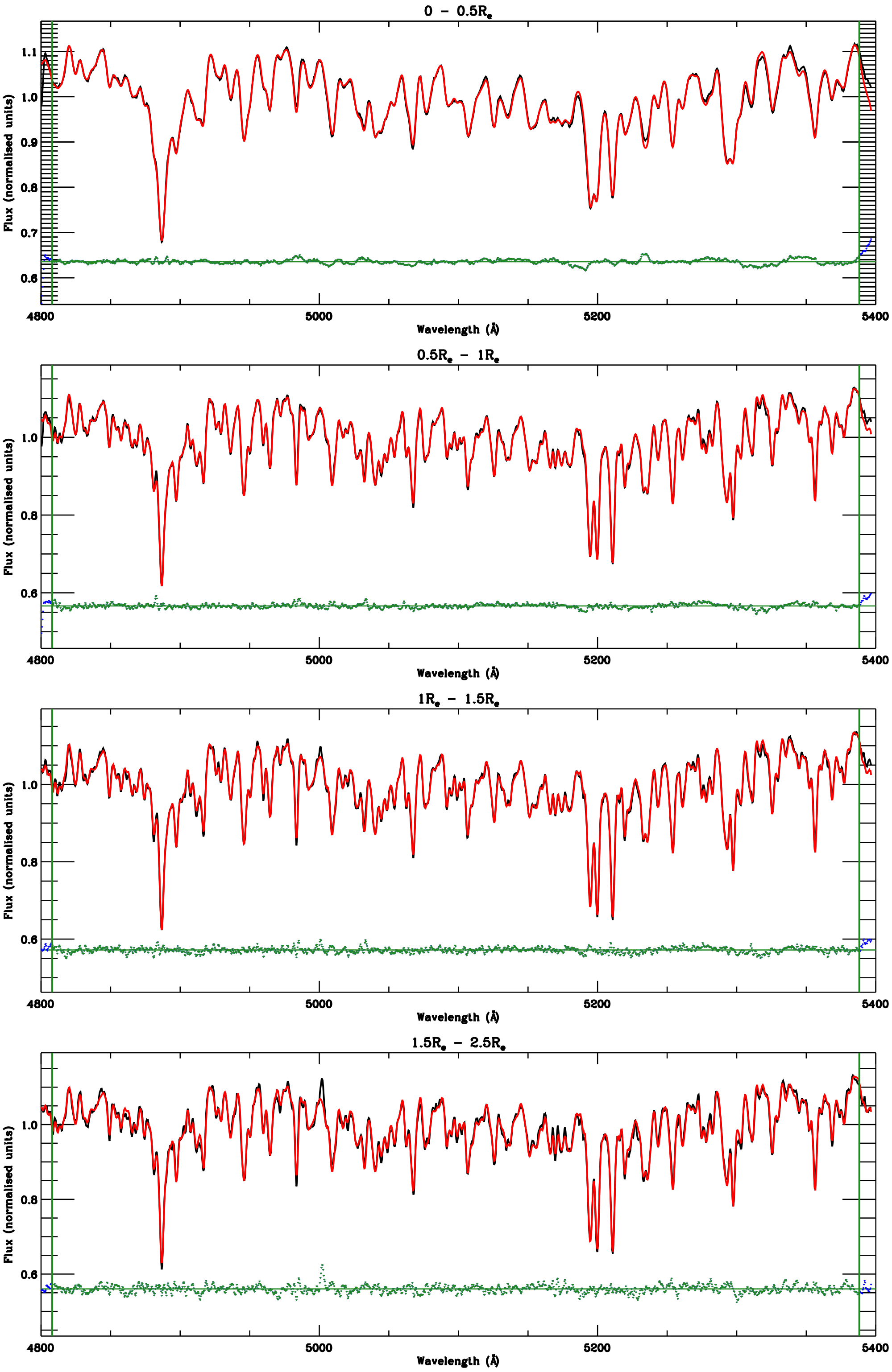

Figure 2.19: pPXF fits to combined gas-cleaned spectra for NGC 3626. The top window shows the central aperture, with lower windows showing fits to annuli of successively larger radii. All lines and symbols are as in Figure 2.8.

$$M_*/L_V = \frac{\sum_{k=1}^{K} w_k M_{k,*}}{\sum_{k=1}^{K} w_k L_{k,V}} \tag{2.16}$$

I present the resulting radial parameter profiles in Figure 2.20, in which radii are given as flux-weighted average radii of the combined spectra. I find radially declining metallicities along with rising ages. I also detect a positive trend in the light-weighted abundance ratio $[\alpha/Fe]$, though the mass-weighted $[\alpha/Fe]$ values show no such feature.

In Figure 2.21, I present the corresponding M_*/L_V profile calculated for NGC 3626. I find that M_*/L_V rises steeply with radius for this galaxy, owing to the gradient in stellar population. I do not attempt to investigate the source of this gradient here, but rather leave such an investigation to be performed on the full sample of 12 ETGs. This gradient in M_*/L_V will likely be important for dynamical models of this galaxy, given the assumption of constant M_*/L that is typically made in dynamical models of ETGs.

In Figure 2.22, I present the SSP mass-weight maps of the regularised SSP pPXF fits to NGC 3626 in terms of age and metallicity, with $[\alpha/Fe]$ marginalised over. I find the fits to predict a significant young stellar population component in the centre of NGC 3626, which becomes increasingly sub-dominant at larger radii. This explains the behaviour of this galaxy seen in Figure 2.20, in which the difference between light-weighted and mass-weighted age increases with radius. Near the centre of NGC 3626, the young stellar populations are significant in both a mass-weighted and light-weighted sense. Further out, such populations contribute little to the mass but continue to contribute to light-weighted parameters due to the relative brightness of young stars.

2.8 Summary

In this chapter, I have conducted a detailed spectroscopic study of the early-type galaxy NGC 3626 out to approximately 3 R_e. I have implemented a series of published methods in order to investigate the kinematics of this galaxy's stellar and ionised gas components, and I have used spectral fitting in order to investigate the properties of the galaxy's stellar populations.

I find NGC 3626 to be rotation-dominated out to 3 R_e, with no detected drops in angular momentum with radius. I also show that NGC 3626 contains ionised gas out to 3 R_e which counter-rotates with respect to the stars. I detect a strong positive age gradient in this galaxy's

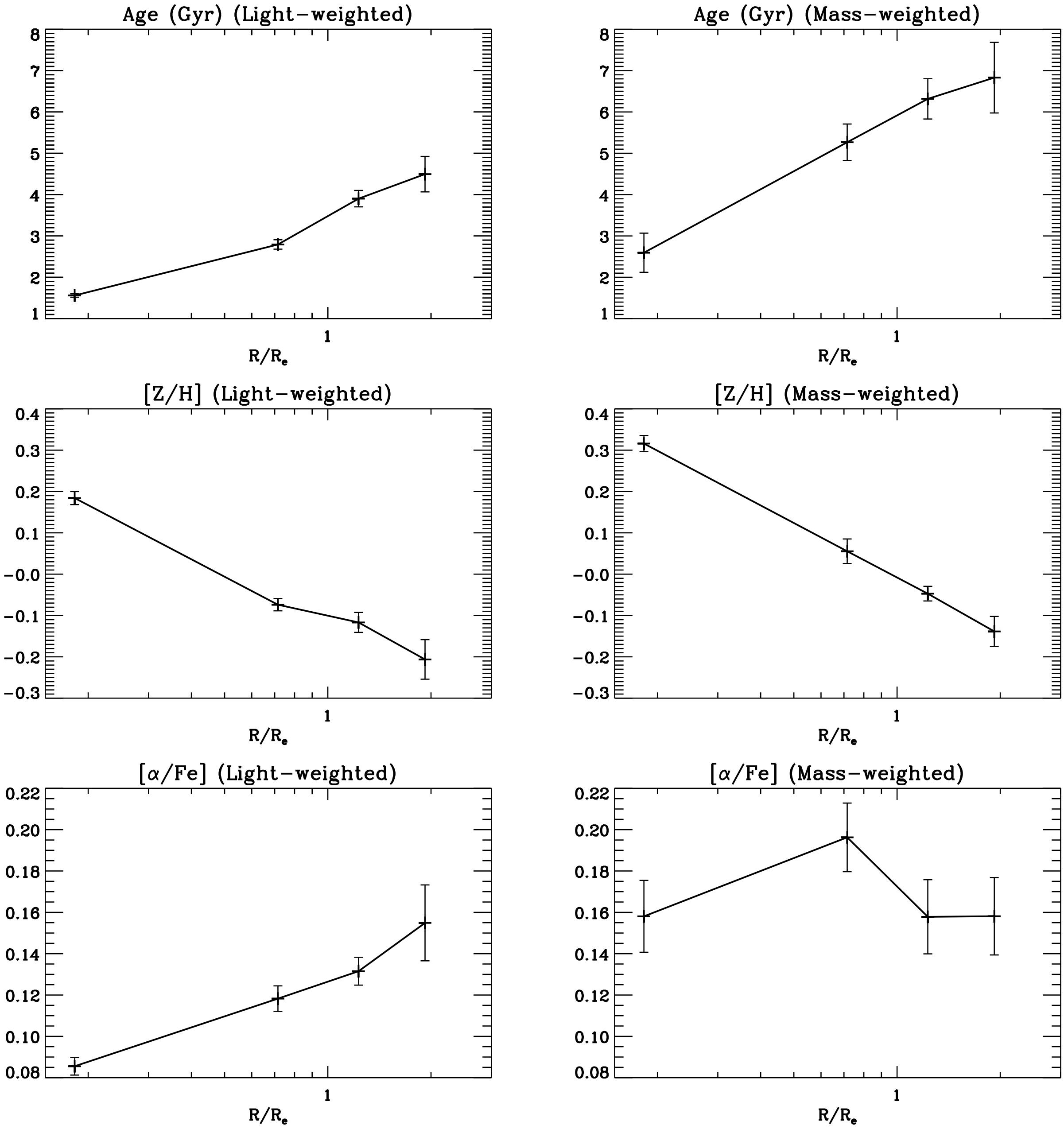

Figure 2.20: Calculated light-weighted (left) and mass-weighted (right) stellar population profiles of NGC 3626, in terms of age (top), metallicity (middle) and elemental abundance ratio (bottom).

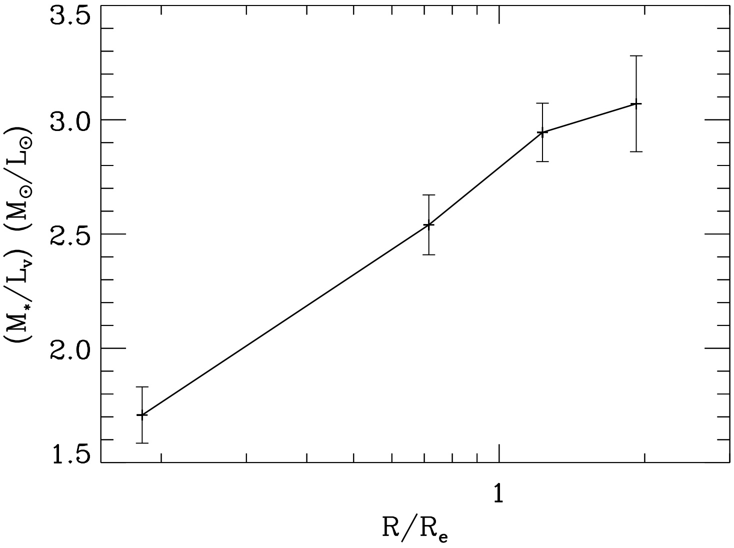

Figure 2.21: Calculated M_*/L_V profile of NGC 3626. I detect a significant rise in M_*/L_V with radius.

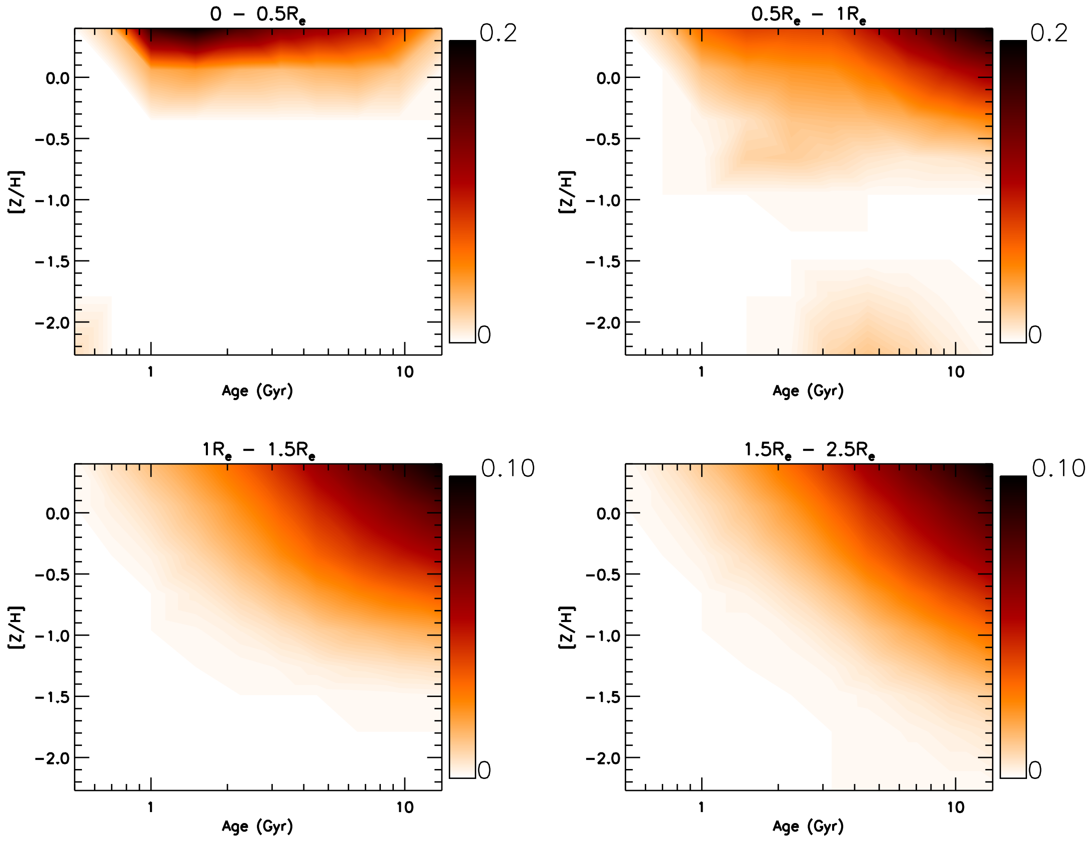

Figure 2.22: Mass-weight maps from pPXF SSP model fits to NGC 3626, with $[\alpha/Fe]$ marginalised over. At the centre, this galaxy contains both significant young and old populations (top left panel); at larger radii, the fits are consistent with the galaxy being dominated by old stars.

stellar populations along with a negative metallicity gradient; in addition, I find the stellar mass-to-light ratio M_*/L_V to vary strongly with position.

In the following chapter, I will implement the above methods on a sample of twelve nearby ETGs, including NGC 3626, in order to probe of evolution histories of these galaxies.

3

Kinematics and stellar populations of Early-type galaxies

In this chapter, I present a sample of twelve nearby ETGs observed with the Mitchell Spectrograph. I apply the methods discussed in the last chapter to these sample galaxies, in order to investigate the properties of their stellar and ionised gas contents beyond the central half-light radius. I then compare my results to those obtained from simulations of ETG formation, in order to investigate possible formation histories for these galaxies. This chapter is heavily based on the work of Boardman et al. (2017), in which this sample was originally presented.

3.1 Sample

My sample consists of twelve nearby ETGs selected from the ATLAS^{3D} survey (Cappellari et al., 2011a). These ETGs were manually selected from those ATLAS^{3D} galaxies detected in H I in Westerbork Synthesis Radio Telescope (WSRT) observations (Serra et al., 2012). I present the basic properties of this sample in Table 4.1. The majority of these ETGs have been found to

Galaxy	RA	DEC	T-type	FR/SR	$R_e('')$	M_K	Distance (Mpc)	$\log_{10}(M_*)$
NGC 680	27.447035	21.970827	-4.0	FR	14.5	-24.17	37.5	11.09
NGC 1023	40.100052	39.063251	-2.7	FR	47.9	-24.01	11.1	11.02
NGC 2685	133.894791	58.734409	-1.0	FR	25.7	-22.78	16.7	10.48
NGC 2764	137.072983	21.443447	-2.0	FR	12.3	-23.19	39.6	10.66
NGC 3522	166.668549	20.085621	-4.9	SR	10.2	-21.67	25.5	9.99
NGC 3626	170.015808	18.356791	-1.0	FR	25.7	-23.30	19.5	10.71
NGC 3998	179.484039	55.453564	-2.1	FR	20.0	-23.33	13.7	10.73
NGC 4203	183.770935	33.197243	-2.7	FR	29.5	-23.44	14.7	10.77
NGC 5582	215.179703	39.693584	-4.9	FR	27.5	-23.28	27.7	10.70
NGC 5631	216.638687	56.582664	-1.9	SR	20.9	-23.70	27.0	10.89
NGC 6798	291.013306	53.624752	-2.0	FR	17.0	-23.52	37.5	10.80
UGC 03960	115.094856	23.275089	-4.9	SR	17.4	-21.89	33.2	10.09

Table 3.1: Summary of my Mitchell Spectrograph sample of ETGs. RA, DEC, R_e, T-type, total absolute magnitude M_K and distances are from Cappellari et al. (2011a) and references therein. $\log_{10}(M_*)$ was calculated using M_K, after applying Equation 2 in Cappellari (2013). The FR/SR classifications are the 1 R_e classifications reported in Emsellem et al. (2011).

be fast-rotating at 1 R_e, using the parametrisation of Emsellem et al. (2011). In addition, the majority of these objects would be classified as lenticular galaxies based on their Hubble T-type parameter, using the parametrisation of Paturel et al. (2003): lenticular galaxies are defined as those with T-type parameters of $-3.5 < T \leq -0.5$, with lower values indicating elliptical galaxies.

In Figure 3.1, I compare the total absolute magnitudes and physical effective radii of my sample galaxies to those of the ATLAS^{3D} and SLUGGs (Brodie et al., 2014) galaxies, as well as with the sample of massive ETGs presented in Greene et al. (2013) and Raskutti et al. (2014); I also show in this figure the upper magnitude limit of the MASSIVE survey (Ma et al., 2014). The masses of my ETG sample tend towards lower values than the latter three samples, with my galaxies' masses all being around or below $10^{11}M_\odot$; as such, my ETG sample is different from other wide-field IFU samples of ETGs that have been published thus far. I obtained M_K and R_e values for my sample from Table 3 of Cappellari et al. (2011a), converting the latter to units of kpc using the distances provided in that table, and I obtained values for the full ATLAS^{3D} sample in the same manner. I obtained R_e values, distances and M_K quantities for the SLUGGs survey from Table 1 of Arnold et al. (2014). I extracted R_e and M_K quantities for the Raskutti et al. (2014) objects directly from Figure 1 of that paper.

My aim in this chapter is to explore the possible formation histories of these galaxies; as such, it is worthwhile to explore what previous observations of these objects may tell us in this

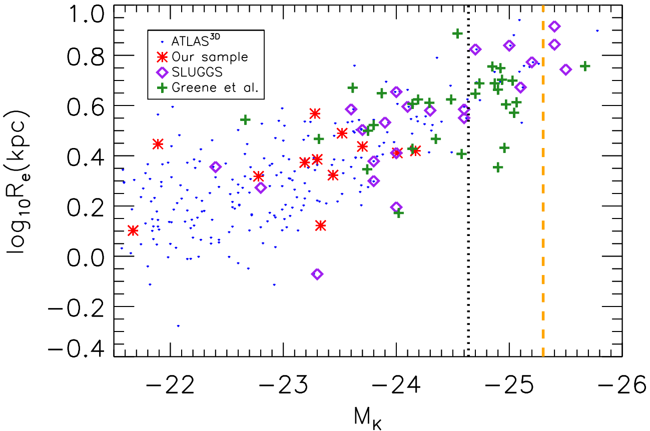

Figure 3.1: Plot of R_e against total absolute magnitude for the full ATLAS^{3D} ETG sample (blue dots), with the Mitchell Spectrograph sample ETGs overlaid (red crosses), the SLUGGS sample (purple diamonds) and the sample of Greene et al. (2013) (green pluses). The vertical dotted line corresponds to $M_{\rm crit} = 2\times10^{11} M_{\odot}$, using Equation 2 from Cappellari (2013), while the orange dashed line corresponds to the upper magnitude limit of the MASSIVE survey (Ma et al., 2014). My ETG sample focusses on a somewhat lower mass region than SLUGGS, Greene et al. (2013) or MASSIVE.

regard. A multitude of observations exist for these galaxies as part of the ATLAS^{3D} survey: as well as IFU observations with SAURON, these galaxies have deep imaging available from the Canada-France Hawaii Telescope (CFHT) as well as H I imaging and velocity maps from the WSRT.

Serra et al. (2012) present H I observations of many ATLAS^{3D} galaxies and classify the morphologies of their H I components. NGC 680 and NGC 1023 are both classified as "u" in that paper, indicating substantially unsettled H I morphologies; the remaining 10 sample galaxies are instead classified as "D", meaning that they contain large-scale regularly-rotating H I structures. The H I velocity maps for all H I-detected ATLAS^{3D} galaxies are presented in Serra et al. (2014), so I direct the interested reader to that paper. Nine of the "D" galaxies show signs of some past disturbance in their H I morphologies, as indicated in Serra et al. (2012); these include counter-rotating H I (NGC 3626 and NGC 6798), polar-rotating H I (NGC 3522), warps (NGC 2685, NGC 2764, NGC 3998, NGC 4203, NGC 5631 and UGC 03960), lopsidedness (NGC 2764, NGC 3998, NGC 4203, NGC 5631 and UGC 03960) and/or misalignments with respect to the galaxy's stellar kinematics (NGC 3998 and NGC 5631). NGC 5582, by contrast, contains a large-scale H I ring that is well-aligned with the galaxy's stars.

The large-scale H I content of the ten "D" galaxies appears to rule out significant late-time major merging, since this would remove the observed large-scale H I disk structures; however, nine of these ten galaxies display signs of disturbances in their H I components, which suggests a need for interaction events in these galaxies' pasts. The observed misalignment between the stellar and gaseous components in several cases likewise suggests a need for past interaction events, with the gas either accreted late into a galaxy's life or else disturbed in some way and then subsequently re-accreted, as seen for instance in the major merger simulation of van de Voort et al. (2015). Such interactions could also have taken place in galaxies for which the stellar and gaseous components are well-aligned, since an accreted gas disk can be expected to subsequently align with a galaxy's stars roughly half of the time (e.g. Katkov et al., 2015). The unsettled H I morphology of NGC 680 and NGC 1023 likewise suggests that some kind of interaction took place in these systems' respective pasts.

Deep imaging with the Canada-France-Hawaii Telescope (CFHT) has revealed faint substructures in the outskirts of many of the sample galaxies, which is indicative of merger and/or accretion events (Duc et al., 2015). These images show tidal disturbances in NGC 680, signs of recent wet merging in NGC 2685 and NGC 2764, a possible disrupted satellite 50 kpc north of NGC 3522 and shells within NGC 5631. Such observations provide further clues to these galaxies' evolutionary pasts.

Much additional information on these galaxies may be acquired from wide integral-field spectroscopy, as was demonstrated for NGC 3626 in the previous chapter. Over the remainder of this chapter, I will present Mitchell Spectrograph observations for the twelve ETGs in my sample, presenting results in terms of stellar kinematics, ionised gas kinematics and stellar populations. I will compare my results to those from a variety of simulations, before relating my findings to the previous observations of these objects discussed above.

3.2 Mitchell Spectrograph observations

Observations of the sample ETGs were taken on the Mitchell Spectrograph using the VP2 grating over 27 nights, spaced over four observing runs in the years 2010 and 2011. Galaxies were observed using a series of thirty-minute exposures, with bracketing sky observations of 15 minutes also taken to enable sky subtraction. Bias frames, flat frames and arc frames were observed at the beginning and end of each night, with Ne+Cd comparison lamps used for the arc frames in all cases. Some galaxies were observed for longer than others, owing to observing time constraints. Certain galaxies were also observed over multiple pointings, to better-capture their structure beyond the central effective radius. Data reduction was carried out using the VACCINE pipeline, as described in the previous chapter.

The Mitchell Spectrograph has a one-third fill factor, and complete sky coverage can be achieved by taking observations at three dither positions. Most of the galaxies were observed over all three dither positions in order to obtain full coverage. However, a couple of galaxies could not be observed in this way due to observing time constraints: NGC 4203 was observed at two dither positions instead, while NGC 2685 was also observed at two dither positions for one of its two pointings. Certain fibre positions on a given observing run were found to fall off the CCD chip or else to contain insufficient wavelength coverage, as was the case for NGC 3626; I masked such fibre positions as before.

I combined all science frames into a single datacube for each galaxy, after interpolating all spectra for a given galaxy onto a common linear scale with step-size 0.4 Å as in Chapter 2 of this thesis. I calculated the instrumental resolutions of the galaxy spectra by fitting Gaussians to the 5154.660 and 5400.56 Å emission lines in the master arc frames, weighting the frames in accordance with that galaxy's observation dates. I then fitted a fifth-order polynomial to the resolution as a function of the one-dimensional fibre position. I found a maximum spectral full-width at half-maximum (FWHM) for the sample of 1.71Å from this process, along with a minimum of 1.25Å; these correspond to instrumental velocity dispersions of approximately 31 and 42 km/s respectively. For a given galaxy, I masked fibres contaminated by foreground objects and I also masked fibres with excessively low signal-to-noise ratio (S/N) if needed; I also broadened each galaxy's spectra to the maximum spectral FWHM obtained for that galaxy.

In Figure 3.2 I compare the radial extent of the Mitchell Spectrograph data with that of the ATLAS^{3D} and SLUGGS samples, as parametrised via the R_{max} parameter. I define R_{max} to be the maximum radius of a circular aperture with area equal to an ellipse that is at least 85% filled with spectra; I symmetrised the fibre positions for NGC 1023 and NGC 3626 when calculating R_{max}, due to these galaxies not being centred on the Mitchell Spectrograph field of view (FOV). I find the data to extend beyond $2R_{\text{e}}$ in most cases, similar to the FOV obtained SLUGGS for less massive ETGs; as such, these data are highly complementary to the ATLAS^{3D} observations of these galaxies. I obtain ATLAS^{3D} R_{max} values from Table B1 in Emsellem et al. (2011), using the same R_{e} values as before, and I obtain SLUGGS R_{max} values using Table 1 of Arnold et al. (2014).

I binned together spectra in the galaxies' outer regions using the Voronoi-binning algorithm

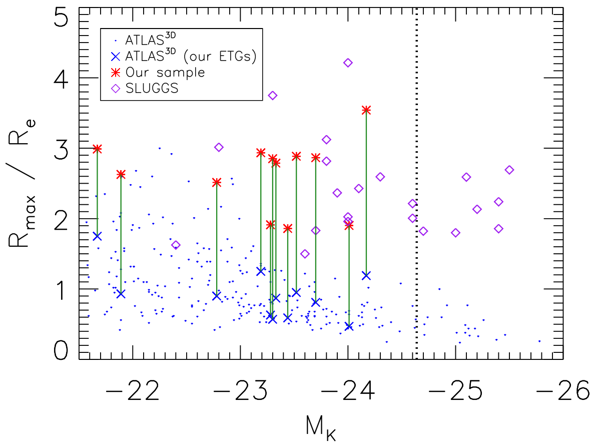

Figure 3.2: Plot of $R_{\rm max}/R_{\rm e}$. Blue crosses represent the ATLAS^{3D} values for our galaxies, and green lines show the difference between our values and the ATLAS^{3D} ones. All other lines and symbols are as before. Our coverage beyond $2R_{\rm e}$ in many cases and is comparable to the coverage of SLUGGS over lower-mass ETGs, whereas ATLAS^{3D} generally reaches approximately $1R_{\rm e}$.

Galaxy	Obs. time (s)	Obs. date	Pointings	$R_{\rm max}/R_{\rm e}$	$R_{\rm max}$ (kpc)
NGC 680	9000	Jan 2011	1	3.5	9.3
NGC 1023	39600	Jan 2011	2	1.9	4.9
NGC 2685	44100	Jan 2011	2	2.5	5.2
NGC 2764	81000	Mar 2010	1	2.9	6.9
NGC 3522	12600	Jan 2011	1	3.0	3.8
NGC 3626	21600	Apr 2011	1	2.9	6.9
NGC 3998	66600	Mar 2010	1	2.8	3.7
NGC 4203	12600	Jun 2010	1	1.9	3.9
NGC 5582	59400	Jun 2010	1	1.9	7.1
NGC 5631	25200	Apr 2011	2	2.9	7.8
NGC 6798	21800	Jun 2010	1	2.9	8.9
UGC 03960	18000	Jan 2011	1	2.6	7.3

Table 3.2: Summary of Mitchell spectrograph data for the twelve sample ETGs in terms of observation time, date of observing run, number of pointings and achieved (circular) aperture radius $R_{\rm max}$. The kpc values of $R_{\rm max}$ were calculated using the distances given in Cappellari et al. (2011a) and references therein.

of Cappellari & Copin (2003) in order to improve the S/N of the observations away from the galaxies' centres, after broadening each galaxy's spectra to the largest measured spectral FWHM for that galaxy. As in Chapter 2 of this thesis, I used a target S/N of 20 per spectral pixel ($\simeq$ 30 per Å) for all galaxies. I detail the observation times, observation date, number of pointings and achieved $R_{\rm max}$ for each galaxy in Table 5.1

3.3 Flux calibration

It was not possible to flux-calibrate the Mitchell Spectrograph spectra in the usual manner, due to a lack of suitable flux standard star observations. I therefore performed flux calibration by comparing un-calibrated Mitchell spectra to flux-calibrated data from previous observations of these targets: I compared my spectra for NGC 3522 to the Sloan Digital Sky Survey (SDSS; Ahn et al., 2014) spectrum for that galaxy and I further compared my sample galaxy spectra to SAURON spectra from ATLAS$^{\rm 3D}$, after verifying the flux-calibration to be consistent between the SDSS and ATLAS$^{\rm 3D}$ datasets. NGC 3522 is one of two galaxies that I have in common with the Sloan spectral sample, the other being UGC 03960.

First, I verified that the SAURON and SDSS datasets were consistent. I took the SDSS spectrum of NGC 3522 and obtained an equivalent SAURON spectrum by summing over a three-arcsecond aperture in order to match the SDSS fibre radius. I matched the spectral resolutions and then smoothed both spectra; this latter step negates small-scale differences between the spectra, leaving large scale differences only. I divided the spectra through and then fitted a seventh-order polynomial to derive a correction curve. I find the resulting curve to be almost flat over most of the SAURON wavelength region, as shown in Figure 3.3: the smoothed spectra never show more than a 3 per cent difference, which much of this difference occurring at the far red end of the SAURON spectrum. From this, I conclude that the flux calibration for NGC 3522 is consistent between ATLAS$^{\rm 3D}$ and SDSS.

Next, I tested whether a single flux-calibration curve would be valid for my sample; I did this because of the shorter wavelength range of the ATLAS$^{\rm 3D}$ data with respect to my own data, which means that I could not flux-calibrate my spectra entirely using the ATLAS$^{\rm 3D}$ data alone. I compared the central Mitchell spectrum for each galaxy with a SAURON spectrum obtained by summing over an equivalent region, and I then calculated correction curves in the same manner as described above. I show the results of this process in Figure 3.4. I find that the

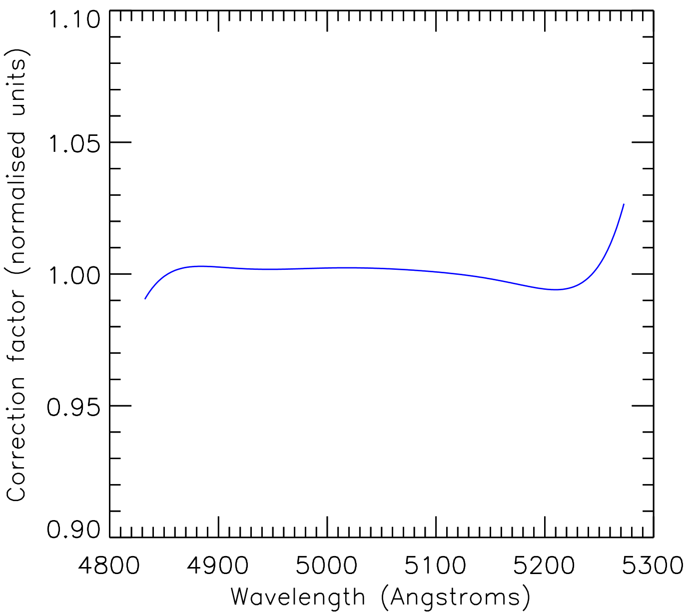

Figure 3.3: Polynomial SAURON-to-SDSS correction curve obtained for NGC 3522 over the wavelength range of the reduced ATLAS^{3D} datacube (4825 - 5280 Å). The curve is near-flat, so the SDSS and ATLAS^{3D} data for this galaxy have consistent flux calibrations.

flux-calibration curves are broadly similar across the whole sample, with the root-mean-square scatter of the curves about the mean being never more than 4.0 per cent. As such, I conclude that a single calibration curve is indeed valid for the galaxies in this sample.

I obtained an initial correction curve by comparing the central Mitchell Spectrograph spectrum of NGC 3522 with the corresponding SDSS spectrum, with the calibration curve derived in the same manner as before. I applied this curve to all Mitchell spectra, and I show the resulting Mitchell-to-SAURON curves in the left-hand panel of Figure 3.5, in which it can be seen that the Mitchell curves still show significant offsets from ATLAS^{3D} at the blue end. I therefore derived an additional correction factor by fitting a seventh-order polynomial to the *average* Mitchell-SAURON calibration offset, while forcing the polynomial to approach unity at wavelengths redder than the SAURON wavelength range. I applied this polynomial curve to the Mitchell-to-SDSS curve found previously, and then applied the resulting final curve to all spectra of the sample galaxies. I show the resulting Mitchell-to-SAURON calibration curves in the right-hand side of Figure 3.5; the mean calibration curve is now consistently below 1% throughout the ATLAS^{3D} wavelength range.

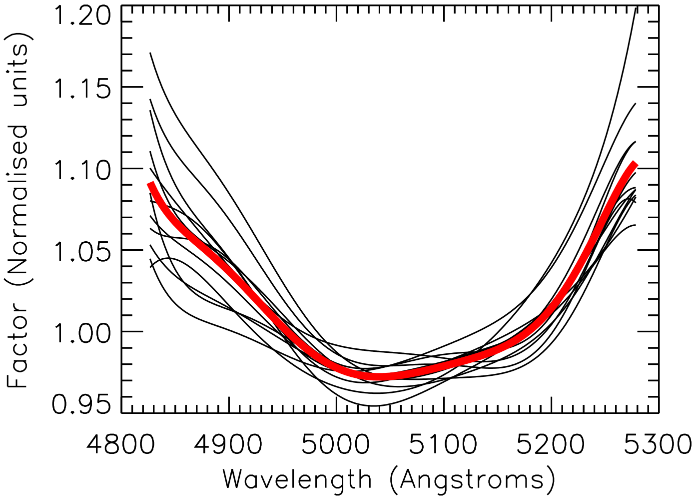

Figure 3.4: Mitchell-to-SAURON flux calibration curves (black lines) calculated for all galaxies in normalised units. The thick red line shows the average curve. The calculated curves are broadly similar, though a degree of scatter is evident. The root-mean square scatter from the mean is at most 4.0 per cent.

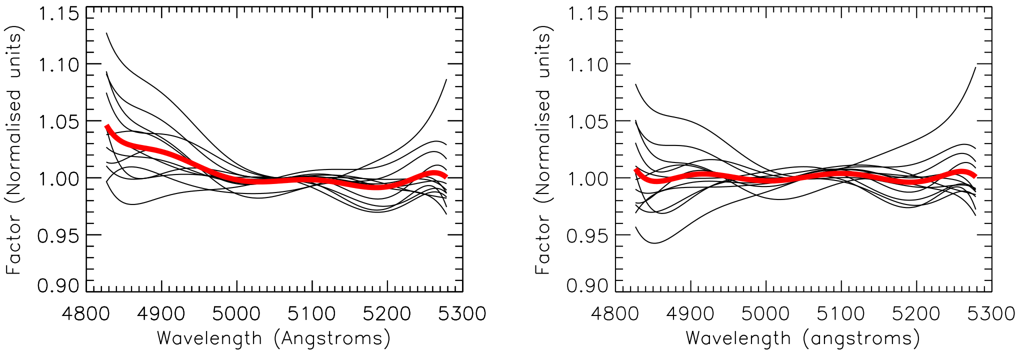

Figure 3.5: Mitchell-to-SAURON flux calibration curves, with all lines as in Figure 3.4. Left side: calibration curves obtained after applying the Michell-to-SDSS correction curve calculated for NGC 3522. Right side: calibration curves obtained after further applying the Mitchell-to-SAURON correction curve discussed in the text. A significantly improved flux-calibration is obtained with respect to ATLAS^{3D}.

3.4 Stellar kinematics

I obtained stellar kinematics for the full galaxy sample using the pPXF method (Cappellari & Emsellem, 2004; Cappellari, 2017). I use ELODIE stars for stellar templates and I use a tenth-degree additive Legendre polynomial correction, as described in the previous chapter. I present line-of-sight kinematics for my full galaxy sample in Figures 3.6-3.9.

I determined random measurement errors by adding Gaussian noise to the spectra and rerunning the fits with zero bias for 100 iterations each. As expected, these errors depend significantly on the S/N of a given spectrum; for spectra with S/N of 25 or below, I obtain mean error values of 3.0 km/s, 4.4 km/s, 0.04 and 0.05 for velocity, velocity dispersion, h_3 and h_4 respectively. However, these errors alone do not accurately represent the true level of uncertainty, as they ignore possible systematic effects such as imperfect sky subtraction and template mismatch (e.g. Arnold et al., 2014). I estimate the level of systematic error by comparing the kinematics presented above with pPXF kinematics derived using the MILES library of observed stars (Sánchez-Blázquez et al., 2006). I apply pPXF in the same manner as for the ELODIE stars, after broadening the spectra to match the MILES library resolution of 2.51 Å (Falcón-Barroso et al., 2011); following this, I calculate the 1σ dispersions between the two sets of kinematics for all spectra of all galaxies with respect to zero. I derive systematic errors of 3.3 km/s, 4.3 km/s, 0.03 and 0.04 for the velocity, dispersion, h_3 and h_4 respectively, which I add in quadrature to the original errors; this results in median overall errors values of 4.1 km/s, 5.7 km/s, 0.04 and 0.05 respectively.

The treatment of errors in the above manner is not strictly correct, in that *systematic* sources of error are being added in quadrature with *random* sources of error; however, this is necessary for the purpose of later modelling of the kinematics, as the use of Monte Carlo errors alone would result in the "true" level of error being severely underestimated. One possible alternative here would be to symmetrise the kinematics in some manner before performing modelling; however, this would be difficult to accomplish for the Mitchell data, due to galaxy centres typically being neither in the centre of a Mitchell fibre nor exactly between the fibres.

I compare the kinematics from ELODIE and MILES templates in Figure 3.10. I find 1-1 agreement in the mean velocity, h_3 and h_4 values, though with non-negligible levels of scatter. However, the MILES velocity dispersions are systematically higher overall, particularly when the ELODIE velocity dispersion is low. This means that the outskirts of my ETGs are found

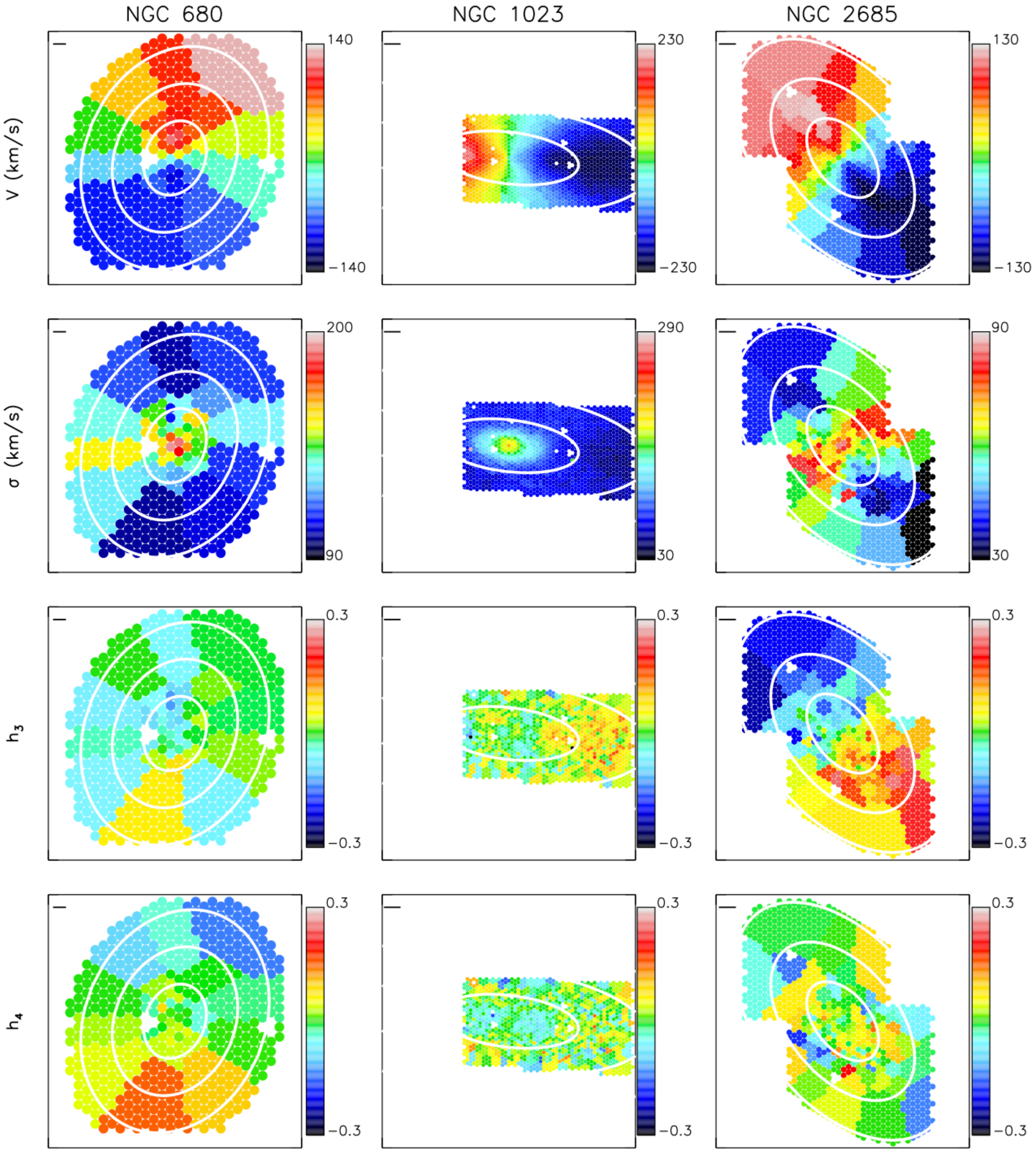

Figure 3.6: Stellar kinematics maps of NGC 680, NGC 1023 and NGC 2685. Rows from top to bottom: velocity (km/s), velocity dispersion (km.s^{-}1), h_3 and h_4. The solid black lines mark a length of 1 kpc. The white contours are spaced in steps of R_e. Fibre positions from the missing NGC 2685 dither in the top-left pointing have been re-added for presentational purposes, with kinematics assigned to each from the nearest Voronoi bin.

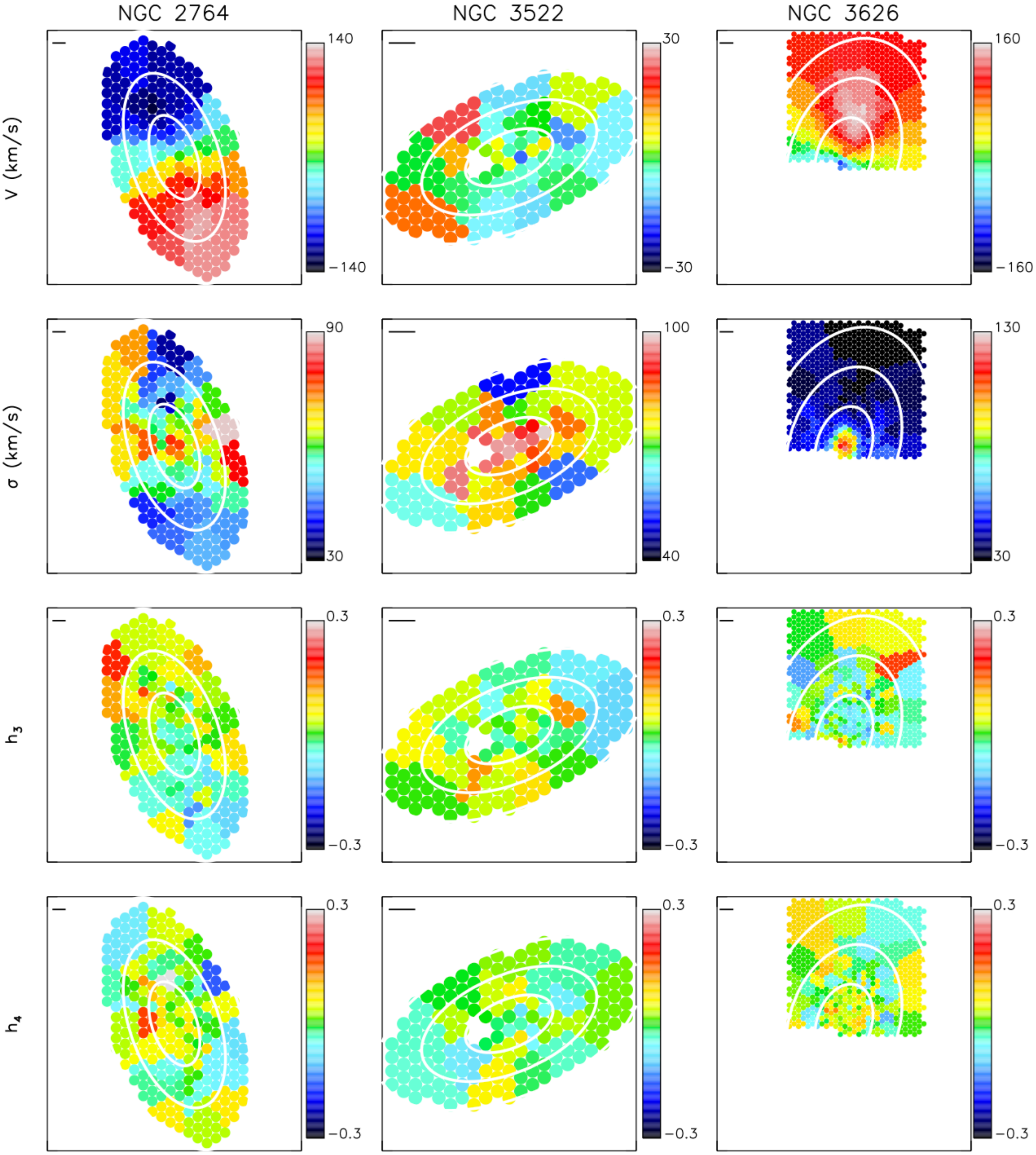

Figure 3.7: As in Figure 3.6, but for galaxies NGC 2764, NGC 3522 and NGC 3626.

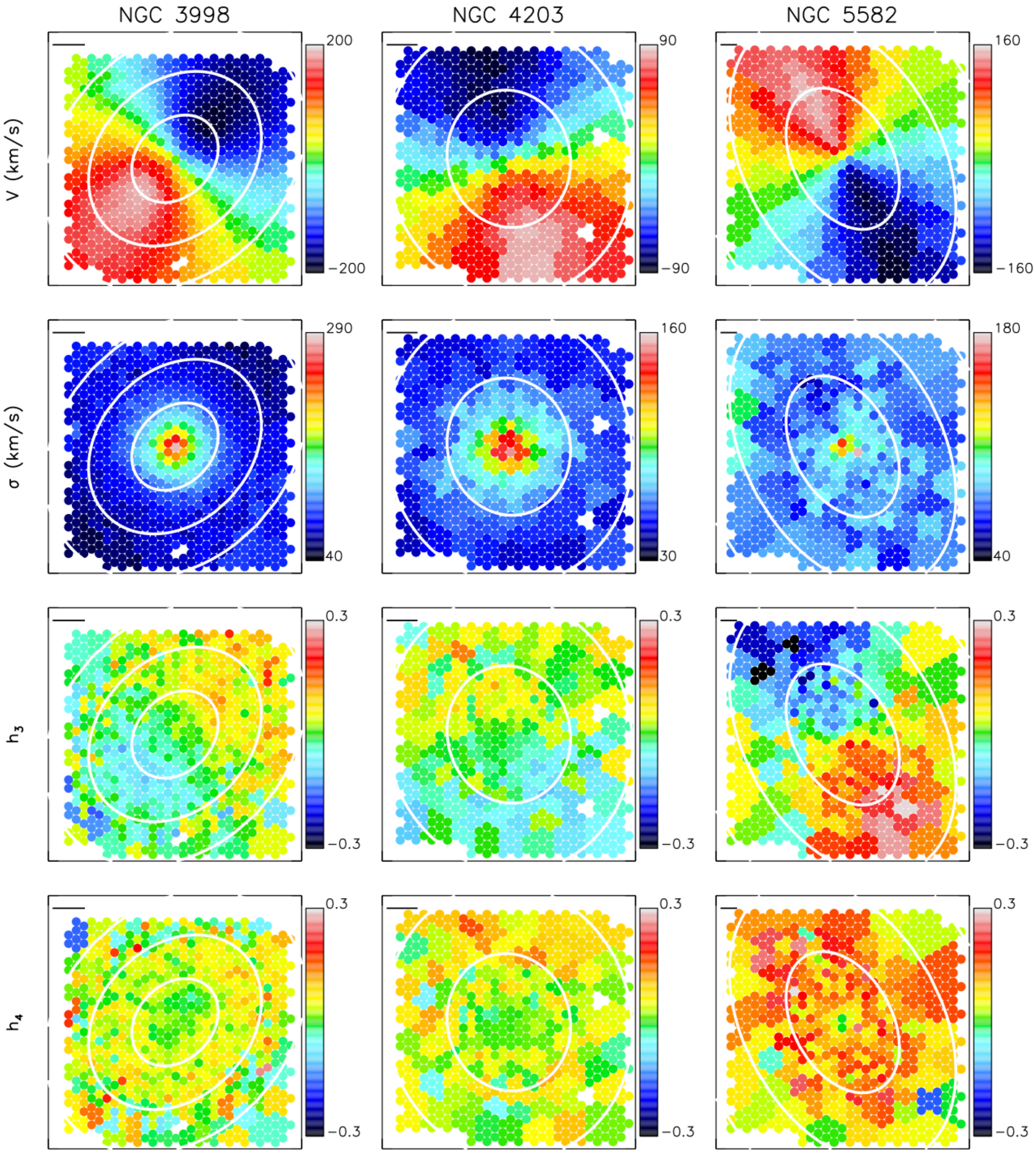

Figure 3.8: As in Figure 3.6, but for galaxies NGC 3998, NGC 4203 and NGC 5582. Fibre positions from the missing NGC 4203 dither have been re-added for presentational purposes, with kinematics assigned to each from the nearest Voronoi bin.

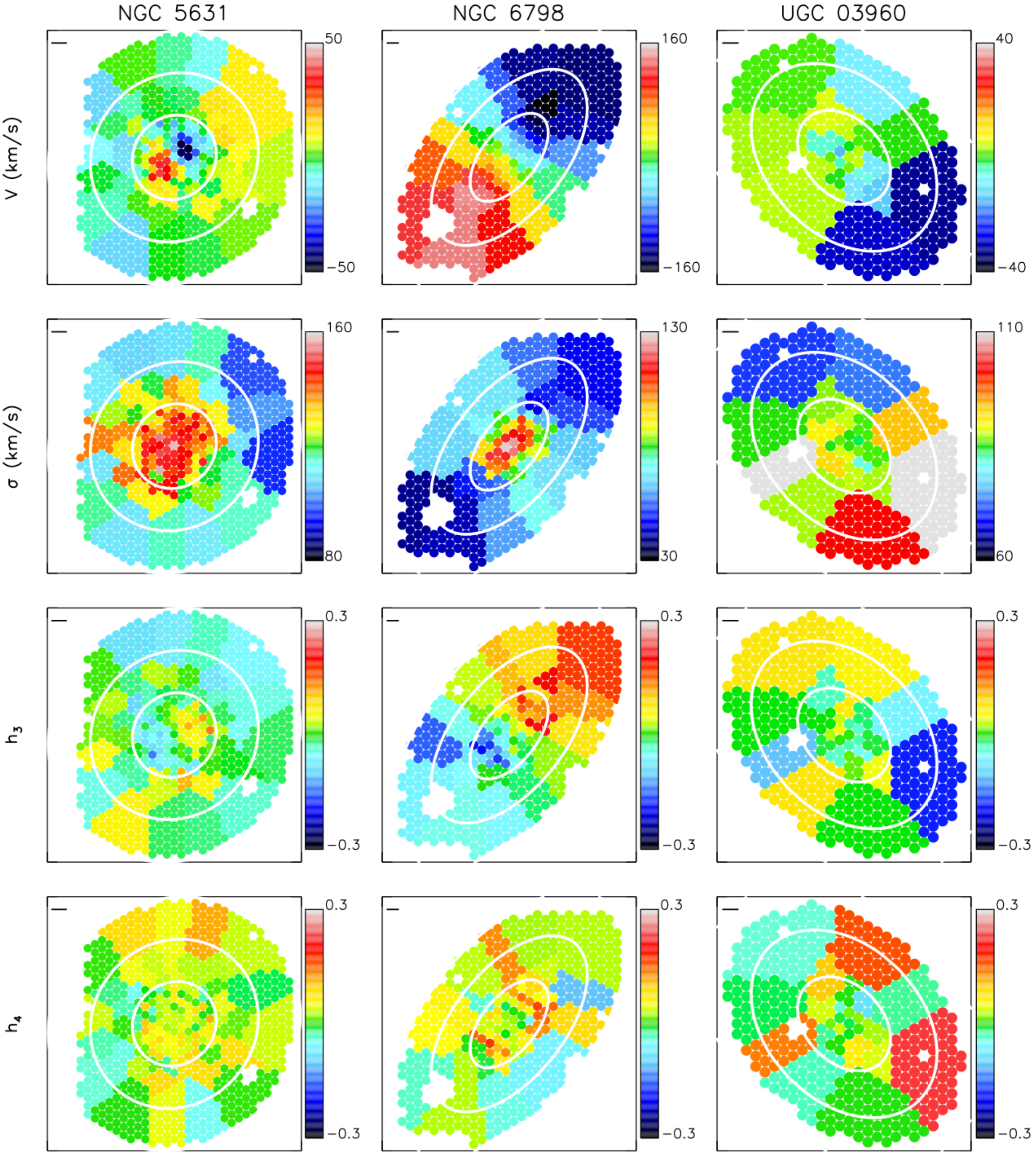

Figure 3.9: As in Figure 3.6, but for galaxies NGC 5631, NGC 6798 and UGC 03960.

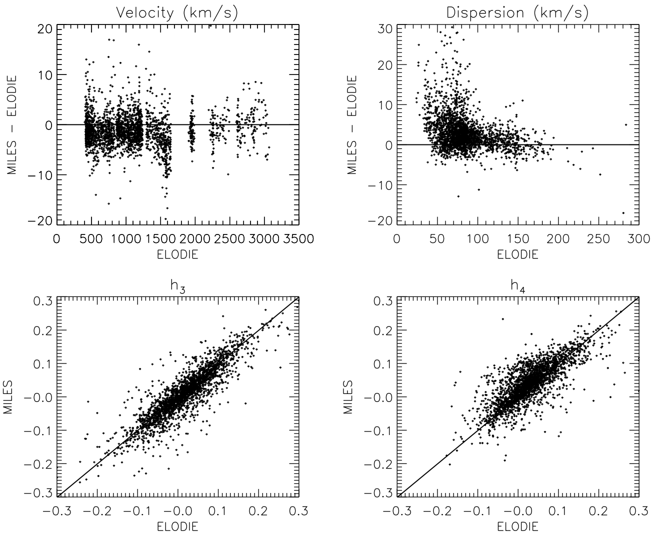

Figure 3.10: Comparison of Mitchell stellar kinematics for the twelve sample galaxies derived using ELODIE and MILES libraries in pPXF. I show the values of h_3 and h_4 from both ELODIE and MILES libraries, while I show the relative differences between ELODIE and MILES mean velocities and velocity dispersions in order to emphasise differences. There is good overall agreement in the mean velocity, h_3 and h_4 values, though with non-negligible scatter. The MILES dispersions are larger when the ELODIE values are low, which I argue to be due to the MILES library's higher intrinsic spectral resolution FWHM.

to have higher velocity dispersions on average when the MILES library is used rather than ELODIE. I view the ELODIE results as being more reliable in such cases, however, due to the MILES library's lower spectral resolution, which corresponds to a velocity dispersion of ~ 60 km/s: this is above what I find with ELODIE in most of the galaxies' outskirts, which suggests that MILES is not an ideal library for studying such regions' kinematics. For ELODIE velocity dispersions below 60 km/s, the derived MILES dispersions are 5.5km/s higher on average.

Aside from the choice of stellar templates, other potential sources of systematic error include imperfect sky subtraction and the choice of corrective polynomial when applying pPXF. I assess the importance of the latter effect by re-running pPXF with a tenth-order *multiplicative* polynomial correction using ELODIE stars in the same manner as described previously. I again used pPXF to fit and subtract the sky, therefore obtaining model galaxy spectra of the form

$$G_{\mathrm{mod}}(x) = \sum_{k=1}^{K} w_k[\mathscr{L}(cx) * T_k](x) \times \sum_{l=1}^{L} b_l \mathscr{P}_l(x) + \sum_{n=1}^{N} s_n S_n(x), \tag{3.1}$$

in which all symbols are as before. I compare the resulting kinematics with those obtained with an additive polynomial in Figure 3.11, demonstrating near 1-1 agreement between the

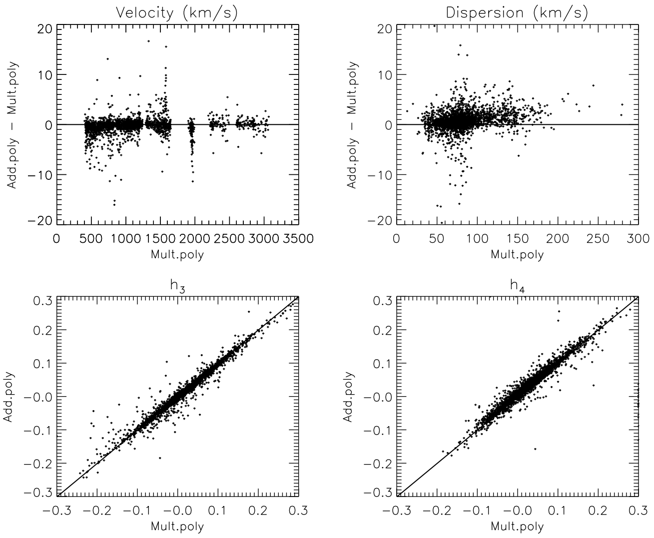

Figure 3.11: Comparison of stellar kinematics derived from ELODIE stars in pPXF when using additive and multiplicative polynomial corrections. "Add. poly" refers to kinematics extracted using an additive polynomial, while "Mult. poly" refers to those extracted using a multiplicative polynomial. There is good agreement between all four moments; the velocity dispersion tends to slightly higher values when an additive polynomial is used, but this effect is small compared to the derived uncertainties.

two approaches. I assess the level of systematic error arising from the choice of polynomial by calculating 1σ dispersion between the kinematics with respect to zero for all spectra of all galaxies, finding error values of 0.8 km/s, 1.7 km/s, 0.007 and 0.01 for mean velocity, velocity dispersion, h_3 and h_4 in turn. These are much lower than those arising from the choice of template stars, indicating that the choice of polynomial does not significantly impact upon the kinematics; I therefore do not factor this into my calculated errors.

I also estimated the systematic error arising from imperfect sky subtraction, by comparing the kinematics described above to two sets of kinematics obtained after over-subtracting and under-subtracting the sky by 10% respectively; this is similar to the check performed in Weijmans et al. (2009). I find a median variation of 10.3% between neighbouring Mitchell sky frames, meaning that 10% is a reasonable amount by which to over- or under-subtract the sky when performing this comparison. For each of these new kinematic datasets, I compared to the original kinematic dataset and then calculated systematic errors in the same manner described previously. From this process, I derived systematic errors of 1.7 km/s, 1.7 km/s, 0.02 and 0.02 for velocity, dispersion, h_3 and h_4 respectively; these values are also small compared to systematic errors inferred from comparing the MILES and ELODIE stellar libraries, so I do not factor this into my error calculations.

I also derived pPXF kinematics for the first two moments (V, σ) only, in order to prevent any dependence of (V, σ) on h_3 and h_4 or on the pPXF penalty parameter in cases where only V and σ are needed. I obtained errors in the same way as before, first running Monte-Carlo resimulations of the pPXF fits with added Gaussian noise and then deriving systematic errors by comparing the kinematics obtained with the ELODIE and MILES template libraries for all spectra of all galaxies. I obtained systematic errors of 5.9 km/s and 8.2 km/s for the mean velocities and velocity dispersions in turn; adding in quadrature with the Monte-Carlo errors, this produces median overall error values of 6.5 km/s and 9.1 km/s, respectively. As before, this treatment of the errors is not strictly correct, but is needed for later modelling work.

3.4.1 Comparison with ATLAS^{3D}

As all of the sample galaxies are included in the ATLAS^{3D} survey, it is useful to compare the derived kinematics with those derived previously with the SAURON instrument. Such a comparison is particularly interesting to carry out in light of the previously reported offsets in stellar velocity dispersion between ATLAS^{3D} and SLUGGS kinematics, with ATLAS^{3D} dispersions typically being somewhat higher in regions where the datasets overlap (Foster et al., 2016).

I first compare my kinematics to those of ATLAS^{3D} by finding all Mitchell spectra for which at least one ATLAS^{3D} Voronoi bin lies within the radius of a Mitchell fibre (2.08″); I then compare the kinematics of these spectra with those of the closest ATLAS^{3D} spectral bin. I compare the mean velocities and velocity dispersions calculated from 2-moment pPXF fits, as well as the kinematics calculated from 4-moment fits. I show the results of this comparison in Figure 3.12. I find excellent agreement in the mean line-of-sight velocities calculated between the two datasets; however, I also find the ATLAS^{3D} velocity dispersions to be systematically higher on average when h_3 and h_4 are included, with the h_3 and h_4 comparisons showing a high degree of scatter.

There are several potential confounding factors in this comparison. The ATLAS^{3D} spectra for these galaxies have an instrumental dispersion of $\sigma_{\mathrm{instr}} \approx 98$ km/s, whereas my pPXF fits imply some of these galaxies to have stellar velocity dispersions below this value even within the FOV covered by ATLAS^{3D}. In addition, the ATLAS^{3D} datacubes are often significantly binned towards the edge of their FOV, which could serve to artificially enhance the measured stellar velocity dispersion away from the galaxies' centres (e.g. Arnold et al., 2014). Lastly, the Mitchell fibres are significantly larger than the $0.8'' \times 0.8''$ spaxels employed by ATLAS^{3D},

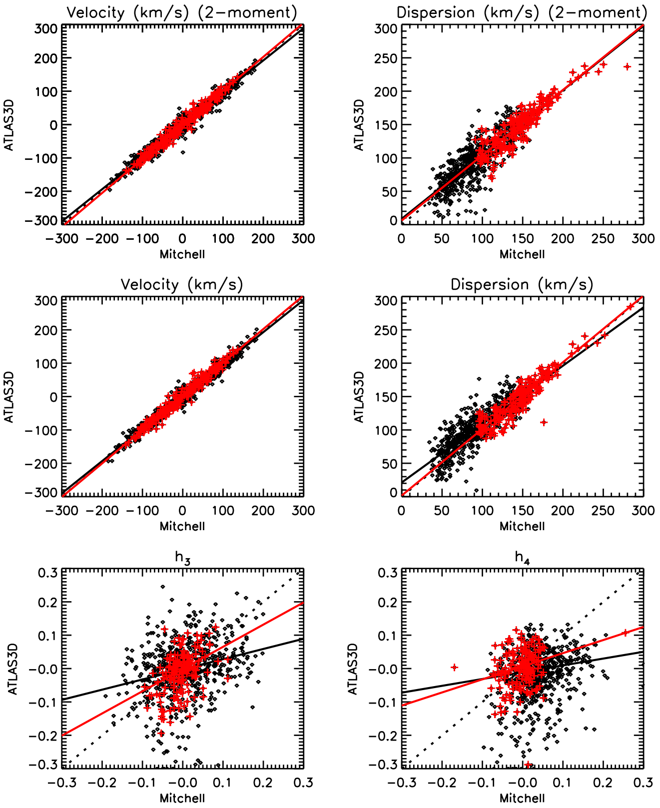

Figure 3.12: Comparison of the stellar kinematics of the twelve sample galaxies from Mitchell Spectrograph observations with the kinematics reported by ATLAS^{3D}. The dotted lines show the 1-1 relation, while the solid lines are obtained from a robust least-absolute-deviation fit. Unbinned datapoints with high velocity dispersions are highlighted with red crosses; the red solid lines show robust least-absolute-deviation fits to these points. I find good consistency between the two datasets once low velocity dispersion datapoints are excluded.

which could likewise alter the inferred stellar kinematics.

Motivated by the above, I performed a second comparison in the following way. I first selected datapoints to compare in the same manner as before. I then excluded any datapoint for which the Mitchell Spectrograph velocity dispersion is below 98 km/s, and I further excluded datapoints for h_3 and h_4 for which the Mitchell velocity dispersion was below 120 km/s; this is to ensure that the dispersion could be accurately measured in ATLAS^{3D} without strong penalisation of h_3 or h_4. I further limited myself to data points in which neither the Mitchell nor the ATLAS^{3D} spectra have been binned, in order to ensure that the velocity dispersion in one or both datasets is not being enhanced by binning. I show the results of this in Figure 3.12, along with the results of the first comparison discussed previously. I now find excellent agreement between the mean velocity and velocity dispersion of the two datasets, though h_3 and

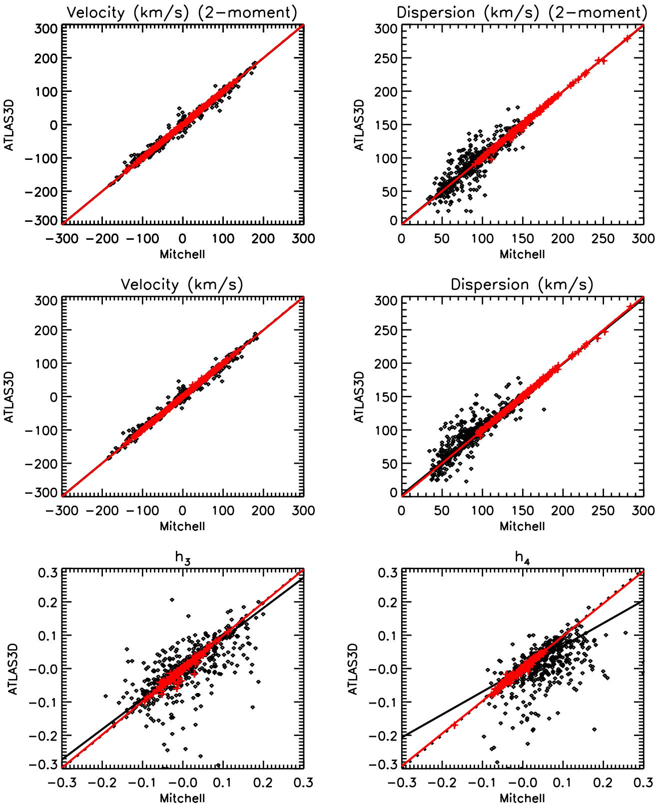

Figure 3.13: As in Figure 3.12, except that the Mitchell datapoints have been matched to the SAURON datapoint within 2.08 arcseconds that is *closest in value*. I obtain very good agreement between the Mitchell and ATLAS^{3D} kinematic datasets once binned datapoints and datapoints with low velocity dispersions have been removed, with almost no scatter; I conclude from this that the Mitchell and ATLAS^{3D} datasets are fully consistent.

h_4 continue to show significant scatter.

These two comparisons suggest that spatial binning is at least partly responsible for the observed offsets in velocity dispersion between my results and those of ATLAS^{3D}, which in turn suggests that binning could play a role in observed ATLAS^{3D}-SLUGGS offsets. A similar conclusion was reached by Foster et al. (2016), who found that the level of systematic velocity dispersion offset reduced significantly between the ATLAS^{3D} and SLUGGS datasets when only unbinned ATLAS^{3D} datapoints were considered; Pastorello et al. (2016) likewise compare ATLAS^{3D} dispersions with their new SLUGGS data of NGC 1023, which largely overlap with unbinned ATLAS^{3D} regions, and obtain good agreement between the dispersions.

I present one final comparison between the Mitchell and ATLAS^{3D} stellar kinematic datasets in Figure 3.13. Here, I take each Mitchell kinematic datapoint in turn and find all SAURON

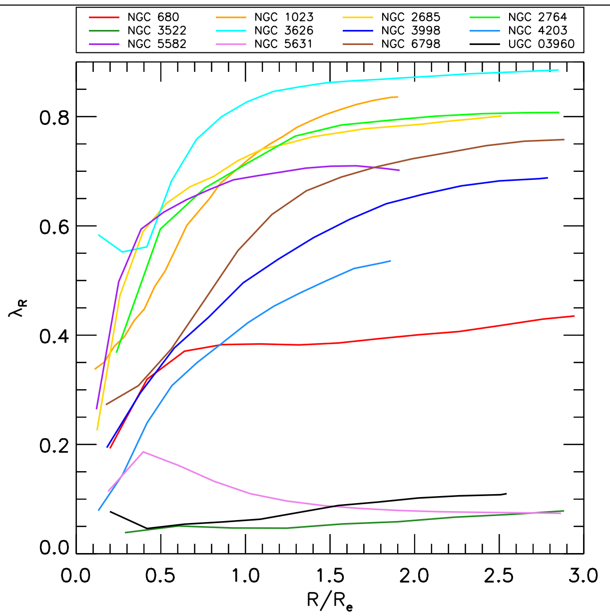

Figure 3.14: λ_R profiles constructed from Mitchell Spectrograph stellar kinematics of the twelve sample ETGs. I find no abrupt drop in λ_R beyond the central half-light radius, with all but one galaxy (NGC 5631) showing a slightly rising or flat profile overall.

datapoints within the Mitchell fibre radius as before; I then compare each Mitchell datapoint to the SAURON datapoint that is *closest in value* to the Mitchell datapoint being considered. I then select a subset of high velocity dispersion unbinned datapoints in the same manner as described above, highlighting these on the same figure. I find tight 1-1 relations with almost no scatter in this case; thus, I find that the stellar kinematics from the Mitchell observations are fully consistent with the stellar kinematics from the ATLAS^{3D} survey.

3.4.2 Angular momentum

I considered the angular momenta of the sample galaxies using the λ_R and Λ_R parameters as proxies. I present λ_R spin profiles for the sample galaxies in Figure 3.14; these profiles were constructed with mean velocities and velocity dispersions from pPXF fits to V and σ only with additive polynomial corrections, using Equation 2.7 of this thesis. I symmetrized the kinematics for NGC 1023 and NGC 3626, due to these two galaxies not being centred on my FOV. I find all but one galaxy to show a λ_R profile beyond 1 R_e that is rather constant or else slightly rising; the exception here is NGC 5631, which is a known kinematically-decoupled core (KDC) host and which displays a slightly falling λ_R profile over much of the FOV. I therefore find that galaxies in this sample that are FRs (SRs) at 1 R_e, following the Emsellem et al. (2011) definitions, keep their high (low) λ_R profiles over the full FOV.

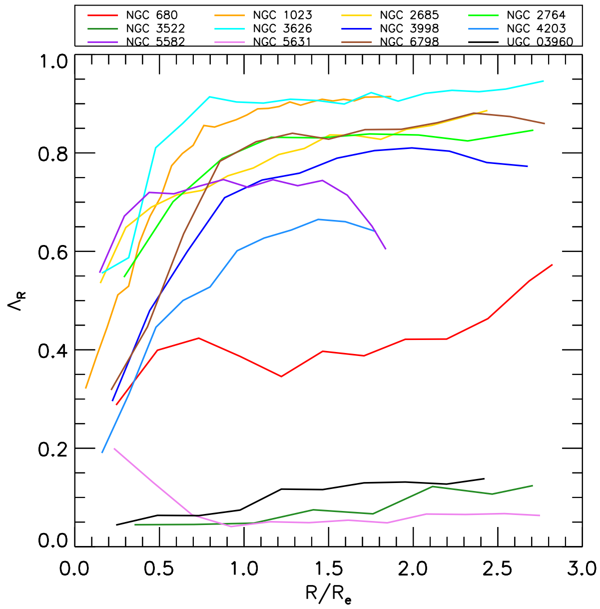

Figure 3.15: Λ_R profiles for the twelve sample ETGs. I find no major change in the profiles' behaviour, similar to the λ_R case, thus confirming my previous result that no abrupt change in these galaxies' spin properties takes place.

I present Λ_R profiles for the sample galaxies in Figure 3.15. I constructed these profiles using the same method as described in Section 2.4 of this thesis, applying Equation 2.7 to successive overlapping elliptical annuli of width 5" with centres spaced in steps of 1". My results here are similar to the λ_R case, with no major changes in the behaviour of the Λ_R profiles beyond the central effective radius. Such a result is not surprising, given my findings for λ_R: though Λ_R is better-suited to emphasise transitions, profiles of Λ_R are typically very similar in shape to profiles of λ_R (e.g. Bellstedt et al., 2017).

3.5 Ionised gas kinematics

I extracted ionised gas kinematics and fluxes using the GANDALF code of Sarzi et al. (2006), following the methodology outlined in the previous chapter. I fitted for the Hβ, [O III] and [N I] emission features, fitting first to [O III] only and then fixing the gas kinematics to those of the [O III] feature, while also allowing for a tenth-order multiplicative polynomial correction. I extracted all [O III] features with $A/N > 4$ and I extracted all Hβ and [N I] features with $A/N > 3$. I applied the GANDALF-derived continuum correction to each of our spectra before proceeding, in order to account for any residual continuum contamination.

Although the above procedure produced good fits for the vast majority of spectra in my sample, I noted significant fit residuals around the Hβ region over much of the FOV for NGC

Galaxy	θ_*	θ_{ion}	$\lvert\theta_* - \theta_{ion}\rvert$ (°)
NGC 680	359.5 ± 8.5	22.5 ± 10.3	23.0
NGC 1023	86.5 ± 1.5	N/A	N/A
NGC 2685	38.0 ± 3.8	88.5 ± 5.5	50.5
NGC 2764	196.5 ± 7.8	185.5 ± 13.0	9.0
NGC 3522	116.5 ± 89.8	181.0 ± 24.5	64.5
NGC 3626	343.0 ± 4.0	168.0 ± 4.8	175.0
NGC 3998	136.5 ± 2.0	87.5 ± 2.5	49.0
NGC 4203	194.5 ± 6.8	198.0 ± 5.8	3.5
NGC 5582	29.0 ± 3.3	30.5 ± 3.5	1.5
NGC 5631	132.5 ± 31.5	319.5 ± 6.5	173.0
NGC 6798	139.0 ± 7.8	310.5 ± 7.0	171.5
UGC 03960	33.5 ± 89.8	97.0 ± 39.8	57.2

Table 3.3: Stellar and ionised gas kinematic position angles and uncertainties for the sample ETGs, measured anticlockwise from north to the receding part of the velocity map using the method of Krajnović et al. (2006), along with the misalignment angles between the two. I do not report an ionised gas position angle for NGC 1023 due to this galaxy's highly irregular gas kinematics.

2764. I found that I could reduce the level of the residuals by fitting to the Hβ feature independently of [O III], though the residuals remained non-negligible in this case. I note that NGC 2764 displays a relatively large Hβ flux, similarly to what I found for NGC 3626 in Chapter 2 of this thesis; this is a possible reason for the large residuals around Hβ that the GANDALF fits to NGC 2764 yield. Given that Hβ is the only age-sensitive stellar absorption feature within the wavelength range of the Mitchell Spectrograph data, I chose to exclude NGC 2764 from the stellar population analysis described in Section 3.7.

I present maps of [O III] flux and mean velocity extracted for the sample galaxies in Figures 3.16 and 3.17. I typically detect ionised gas at high A/N significantly beyond the central effective radius of the galaxies, and I also find several instances in which the ionised gas velocity is visibly misaligned with respect to the stellar velocity. I quantified this point by using the method described in Appendix C of Krajnović et al. (2006) to extract the kinematic position angles of the stellar and ionised gas components of my galaxies, by minimising the residuals between the velocity maps and their bisymmetrized equivalents; I present the results of this in Table 3.3, demonstrating the presence of significant star-gas misalignment in many of the sample galaxies. This is not a new result for these systems, being already apparent from the SAURON ionised gas maps published by ATLAS^{3D} (Davis et al., 2011), but is relevant when considering these galaxies' evolutionary pasts.

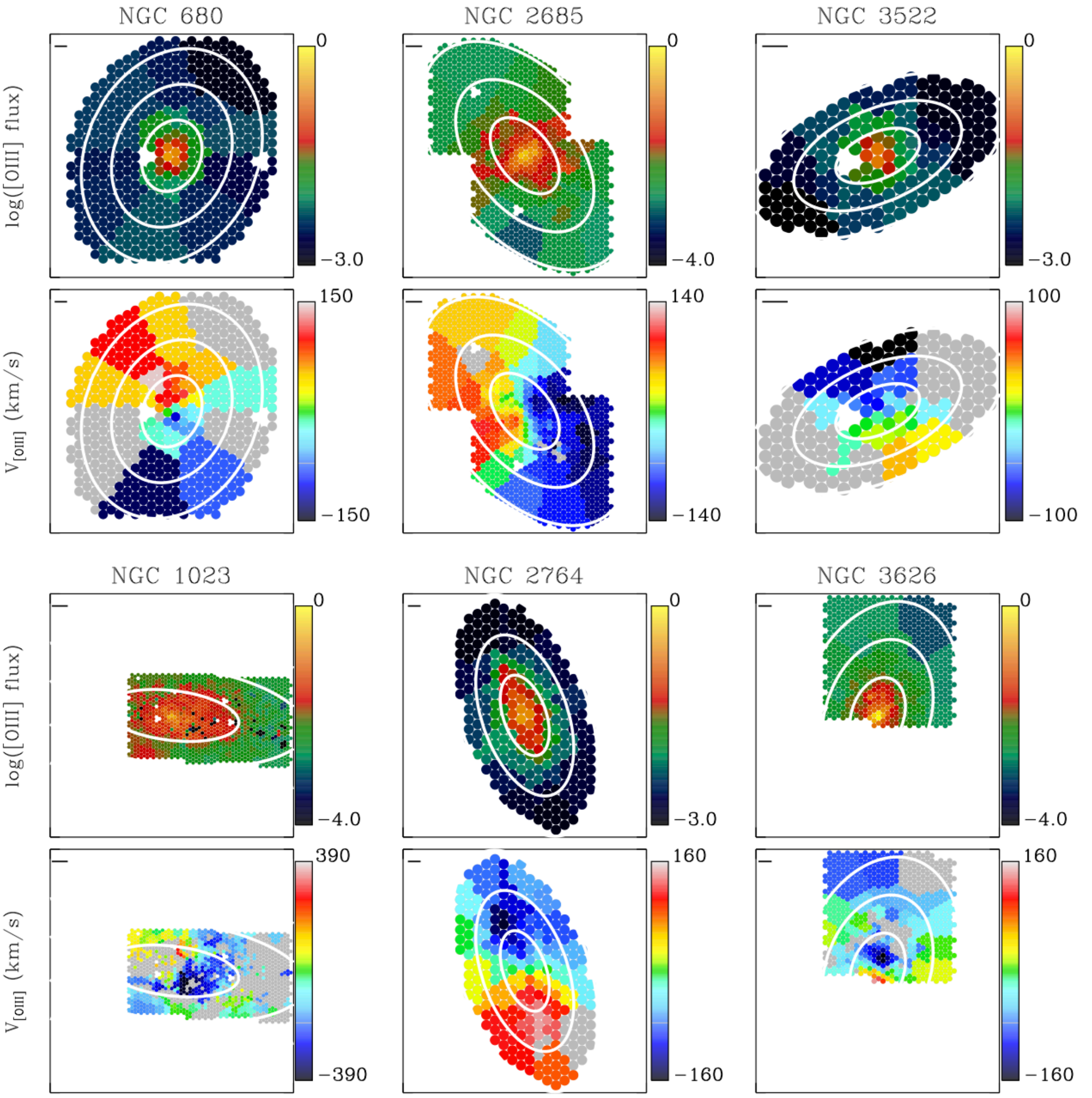

Figure 3.16: Maps of log([O III] flux) (top) and O III velocity (bottom, km/s) for the first six galaxies in the ETG sample. Flux is in arbitrary units, and has been divided through by the number of fibres comprising each spectral bin. Grey bins in the velocity maps indicate regions for which $A/N < 4$. The white contours are spaced in steps of R_e. The solid black lines in the top-left corner mark a length of 1 kpc. Fibre positions from the missing NGC 2685 dither in the top-left pointing have been re-added for presentational purposes, with kinematics and fluxes assigned to each from the nearest Voronoi bin.

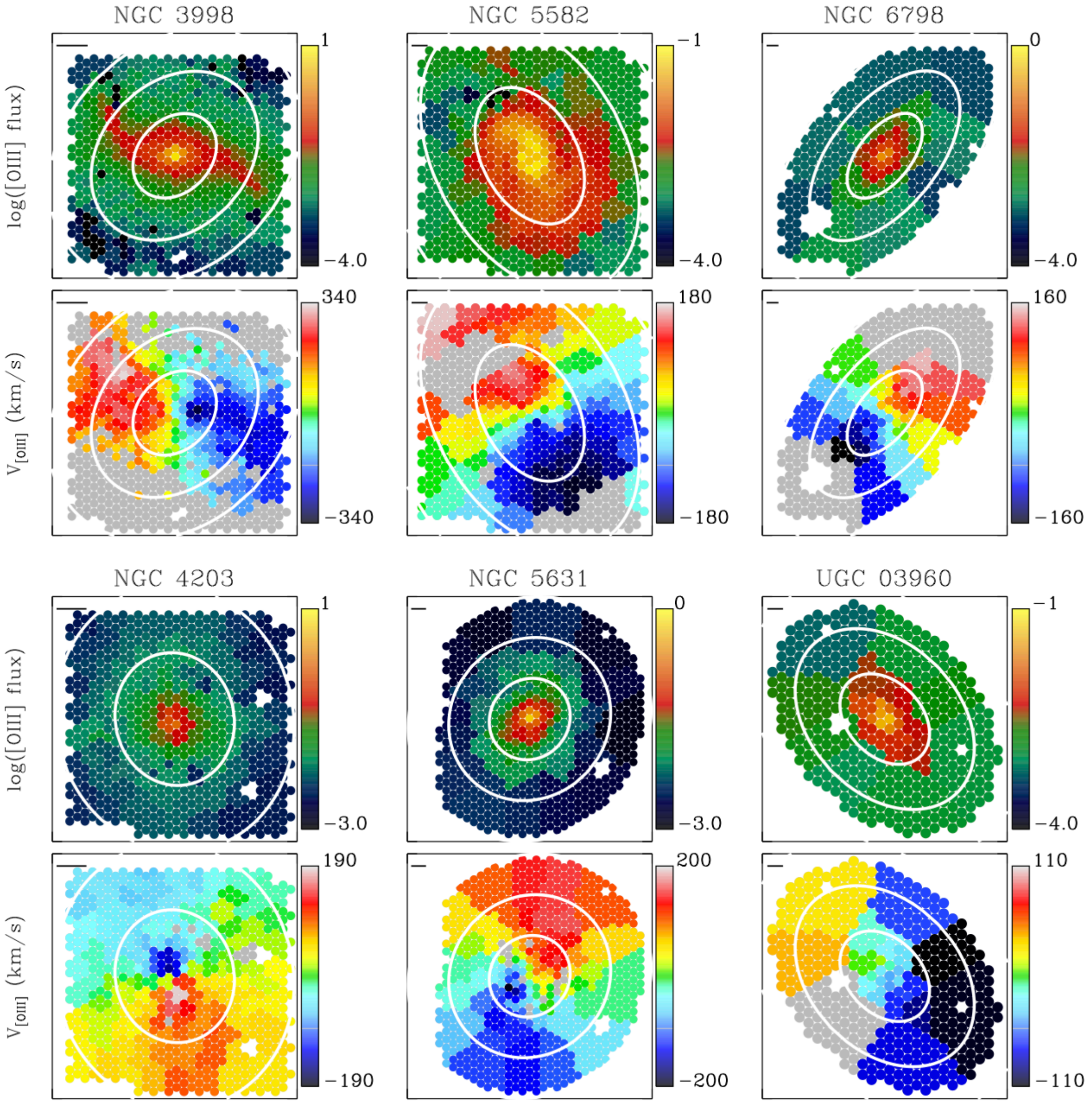

Figure 3.17: As in Figure 3.16, for the remaining ETGs in the sample. Fibre positions from the missing NGC 4203 dither have been re-added for presentational purposes, with kinematics and fluxes assigned to each from the nearest Voronoi bin.

3.6 Line indices

I performed Lick index measurements on my full sample of twelve galaxies, after broadening my spectra to the 14 Å FHWM line-index system (LIS) described by Vazdekis et al. (2010). I calculated the Hβ, Fe5015, Mg b and Fe5270 indices for all galaxies in the sample. I also calculated the Fe5335 index where possible; I was not able to calculate this index for all objects, as its red continuum region was redshifted beyond the available wavelength range in some cases. I calculated errors by performing 500 Monte-Carlo re-simulations, with Gaussian noise added to the spectra and to the input pPXF line-of-sight velocities. I set lower limits on the errors by calculating the differences between the indices from a given spectrum and those from the associated optimal template, likewise broadened to 14 Å FWHM; in practice, the errors from the Monte-Carlo re-simulations are typically larger than these lower limits. I present the resulting maps of the indices in Figures 3.18-3.21.

I calculated smoothed Hβ and Mg b profiles for the galaxies, using the same methodology outlined in the previous chapter for NGC 3626. I present these profiles in Figure 3.22. I find the majority of the sample galaxies to show roughly a flat Hβ profile. I observe steep Hβ rises for the galaxies NGC 2685 and NGC 6798, while I instead see significant falls for the galaxies NGC 2764 and NGC 3626. I find Mg b to fall with radius for most of my galaxies; NGC 2764 and NGC 3626 instead display a Mg b profile that is is near-flat.

In Figure 3.23, I assess the correlation between Mg b and $\sigma_{\rm e}$, the stellar velocity dispersion calculated over 1 half-light radius, out to multiple effective radii. I vary the Mg b aperture only: I take an elliptical aperture of major axis radius 0.5 $R_{\rm e}$ along with two elliptical annuli with boundaries at 0.5, 1 and 2 $R_{\rm e}$. I take the flux-weighted mean of all relevant Voronoi bins in each case, with errors propagated accordingly. I present the results in Figure 3.23, in which I also show least-absolute-deviation fits to the data. My least-absolute-deviation fits yield gradients of $\Delta(\mathrm{Mg}\,b)$/dex of 4.1, 2.5 and 4.3 for the aperture, inner annulus and outer annulus respectively. From visual inspection, I noted that differences between these gradients are largely driven by the galaxies NGC 2764 and NGC 3626, which both have a flat Mg b profile and low Mg b values; if I exclude these two galaxies, I obtain gradients of 4.0, 3.9 and 3.6 from the straight-line fits. As such, I find that a Mg b-σ correlation exists even out to large radii, similarly to the results of Greene et al. (2012) for massive galaxies.

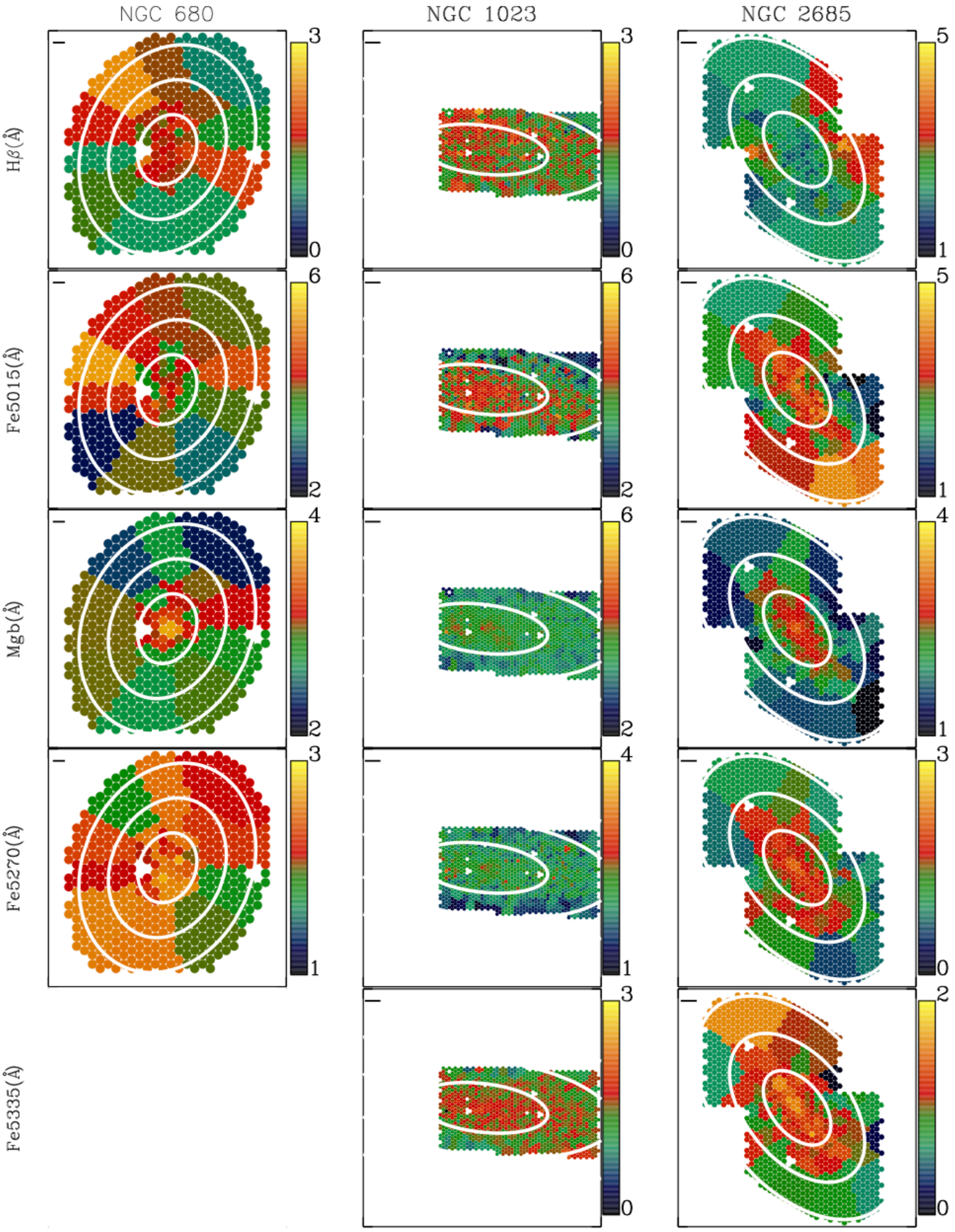

Figure 3.18: Maps of absorption line indices Hβ, Fe5015, Mgb, Fe5270 and Fe5335 for NGC 680, NGC 1023 and NGC 2685. All indices are calculated on the 14 Å line index system of Vazdekis et al. (2010). The solid black lines in the top left corner mark a length of 1 kpc. The white contours are spaced in units of R_e. Fibre positions from the missing NGC 2685 dither in the top-left pointing have been re-added for presentational purposes, with values assigned to each from the nearest Voronoi bin.

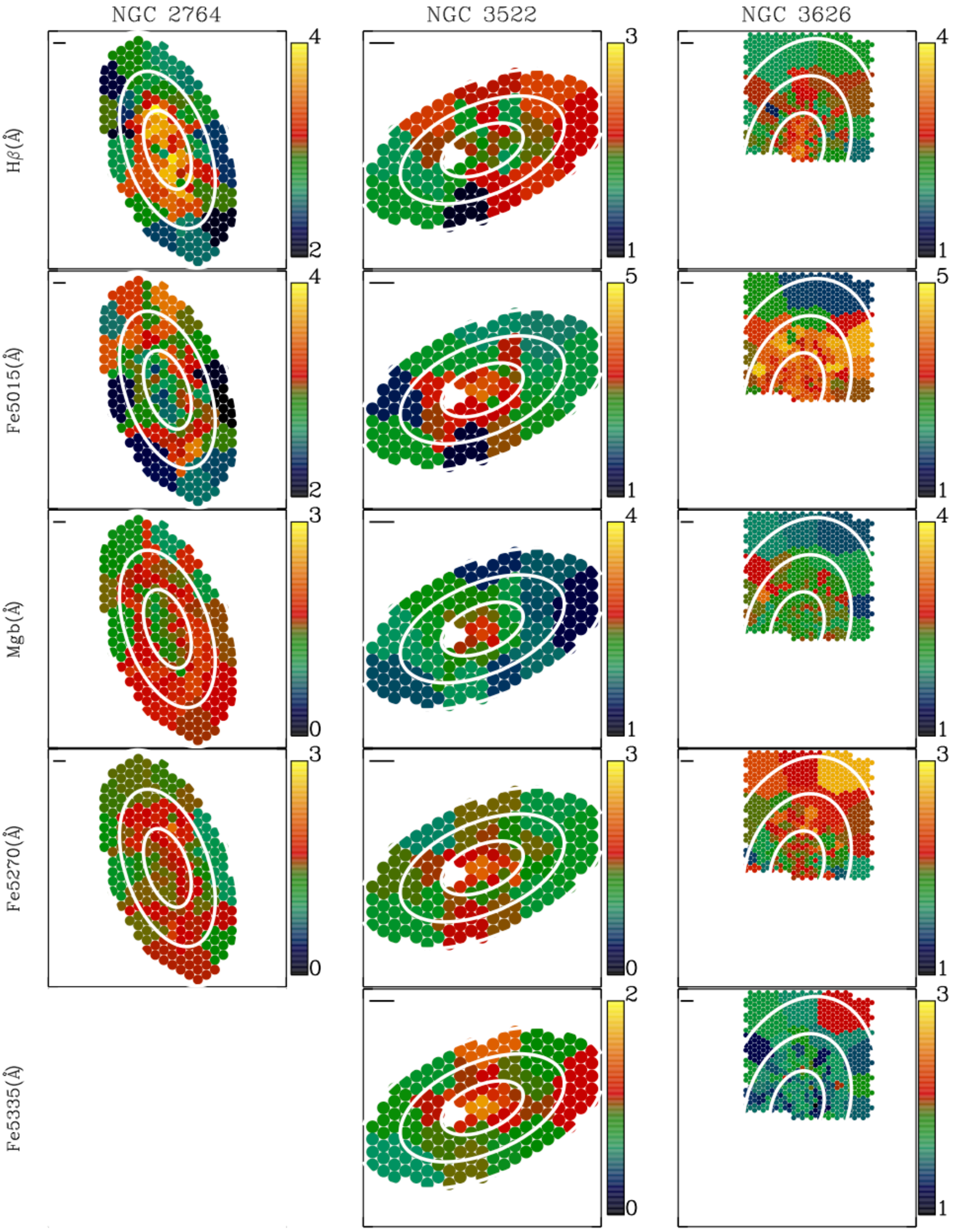

Figure 3.19: As in Figure 3.18, but for galaxies NGC 2764, NGC 3522 and NGC 3626.

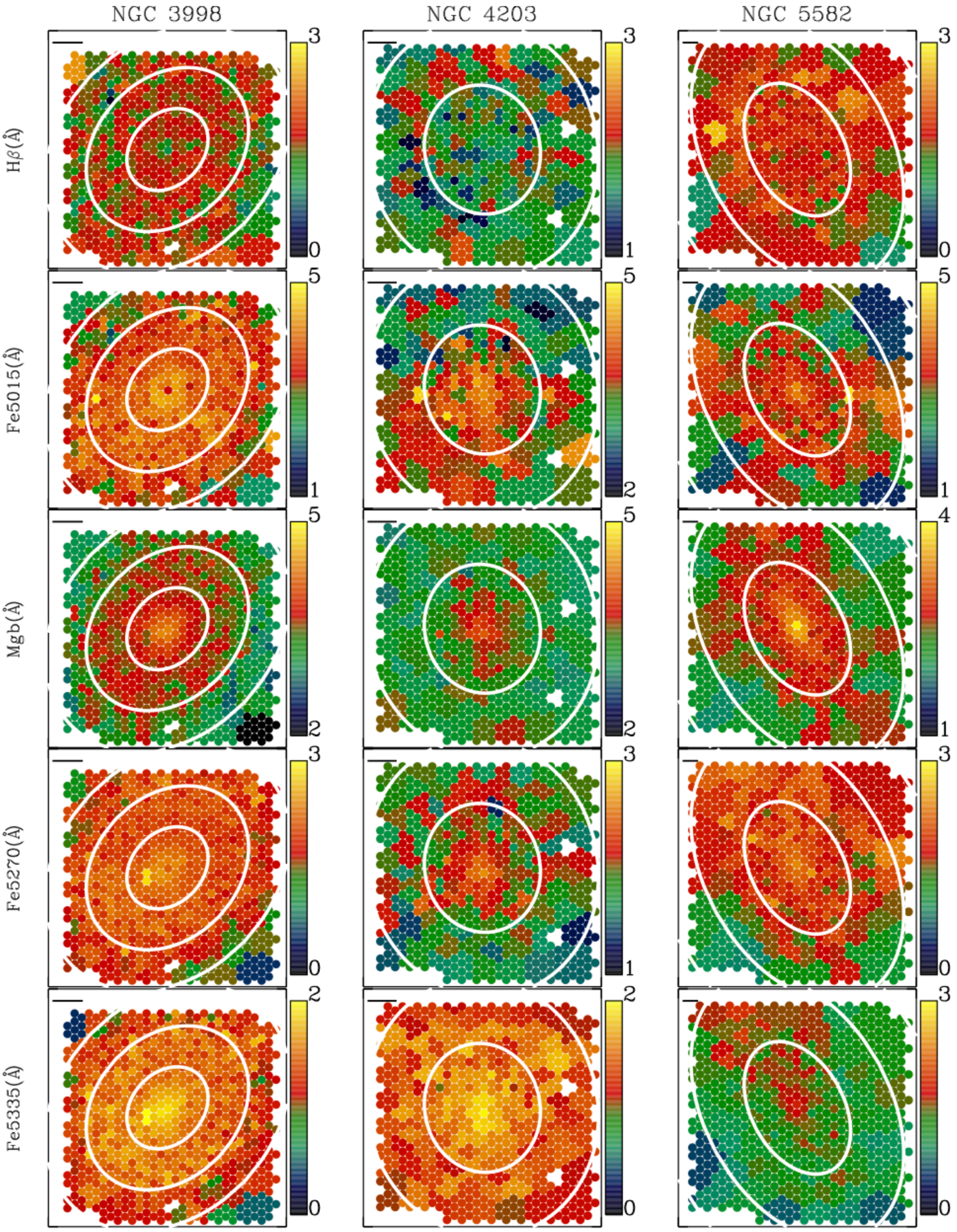

Figure 3.20: As in Figure 3.18, but for galaxies NGC 3998, NGC 4203 and NGC 5582. Fibre positions from the missing NGC 4203 dither have been re-added for presentational purposes, with values assigned to each from the nearest Voronoi bin.

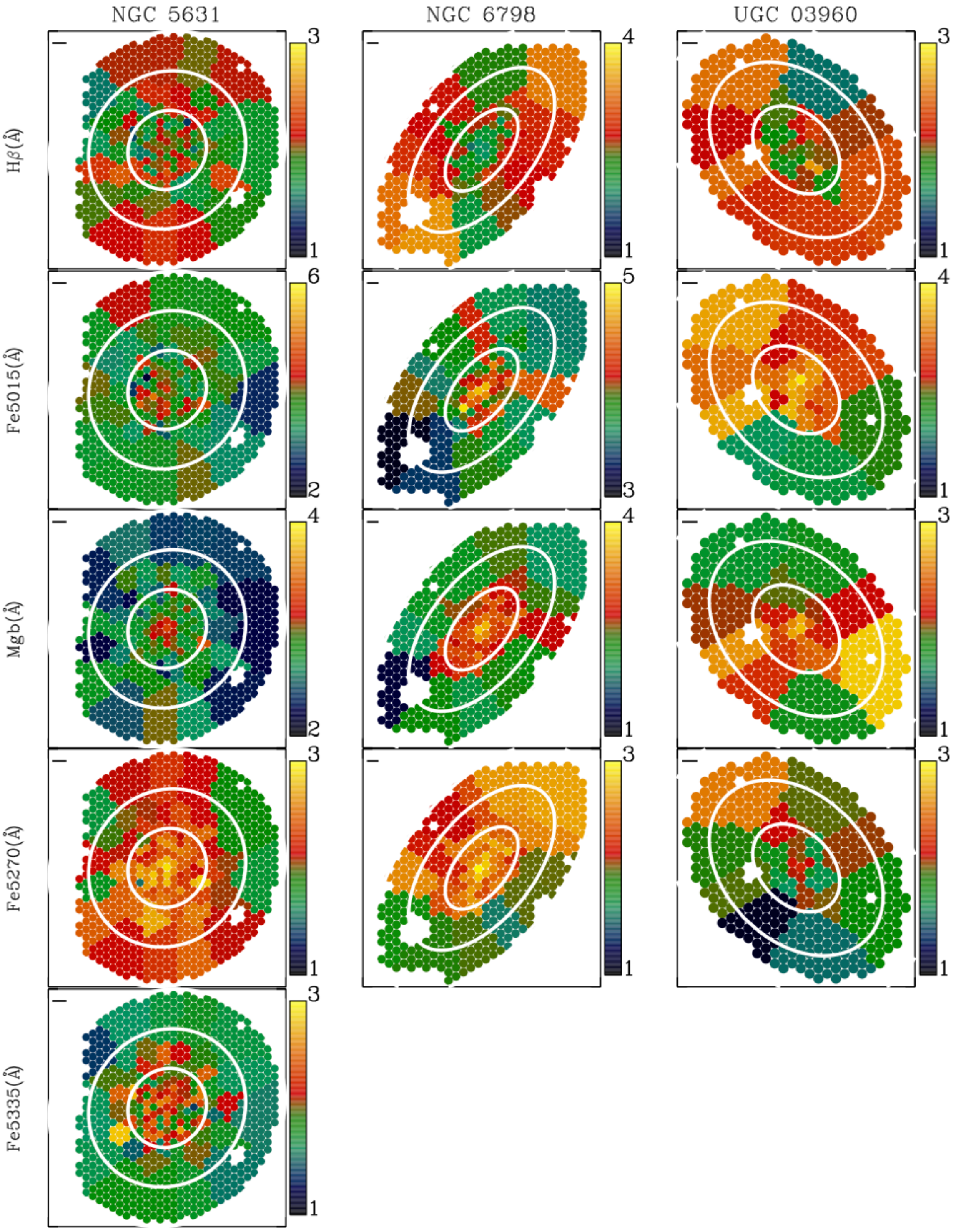

Figure 3.21: As in Figure 3.18, but for galaxies NGC 5631, NGC 6798 and UGC 03960.

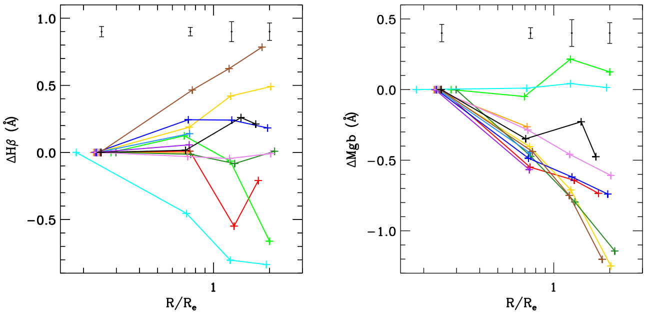

Figure 3.22: Relative Hβ and Mg *b* profiles for the Mitchell Spectrograph ETG sample. I find declining Mg *b* profiles for most of the sample, but I find a wide range of Hβ behaviours. Lines are as in Figure 3.14. The black error bars give the mean errors for all lines.

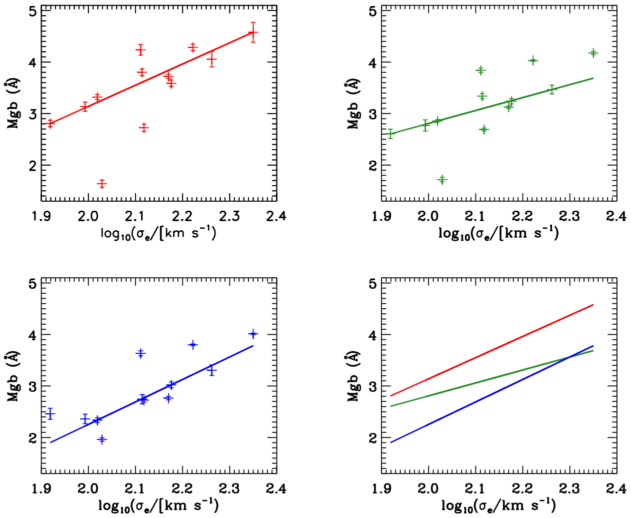

Figure 3.23: Mg *b*-σ relation computed over a 0.5R_e aperture (red; top left window), a 0.5-1R_e annulus (green; top right window) and a 1-2R_e annulus (blue; bottom left window), for each of the twelve sample galaxies. The thick lines show a least-absolute-deviation straight line fit for each set of points. The bottom right window shows the three straight line fits together. Values of σ_e, the velocity dispersion calculated over a 1R_e aperture, are taken from Cappellari et al. (2013b) and references therein.

3.7 Stellar population modelling

I constrained the ages, metallicities $[Z/H]$, alpha-element abundance ratios $[\alpha/Fe]$ and V-band mass-to-light ratios M_*/L_V by using pPXF to fit sets of simple stellar population (SSP) models to galaxy spectra, following the methodology outlined in the previous chapter. I removed all detected gas emission from the galaxy spectra, de-redshifted all galaxy spectra and then binned the spectra into a series of elliptical apertures/annuli with boundaries at 0.5, 1, 1.5 and 2.5 R_e. I discounted the outer annulus for galaxies with $R_\mathrm{max} < 2.5$ R_e to ensure good coverage across all radii. As stated in Section 3.5, NGC 2764 is excluded from my stellar population analysis; this is due to large GANDALF fit residuals around the $H\beta$ region of this galaxy's spectra.

I performed both unregularised and regularised pPXF fits on the combined spectra, using the solar-scaled ($[\alpha/Fe] = 0$) and alpha-enhanced ($[\alpha/Fe] = 0.4$) MILES models presented in Vazdekis et al. (2015). I used model ages of 0.5, 0.7, 1 Gyr, 1.5, 2.25, 3.25, 4.5, 6.5, 9.5 and 14 Gyr; I used model metallicities $[Z/H]$ of -2.27, -1.79, -1.49, -1.26, -0.96, -0.66, -0.35, 0.06 and 0.4. I also tracked the stellar mass M_* and luminosity L_V of each model, where M_* includes the mass of stellar remnants but excludes the gas lost during stellar evolution, in order to derive M_*/L_V for all fitted spectra. I allowed for four kinematic moments in the fit, as well as a 10th-degree multiplicative polynomial. I used a pPXF penalty parameter of 0.2, as before. For certain galaxies, I noted sharp sky features in the combined spectra that pPXF had not previously been able to subtract out; I created narrow masks over these features in such cases. I optimised the amount of regularisation in the regularised fits such that $\Delta\chi^2 \simeq \sqrt{2N}$ for a given fit, where N is the number of good pixels, after scaling the error spectra such that $\chi^2 = N$. In Figure 3.24, I present as an example the mass-weight maps derived for the $1-1.5$ R_e annulus around NGC 3522, both without regularisation and with the regularisation optimised. I present regularised pPXF fits to the four annuli/apertures for all fitted galaxies except NGC 3626 in Figures 3.25-3.34; I refer the reader to Chapter 2 for the fits to NGC 3626.

I compared the light-weighted stellar population parameters inferred from regularised and non-regularised pPXF fits, in order to verify that the parameters do not significantly depend on the regularisation. I use light-wanted quantities because these relate more closely to the observed (light) spectrum, meaning that they should be less dependent on assumptions made as part of the fitting process. I show the results of this comparison in Figure 3.35. I find

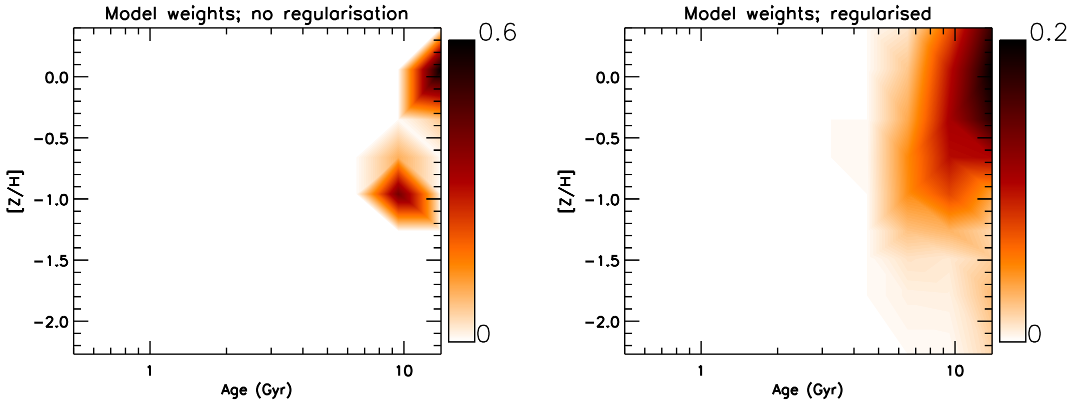

Figure 3.24: Mass-weight maps from pPXF SSP model fits to the $1R_\mathrm{e}$-$1.5R_\mathrm{e}$ annulus of NGC 3522, for both the regularised and unregularised case, in terms of age and metalicity. The unregularised fit yields multiple sharp components in the parameter space, whereas the regularised fit shows the data to be consistent with a single smooth stellar population component.

near one-to-one agreement overall between the two sets of values, though with a slight trend towards lower ages and higher metallicities for the regularised results.

The fits to the outermost binned spectrum of UGC 03960 produce a significant anomaly in terms of age, with the non-regularised fit producing an age of 14 Gyr and the regularised fit an age of 5.4 Gyr. I compare the light-weight maps of the unregularised and regularised pPXF fits to this spectrum in Figure 3.36; I find the anomaly to be caused by the non-regularised fit's age being at the edge of the model grid, along with the large degree of regularisation applied to the regularised fit as a result of its relatively low S/N. The regularisation increases the relative weights of young SSP models, thus lowering the light-weighted age in cases when the age is not well-constrained by the data.

In Figure 3.37, I compare my light-weighted and mass-weighted ages and $[Z/H]$ values calculated within 1 R_e apertures to the ATLAS^{3D} values within 1 R_e apertures reported in McDermid et al. (2015). I compare my light-weighted values with values calculated by McDermid et al. (2015) from fits to absorption line indices, which used Schiavon (2007) SSP models. The mass-weighted values in McDermid et al. (2015) were calculated using a very similar procedure to the one used here, but with MIUSCAT SSP models (Vazdekis et al., 2012) rather than MILES models. My derived ages compare well with McDermid et al. (2015) and are consistent with a one-to-one relation; however, my $[Z/H]$ values are higher overall, with average offsets of 0.13 and 0.32 for the light-weighted and mass-weighted cases, respectively.

To investigate the source of this offset, I performed an additional series of pPXF fits using

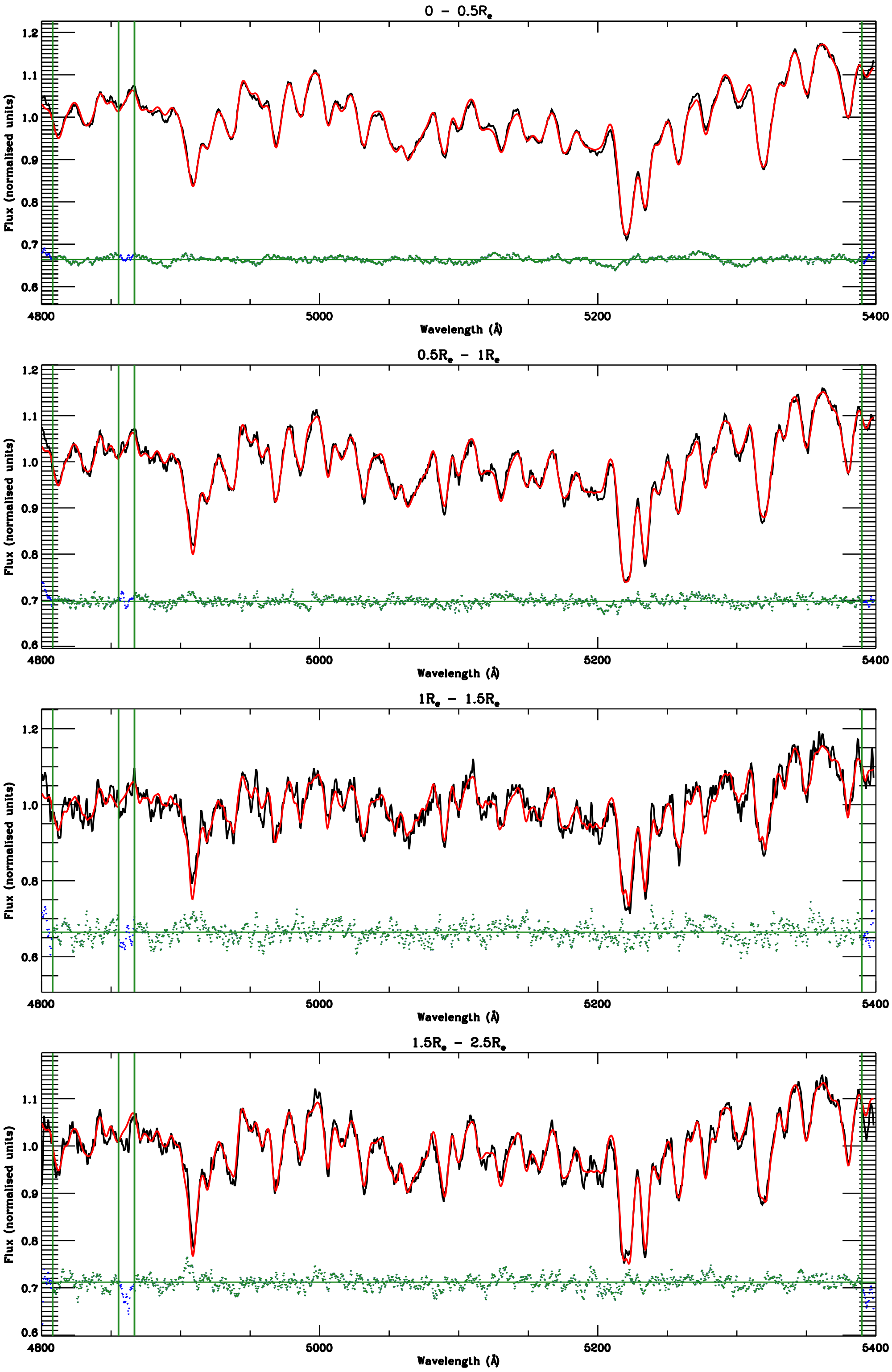

Figure 3.25: pPXF fits to combined gas-cleaned spectra for NGC 680. Black lines show the observed spectra and red lines show the best-fit superposition of templates. Vertical green lines indicate masked regions of the spectra, while the blue and green dots show the fit residuals.

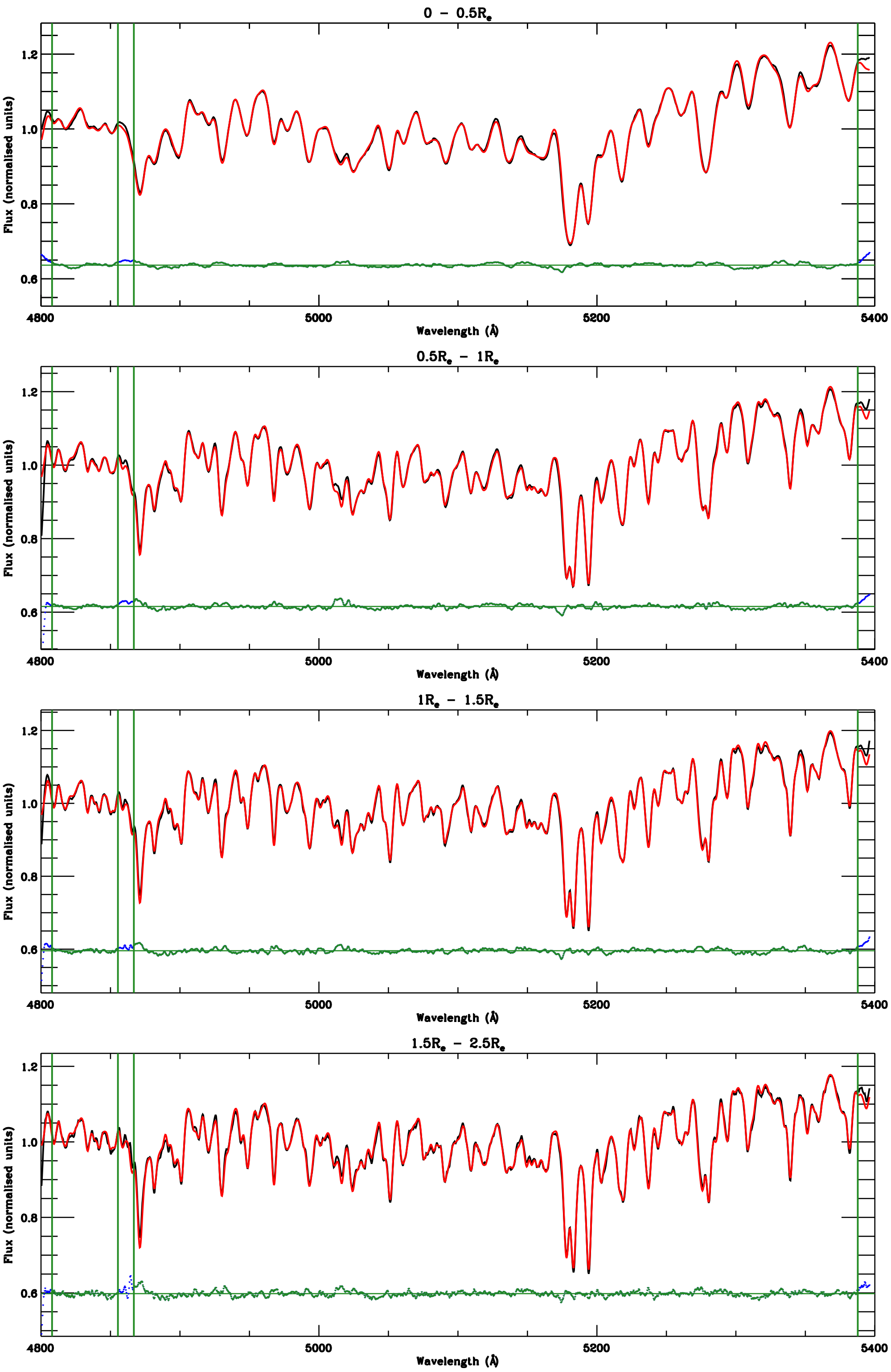

Figure 3.26: pPXF fits to combined gas-cleaned spectra for NGC 1023.

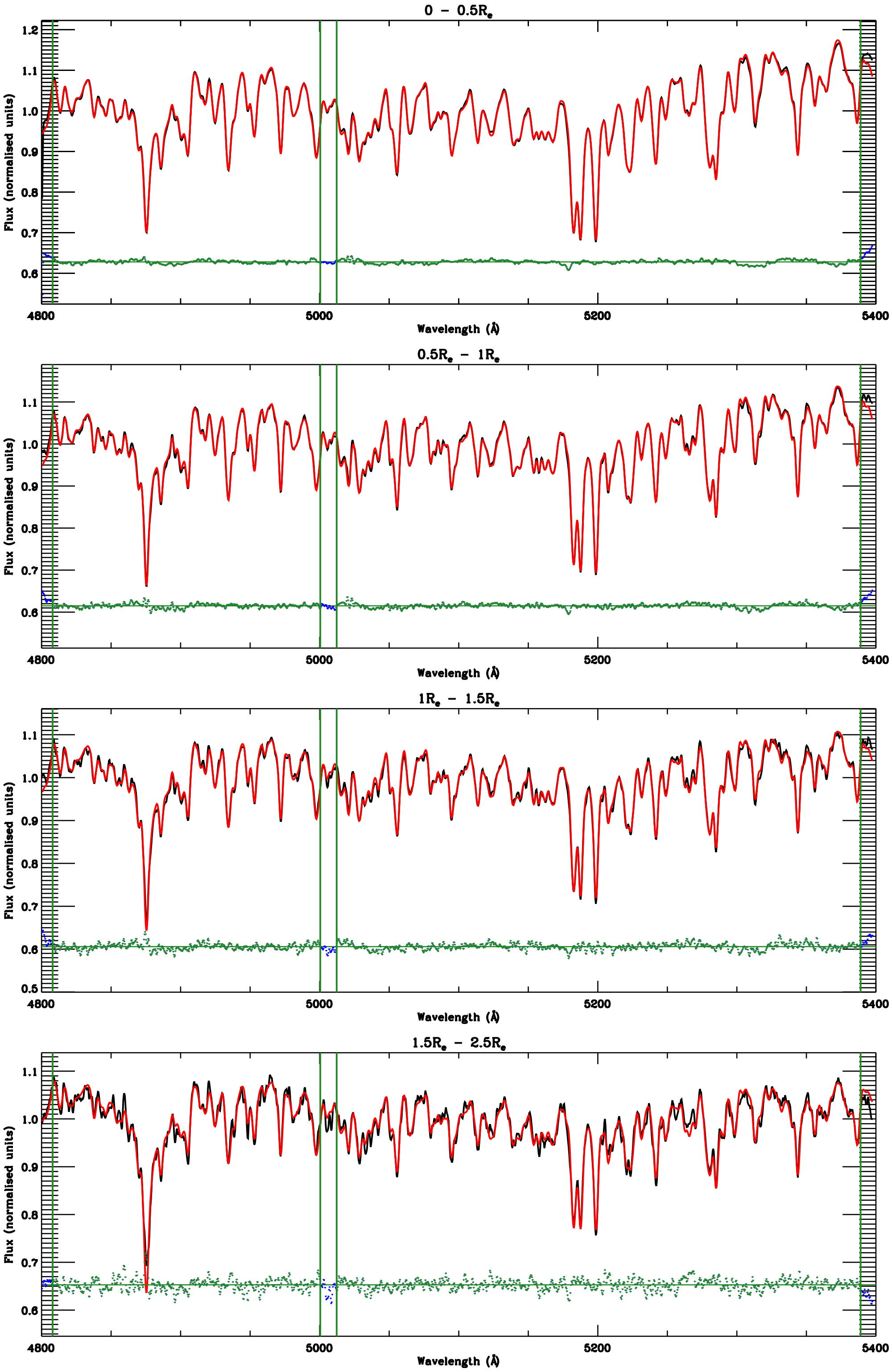

Figure 3.27: pPXF fits to combined gas-cleaned spectra for NGC 2685.

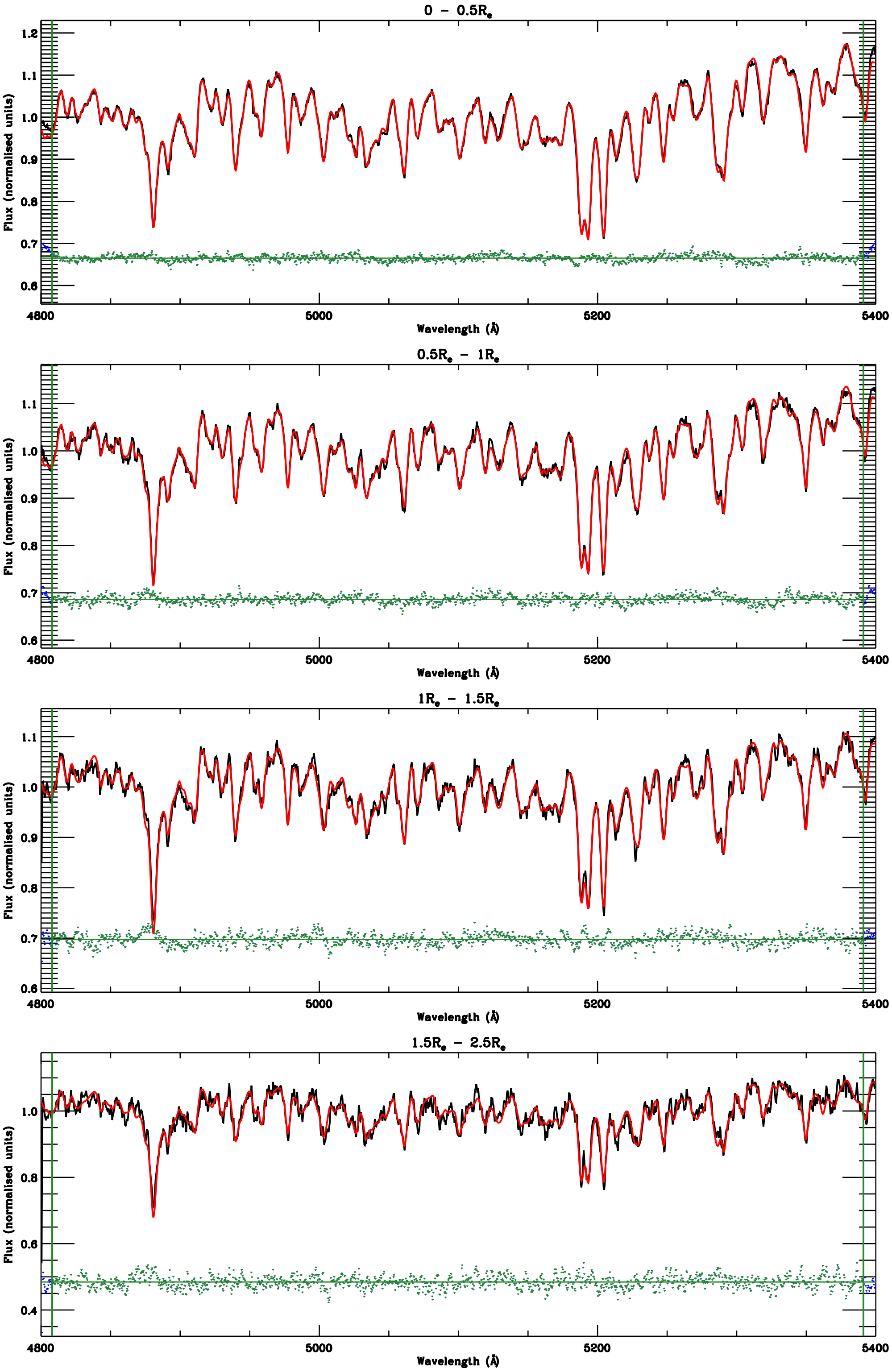

Figure 3.28: pPXF fits to combined gas-cleaned spectra for NGC 3522.

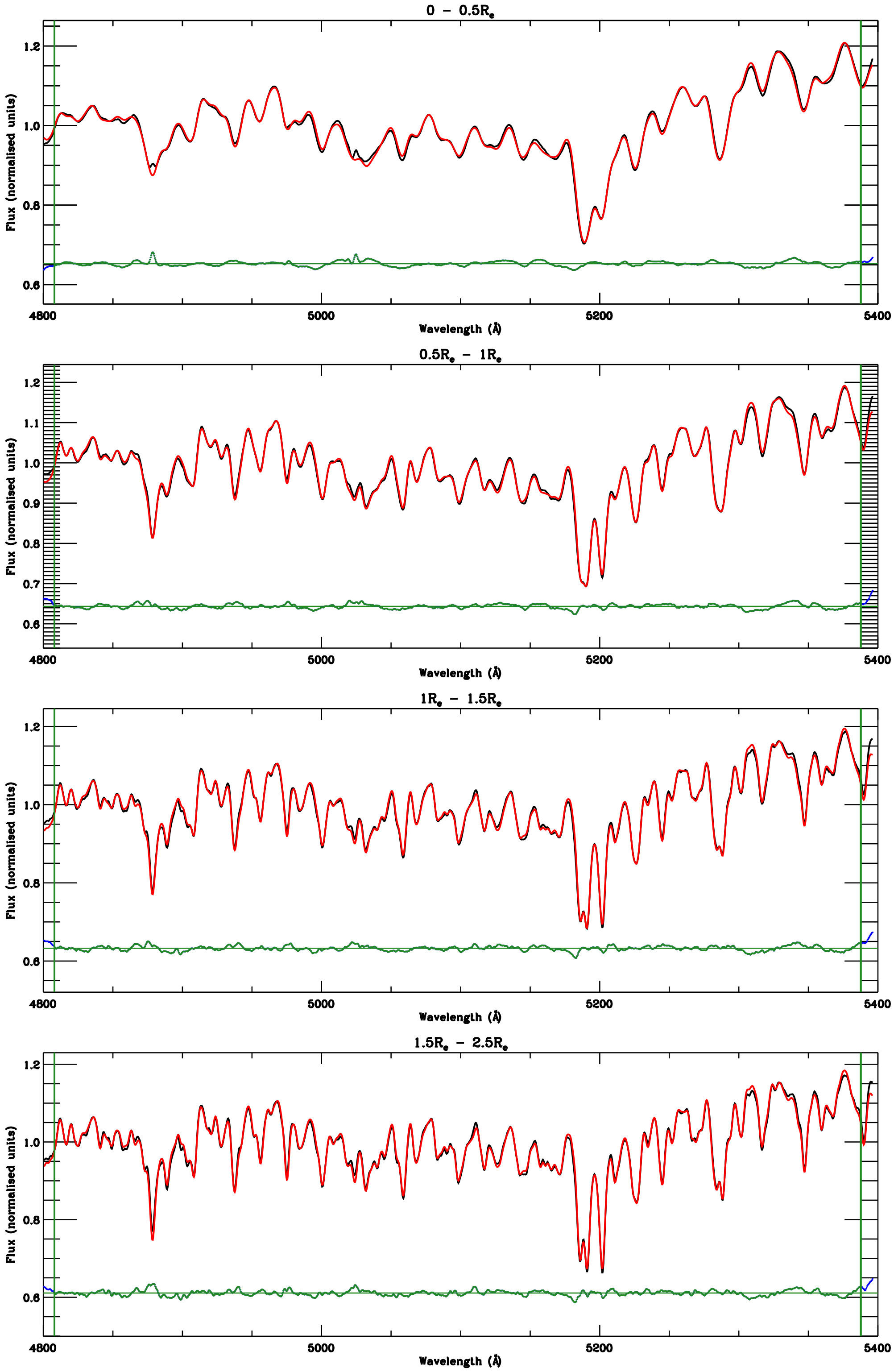

Figure 3.29: pPXF fits to combined gas-cleaned spectra for NGC 3998.

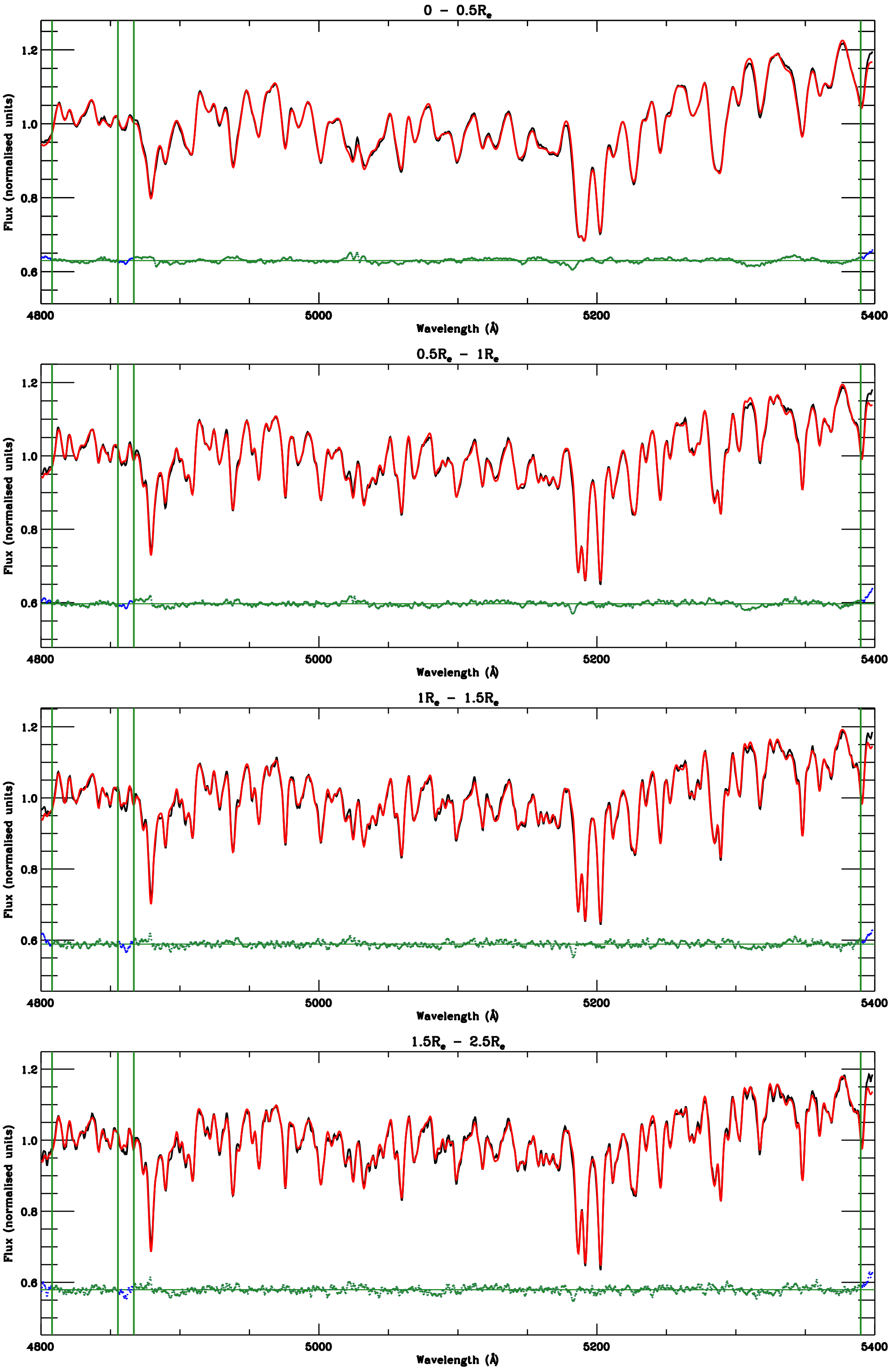

Figure 3.30: pPXF fits to combined gas-cleaned spectra for NGC 4203.

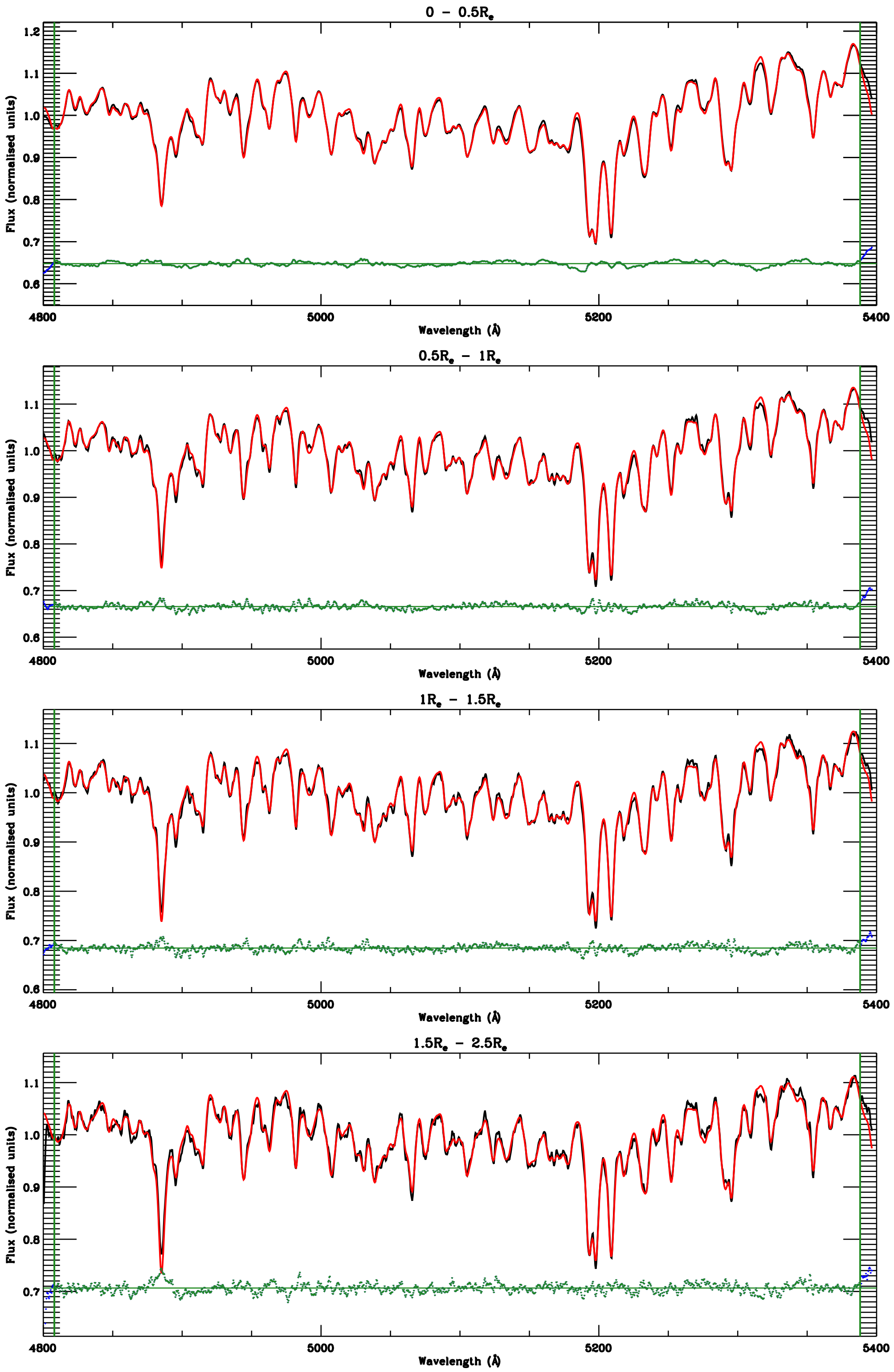

Figure 3.31: pPXF fits to combined gas-cleaned spectra for NGC 5582.

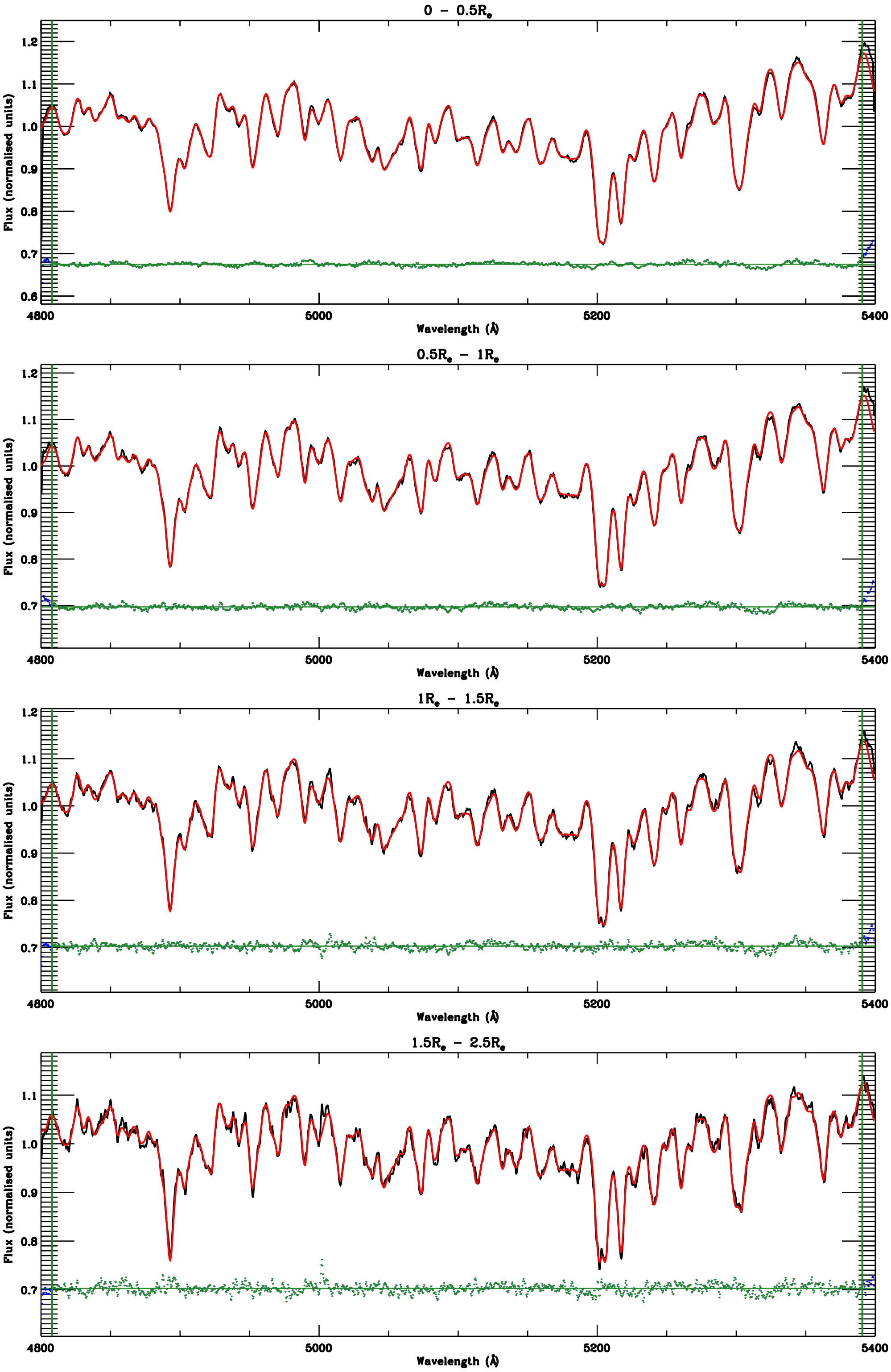
0 – 0.5R$_e$

0.5R$_e$ – 1R$_e$

1R$_e$ – 1.5R$_e$

1.5R$_e$ – 2.5R$_e$

Figure 3.32: pPXF fits to combined gas-cleaned spectra for NGC 5631.

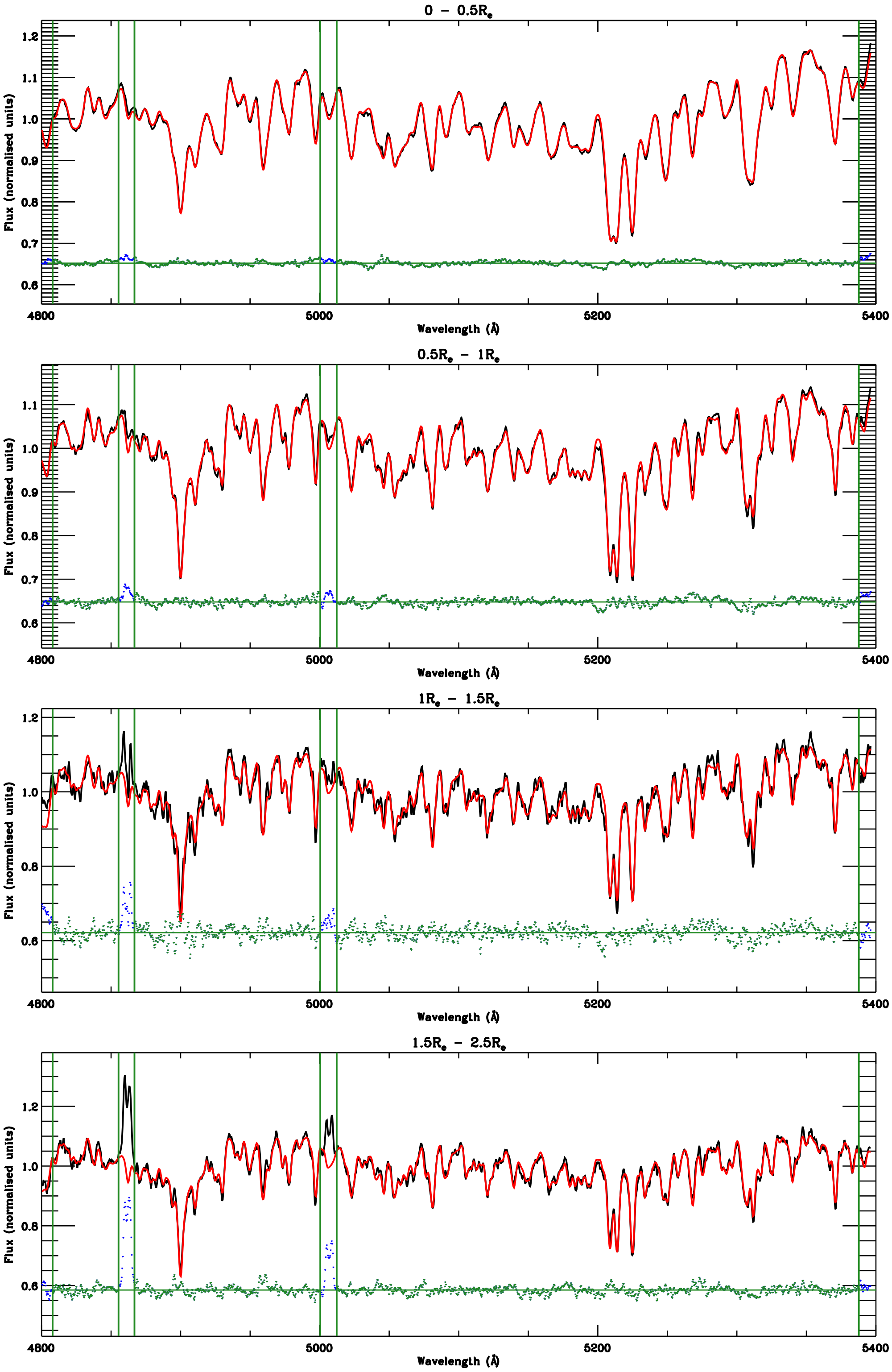

Figure 3.33: pPXF fits to combined gas-cleaned spectra for NGC 6798.

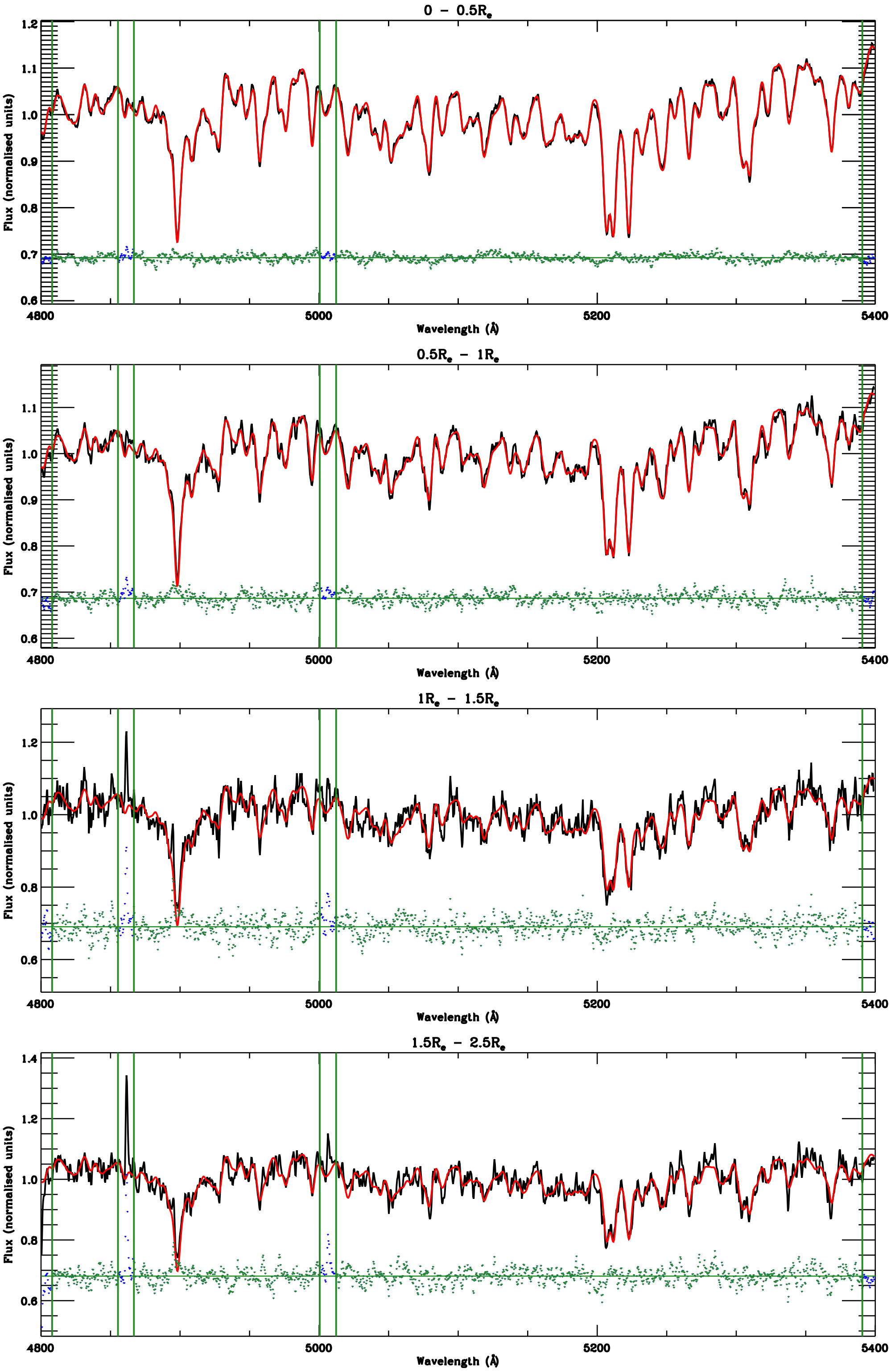

Figure 3.34: pPXF fits to combined gas-cleaned spectra for UGC 03960.

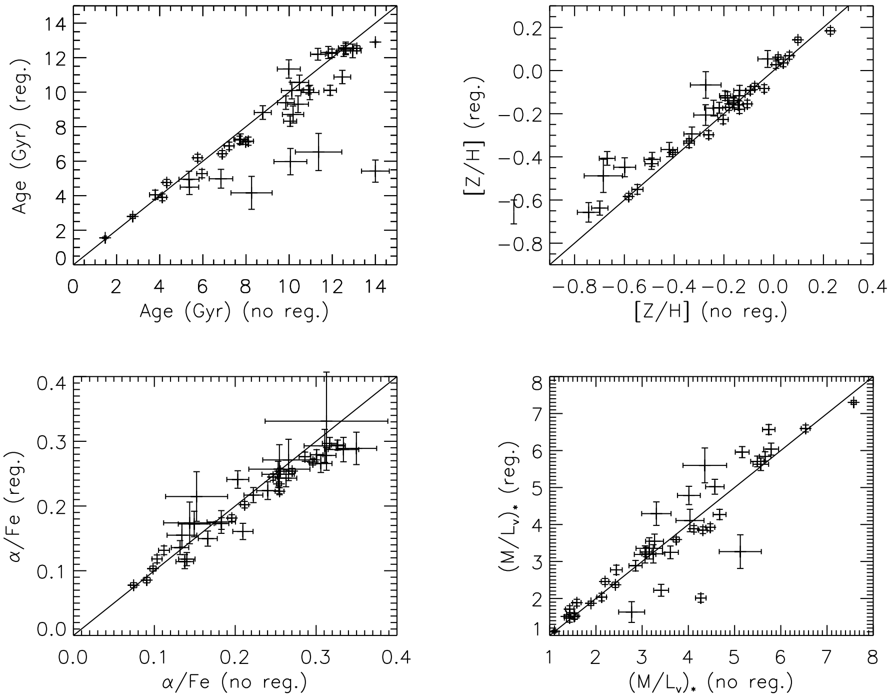

Figure 3.35: Comparison between stellar population parameters obtained from regularised and non-regularised pPXF fits, with black solid lines indicating 1-1 relations. I find good agreement between the two sets of fits, and so I conclude that the derived parameters are not significantly affected by my chosen regularisation scheme.

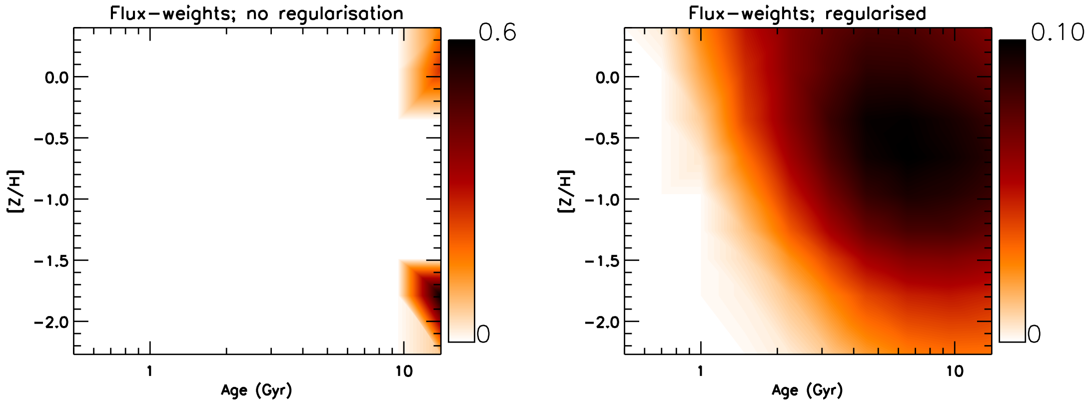

Figure 3.36: Flux-weight map from pPXF SSP model fits to the outer annulus of UGC 03960, for both the unregularised (left panel) and regularised (right panel) case. The unregularised fit supports high stellar ages, whereas the regularised fit returns a much lower average stellar age.

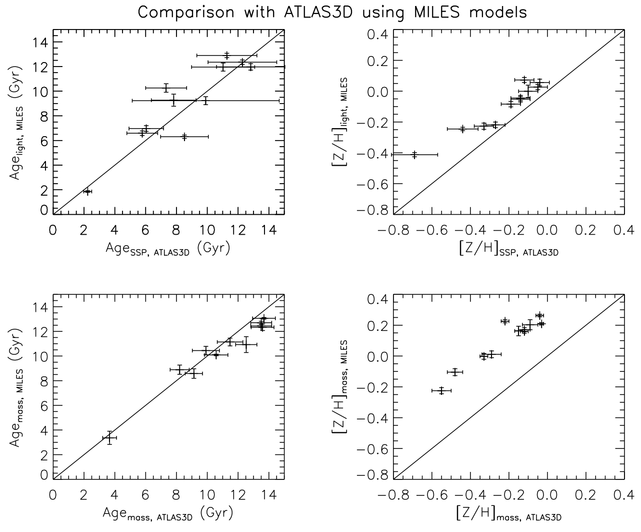

Figure 3.37: Comparison between stellar population parameters calculated within 1 R_e apertures from Mitchell Spectrograph data and those reported in McDermid et al. (2015) from ATLAS^{3D} data. The black solid lines indicate 1-1 relations. I find good agreement in terms of age, but find significant offsets in terms of $[Z/H]$.

MIUSCAT (Vazdekis et al., 2012) SSP models, using the same methodology as outlined in the case of the MILES models. As in McDermid et al. (2015), I use MIUSCAT models spanning a regular grid of log(age) and metallicity, using ages of 0.1-14 Gyr and metallicities $[Z/H]$ of -1.71 to 0.22, giving 264 models in total. I optimised the amount of regularisation in the same manner as described previously. I compare the resulting stellar population parameters to the McDermid et al. (2015) values in Figure 3.38. I now obtain near one-to-one agreement in the galaxies' ages as well as in their light-weighted metallicity, though my mass-weighted $[Z/H]$ values are higher than in McDermid et al. (2015) by 0.08 on average. I therefore argue that the metallicity offsets seen in Figure 3.37 are largely due to our different choices of SSP model libraries.

At this point, I quantified the quality of the fits from the two SSP libraries (MILES with variable abundance ratios, and MIUSCAT) by comparing the fluxes of the binned spectra with the of scatter of the residuals in the non-regularised pPXF fits in order derive an estimated signal-to-noise $(S/N)_\mathrm{fit} = \bar{G}/\sigma_\mathrm{robust}$ for each binned spectrum, where $\bar{G}$ is mean flux of the spectrum G and σ_robust the robust 1σ scatter of the residuals from the data in the pPXF fit. I show the results of this comparison in Figure 3.39, which shows results from fits to the central 0.5 R_e aperture of each galaxy as well as fits to all annuli. I find the MILES models to produce superior fits to the spectra on average. Considering that the MIUSCAT model abundances are based on the solar neighbourhood, this is unsurprising: ETGs typically have super-solar

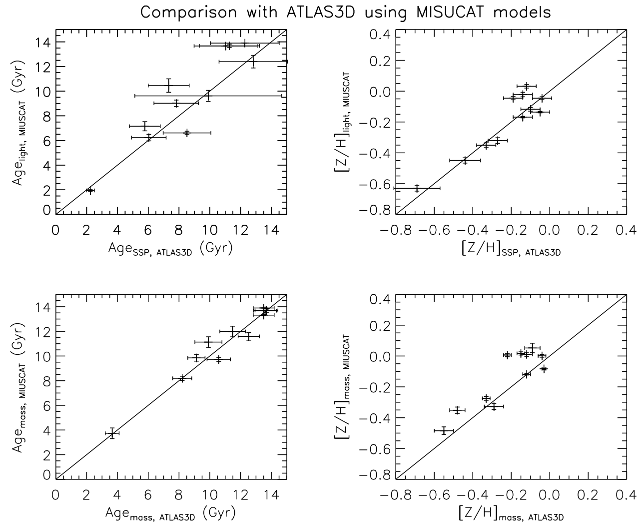

Figure 3.38: Comparison between stellar population parameters calculated around $1R_\mathrm{e}$ apertures of Mitchell data with MIUSCAT models with those reported in McDermid et al. (2015) from $1R_\mathrm{e}$ apertures around ATLAS^{3D} data. The black solid lines indicate one-to-one relations. I now obtain good agreement in terms of age and light-weighted $[Z/H]$, though I continue to find mild offsets in terms of mass-weighted $[Z/H]$.

abundance ratios, meaning that SSP model grids allowing for such abundances can be expected to produce superior fits. For this reason, I focus on results from the pPXF fits with the MILES SSP models for the remainder of this chapter.

I present profiles of light-weighted age and metallicity and $[\alpha/Fe]$ ratio in Figure 3.40, in which the radius is given as the flux-weighted average radius for a given combined spectrum. I find negative metallicity gradients for all tested galaxies. I find age gradients that are negative on average, but detect a wide degree of variation between individual systems. NGC 3626 is particularly notable, both due to its low central age and its strong positive age gradient. I note here that the age resolution of the SSP model grid is very coarse at 9 Gyr and above, and so caution against over-interpreting the age results in that region. I also find the galaxies in this sample to have slightly positive $[\alpha/Fe]$ gradients overall, though I caution that the employed grid sampling in terms of $[\alpha/Fe]$ is likewise coarse.

I present profiles of M_*/L_V Figure 3.41. I find a positive M_*/L_V gradient for NGC 3626, a near-flat gradient for NGC 5631, and negative gradients for the remainder of the sample. I considered the source of these gradients in terms of stellar population parameters as follows. I first calculated global parameter gradients for each galaxy by performing least-absolute-deviation fits to the profiles presented in Figure 3.40, and I then compared these gradients to the gradients inferred for M_*/L_V. I show the results of this comparison in Figure 3.42, in which I also

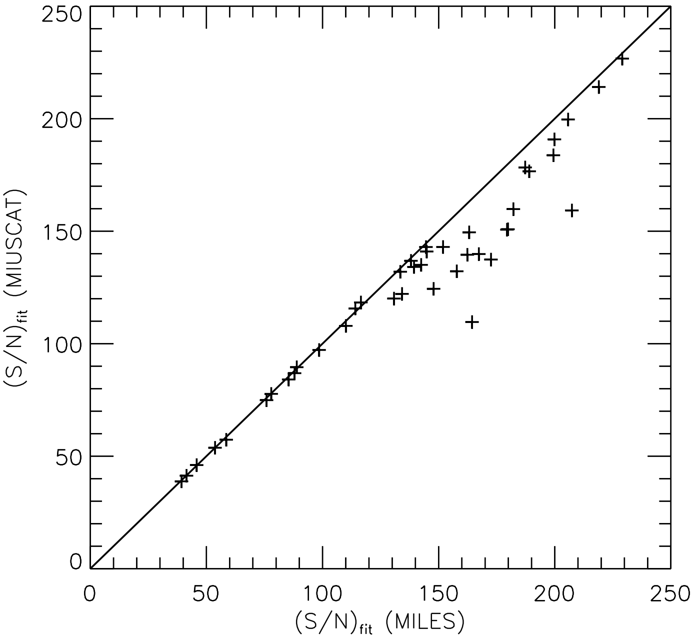

Figure 3.39: Comparison of $(S/N)_{fit}$ obtained from pPXF stellar population fits using MILES and MIUSCAT model libraries. I find that the MILES library produces superior fits in certain cases, which I ascribe to the variable abundance ratio $[\alpha/Fe]$ used in those models.

show the linear Pearson correlation coefficient R in each instance. I find a strong correlation between the gradients for M_*/L_V and age, with only weak correlations between the gradients in M_*/L_V and those for metallicity or abundance ratio. I therefore find that age gradients are the key driver of gradients in M_*/L_V; such a conclusion was also reached by Tortora et al. (2011), who investigated M_*/L gradients in galaxies by modelling SDSS imaging data out to $1R_e$. I find median gradients of -0.047 dex/dex, -0.38 dex/dex and 0.056 dex/dex for galaxies' light-weighted age, metallicity and abundance ratio respectively. I also find a median M_*/L_V gradient of -0.16 dex/dex.

In Figure 3.43, I plot the difference in light-weighted and mass-weighted values obtained for the galaxies' stellar age profiles. Most of the galaxies show mild differences of approximately $1-2$ Gyr, with little variation with radius, indicative of stellar populations that are largely uniform with age at a given radius. NGC 6798 is an exception here, showing large differences at low radii. NGC 3626 notably does *not* show differences significantly higher than the remainder of the sample, despite appearing significantly younger than NGC 6798 in a light-weighted sense; however, I note that NGC 3626 displays larger differences away from its central aperture.

In Figure 3.44, I present the SSP mass-weight maps from the regularised SSP pPXF fits to

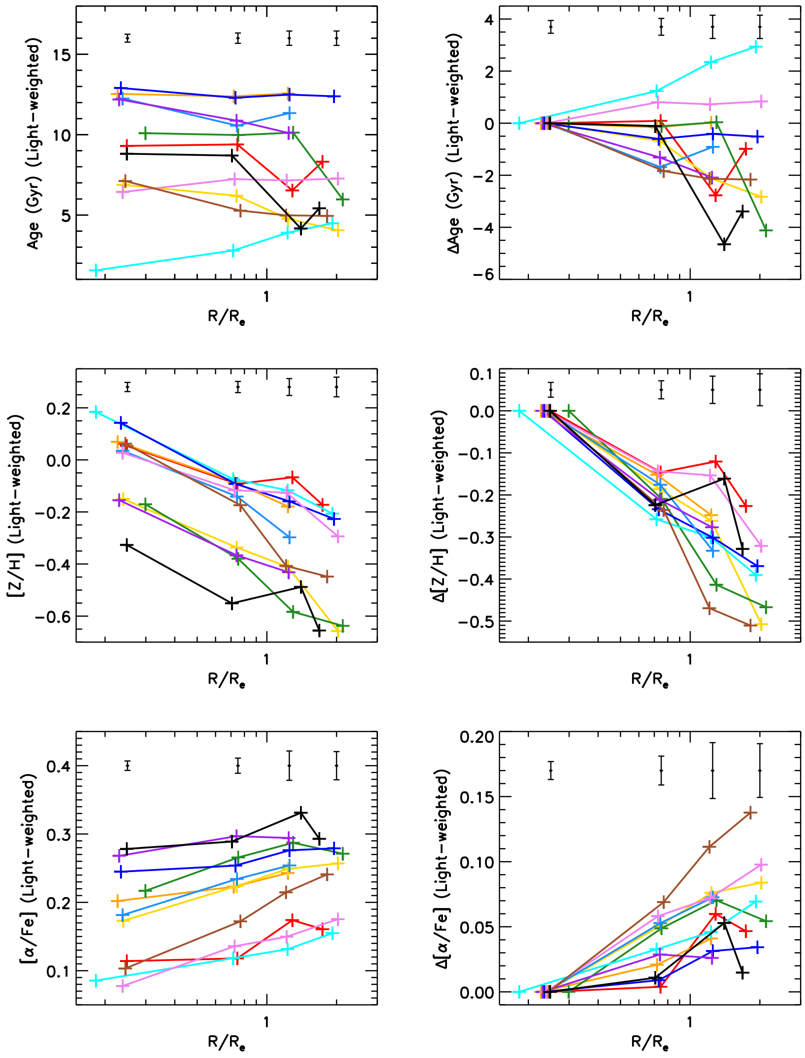

Figure 3.40: Absolute (left) and relative (right) profiles of light-weighted age (top), metallicity (middle) and $[\alpha/Fe]$ abundance ratio, derived from pPXF fits to combined spectra. Lines are as in Figure 3.14. The black error bars show the mean error at a given aperture or annulus position.

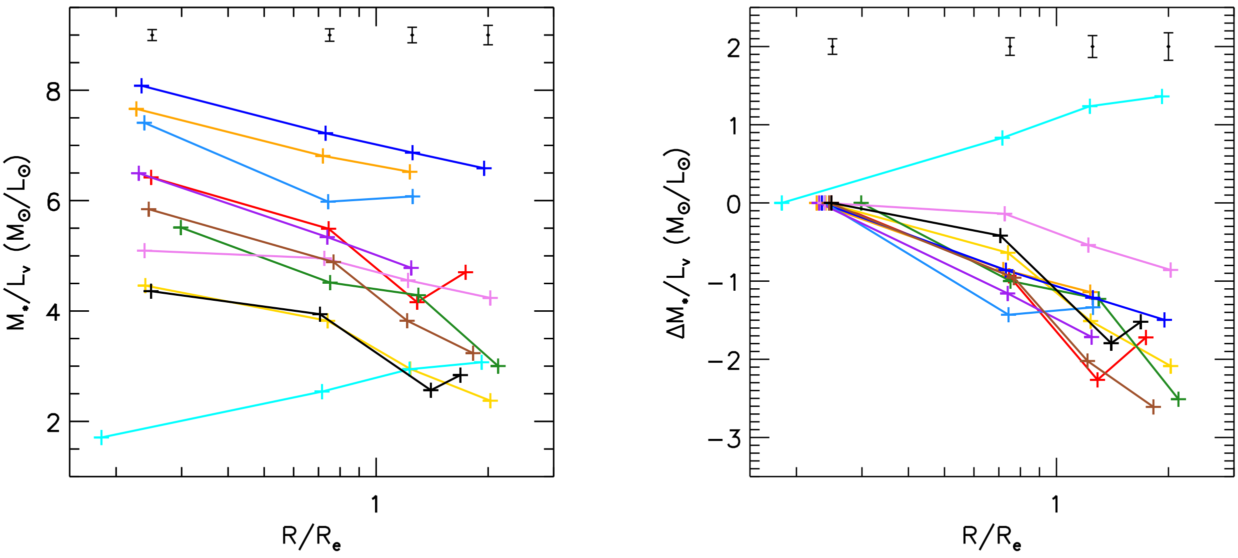

Figure 3.41: Absolute (left) and relative (right) profiles of stellar mass-to-light ratio M_*/L_V, derived from pPXF fits to combined spectra. Lines are as in Figure 3.14, with error bars showing the mean error at a given aperture or annulus.

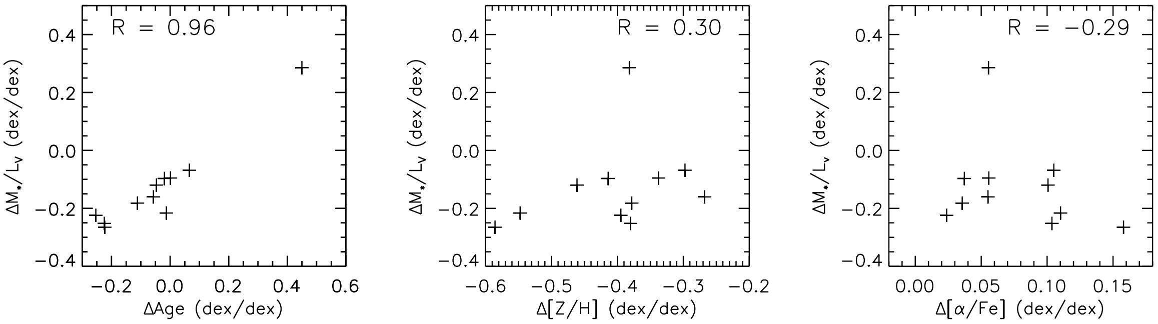

Figure 3.42: Gradients in M_*/L_V plotted as a function of age, metallicity and abundance ratio. Individual parameters are as discussed in the text. The M_*/L_V gradient correlates strongly with age while showing little dependence on metallicity or abundance ratio, implying that age variations are the main driver of the M_*/L_V gradients in my results.

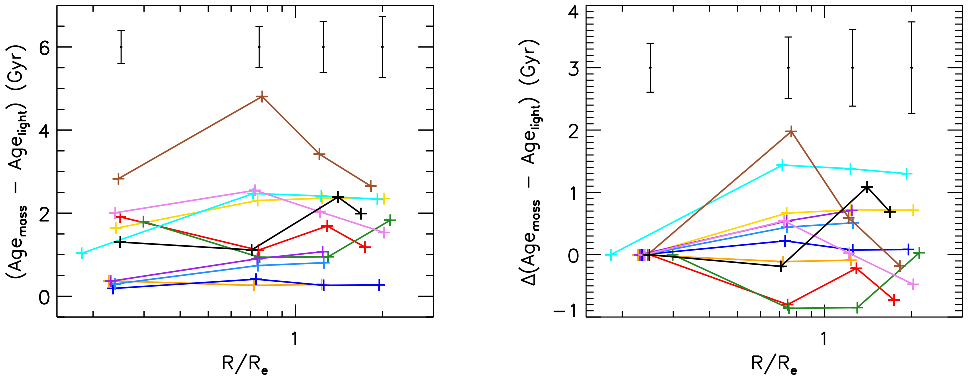

Figure 3.43: Profiles of the difference between light-weighted and mass-weighted galaxy ages. Line colors are as in Figure 3.14. I find mild differences of approximately 1-2 Gyr in most cases, but I note a larger difference for NGC 6798 (brown line).

NGC 3626 in terms of age and metallicity. The maps show a significant young stellar population component in the centre of NGC 3626, which becomes increasingly sub-dominant at larger radii. This explains the behaviour for this galaxy seen in Figure 3.43: the young stellar populations are significant near the centre in both a mass-weighted and light-weighted sense, but only contribute significantly to light-weighted parameters further out due to the relative brightness of young stars.

I present NGC 6798's mass-weight maps in Figure 3.45, in which I find NGC 6798 to be dominated by an old population throughout the tested FOV. A significant young sub-population is also present, however, which is emphasised by the spike in this galaxy's profile seen in Figure 3.43; this sub-population becomes significantly more apparent when flux-weighting is considered, as shown in Figure 3.46.

3.8 Discussion

In the previous sections, I presented stellar kinematics for our sample of ETGs. I probed for any stellar kinematics transitions beyond $1R_\mathrm{e}$, using the λ_R and Λ_R parameters as proxies for angular momentum. I extracted ionised gas fluxes and kinematics, and I showed a significant fraction of our galaxies to contain ionised gas that is misaligned with the galaxies' stars. Lastly, I performed spectral fitting with SSP models in order to investigate the galaxies' stellar populations.

Visually, I find that the stellar kinematics within $1R_\mathrm{e}$ are good indicators of the kinematics further out beyond $1R_\mathrm{e}$, with no dramatic changes in behaviour observed. My λ_R and Λ_R

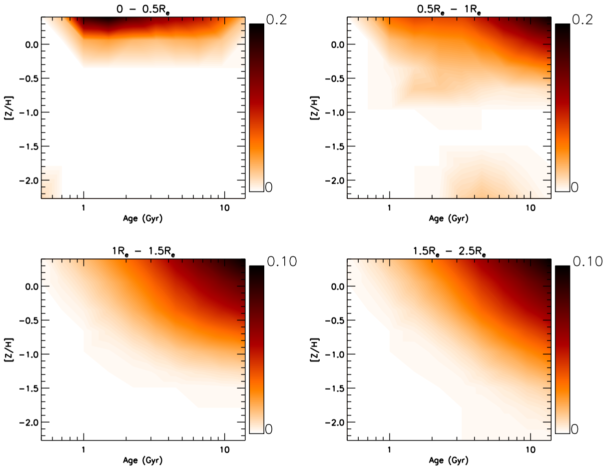

Figure 3.44: Mass-weight maps from pPXF SSP model fits to NGC 3626, with $[\alpha/Fe]$ marginalised over. At the centre, this galaxy contains both significant young and old populations (top left panel); at larger radii, the fits are consistent with the galaxy being dominated by old stars.

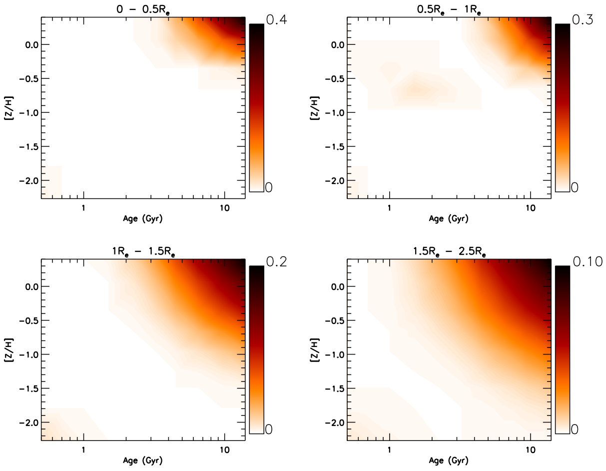

Figure 3.45: Mass-weight maps from pPXF SSP model fits to NGC 6798. I find this galaxy's stellar mass to be dominated by old stars across the tested FOV, with signs also of younger sub-populations as seen in the right-hand windows.

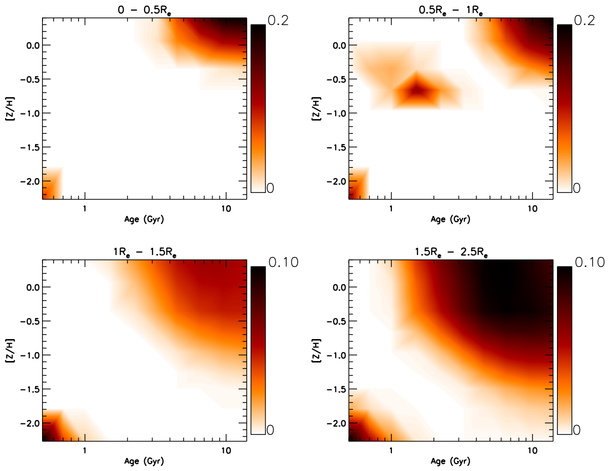

Figure 3.46: Flux-weight maps from pPXF SSP model fits to NGC 6798. Young sub-populations of stars are apparent in the fits.

profiles support this view, being flat or close to flat beyond the central half-light radius. I therefore find that the fast/slow rotator classification of (Emsellem et al., 2007) holds for my ETGs out to significantly further than $1R_{\rm e}$. My kinematics results are similar to the results of Raskutti et al. (2014), who likewise find no dramatic changes in behaviour from their Mitchell Spectrograph kinematics of massive ETGs; however, my results are different to those of Arnold et al. (2014), who indeed report $\Lambda_{\rm R}$ decreases beyond $1R_{\rm e}$ in a few cases and argue them to signify a transition to stellar halo dominated outskirts and so late dry accretion.

The apparent contrast between my results and those of Arnold et al. (2014) is most likely due to differences between this sample and theirs. 8 out of the 9 FRs in this sample would be classified as lenticular galaxies on the basis of their Hubble T-type parameter ($-3.5 < T \leq -0.5$; Paturel et al., 2003); the majority of the Arnold et al. (2014) FRs would be classified as ellipticals ($T \leq -3.5$) on this basis. The Arnold et al. (2014) sample also includes multiple elliptical galaxies with signs of embedded stellar disks, which only dominate the galaxies' light within the central regions; this leads to drops in the observed level of rotation beyond approximately $1R_{\rm e}$, as can be seen for instance in Figure 9 of Bellstedt et al. (2017).

I also note at this point that my FR $\lambda_{\rm R}$ profiles are very similar in shape to those presented in Naab et al. (2014) for galaxies that have experienced late ($z < 2$, look-back time ~ 3 Gyr) gas-rich mergers and/or gradual dissipation (the type A and type B galaxies as defined in Naab et al. (2014)). As such, I find my obtained $\lambda_{\rm R}$ profiles to be consistent with gas-rich histories for these galaxies. Given that my galaxy sample was selected based on the presence of H I, such a consistency is not surprising but is nonetheless encouraging.

The ionised gas content of these galaxies also supports the idea of several of them having experienced gas-rich events in their pasts, with significant misalignments between the gaseous and stellar components in several cases. The case of NGC 3998 is particularly striking, with its ionised gas content resembling the re-accreted gas disc in the merger simulation of van de Voort et al. (2015). In addition, I see signs of warping in the gas kinematics of NGC 2685, I see polar-rotation in the gas of NGC 3522, and I find counter-rotating gas in NGC 3626, NGC 5631 and NGC 6798. Such features have two broad explanations, as was discussed for these galaxies' H I features in Section 3.1: the gas was either accreted by these galaxies after the galaxies themselves were formed, or else the gas was disturbed in some way and then subsequently re-accreted.

I used my gas measurements to clean my galaxy spectra of emission lines, and then measured absorption line strengths for the spectra using the 14 Å Line Index System of Vazdekis et al. (2010). I used these measurements to investigate the Mg b-σ relation, and found this relation to persist beyond the central effective radius. I found little change in the gradient of the relation with radius, owing to the similarity of the Mg b gradients in most of my sample galaxies;. I argue from this that the galaxies in my sample have had broadly similar evolution histories, which I ascribe to the H I selection employed for this sample.

My stellar population modelling results provide further insight into how these galaxies may have formed. I find negative metalicity gradients for all eleven galaxies that I modelled, with a mean gradient of -0.38 dex/dex and little change seen the gradients beyond $1R_{\mathrm{e}}$. Gas-poor major mergers are predicted to to produce remnants with flatter gradients than this; Kobayashi (2004), for instance, find a mean typical metallicity gradient of -0.19 dex/dex from their major merger simulations. As such, my stellar population modelling appears to disfavour late dry major mergers. I also observe no clear evidence of the metallicity gradients steepening within the inner $\sim 1R_{\mathrm{e}}$, which is predicted to occur in the event of major mergers (Hopkins et al., 2009); as such, my stellar population modelling appears to disfavour late major mergers in general.

My metallicity gradients are not inconsistent with minor mergers and/or accretion events, however. Hirschmann et al. (2015), for instance, obtain an average metallicity gradient of -0.35 dex/dex on average in their cosmological simulations that include galactic winds; they find that galactic winds delay star-formation and so delay metal-enrichment in galaxies, which lowers the metallicities of stars accreted into massive galaxies and so steepens metallicity gradients of massive galaxies as stars are accreted. By contrast, the Hirschmann et al. (2015) simulations without galactic winds yield a mean metallicity gradient of just -0.11 dex/dex.

I found positive $[\alpha/Fe]$ gradients for all galaxies for which I performed stellar population modelling. This suggests that ETGs have shorter star formation time-scales at larger radii, since populations with greater α-enhancement have previously been shown to have shorter time-scales on average (e.g. Thomas et al., 2005; McDermid et al., 2015). Similar results have previously been reported for bulges of galaxies across the Hubble sequence (Jablonka et al., 2007), as well as for vertical gradients of barred disk galaxies (Molaeinezhad et al., 2017).

I found negative age gradients in most cases, with a strong positive age gradient for NGC 3626 and large variations in gradient between individual galaxies. I found these age gradients to drive gradients in the inferred M_*/L_V of the galaxies' stars: I found a positive M_*/L_V gradient for NGC 3626 and negative M_*/L_V gradients in the rest of the sample. Given that ETG dynamical models typically assume constant values for the stellar mass-to-light ratio, this result could have important implications for future dynamical models of ETGs. In particular, the assumption of a constant mass-to-light ratio could lead to biasses in dark matter determinations for ETGs with large stellar mass-to-light gradients, which is a possible explanation for the apparent low dark matter fractions seen in many nearby ETGs (e.g. Cappellari et al., 2013a). My M_*/L_V results are in good agreement with Tortora et al. (2011), who fit stellar population models to SDSS imaging of galaxies out to $1R_\mathrm{e}$; they find negative M_*/L gradients in ETGs with centres older than 6 Gyr, and positive M_*/L gradients in ETGs with younger centres.

I find NGC 3626 to be relatively young compared to most ETGs, being younger than 5 Gyr throughout the tested FOV in a light-weighted sense. I also found NGC 6798 to contain a significant young sub-population of stars, which results in large differences in the inferred mass-weighted and light-weighted values for that galaxy's stellar age. A likely explanation for these findings is that these galaxies have experienced a degree of recent star formation triggered by a gas-rich interaction. An alternative explanation is that these galaxies are experiencing quenching of star formation for the first time; however, the presence of counter-rotating gas in these galaxies means that this explanation is less likely.

My results here match well with the data on these galaxies presented at the start of this chapter from H I observations and deep imaging. The presence of H I in these galaxies suggests some manner of gas-rich events in their pasts, which is consistent with my extracted stellar kinematics and ionised gas features as well as with my stellar population modelling. The presence of faint substructures in several of these objects likewise supports interaction events having occurred. At the same time, the regular structure of most of the galaxies' H I suggests against recent major merging events in these systems, which is again supported by my stellar population results.

An important caveat is that I did not attempt to account for dust attenuation in the SSP fits. This is because of the relatively small wavelength range of my Mitchell Spectrograph spectra, over which the effects of attenuation will be degenerate with the continuum correction. Undetected dust gradients could thus be playing a role in my inferred stellar population gradients.

3.9 Summary

In this chapter, I presented a sample of twelve ETGs observed with the Mitchell Spectrograph. I presented results in terms of stellar kinematics, ionised gas kinematics and stellar populations, before comparing to various simulations in order to investigate the galaxies' evolutionary pasts. I showed that all approaches of analysing these spectra paint a consistent evolutionary picture, in which the galaxies in this sample were likely shaped by at least one gas-rich interaction event apiece; these interactions likely occurred late, at redshifts $z <\sim 2$. This result is consistent with previous deep imaging of these galaxies, as well as with H I observations of these objects.

In the following chapter, I will begin to investigate the mass distributions of these galaxies using dynamical modelling, in order to further understand their visible structure as well as to investigate the structure of their dark matter halos.

4

Jeans modelling of early-type galaxies

In this chapter, I present results from Jeans dynamical modelling of the twelve early-type galaxies in my sample, using the Jeans Anisotropic Modelling (JAM) method of Cappellari (2008). I construct models of the true second velocity moment, $V_{rms} = \sqrt{V^2 + \sigma^2}$, in order to constrain the mass distribution of these galaxies in terms of both their dark and visible components. The results presented in this chapter represent ongoing work, and serve to demonstrate the power of dynamical modelling for investigating samples of ETGs; I will expand the analysis presented here for future work.

Dynamical models of galaxies allow one to obtain line-of-sight kinematics for simulated mass distributions with known extent and viewing angle, allowing comparisons to be made with observations. Typically, the aim of galaxy dynamical models is to obtain useful constraints on galaxies' mass distributions; such constraints may concern the stellar and dark halo mass distributions of galaxies, as well as the masses of their central supermassive black holes.

Dynamical modelling of a given galaxy requires both photometric data and kinematic data for that galaxy. The photometric data yields a galaxy's two-dimensional surface brightness distribution, which in turn provides a three-dimensional visible mass distribution for a given viewing angle for a given assumed galaxy geometry; the kinematic data is then used to compare to the model (as in the JAM method), or else is used to fit the model directly.

4.1 Multi-Gaussian Expansion

I modelled the two-dimensional surface brightness of the sample ETGs using the Multi-Gaussian Expansion (MGE) fitting method of Cappellari (2002). In this method, a galaxy's surface brightness is modelled as a superposition of a set of two-dimensional Gaussian shapes, each of which may have a different width, axial ratio and peak surface brightness; the individual Gaussians may also have different viewing angles unless axisymmetry is being assumed. This enables optical images of galaxies to quickly be processed into a form suitable for dynamical modelling. The MGE method was originally introduced for the spherical case by Bendinelli (1991); it was subsequently developed and made applicable to real galaxies by Monnet et al. (1992), before being developed further by Emsellem et al. (1994).

This section is laid out as follows. Firstly, I explain the formalism of the MGE method in general in Section 4.1.1, and then describe the Cappellari (2002) fitting procedure in Section 4.1.2. I then explain my implementation of MGE modelling in Section 4.1.3.

4.1.1 Multi-Gaussian Expansion formalism

In the MGE method, the surface brightness of a galaxy parametrised as a sum of Gaussian components. The MGE formalism employs a Cartesian coordinate system, (x', y', z'), where x' and y' point along the major and minor axes of the target galaxy respectively whereas z' points away from the observer. The observed surface brightness of the galaxy, $\tilde{\sum}(x', y')$, can then be written as

$$\tilde{\sum}(x', y') = \sum_{j=1}^{N} \frac{L_j}{2\pi\tilde{\sigma}_j^2\tilde{q}_j} exp\left[-\frac{1}{2\tilde{\sigma}_j^2}\left(x^2 + \frac{y^2}{\tilde{q}_j^2}\right)\right] \tag{4.1}$$

where L_i is the total luminosity of the ith Gaussian component and $\tilde{\sigma}_i$ the apparent width (standard deviation) of that gaussian. $\tilde{q}_i$ describes the axial ratio of the Gaussian, such that $\tilde{\sigma}_i\tilde{q}_i$ is the apparent width of the Gaussian along the minor axis. Both $\tilde{\sigma}_i$ and $\tilde{\sigma}_i\tilde{q}_i$ are influenced by the point spread function (PSF) of the observations, which is also treated as a sum of one or more Gaussians.

Here, I will assume that the PSF of the imaging observations can be modelled as a single circular Gaussian with width σ_{psf}, such that the "true" gaussian parameters (σ, q') can be obtained from (Cappellari, 2002):

$$\tilde{\sigma}_j^2 = \sigma_j^2 + \sigma_{psf}^2 \tag{4.2}$$

$$\tilde{q}_j^2 \tilde{\sigma}_j^2 = q_j'^2 \sigma_j^2 + \sigma_{psf}^2 \tag{4.3}$$

For a given galaxy inclination, this density profile may then be deprojected to yield to true volume density profile of the galaxy of interest by calculating the intrinsic axial ratio of each Gaussian component; this is given in the oblate axisymmetric case by

$$q_j^2 = \frac{q_j'^2 - \cos^2(i)}{\sin^2(i)} \tag{4.4}$$

where i is the inclination of the galaxy, with $i = 90°$ corresponding to the edge-on case. Seeing as the peak value of a 1D Gaussian can be related to its area by $H = A\sqrt{2\pi}\sigma$, where H and A are the peak value and area respectively, one can therefore obtain a volume density of the form

$$\rho(R, z) = \sum_{j=1}^{N} \frac{L_j}{(\sqrt{2\pi}\sigma_j)^3 q_j} exp\left[-\frac{1}{2\sigma_j^2}\left(R^2 + \frac{z^2}{q_j^2}\right)\right] \tag{4.5}$$

This deprojection introduces a potential problem: it is only defined if $\cos^2(i) < q_j'$ for all Gaussians, meaning that the minimum possible inclination in the fit is constrained by the flattest Gaussian (Cappellari, 2002); I address this problem when detailing my implementation in Section 4.1.3.

4.1.2 The MGE fitting method

I fitted MGE models to galaxy observations using the fitting method of Cappellari (2002). I detail the key steps of this method below, as applied to a two-dimensional galaxy image.

Firstly, a series of radial photometric profiles are measured around an optical image of the target galaxy. The profiles are spaced linearly in position angle, and together serve to constrain the axial ratio of the galaxy. Each profile is measured by grouping pixels into logarithmically-spaced groups, in order to improve the signal-to-noise (S/N) at large radii without lowering the resolution of the image at smaller scales.

Next, one-dimensional MGE fits are simultaneously performed on each profile taken along a given position angle. These fits proceed as follows. Firstly, the σ_j of the Gaussians are logarithmically spaced between the maximum radius of the photometric profiles and a minimum radius defined by $R_{min} = 0.75\sigma_{psf}$. The non-linear least-squares minimization problem is then solved iteratively for $\log(\sigma_j)$, with the added constraint that σ_j remain within the bounds of the aforementioned minimum and maximum radii. For each step of this process, the best-fitting L_j and q'_j for a given σ_j is then found so as to minimise the relative error, which is parametrized using

$$\chi^2 = \sum_{j=1}^{M} \left[\frac{C_j - \Sigma(R_j)}{C_j} \right]^2 \tag{4.6}$$

where M is the number of photometric datapoints, C_j a photometric datapoint, R_j the isophote major axis radius and $\Sigma(R_j)$ the surface brightness predicted by the MGE model.

The end result of this process is an MGE model of an observed galaxy given as superposition of Gaussians with different L_j, σ_j and q'_j. This model, among other things, may be used to conveniently parametrise the visible light of a galaxy for the purpose of dynamical modelling.

4.1.3 MGE implementation

I fitted MGE surface brightness models to wide-field images of the sample galaxies taken with the MegaCam instrument on the Canada-France-Hawaii Telescope (CFHT). These images were taken as part of the MATLAS survey, with images of the majority of this sample presented in Duc et al. (2015). I used g-band images of the galaxies whenever possible, due to the g-band being closest to the wavelength range of the Mitchell spectra; however, no g-band images were available for NGC 3626, prompting me to use r-band MATLAS images instead for that system instead. I estimated the sky level on the images using the "sky" procedure from the Interactive Data Language (IDL) astrolib library; the "sky" procedure selects approximately

Galaxy	Band	Quality
NGC 680	g	0
NGC 1023	g	1
NGC 2685	g	1
NGC 2764	g	0
NGC 3522	g	0
NGC 3626	r	1
NGC 3998	g	1
NGC 4203	g	1
NGC 5582	g	1
NGC 5631	g	0
NGC 6798	g	0
UGC 03960	g	0

Table 4.1: Summary of photometric data used for MGE modelling of the galaxy sample. A quality flag of 1 indicates that the central region of the galaxy image is saturated, where as a flag of 0 indicates no detected problems.

10000 uniformly-spaced pixels on an image and then computes their modal value. I corrected for Milky Way dust extinction in each image using (Schlafly & Finkbeiner, 2011), respectively adjusting the g-band and r-band galaxy images as follows:

$$I_g = I_{g,obs} \times 10^{\left(\frac{3.303E(B-V)}{2.5}\right)} \tag{4.7}$$

$$I_r = I_{r,obs} \times 10^{\left(\frac{2.285E(B-V)}{2.5}\right)} \tag{4.8}$$

where I is the number of counts in a given CCD pixel and $E(B-V)$ describes the reddening due to dust and is defined as the difference between an object's observed and intrinsic $(B-V)$ colour index. I obtained $E(B-V)$ values for each galaxy using Schlafly & Finkbeiner (2011).

I found several of the MegaCam images to be saturated in their central regions, making it impossible to precisely model the galaxies' centres in such cases. The affected areas always cover a region of much smaller radius than the Mitchell fibre radius, and so I argue that these images are sufficient for constructing dynamical models of my wide-field Mitchell data. I note that short-exposure MATLAS images have recently been made available for these galaxies; part of my future work will consist of implementing these into my MGE models along with MATLAS images discussed previously. I provide a summary of the galaxy images used in Table 4.1.

I hand-masked nearby foreground stars on all the images prior to MGE fitting. I also masked other features on the image when needed. In the case of NGC 3998 I placed a wide mask around nearby galaxy NGC 3990 to prevent it from distorting the MGE model of NGC 3998. I masked the left-hand side of NGC 1023, due to the asymmetric surface brightness feature evident on the bottom left of that galaxy's image. I also masked the top half of NGC 2685's image due to the severe dust-attenuation apparent in that galaxy's imaging.

After masking and sky-subtracting the images, I proceeded to perform the MGE fits. For each image, I assumed a single Gaussian point spread function with FWHM equal to the seeing given in Table 1 in Duc et al. (2015). I also assumed a single position angle for the MGE Gaussians equal to the global position angles derived in Krajnović et al. (2011). I performed an initial MGE fit for each sample galaxy with no prior constraint on the MGE axial ratios q'_j, in order to determine the range of q'_j values required to achieve a good fit. I then performed a set of regularised MGE fits using the procedure described in Section 3.2 of Scott et al. (2013), in which the allowed range of q'_j for a given galaxy was iteratively reduced until the mean absolute deviation of the MGE model increased by more than 10% in a single iteration. I perform this second set of fits to avoid artificially constraining galaxy inclinations in dynamical modelling, since deprojections of MGE models may only be performed if $\cos^2(i)$ is lower than the lowest value of q'_j.

In Figure 4.1, I present contour maps of the MegaCam photometry of the sample galaxies with the MGE models overlaid. I generally obtain excellent agreement between the models and the data, particularly on large scales. I also present 1-dimensional residual profiles for the galaxies in Figures 4.2-4.5. The saturated pixels in certain galaxy images result in a characteristic "hump" in the residual profiles at low scales, though the MGE models generally reproduce the data very well further out.

4.2 Jeans modelling

In this section, I describe the construction of Jeans dynamical models for my sample of galaxies using the JAM method presented in Cappellari (2008). I first describe the method itself in Section 4.2.1, before describing my implementation of the method in Section 4.2.2

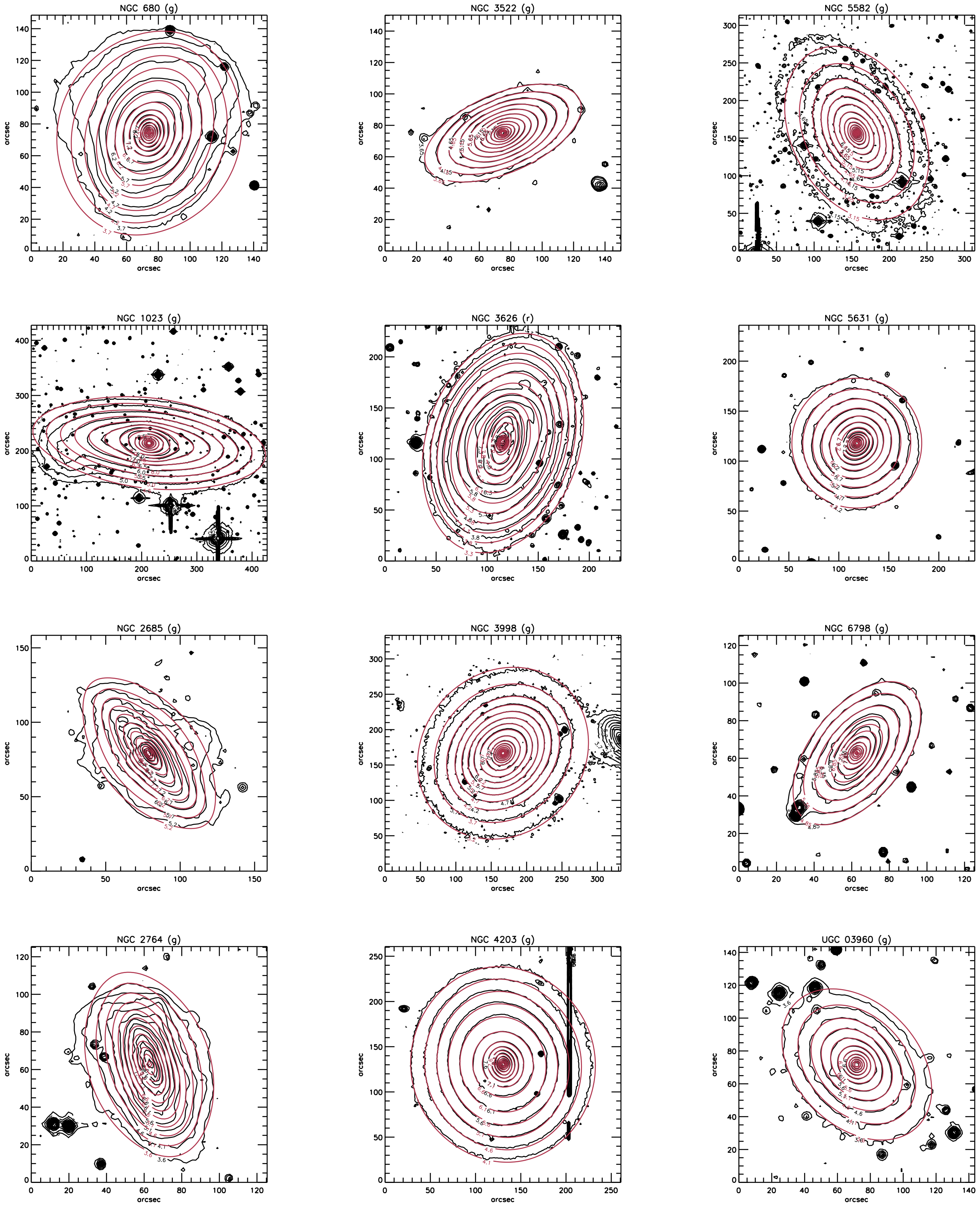

Figure 4.1: Contours of galaxy surface brightness from CFHT MegaCam images, with MGE models overlaid.

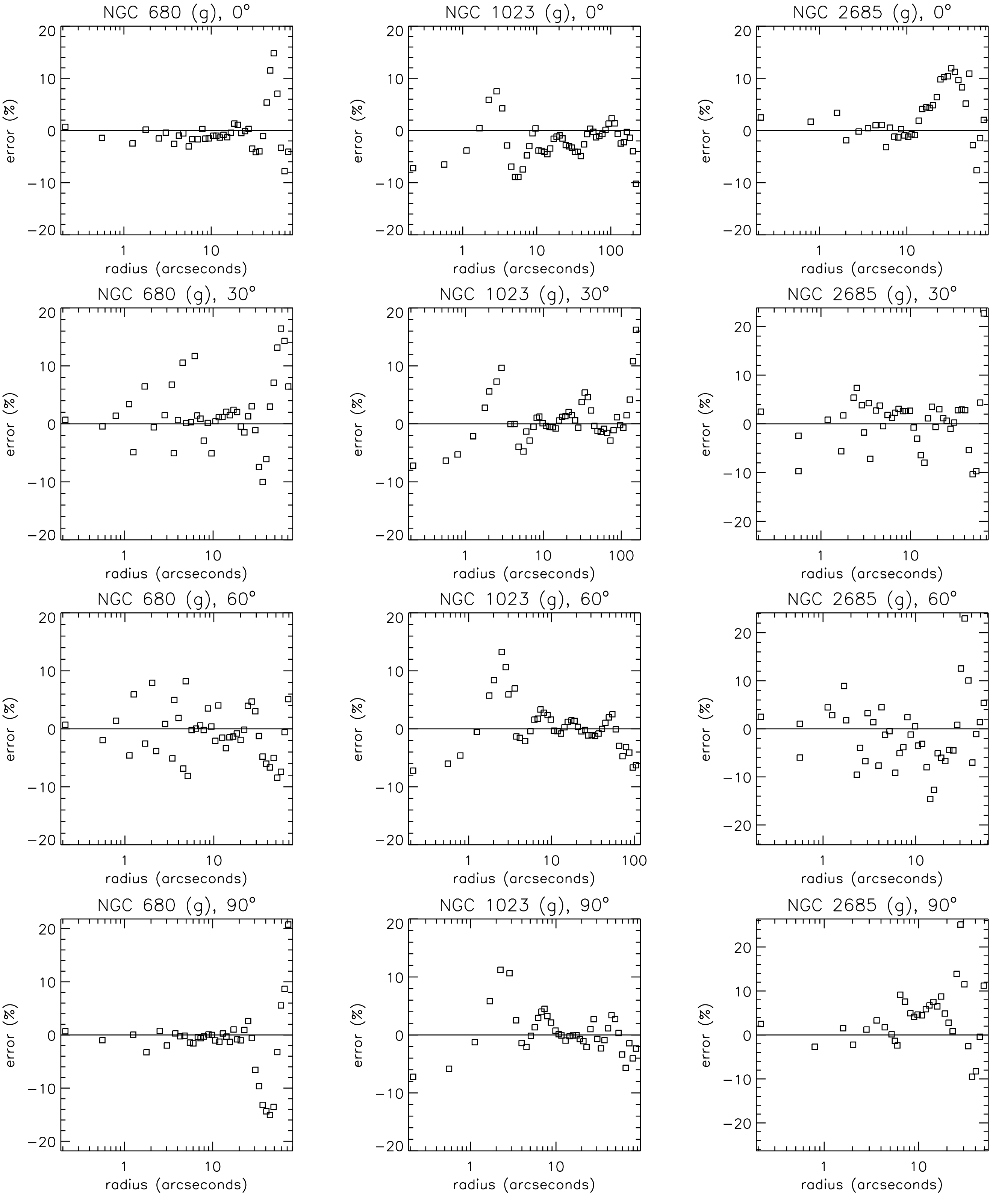

Figure 4.2: One-dimensional MGE residual profiles for NGC 680, NGC 1023 and NGC 2685.

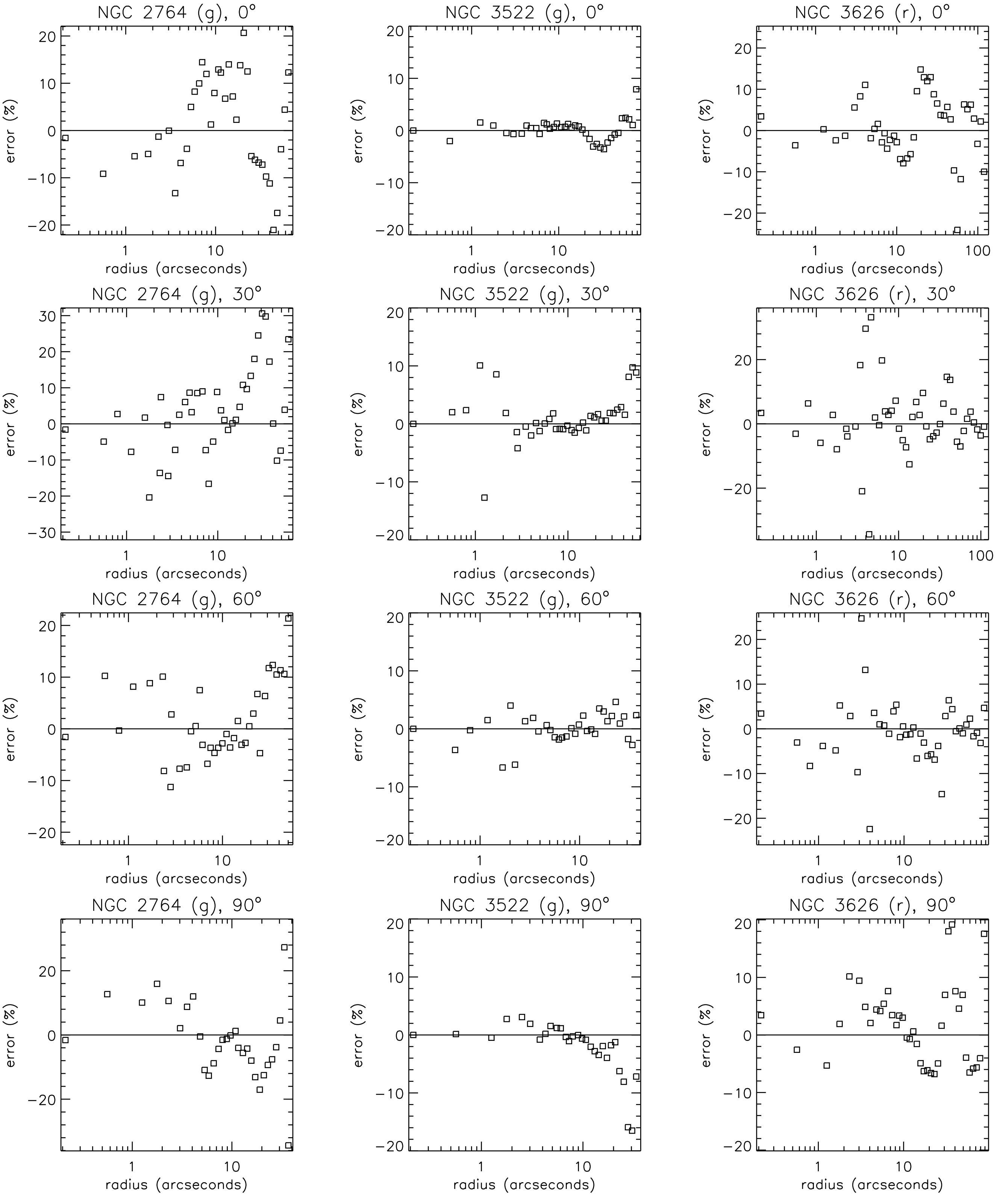

Figure 4.3: One-dimensional MGE residual profiles for NGC 2764, NGC 3522 and NGC 3626.

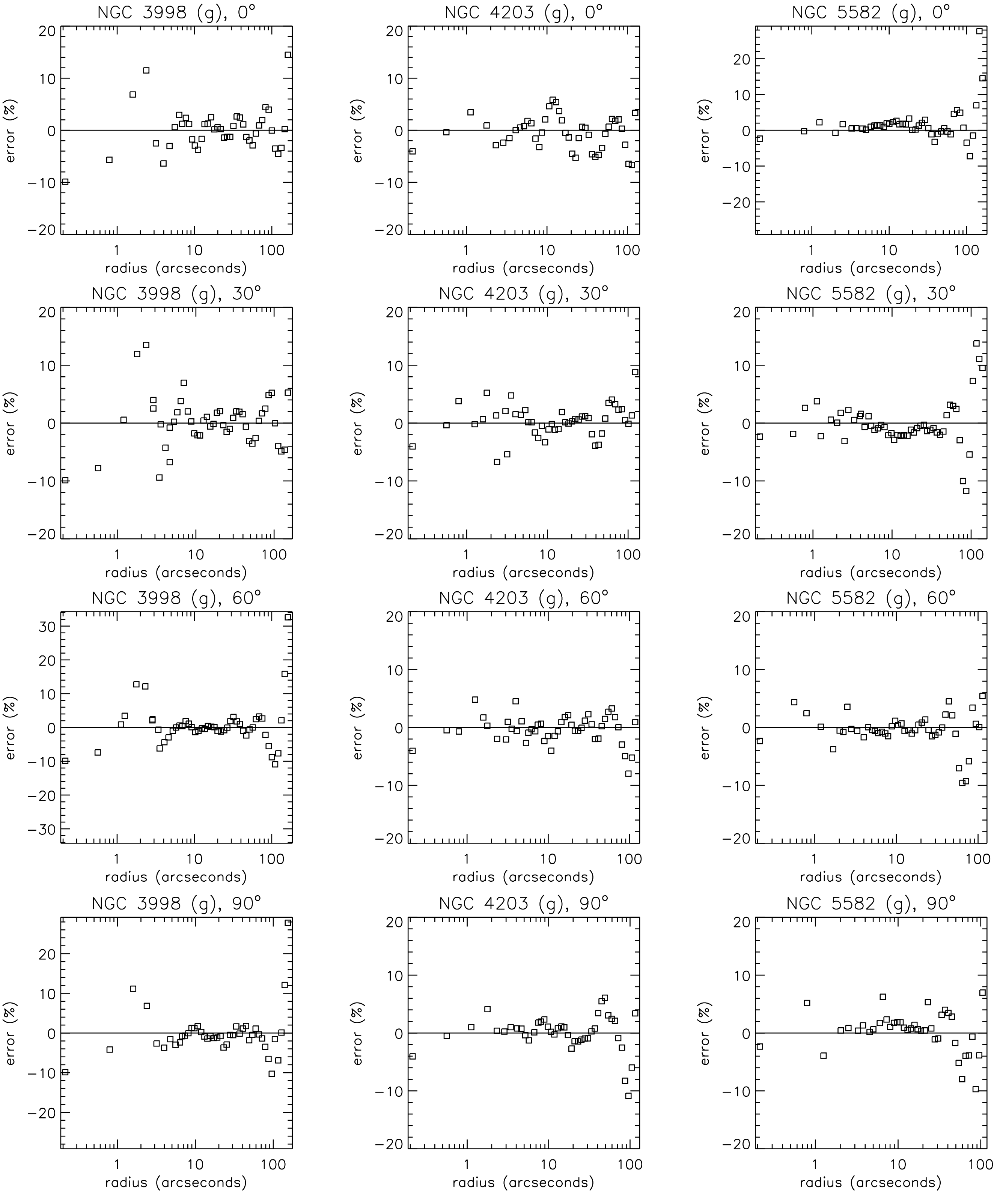

Figure 4.4: One-dimensional MGE residual profiles for NGC 3998, NGC 4203 and NGC 5582.

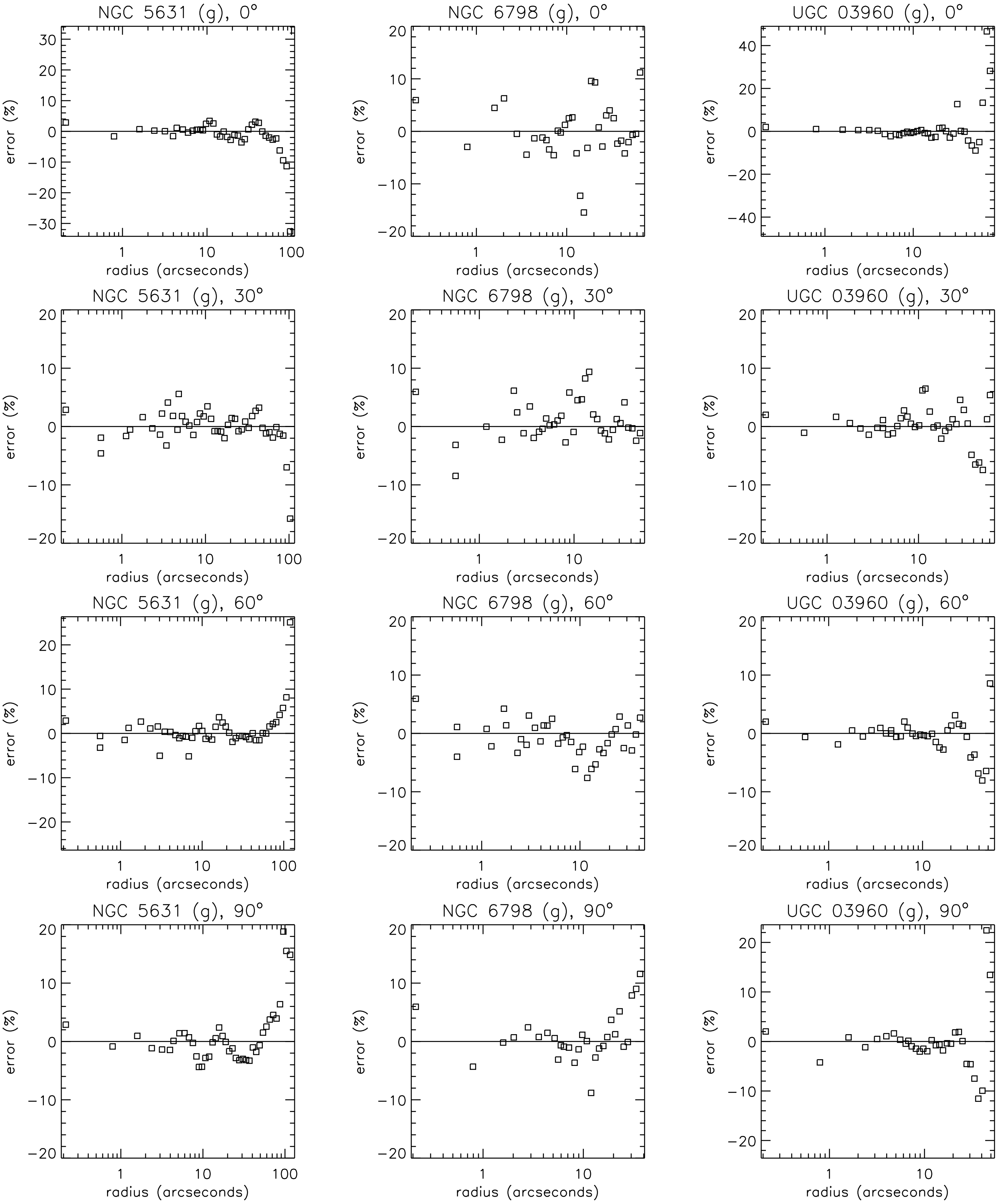

Figure 4.5: One-dimensional MGE residual profiles for NGC 5631, NGC 6798 and UGC 03960.

4.2.1 The JAM method

The JAM method is a specific implementation of the Jeans equations (Jeans, 1922), for the case of an axisymmetric galaxy parametrised via the MGE approach. The JAM code requires an assumed galaxy inclination i and anisotropy parameter β_z as inputs, along with a surface brightness distribution parametrised via the MGE formalism. The anisotropy parameter is given by

$$\beta_z = 1 - (\sigma_z^2/\sigma_R^2) \tag{4.9}$$

where σ_z and σ_R are in a cylindrical coordinate system aligned with the plane of a galaxy; they give the velocity dispersion in the radial and z directions respectively. These two values collectively describe what is commonly referred to as a *velocity ellipsoid*, which in the JAM formalism is assumed to be cylindrically aligned and so may be described by two σ terms alone. For a given i and β_z, the JAM method predicts the second velocity moment $V_{RMS} = \sqrt{V^2 + \sigma^2}$ from a supplied MGE surface density distribution which may consist of both dark and visible galaxy mass; the visible component is obtained by multiplying a galaxy's surface brightness distribution by a stellar mass-to-light ratio M_*/L.

It is important to remain mindful of the *mass-anisotropy degeneracy* in this instance: the value of β_z impacts upon the kinematics predicted for a galaxy along a given line of sight, which in turn impacts upon the mass distribution that will be inferred from a given set of galaxy kinematics. I tackle this problem by treating β_z as a free parameter in my modelling, as described in Section 4.2.2, ensuring that all reasonable β_z values and mass distributions are allowed. I also verify in Section 4.3 that my assumed form of β_z does *not* unduly affect the mass parameters I imply for the galaxies.

The Jeans equations arise from the steady-state collisionless Boltzmann equation, which any galaxy in a steady state must satisfy. This equation is written as

$$\sum_{i=1}^{3} \left(v_i \frac{\partial f}{\partial x_i} - \frac{\partial \Phi}{\partial x_i} \frac{\partial f}{\partial v_i} \right) = 0 \tag{4.10}$$

where Φ describes a smooth gravitational potential and $f(\mathbf{x}, v)$ is the distribution function describing the positions $\mathbf{x}$ and velocities v of the stars in a galaxy.

We may simplify this equation by rewriting it in cylindrical coordinates and by assuming axisymmetry:

$$\partial\Phi/\partial\phi = \partial f/\partial\phi = 0 \tag{4.11}$$

Then, by multiplying respectively by v_z and v_R and integrating over all velocities, one obtains the two cylindrical Jeans equations:

$$\frac{n\overline{v_R^2} - n\overline{v_\phi^2}}{R} + \frac{\partial(n\overline{v_R^2})}{\partial R} + \frac{\partial(n\overline{v_R v_z})}{\partial z} = -n\frac{\partial\Phi}{\partial R} \tag{4.12}$$

$$\frac{n\overline{v_R v_z}}{R} + \frac{\partial(n\overline{v_R^2})}{\partial z} + \frac{\partial(n\overline{v_R v_z})}{\partial R} = -n\frac{\partial\Phi}{\partial z} \tag{4.13}$$

where n represents a galaxy's luminosity density, with the following notation used as per Cappellari (2008):

$$n\overline{v_k v_j} = \int v_k v_j f \, \mathrm{d}^3\mathbf{v} \tag{4.14}$$

By assuming constant anisotropy, and by assuming the velocity ellipsoid to be aligned with a cylindrical coordinate system parallel to the galaxy's axis of symmetry, the two Jeans equations reduce to

$$\frac{bn\overline{v_z^2} - n\overline{v_\phi^2}}{R} + \frac{\partial(bn\overline{v_z^2})}{\partial R} = -n\frac{\partial\Phi}{\partial R} \tag{4.15}$$

$$\frac{\partial(n\overline{v_z^2})}{\partial z} = -n\frac{\partial\Phi}{\partial z} \tag{4.16}$$

where $b = \overline{v_R^2}/\overline{v_z^2}$, with $\beta_z = 1 - 1/b$.

The gravitational potential Φ is generated from the MGE volume density and so is given by (Emsellem et al., 1994):

$$\Phi(R,z) = -\sqrt{2/\pi}G \int_0^1 \sum_{j=1}^{M} \frac{M_j \mathcal{H}_j(u)}{\sigma_j} du \tag{4.17}$$

where G is the gravitational constant and M_j the total MGE Gaussian mass. $\mathscr{H}_j(u)$ is given by

$$\mathscr{H}_j(u) = \frac{\exp\left(-\frac{u^2}{2\sigma_j^2}\left[R^2 + \frac{z^2}{1-(1-q_j^2)u^2}\right]\right)}{\sqrt{1-(1-q_j^2)u^2}} \tag{4.18}$$

The two reduced Jeans equations can be integrated by using the boundary condition $n\overline{v_z^2} = 0$ as $z \to \infty$ (Cappellari, 2008). Then, by parametrizing the target galaxy's potential and density with the MGE formalism and integrating derived quantities along the line of sight, the total observed second velocity moment $\Sigma\overline{v_{los}^2}$ can be calculated at any given location using equation 28 in Cappellari (2008):

$$\begin{aligned}\Sigma\overline{v_{los}^2}(x',y') = 4\pi^{3/2}G \int_0^1 \sum_{k=1}^{N}\sum_{j=1}^{M} \nu_{0k} q_j \rho_{0j} u^2 \\ \times \frac{\sigma_k^2 q_k^2(\cos^2 i + b_k \sin^2 i) + \mathscr{D}x'^2 \sin^2 i}{(1-\mathscr{C}u^2)\sqrt{(\mathscr{A}+\mathscr{B}\cos^2 i)[1-(1-q_j^2)u^2]}} \\ \times \exp\left(-\mathscr{A}\left[x'^2 + \frac{(\mathscr{A}+\mathscr{B})y'^2}{\mathscr{A}+\mathscr{B}\cos^2 i}\right]\right) du\end{aligned} \tag{4.19}$$

in which $\nu_{0k} = \nu_k(0,0)$ and $\rho_{0j} = \rho_j(0,0)$, with k indices referring to the Gaussian components of the MGE model describing the galaxy's *visible* mass distribution and j indices referring to the Gaussians describing the *total* mass distribution. Each luminous component $[\Sigma\overline{v_{los}^2}]_k$ may be calculated separately from the total mass MGE, with the observed $\Sigma\overline{v_{los}^2}$ then obtained by summing these components together. b_k is the anisotropy of luminous Gaussian component k. The parameters $\mathscr{A}$, $\mathscr{B}$, $\mathscr{C}$ and $\mathscr{D}$ are defined as follows:

$$\mathscr{A} = \frac{1}{2}\left(\frac{u^2}{\sigma_j^2} + \frac{1}{\sigma_k^2}\right) \tag{4.20}$$

$$\mathscr{B} = \frac{1}{2}\left(\frac{1-q_k^2}{\sigma_k^2 q_k^2} + \frac{(1-q_j^2)u^4}{\sigma_j^2[1-(1-q_j^2)u^2]}\right) \tag{4.21}$$

$$\mathscr{C} = 1 - q_j^2 - \frac{\sigma_k^2 q_k^2}{\sigma_j^2} \tag{4.22}$$

$$\mathscr{D} = 1 - b_k q_k^2 - [(1-b_k)\mathscr{C} + (1-q_j^2)b_k]u^2 \tag{4.23}$$

in which σ_j and σ_k refer to the widths of individual MGE Gaussians.

In practice, $\Sigma\overline{v_{los}^2}$ is a good approximation for the observational quantity $V_{RMS}^2 = V^2 + \sigma^2$ (e.g. Cappellari et al., 2006). As such, I assume these two quantities to be equivalent from this point on.

4.2.2 JAM implementation

I constructed a series of JAM models of the twelve ETGs in my sample in order to model their V_{rms}, using the Mitchell Spectrograph kinematics as inputs. I used the pPXF fits to V and σ only in this case, to remove any dependence of pPXF penalty parameter on the kinematics. In all cases, I assumed a point spread function for the Mitchell observations of 1.4 arcseconds, based on the calculation for NGC 3998 in Boardman et al. (2016). I detected Voronoi bins with unreliable kinematics by comparing the kinematics obtained when using additive and multiplicative polynomial corrections in the pPXF fits, and masked any bins for which the difference was more than twice the calculated error from the pPXF fits with additive polynomial corrections. I also masked fibre positions with centres within 3 arcseconds of the galaxy centre, in order to remove any dependence in the models on galaxies' central supermassive black holes; this also serves to limit any potential problems associated with saturated pixels in galaxy images, and also minimises the role played by the Mitchell Spectrograph PSF.

My aim in constructing these models was to investigate both the dark and luminous structure of these galaxies; as such, it was also necessary to include a dark matter halo component in the input MGE surface density for the JAM models. For this purpose, I assumed a dark matter halo described by an NFW density profile (Navarro et al., 1996):

$$\frac{\rho(r)}{\rho_{crit}} = \frac{\delta_c}{(r/r_s)(1+r/r_s)^2} \tag{4.24}$$

where $r_s = r_{200}/c$ is a characteristic break radius and $\rho_{crit} = 3H^2/8\pi G$ is the critical density of the universe. r_{200} is the radius of a sphere with mean density $200\rho_{crit}$ and H is the Hubble parameter. c is the concentration parameter, while δ_c is the characteristic overdensity. Both values are dimensionless, and can be related via

$$\delta_c = \frac{200c^2}{3A(c)} \tag{4.25}$$

where $A(x) = \ln(1+x) - x/(1+x)$; this represents the requirement that $\rho_{200} = 200\rho_{crit}$ (Navarro et al., 1996).

At present, there are two free parameters associated with the dark matter halo. The first is the aforementioned concentration parameter; the second is the mass of the halo, $M_{200} = 200(4\pi/3)\rho_{crit} r_{200}^3$. However, given that the characteristic break radius of the dark halo will typically be beyond the reach of even wide-field IFU data (e.g. Yıldırım et al., 2015; Boardman et al., 2016), these two free parameters are typically highly degenerate and so cannot generally be uniquely determined. I therefore assumed a concentration parameter of 10 for all galaxies, leaving M_{200} as the sole free parameter associated with the dark matter halo; such a concentration parameter appears to be a reasonable assumption for galaxy-sized dark mater halos, based on both N-body simulations (Bullock et al., 2001) and weak lensing observations (Mandelbaum et al., 2008).

Given the field of view (FOV) of my data, the M_{200} value for a given dark halo is dependent on the assumed concentration parameter and so is not in itself physically meaningful; however, it allows me to subsequently calculate the dark matter fraction f_{dm} for each galaxy. In particular, I calculate the dark matter fraction at $1R_e$, $f_{dm,e}$. I calculate this parameter by circularising the luminous MGE model of the galaxy and then computing the spherical dark matter fraction at radius R_e, after multiplying the luminous MGE by the inferred M_*/L.

I initially constructed a set of JAM models which assumed an NFW dark halo and which assumed a single orbital anisotropy β_z across the whole of the field of view (FOV). I parametrised the inclination i via the axis ratio q_{min}, which I define as the deprojected axis ratio of the *flattest* MGE surface brightness component. I also assumed a constant M_*/L over the whole of the FOV. These models, hereafter referred to as the “base models", therefore have four free parameters: the axis ratio q_{min}, anisotropy β_z, stellar mass-to-light ratio M_*/L and dark halo mass M_{200}. I varied M_{200} logarithmically and allowed a minimum M_200 value of $10^9 M_\odot$, due to the effect of M_200 becoming increasingly negligible at lower masses.

While it is common to assume a single β_z parameter, The JAM formalism allows a unique β_z to be assigned to each luminous MGE Gaussian individually. Given that galaxies should in practice show some variation of β_z with position (e.g. Lablanche et al., 2012), and given the wide FOV of my Mitchell observations, I decided to construct a second set of JAM models that gave greater freedom to galaxies' orbital anisotropy. In these models, I allowed for an "inner" and "outer" β_z parameter (e.g. Cappellari et al., 2015), hereafter referred to as $\beta_{z,in}$ and $\beta_{z,out}$. Given that each MGE Gaussian contributes chiefly to the surface brightness at radii close to its σ (Cappellari, 2002), this effectively results in a transition region in model galaxies' anisotropy profiles from $\beta_{z,in}$ to $\beta_{z,out}$. I assign the "inner" anisotropy parameter to MGE components with σ values lower than $1R_e$, with the "outer" parameter assigned to all other Gaussians. As with the base models, I also treat q_{min}, M_*/L and M_{200} as free parameters; this results in there being five free parameters overall. I refer to these models as "2-β" models over the remainder of this chapter.

Lastly, I constructed a set of JAM models with no dark matter halo, in order to assess the importance of dark matter in modelling the ETGs in my sample. I allowed for two β_z parameters in this case as described in the previous paragraph. Since I have no dark halo in this case, these models have four free parameters: q_{min}, $\beta_{z,in}$, $\beta_{z,out}$ and M_*/L. I refer to these models as the "DM-free" models over the remainder of this chapter.

For all three sets of models, I constrain the free parameters of the JAM models using a Metropolis algorithm, which is an example of a Markov Chain Monte Carlo (MCMC) method. This can be viewed as a specific application of *Bayes' theorem*, which in its simplest form is given as

$$p(y|x) = \frac{p(x|y)p(y)}{p(x)} \tag{4.26}$$

where $p(a)$ describes the likelihood of some event "a" and $p(b|a)$ describes the likelihood of event "b" given that "a" holds true. In terms of the inference of a single free parameter, Bayes' Theorem can be written as.

$$p(\theta|D) = \frac{p(D|\theta)p(\theta)}{p(D)} \tag{4.27}$$

where θ signifies a free parameter and D a set of data. $p(D|\theta)$ is the liklihood, which describes the raw goodness of fit of the model constructed with θ; this is related χ^2 statistic, in that $p(D|\theta) \propto e^{-\chi^2/2}$. $p(D)$ is termed the "evidence" and serves as a normalisation factor; its value is unimportant for the purposes of this work and so will hereafter be ignored. $p(\theta)$ is called the "prior" and parametrises our current state of knowledge. $p(\theta|D)$ is the *posterior*, which parametrises the probability density of θ.

Ideally, I would constrain the JAM modelling parameters analytically by integrating the probability distribution over all parameter space; however, as is frequently the case, it is not possible here to know $p(\theta|D)$ without first calculating it for a given θ, rendering a direct integration impossible. We can overcome this problem by *sampling* over the probability space with an MCMC method: by taking N samples θ_i with density $\Delta(\theta_i) \propto p(\theta|D)$, one can derive robust confidence intervals on all parameters of interest.

I use a uniform prior function, meaning that I use no prior knowledge of these galaxy's properties. An alternative here would be to make use of the ATLAS^{3D} JAM results reported in Cappellari et al. (2013b); however, due to the wider FOV of my observations, I have chosen to perform my modelling fully independently of theirs.

The likelihood function is therefore given by

$$p(data|model) \propto \exp(-\chi^2/2) \tag{4.28}$$

with χ^2 in this case given by

$$\chi^2 = \sum \left(\frac{[V_{rms} - \langle \sum \overline{v_{los}} \rangle^{1/2}]^2}{\epsilon(V_{rms})^2} \right) \tag{4.29}$$

An MCMC chain will therefore generate a posterior distribution given by

$$p(model|data) \propto p(data|model) \tag{4.30}$$

Given the above discussion, the Metropolis algorithm I employ may be written as follows:

1. Begin at some position θ_i in the parameter space.
2. Attempt to move to position θ_{i+1}, based on the input proposal distribution
3. If $p(\theta_{i+1}|D) > p(\theta_i|D)$ then accept the move; else, accept the move with probability $p(\theta_{i+1}|D)/p(\theta_i|D)$

4. If the move is accepted, complete the move and return to 2.

5. If the move is rejected, set $\theta_{i+1} = \theta_i$ and return to 2.

For a given set of models, I generated two Metropolis chains for each galaxy. The first chain uses an arbitrary proposal distribution; this serves to explore the parameter space, allowing me to calculate the covariance between the free parameters as well as to calculate the χ^2 of the best-fitting model. I run this chain for 2000 iterations, after a burn-in period that serves to locate the approximate region of the χ^2 minimum. Afterwards, I calculate the covariance matrix between the free parameters, which I would subsequently use to construct a proposal distribution for a second optimised MCMC chain which can explore the parameter space in a more efficient way.

However, a problem arises due to the large number of datapoints available for the majority of the sample galaxies, in that even a small change to the model parameters can produce large changes in the derived likelihood; this serves to artificially lower the derived confidence ranges on free parameters unless it is properly accounted for. This problem was noted in van den Bosch et al. (2008) for their Schwarzschild (1979) dynamical models, and they in turn advocated setting confidence ranges on free parameters using the standard deviation of the χ^2 statistic itself; this approach was subsequently validated in van de Ven et al. (2008) and van den Bosch & van de Ven (2009). The standard deviation of χ^2 is given as $\sqrt{2(N_{obs} - N_{par})}$, where N_{obs} describes the number of observed datapoints and N_{par} the number of free parameters, though in practice it is often approximated as $\sqrt{2N_{obs}}$ due to N_{obs} typically being much larger than N_{par}. I adopt a similar approach for setting confidence ranges here, following a similar procedure to that described in Mitzkus et al. (2017). I scale the errors on the V_{rms} maps such that $\chi^2/(N_{obs} - N_{par}) = 1$ for the best-fitting model. I then multiply my errors by $(2(N_{obs} - N_{par}))^{1/4}$; this means that a JAM model fit with $\Delta\chi^2 = \sqrt{2(N_{obs} - N_{par})}$ from the best fit model under the "old" errors will yield $\Delta\chi^2 = 1$ under the rescaled errors. I run the second Metropolis chain using these rescaled errors; I construct a proposal distribution for this chain by multiplying the initial MCMC chain's covariance matrix first by $\chi^2/(N_{obs} - N_{par}) = 1$ and then by $(2(N_{obs} - N_{par}))^{1/4}$.

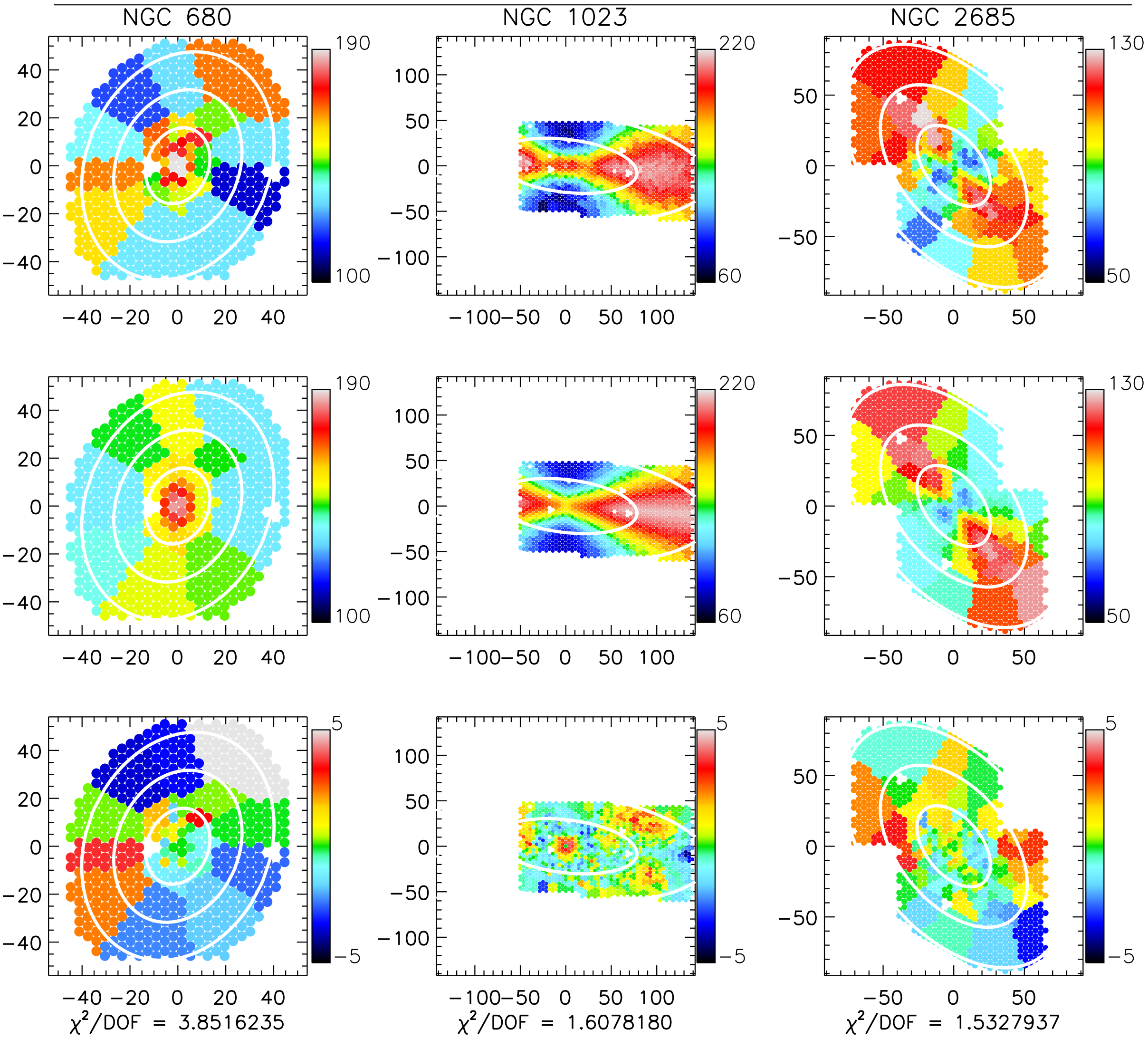

Figure 4.6: V_{rms} maps for NGC 680, NGC 1023 and NGC 2685 along with associated best-fit JAM models and residual maps. These maps use the *unscaled* kinematics errors. Rows from top to bottom: observed V_{rms} in km/s, line-of-sight second velocity moment of best-fitting JAM model in km/s, residual maps in units of σ. The white contours are spaced in units of R_e. Fibre positions from the missing NGC 2685 dither on the top left of the FOV have been re-added for presentational purposes, with values assigned to each from the nearest Voronoi bin.

4.3 Results

In Figures 4.6-4.9, I present the best-fit JAM models obtained from the initial MCMC chains run for the base JAM models. I find that the JAM models generally recreate the observed V_{RMS} well across the FOV, with $\chi^2/DOF < 2$ in most cases. I note that certain galaxies - NGC 1023, NGC 3998 and NGC 4203 - have JAM model residuals that appear highly structured near their centres, suggesting that these objects' kinematics are more complex than what the base models can reproduce.

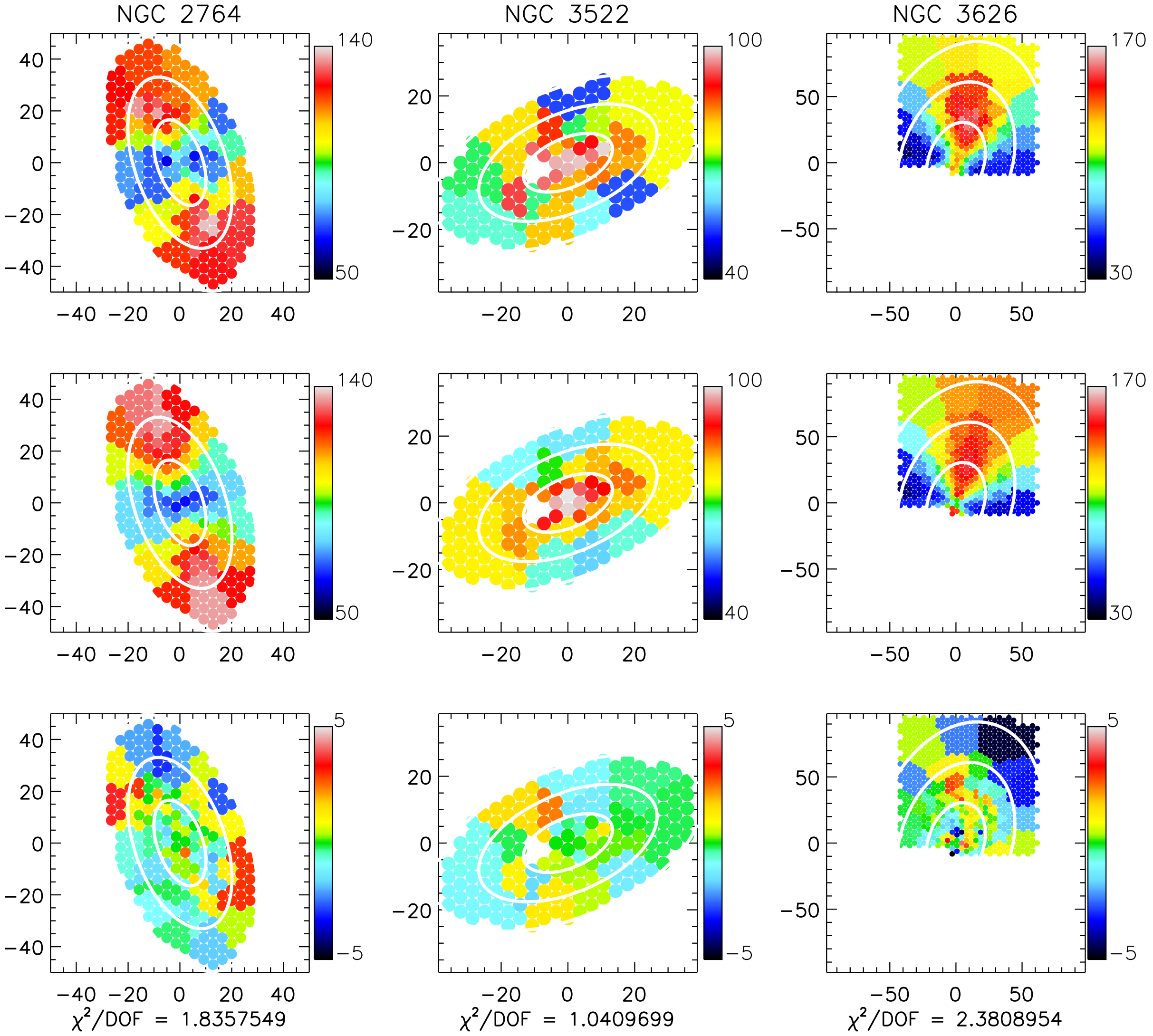

Figure 4.7: As in Figure 4.6, but for galaxies NGC 2764, NGC 3522 and NGC 3626.

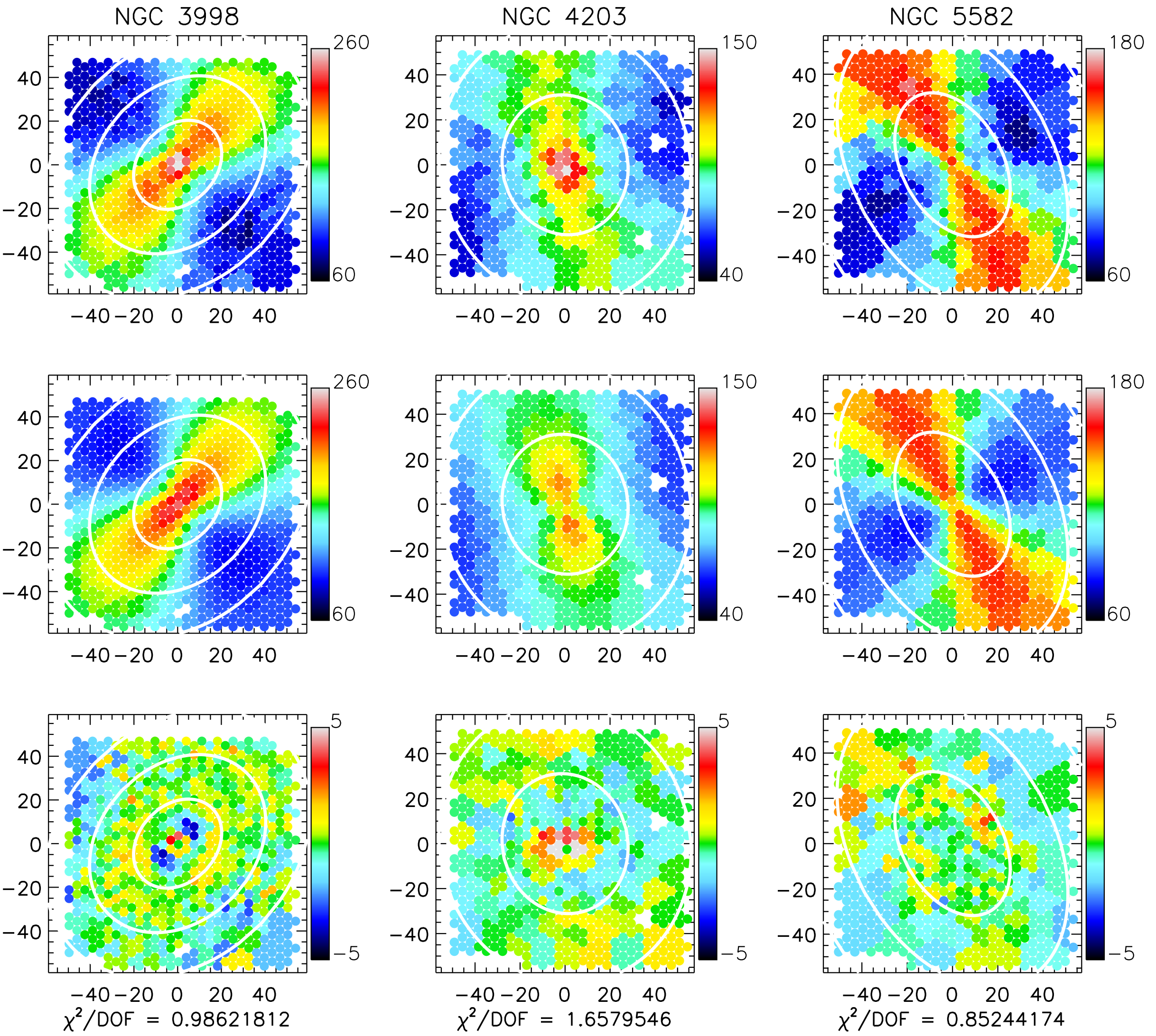

Figure 4.8: As in Figure 4.6, but for galaxies NGC 3998, NGC 4203 and NGC 5582. Fibre positions from the missing NGC 4203 dither have been re-added for presentational purposes, with values assigned to each from the nearest Voronoi bin.

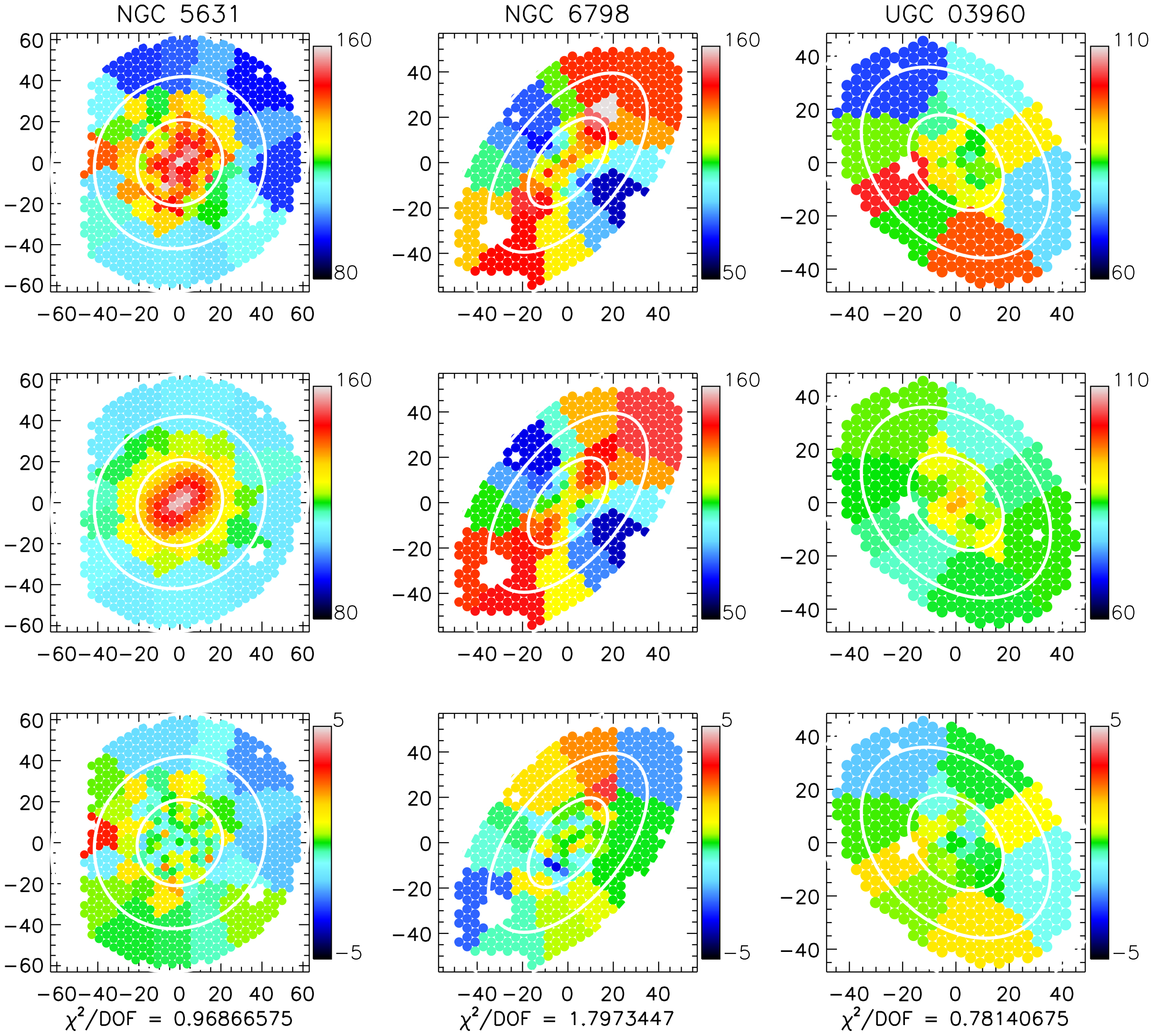

Figure 4.9: As in Figure 4.6, but for galaxies NGC 5631, NGC 6798 and UGC 03960.

After scaling the kinematics errors for each galaxies based on the best fits, I ran a second set of MCMC chains with the kinematics errors scaled so as to derive parameter confidence intervals. I show the resulting final MCMC chains for the 12 galaxies in Figures 4.10-4.21, in terms of each of the four free parameters in turn. I note signs of undesired structure in the chains in several cases. This structure could potentially be eliminated by employing more efficient proposal distributions, or else could be mitigated by generating longer MCMC chains; I intend to investigate both approaches as part of my future work.

Degeneracies between free parameters are a likely cause of such structure in MCMC chains. To better visualise the correlations between the different free parameters, I present maps and histograms of the MCMC chains in Figures 4.22-4.33. Unsurprisingly, I find degeneracies between the parameters in many cases. In particular, M_*/L and M_{200} are always degenerate to at least some degree, in that a higher value of M_*/L corresponds to a lower value of M_{200}. β_z and q_{min} are also often degenerate, in that lower values of q_{min} correspond to more positive values of β_z; this means that for such galaxies, more face-on assumed inclinations are associated with velocity ellipsoids with greater elongation in the z-direction.

The shape parameter q_{min} corresponds to the *flattest* component of the input MGE model, making it difficult to interpret a galaxy's overall shape through this parameter alone. I calculate the corresponding shape of the overall model by first deprojecting it according to q_{min} and then by fitting oblate spheroids of constant luminosity density in order to derive the axis ratio at $1R_e$, hereafter q_e.

In Table 4.2, I give parameter confidence ranges on for the twelve galaxies in my galaxy sample. I estimate the best-fit parameters for each galaxy by taking the median of the corresponding MCMC chain in terms of a given parameter, with errors reported as the standard deviation of the chain. I also give q_e on this table along with the dark matter fraction at $1R_e$, $f_{dm,e}$. This value is calculated using the method described in Cappellari et al. (2013a), in which the MGE surface brightness model is circularised prior to calculating the dark matter fraction within a sphere of radius R_e.

The majority of sample galaxies that are fast-rotating at 1 R_e have axis ratios q_e of approximately or below 0.5. This is similar to the axis ratios reported by Naab et al. (2014) for their Class A and Class B galaxies (galaxies that have experienced minor gas-rich mergers and major gas-rich mergers, respectively). All three galaxies that are slow-rotating at $1R_e$ (NGC 3522,

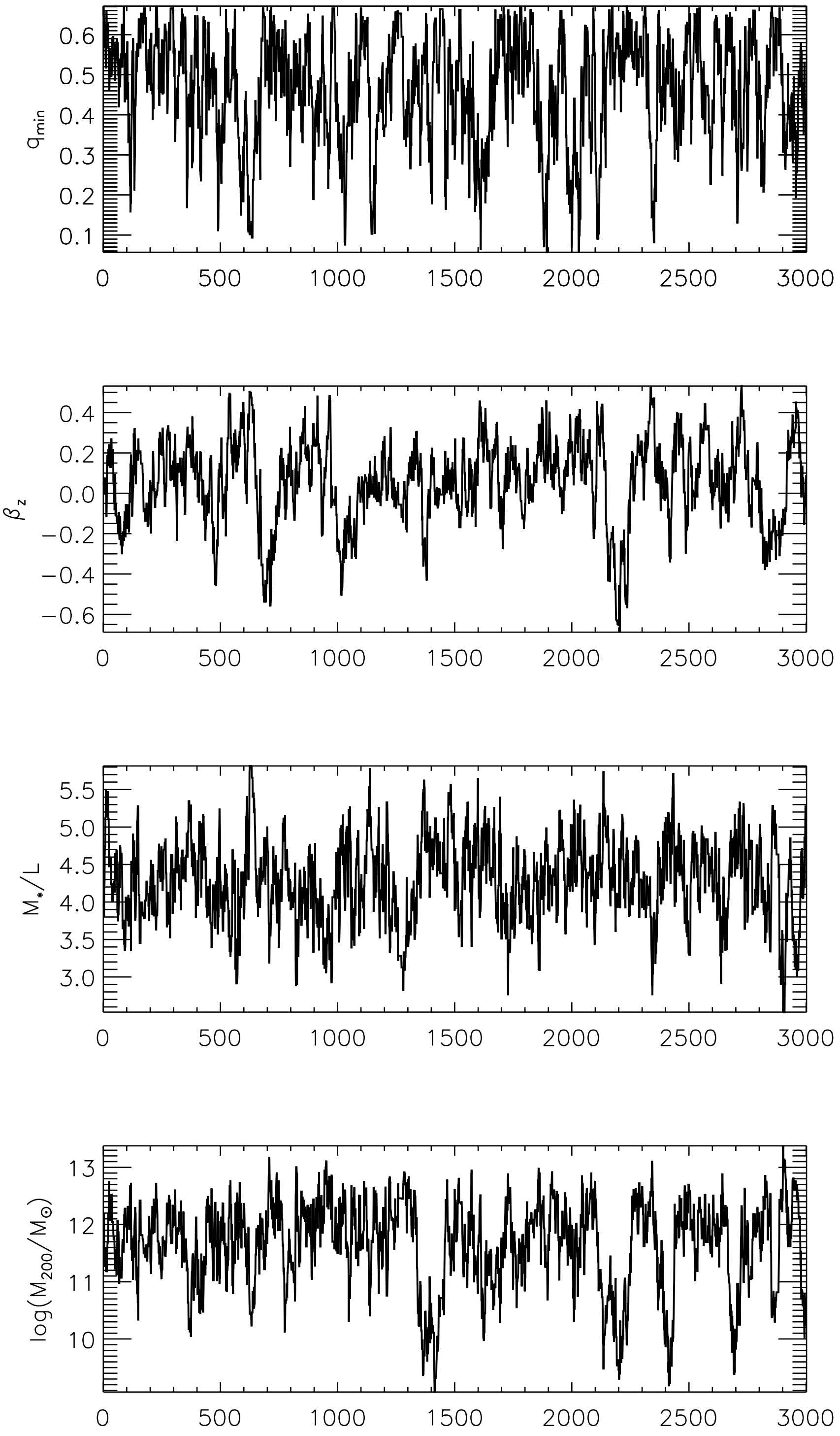

Figure 4.10: MCMC chain for NGC 680, plotted in terms of each free parameter in turn.

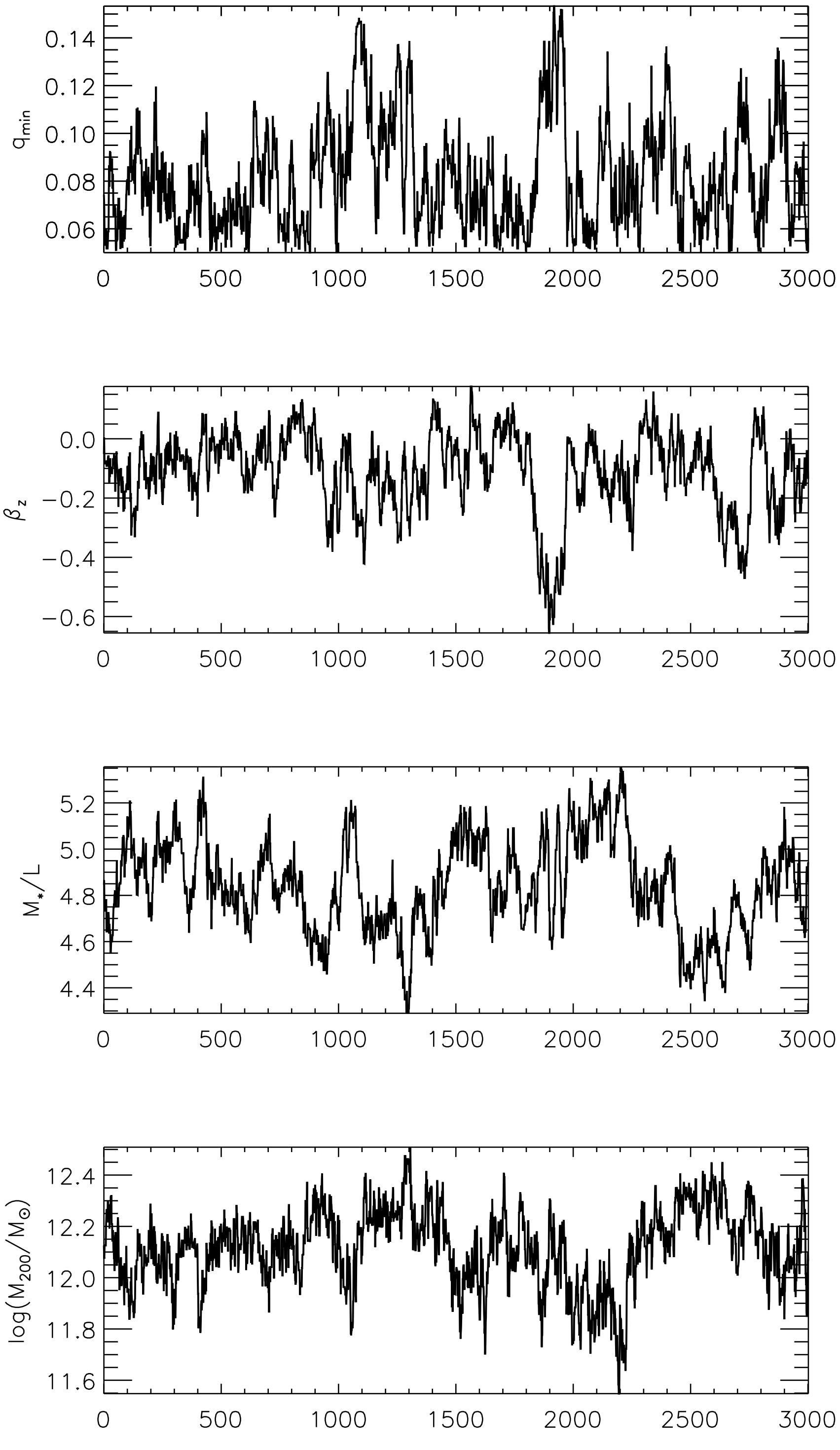

Figure 4.11: MCMC chain for NGC 1023, plotted in terms of each free parameter in turn.

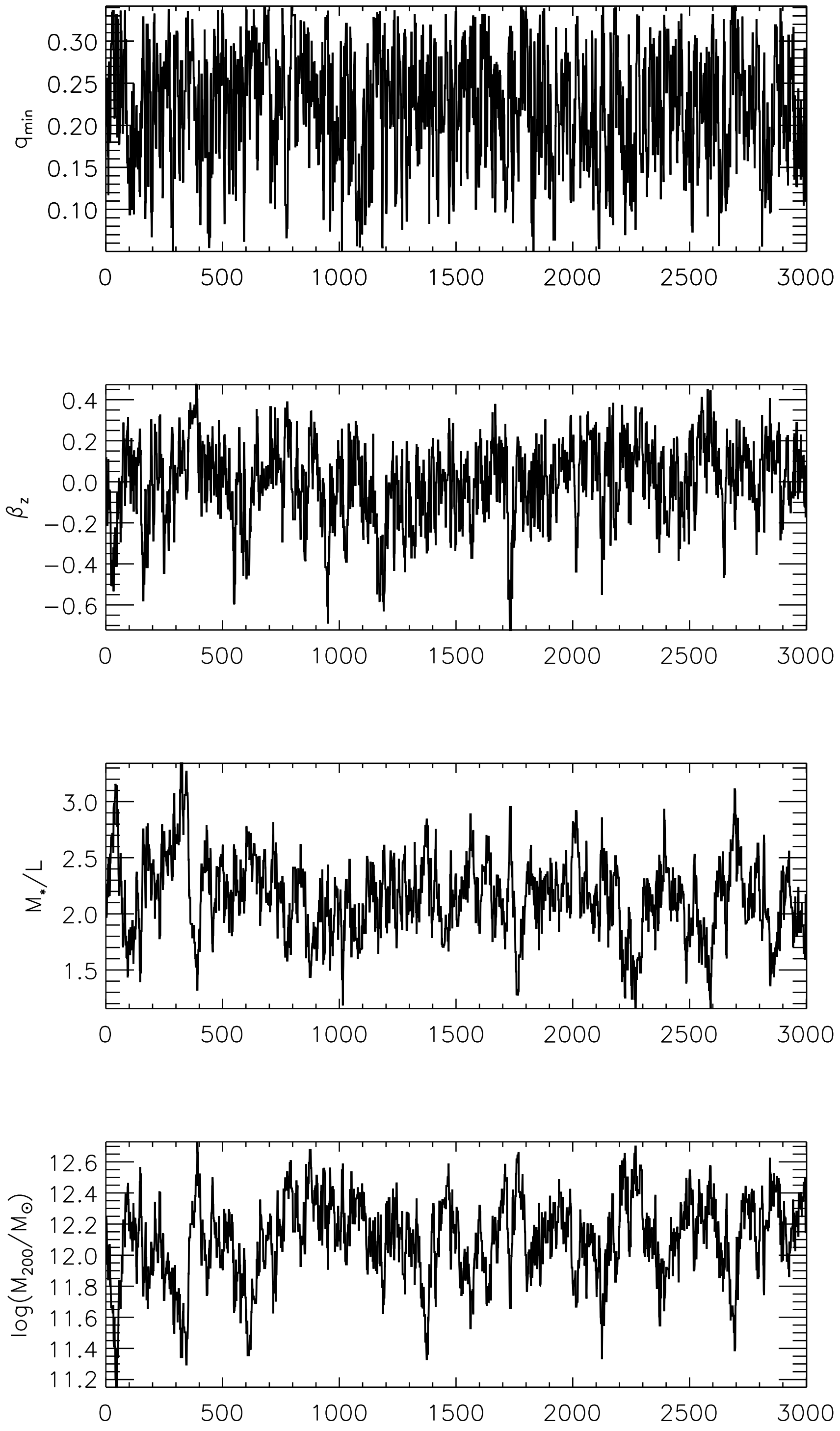

Figure 4.12: MCMC chain for NGC 2685, plotted in terms of each free parameter in turn.

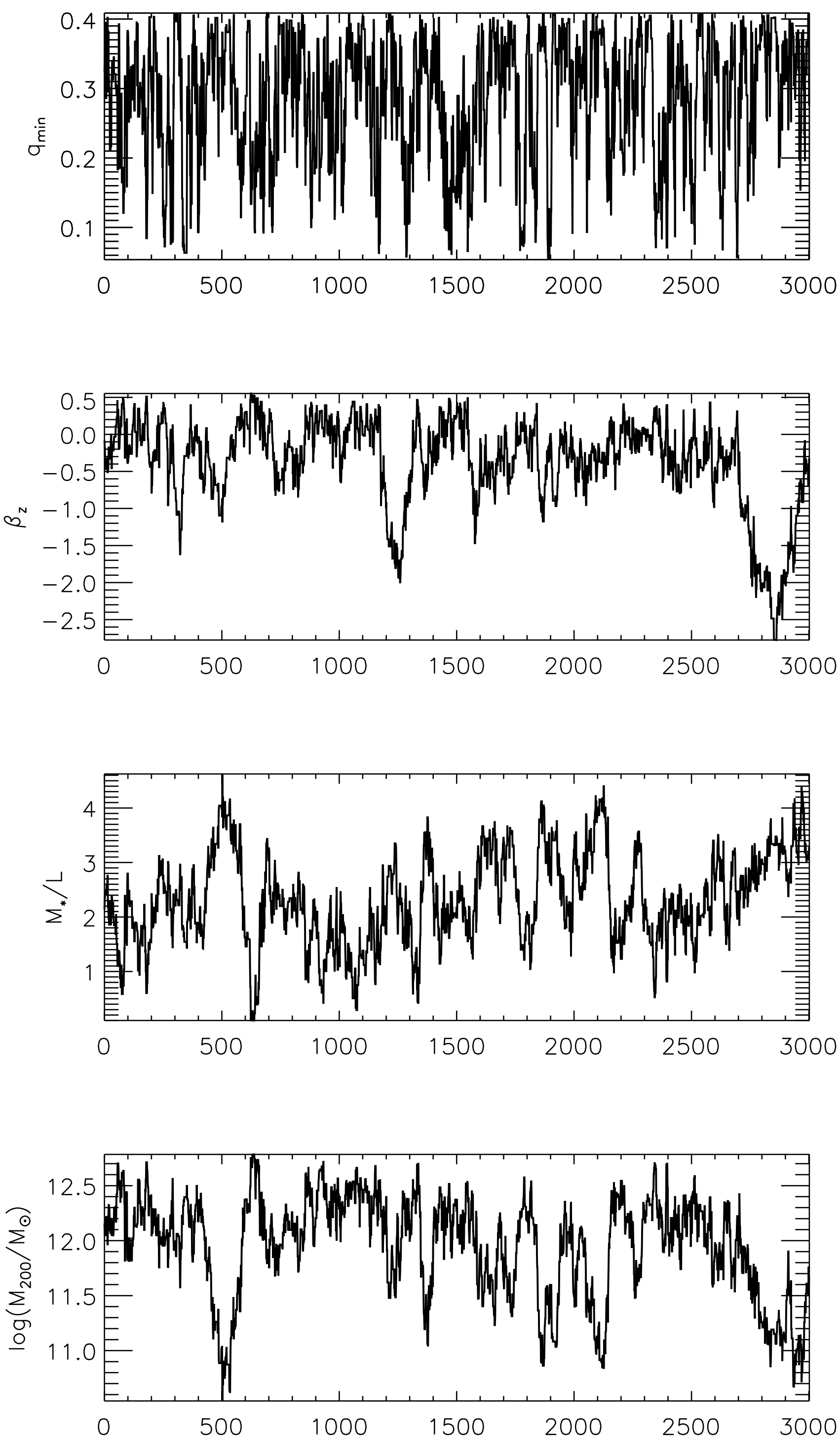

Figure 4.13: MCMC chain for NGC 2764, plotted in terms of each free parameter in turn.

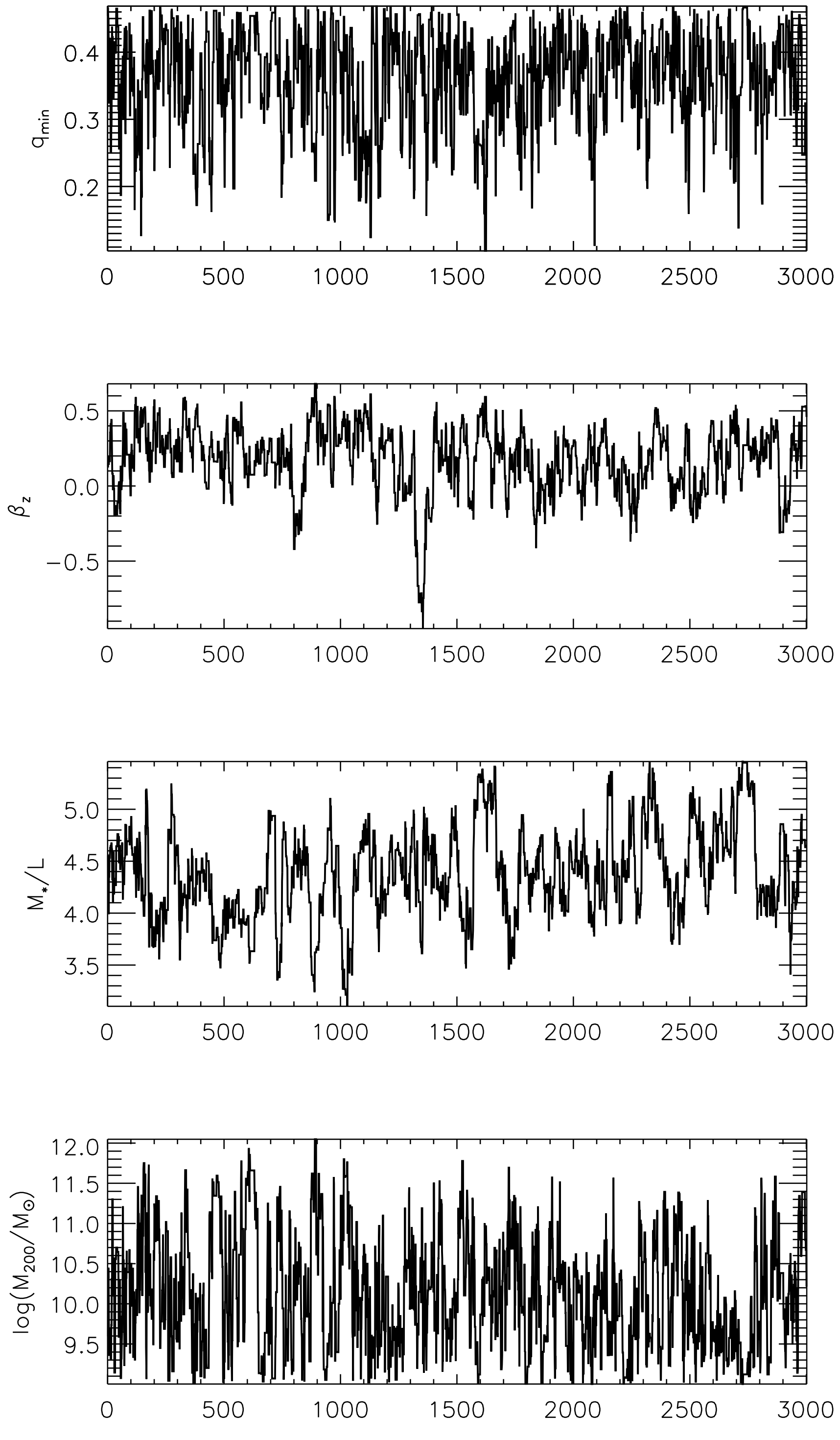

Figure 4.14: MCMC chain for NGC 3522, plotted in terms of each free parameter in turn.

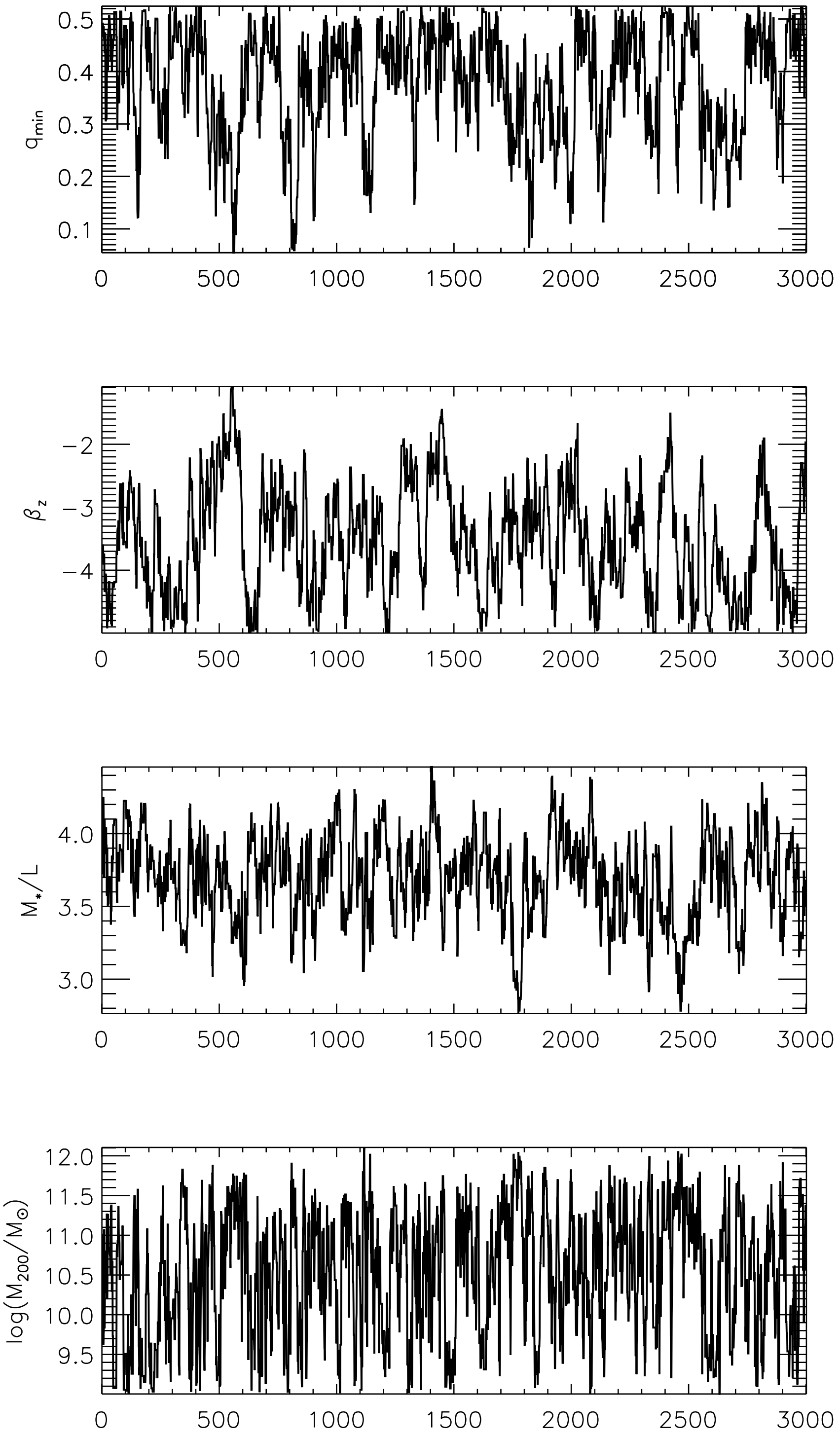

Figure 4.15: MCMC chain for NGC 3626, plotted in terms of each free parameter in turn

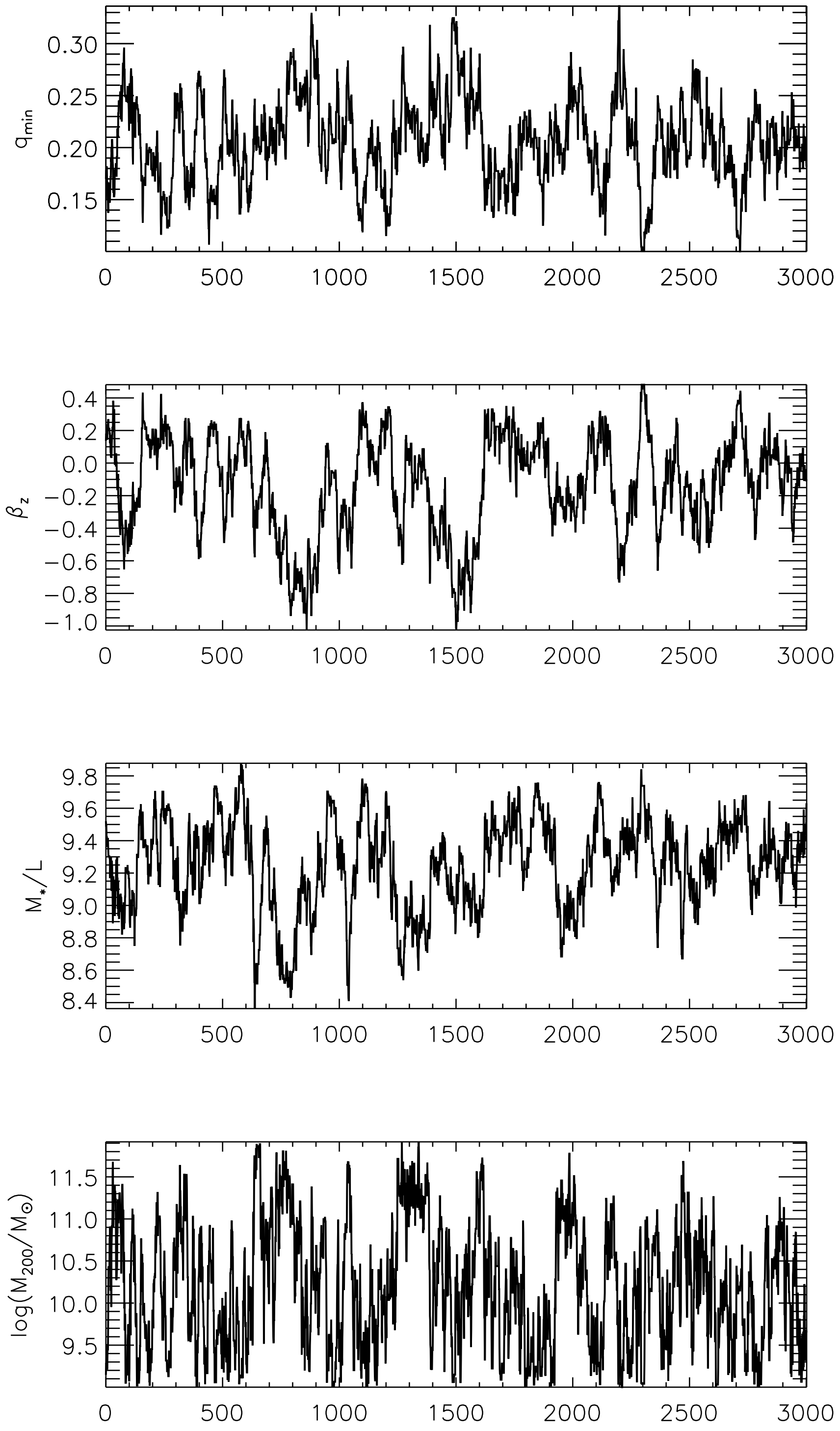

Figure 4.16: MCMC chain for NGC 3998, plotted in terms of each free parameter in turn.

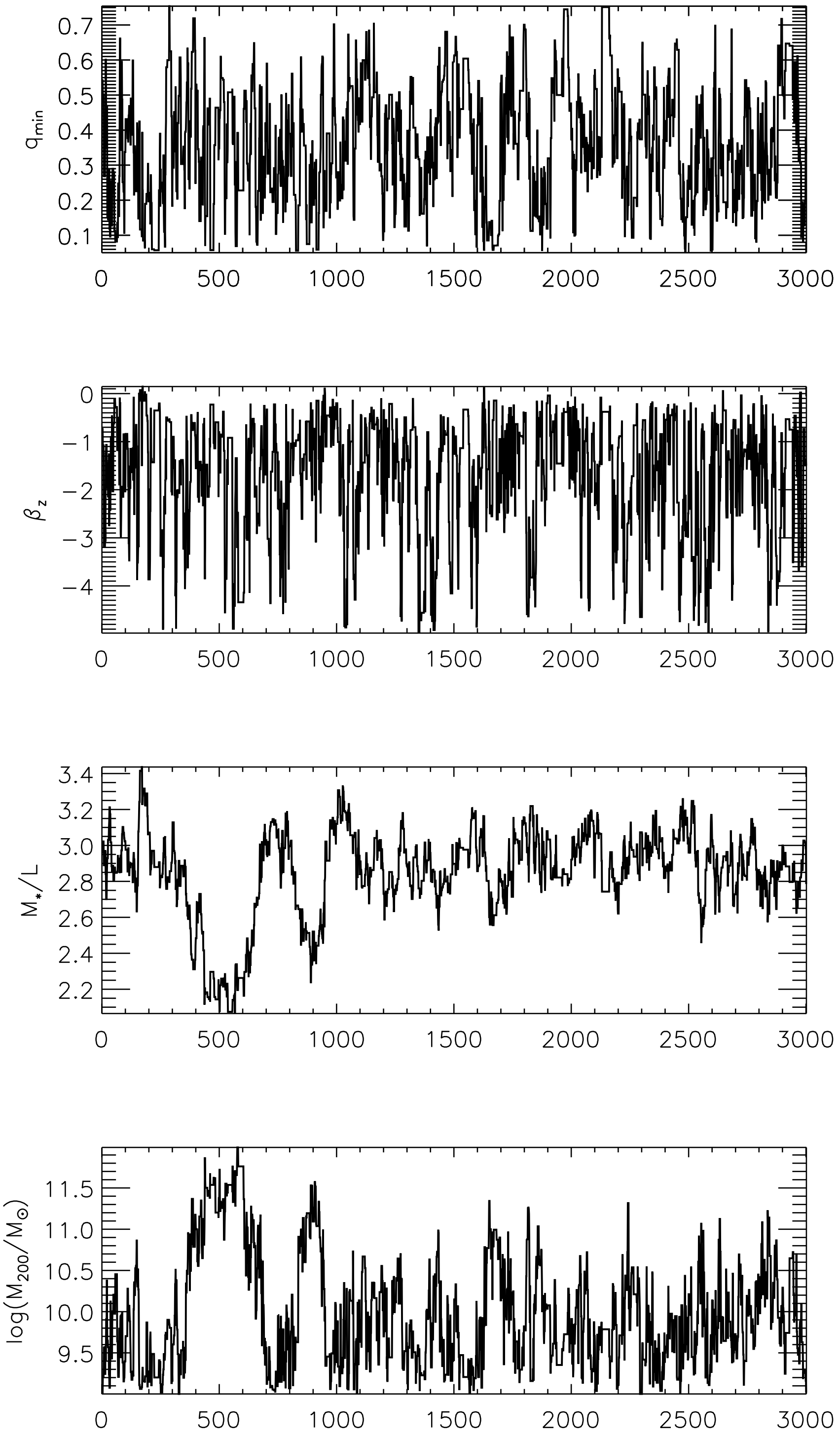

Figure 4.17: MCMC chain for NGC 4203, plotted in terms of each free parameter in turn.

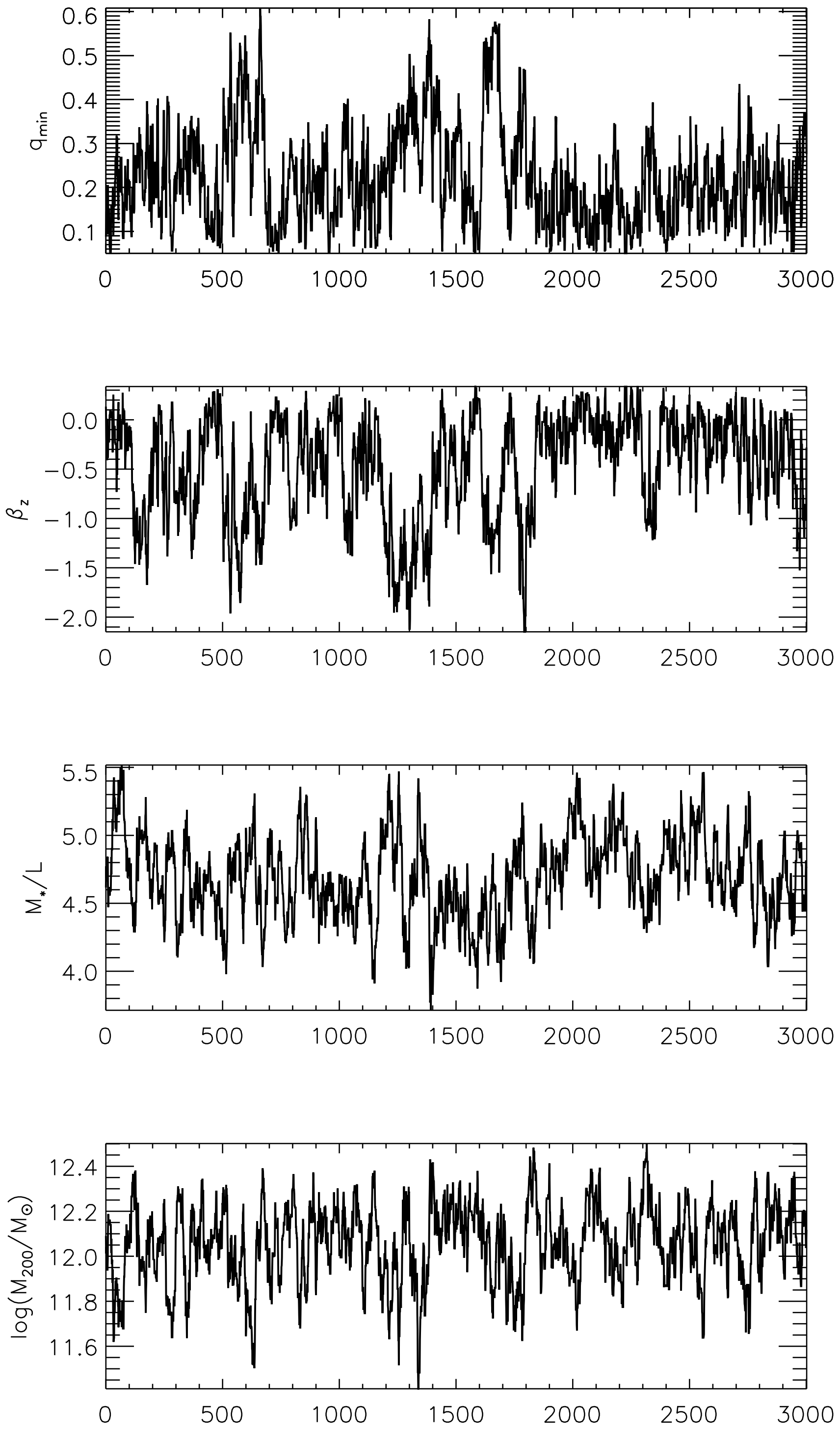

Figure 4.18: MCMC chain for NGC 5582, plotted in terms of each free parameter in turn

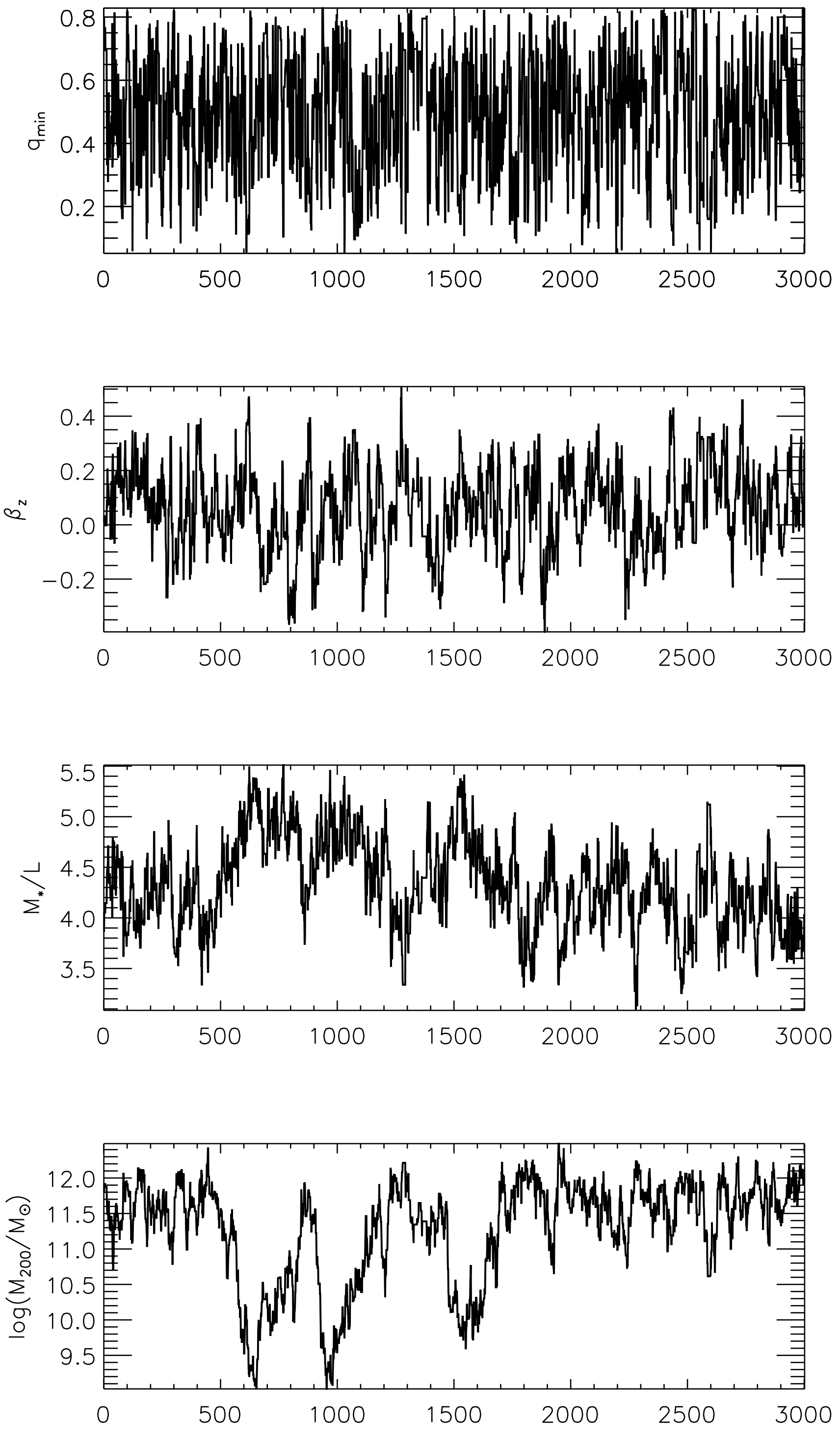

Figure 4.19: MCMC chain for NGC 5631, plotted in terms of each free parameter in turn

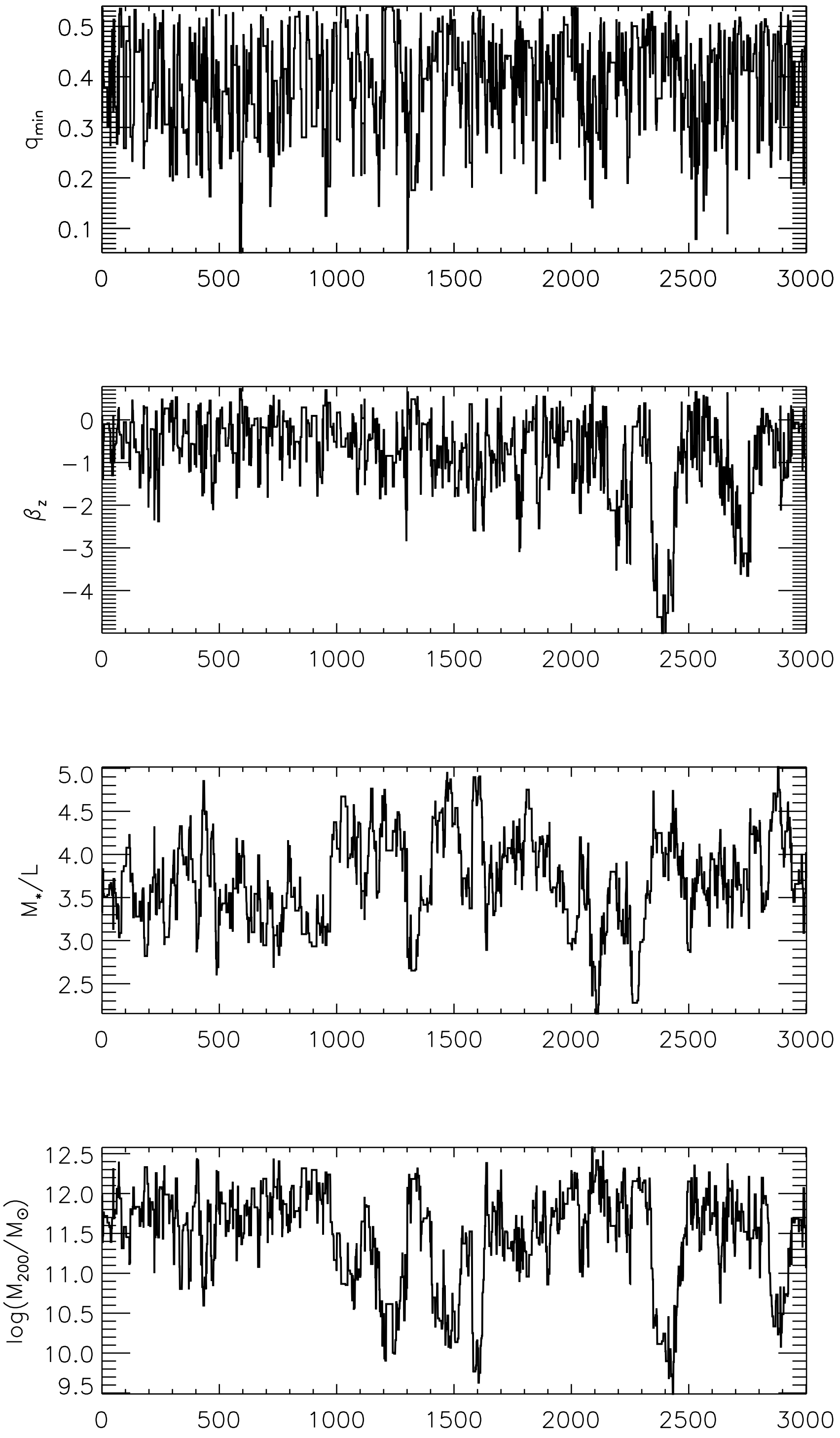

Figure 4.20: MCMC chain for NGC 6798, plotted in terms of each free parameter in turn

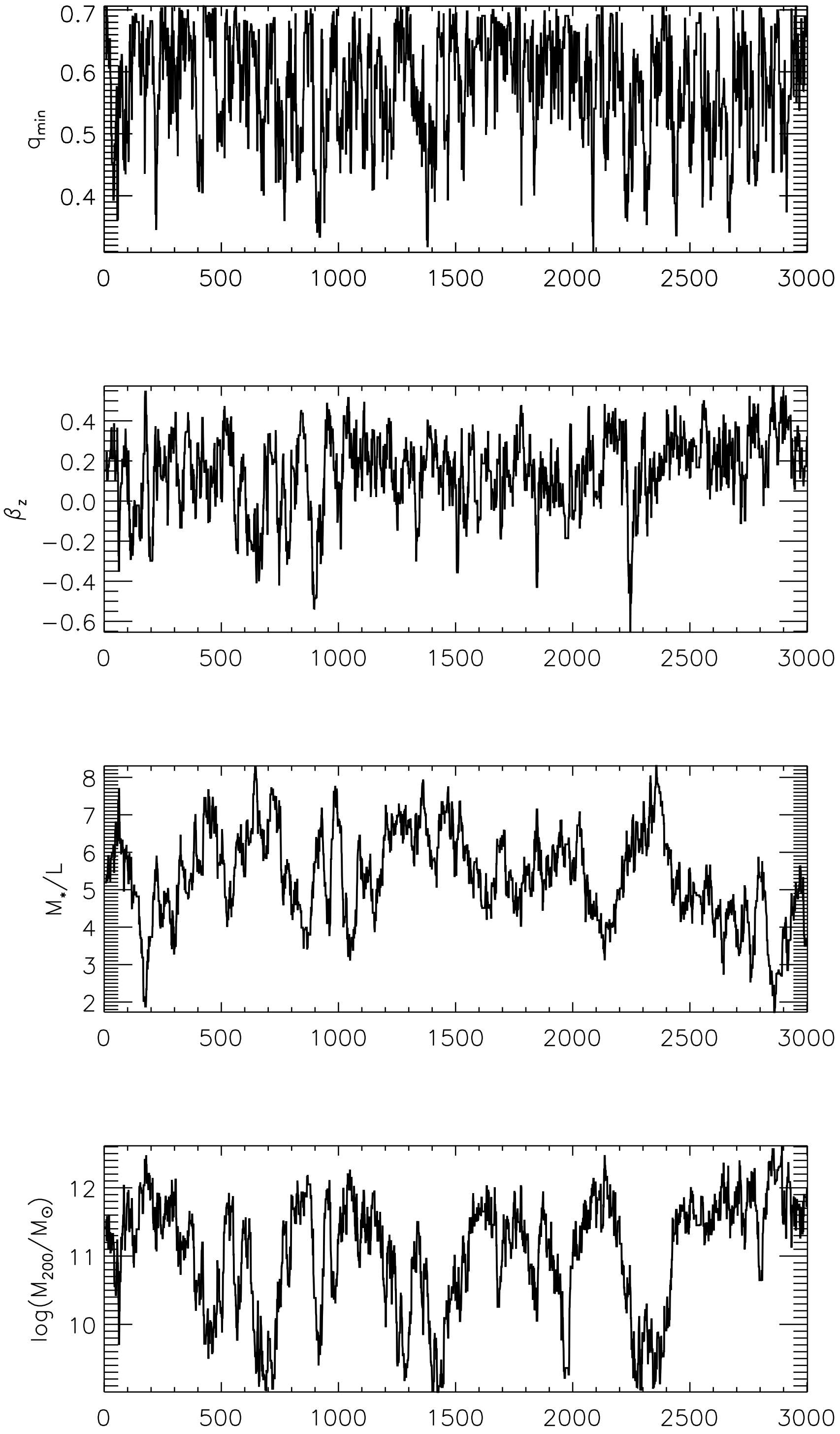

Figure 4.21: MCMC chain for UGC 03960, plotted in terms of each free parameter in turn

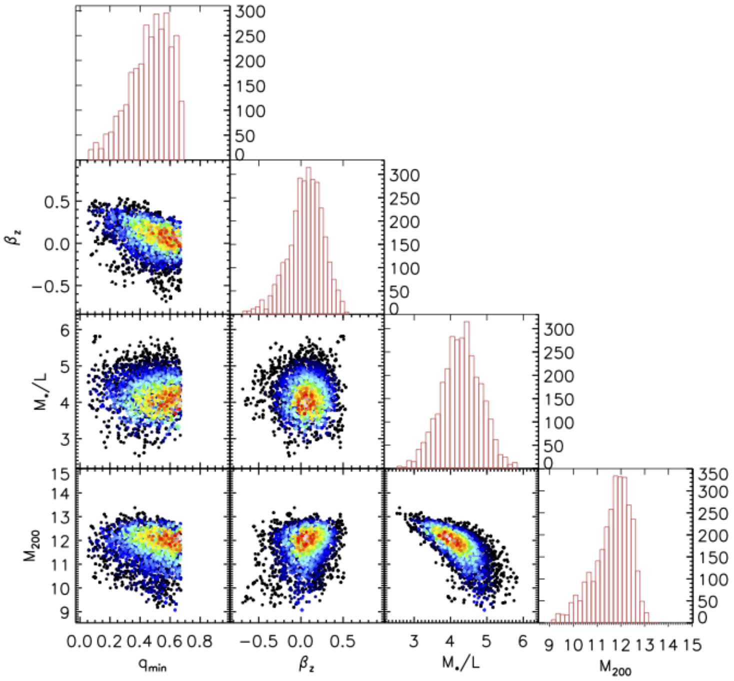

Figure 4.22: MCMC chain for JAM modelling of NGC 680. The color-coding corresponds to the likelihood of a given JAM model, with black points corresponding to models disfavoured by 1σ or greater after re-scaling the errors.

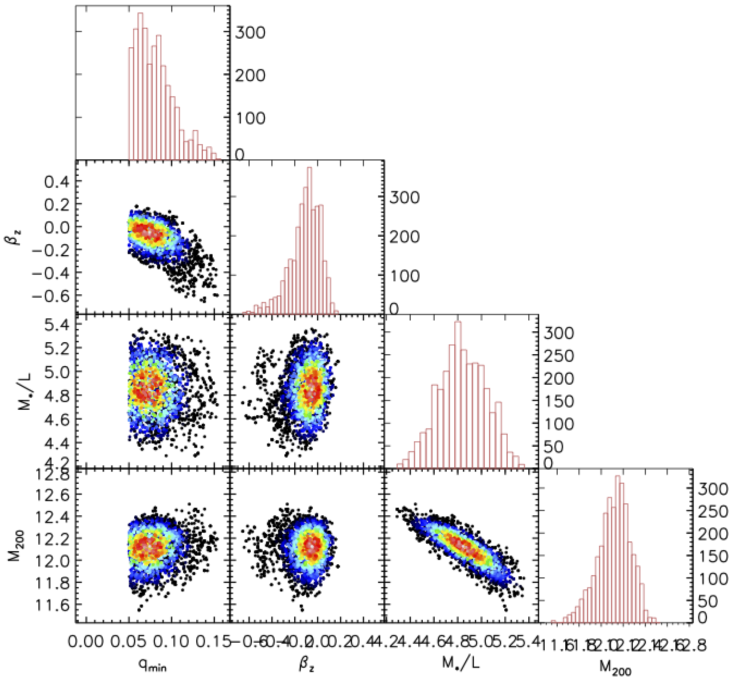

Figure 4.23: MCMC chain for JAM modelling of NGC 1023.

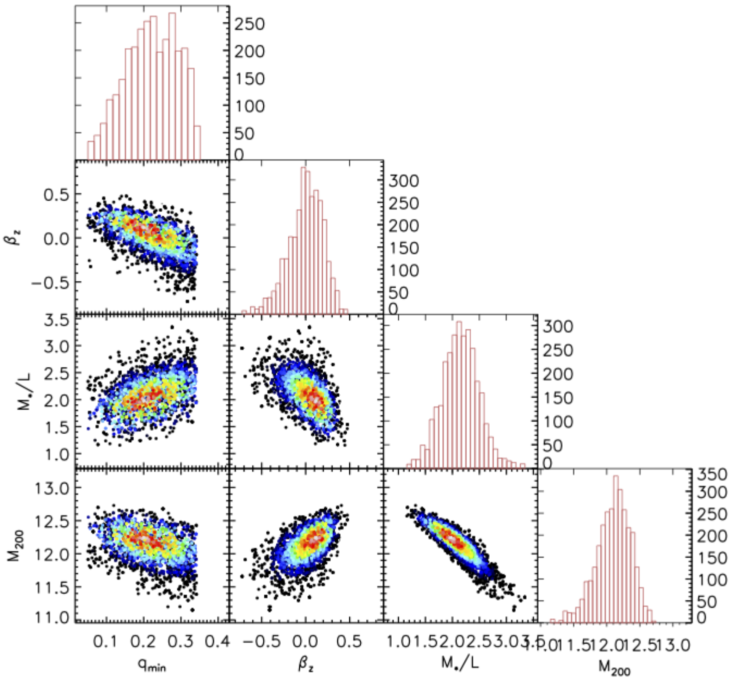

Figure 4.24: MCMC chain for JAM modelling of NGC 2685.

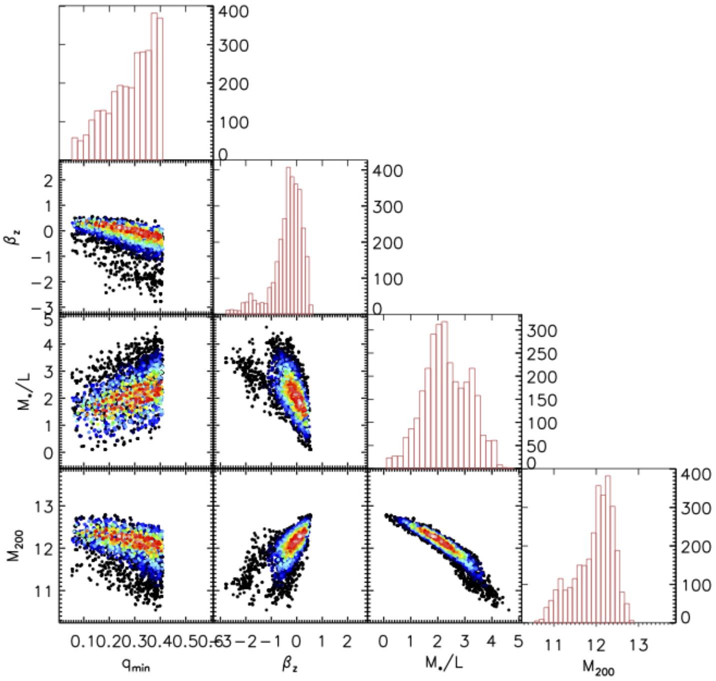

Figure 4.25: MCMC chain for JAM modelling of NGC 2764.

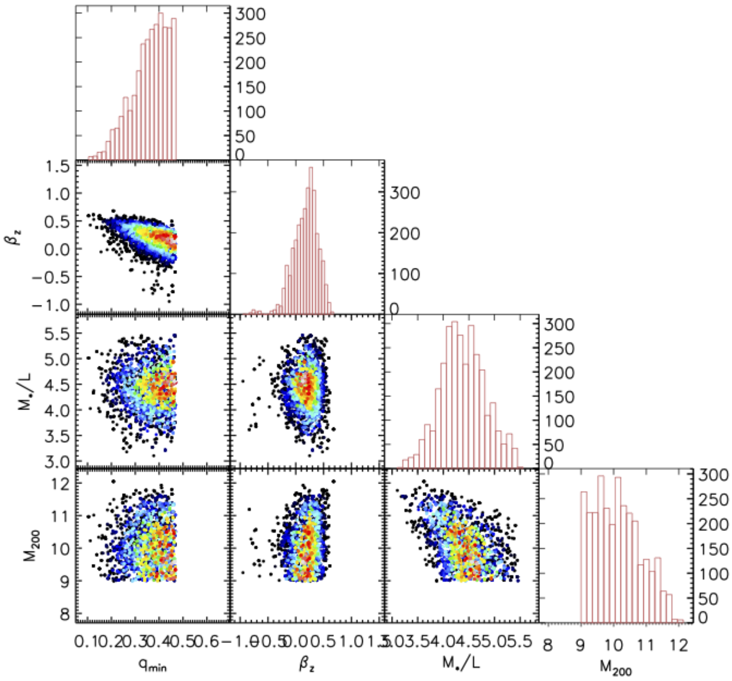

Figure 4.26: MCMC chain for JAM modelling of NGC 3522.

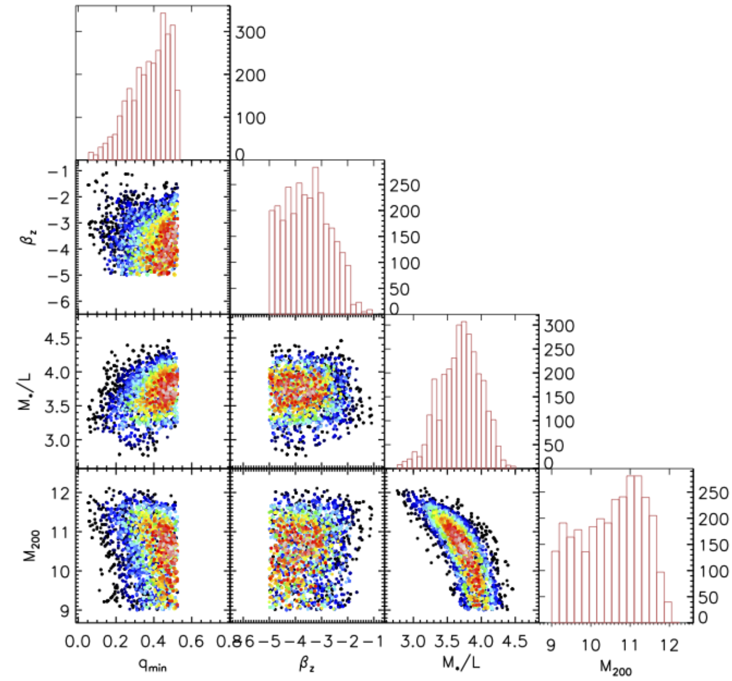

Figure 4.27: MCMC chain for JAM modelling of NGC 3626.

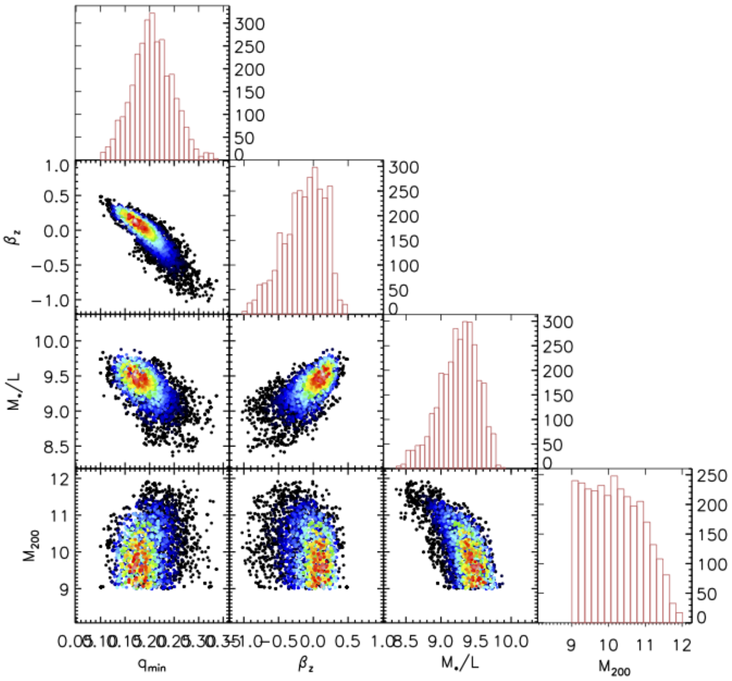

Figure 4.28: MCMC chain for JAM modelling of NGC 3998.

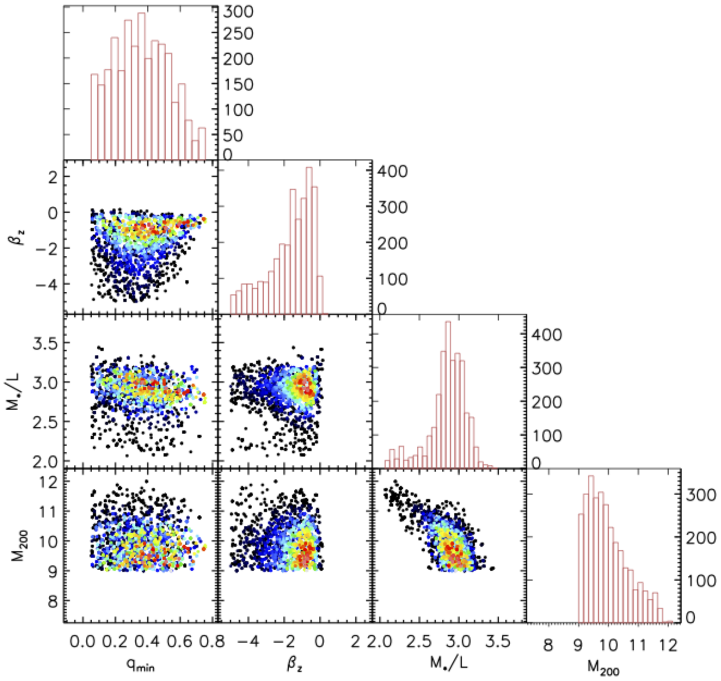

Figure 4.29: MCMC chain for JAM modelling of NGC 4203.

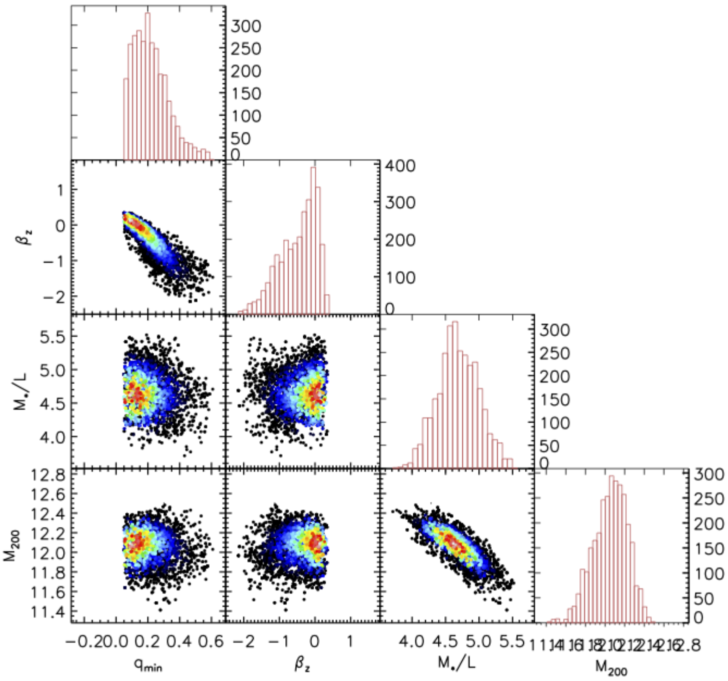

Figure 4.30: MCMC chain for JAM modelling of NGC 5582.

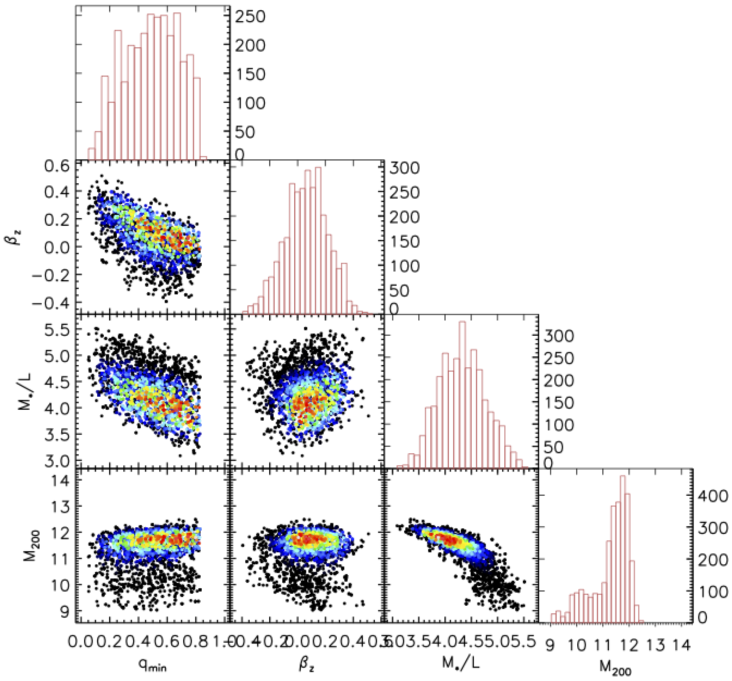

Figure 4.31: MCMC chain for JAM modelling of NGC 5631.

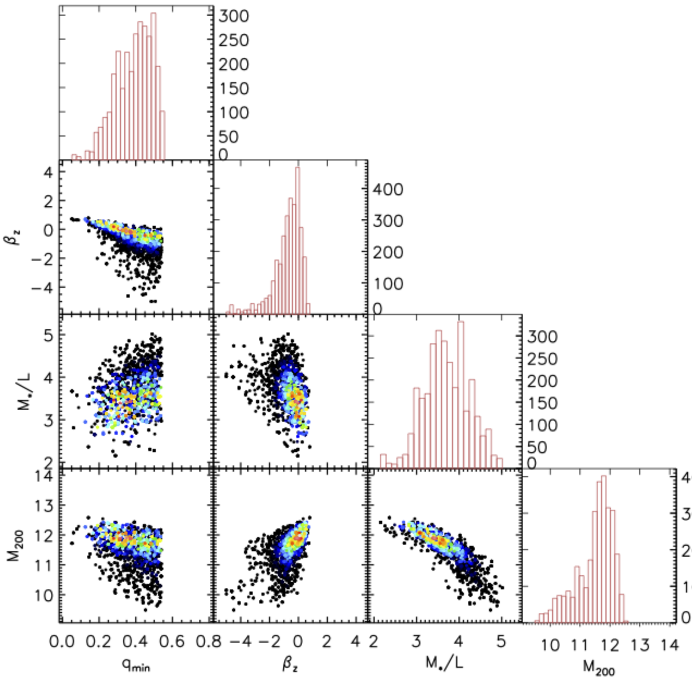

Figure 4.32: MCMC chain for JAM modelling of NGC 6798.

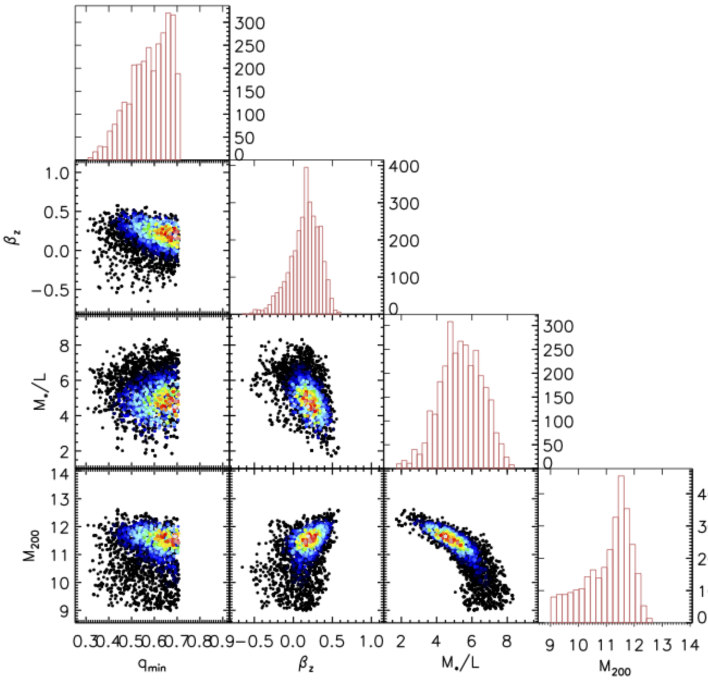

Figure 4.33: MCMC chain for JAM modelling of UGC 03960.

Galaxy	inc (°)	q_{R_e}	β_z	$M_*/L(M_\odot/L_\odot)$	$f_{dm,e}$
NGC 680	$57.8^{+13.3}_{-5.7}$	$0.76^{+0.06}_{-0.06}$	0.07 ± 0.21	4.30 ± 0.54	$0.104^{+0.105}_{-0.057}$
NGC 1023	$72.3^{+0.4}_{-0.3}$	$0.45^{+0.02}_{-0.03}$	-0.09 ± 0.14	4.83 ± 0.20	$0.085^{+0.014}_{-0.012}$
NGC 2685	$74.5^{+4.7}_{-2.6}$	$0.42^{+0.04}_{-0.04}$	0.01 ± 0.20	2.15 ± 0.35	$0.25^{+0.080}_{-0.063}$
NGC 2764	$73.3^{+10.4}_{-4.3}$	$0.31^{+0.09}_{-0.09}$	-0.25 ± 0.61	2.25 ± 0.84	$0.35^{+0.21}_{-0.14}$
NGC 3522	$72.1^{+9.0}_{-4.5}$	$0.63^{+0.04}_{-0.04}$	0.21 ± 0.22	4.36 ± 0.44	$0.043^{+0.050}_{-0.025}$
NGC 3626	$67.8^{+11.3}_{-5.1}$	$0.40^{+0.11}_{-0.10}$	-3.5 ± 0.86	3.71 ± 0.30	$0.049^{+0.059}_{-0.029}$
NGC 3998	$38.9^{+0.5}_{-0.4}$	$0.44^{+0.03}_{-0.03}$	-0.1 ± 0.30	9.28 ± 0.28	$0.009^{+0.010}_{-0.005}$
NGC 4203	$43.6^{+5.7}_{-2.6}$	$0.999^{+0.0004}_{-0.0008}$	-1.4 ± 1.2	2.88 ± 0.24	$0.038^{+0.048}_{-0.023}$
NGC 5582	$52.6^{+2.4}_{-1.2}$	$0.33^{+0.08}_{-0.08}$	-0.34 ± 0.52	4.67 ± 0.31	$0.26^{+0.046}_{-0.041}$
NGC 5631	$40.0^{+10.1}_{-4.1}$	$0.99^{+0.006}_{-0.006}$	0.07 ± 0.15	4.31 ± 0.45	$0.11^{+0.11}_{-0.06}$
NGC 6798	$66.6^{+9.6}_{-4.8}$	$0.42^{+0.09}_{-0.07}$	-0.54 ± 0.99	3.66 ± 0.54	$0.13^{+0.098}_{-0.059}$
UGC 03960	$61.2^{+13.1}_{-6.3}$	$0.83^{+0.04}_{-0.03}$	0.17 ± 0.19	5.37 ± 1.19	$0.25^{+0.24}_{-0.15}$

Table 4.2: Parameter confidence ranges derived from the base JAM models, after scaling errors on the kinematics. Values and errors are reported as the medians of the MCMC chains and the standard deviations, respectively.

NGC 5631 and UGC 03960) have deprojected axis ratios greater than 0.5; in addition, NGC 680 and NGC 4203 (both fast-rotators) also have axis ratios significantly above 0.5. I note that the models for NGC 4203 and NGC 5631 have axis ratios of almost 1 even after deprojection, implying galaxies that are near-spherical at $1R_e$. However, these galaxies appear to be relatively face-on objects, meaning that the deprojection is highly degenerate, with small changes to the (projected) MGE models potentially leading to large changes in the inferred (deprojected) mass distributions; I will investigate these galaxies' photometry in more detail as part of my future work.

In Table 5.1, I present the χ^2/DOF obtained from the base JAM models, along with the 2-β and DM-free models described in the preceding section. I find that the base models and 2-β models typically yield a very similar performance in a χ^2 sense, whereas the DM-free models are formally poorer for most of the galaxies. The exceptions here are NGC 3522, NGC 3998 and NGC 4203, for which the DM-free models provide marginally better performance than the base models; perhaps unsurprisingly, these three galaxies also have the lowest dark matter fractions as derived from the base models.

Galaxy	$(\chi^2/DOF)_{base}$	$(\chi^2/DOF)_{2-\beta}$	$(\chi^2/DOF)_{DM-free}$
NGC 680	3.85	3.89	6.03
NGC 1023	1.61	1.43	2.31
NGC 2685	1.53	1.54	4.03
NGC 2764	1.84	1.83	3.87
NGC 3522	1.04	0.91	0.90
NGC 3626	2.38	2.40	2.61
NGC 3998	0.99	0.84	0.84
NGC 4203	1.66	0.92	0.89
NGC 5582	0.85	0.83	2.73
NGC 5631	0.97	1.02	1.66
NGC 6798	1.80	1.82	3.02
UGC 03960	0.78	0.51	1.53

Table 4.3: χ^2/DOF values obtained from best-fitting JAM models, for the base models, 2-β models and DM-free models in turn. The base models and 2-β models typically perform similarly in a χ^2 sense, while the DM-free models are formally poorer for most of the galaxies; the three exceptions are NGC 3522, NGC 3998 and NGC 4203, for which the DM-free models are formally slightly better than the base models.

In Figure 4.34, I plot the derived $\beta_{z,in}$ and $\beta_{z,out}$ parameters for the galaxy sample from the 2-β models. Generally, my $\beta_{z,in}$ parameters are consistent with isotropy to the 1σ level; the one exception here is NGC 3626, for which the models imply significant tangential anisotropy within the central effective radius. In the case of $\beta_{z,out}$, I find only five galaxies to be consistent with isotropy within the 1σ level; I find JAM modelling of six galaxies (NGC 1023, NGC 2685, NGC 3626, NGC 4203 NGC 5582 and NGC 6798) to be instead consistent with tangential anisotropy within the 1σ level in this case, with JAM models of UGC 03960 instead favouring radial anisotropy.

In Figure 4.35, I compare the mass-to-light ratios and dark matter fractions inferred from the base JAM models with those inferred from the $2-\beta$ models. I obtain near 1-1 agreement between the two sets of models, implying that the treatment of β_z in the JAM models does *not* significantly affect the derived mass contents. As such, I focus on the base models for the remainder of this chapter.

In Figure 4.36, I present the total localised mass density profiles obtained from the best-fit base JAM models. I calculated the density profiles for each galaxies using the best-fit inclination, M_*/L and M_{200} values as inputs. I computed the dark matter component of the profiles using Equation 4.24, while for the visible component I used the equation given the fourth footnote of Cappellari et al. (2015):

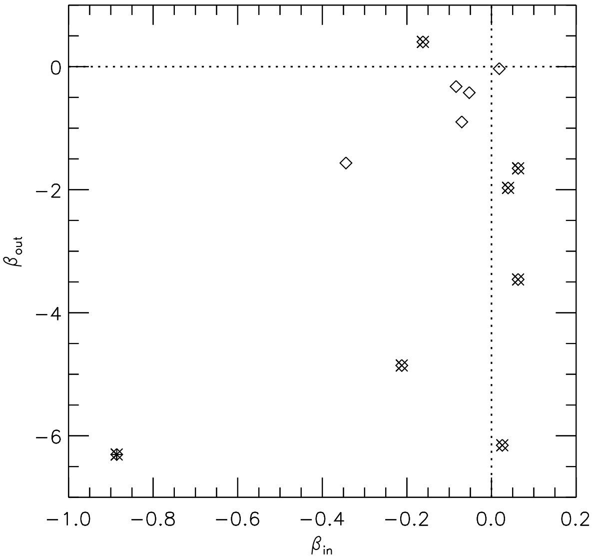

Figure 4.34: $\beta_{z,out}$ vs $\beta_{z,in}$ obtained from JAM modelling of the sample ETGs, with definitions of these parameters as described in the text. The dashed lines correspond to isotropic galaxy dynamics. X symbols signify values of β_{out} more than 1σ away from isotropy, while crosses signify values of β_{in} more than 1σ away from isotropy. My derived β_{in} parameters are typically consistent with isotropy. My β_{out} values are generally negative (tangential anisotropy), with a significant subset being inconsistent with isotropy at the 1σ level. Error bars are not displayed, for the purpose of readability.

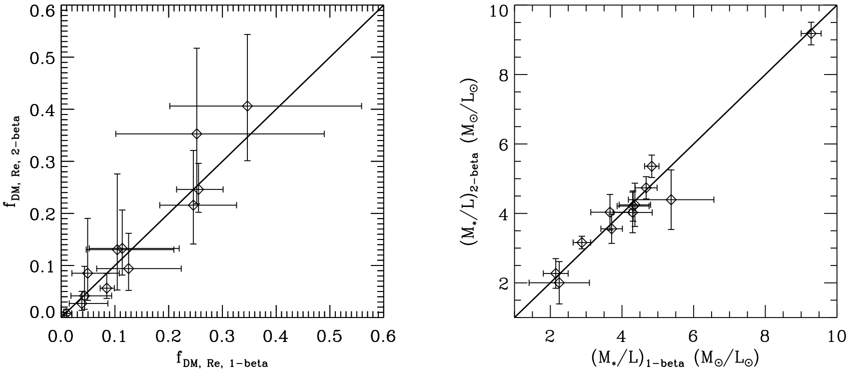

Figure 4.35: Comparison of dark matter fractions (left) and stellar mass-to-light ratios (right) inferred from base JAM models and 2-β JAM models. I find good agreement in both parameters between the two sets of models, and so conclude that the treatment of anisotropy β_z does *not* significantly affect the inferred mass parameters.

$$\rho_{tot}(r) = \sum_{j=1}^{M} \frac{M_j \exp\left[-r^2/(2\sigma_j^2)\right] \mathrm{erf}\left[r\sqrt{1-q_j^2}/(q_j\sigma_j\sqrt{2})\right]}{4\pi\sigma_j^2 r\sqrt{1-q_j^2}} \tag{4.31}$$

where M_j describes the total mass of a given MGE Gaussian component and all other symbols are as previously defined. The erf term in this equation arises from integrating over MGE Gaussian components. These profiles were calculated linearly, in steps of $0.1R_e$ out to $2R_e$. I performed least-absolute-deviation fits to these profiles for radii beyond $1R_e$ in order to calculate the logarithmic slope of these profiles; I obtain a mean logarithmic slope of -2.13, with a standard deviation of 0.29. As such, I find JAM modelling of these galaxies to imply total density slopes that are very close to isothermal, with the slopes being slightly steeper than isothermal on average. This is in very good agreement with the results of Cappellari et al. (2015), who report an average logarithmic slope of -2.19 ± 0.03 with a RMS scatter of 0.11 from JAM modelling of combined ATLAS$^{3\mathrm{D}}$+SLUGGS IFU observations, with density profiles fitted over $0.1R_\mathrm{e} - 4R_\mathrm{e}$.

In Figure 4.37, I compare the M_*/L ratios inferred from my base JAM models with the equivalent ratios derived from simple stellar population (SSP) modelling of galaxy spectra. The SSP modelling used here was carried out using MIUSCAT SSP models, using the methodology described in Chapter 3 of this thesis; as in that chapter, NGC 2764 is excluded from this comparison. I use g-band M_*/L ratios for all galaxies except NGC 3626, while for NGC 3626 I use r-band M_*/L ratios. I compare the JAM M_*/L ratios to those derived from the central $0.5R_e$ apertures, as well as to those derived from the outermost annuli for each galaxy. I find that the M_*/L ratios inferred from JAM modelling are typically smaller than the M_*/L ratios derived from SSP modelling of $0.5R_e$ apertures around galaxies; the exceptions here are NGC 3998 and UGC 03960, for which the two M_*/L values show close agreement. On the other hand, I find good agreement in the majority of cases between the JAM M_*/L ratios and the SSP M_*/L ratios derived from galaxies' outer annuli.

In Figure 4.38, I present an additional comparison between the JAM M_*/L ratios and those from SSP modelling. In this case, for each galaxy I have selected the value along the SSP M_*/L profiles that is *closest in value* to the corresponding JAM value. I obtain approximately one-to-one agreement for ten out of the twelve sample galaxies in this case. The two outlying datapoints in this figure correspond to NGC 1023 and NGC 4203, for which JAM modelling yields significantly lower M_*/L values than SSP modelling. Initial Mass Function (IMF) vari-

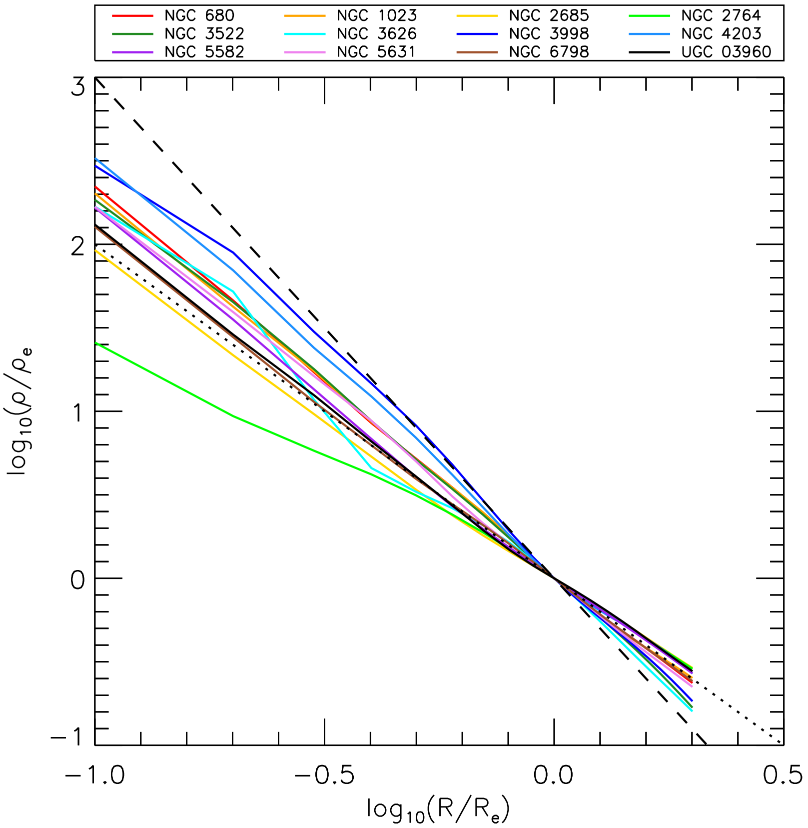

Figure 4.36: Total density profiles inferred from best-fit base JAM models of the twelve ETGs. The dotted line indicates an isothermal density slope, $\rho \propto r^{-2}$, wheras the dashed line indicates $\rho \propto r^{-3}$. The galaxy density profiles appear close to isothermal in the majority, particularly beyond the central effective radius. Beyond the central effective radius, I derive an average logarithmic density slope of -2.17 with a standard deviation of 0.29.

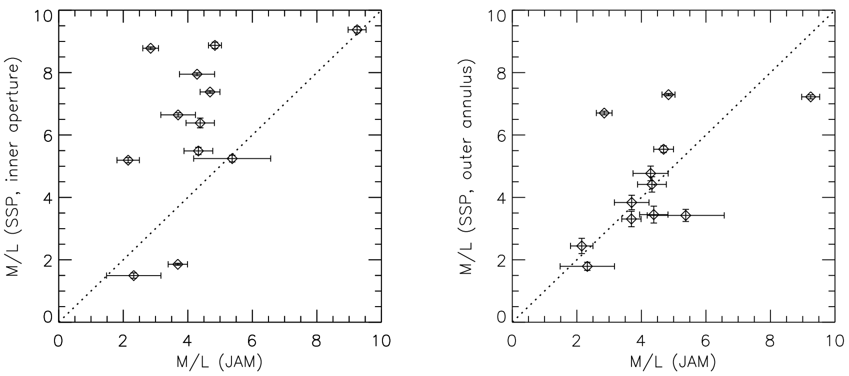

Figure 4.37: Comparison of M_*/L ratios derived from JAM modelling and from SSP modelling with MIUSCAT spectra. I compare the JAM results to SSP fits to $0.5R_e$ apertures on the left window, while on the right window I compare the JAM values to SSP fits galaxies' outermost radii. The JAM models typically return lower M_*/L values than the centremost SSP fits, but often return values comparable to those from SSP fits to outer annulus regions.

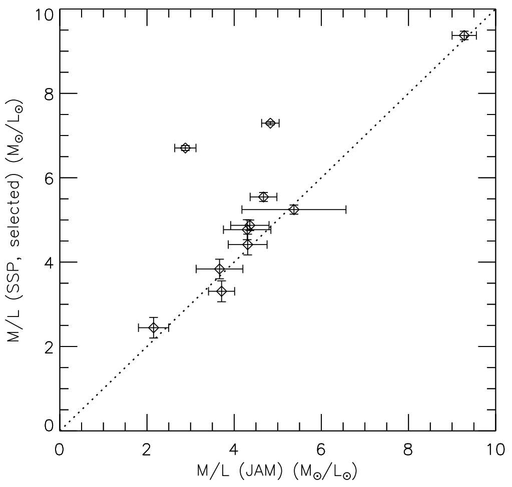

Figure 4.38: Comparison of M_*/L ratios derived from JAM modelling and from SSP modelling with MIUSCAT spectra. For each galaxy, I select the region along the SSP M_*/L profile from which agreement with the JAM models is closest. I find good agreement for most galaxies this way, and so find the JAM models to be consistent with my stellar population modelling of these galaxies. The two high outliers correspond to NGC 1023 and NGC 4203, for which the JAM models return M_*/L values significantly lower than inferred through SSP modelling.

ations are a possible explanation for these outliers.

4.4 Discussion

In the preceding sections, I have presented a Jeans modelling analysis of the twelve ETGs in the Mitchell Spectrograph sample. I have demonstrated that the models provide good descriptions of these galaxies' second velocity moments, making them very useful for investigating the distribution of both their dark and visible mass.

Generally, I find the JAM models to favour non-negligible amounts of dark matter within the central effective radius, with dark-matter-free models providing fits of comparable quality for three out of the twelve sample ETGs. This latter point is particularly interesting in light of the wide FOV of my data, which typically extends to significantly beyond $2R_e$. From my models with a dark halo, I obtain a median dark matter fraction of 11 per cent within $1R_e$; this is lower than typically reported from observations or simulations (e.g. Weijmans et al., 2009; Barnabè et al., 2011; Remus et al., 2013; Wu et al., 2014), but is similar to the median of 13 per cent within $1R_e$ previously reported from JAM fits to ATLAS^{3D} data. I note at this point that my ETGs all have stellar masses of approximately $10^{10} - 10^{11} M_\odot$ and so are relatively close to pivot mass of $4.5 \times 10^{10} M_\odot$ inferred from weak lensing studies of nearby galaxies for the

$M_* - M_{halo}$ relation (Leauthaud et al., 2012); as such, that I find relatively low central dark matter fractions for these objects is perhaps not too surprising.

I also find that for the majority of my sample galaxies, the JAM fits favour near-isothermal total density profiles, particularly beyond the central effective radius. Such a result is in good agreement with previous findings reported in Cappellari et al. (2015) from JAM modelling of combined ATLAS^{3D} and SLUGGS kinematics, and is also in good agreements with the total density profiles inferred in Auger et al. (2010) from strong lensing data. Time-delay measurements of gravitational lenses likewise favour isothermal mass distributions (Kochanek, 2003).

As has been pointed out previously (e.g. Auger et al., 2010; Cappellari et al., 2015), such near-isothermal total density profiles are *not* a generic prediction of ΛCDM cosmology; as such, the apparent existence of these profiles provides important clues as to the physics of galaxy formation. One possible interpretation is that these profiles are signs of repeated merging: Remus et al. (2013) study both isolated binary merger simulations and cosmological galaxy simulations, and find that collisionless mergers serve to push a galaxy's total density slope closer to an isothermal configuration. Total density profiles may also be interpreted as an indicator of the relative importance of expansion and contractions processes on ETGs' dark matter halos: Dutton & Treu (2014) find that the observed total density profiles are best recreated in models that use an un-contracted NFW halo along with a stellar component, and suggest that feedback mechanisms such as active galactic nuclei must serve to counteract dark halo contraction from baryonic cooling.

I generally find the M_*/L ratios implied from the JAM models to be consistent with those implied from the stellar population modelling presented in the previous chapter; this implies that my JAM models are capable of disentangling between dark and visible mass components to at least some degree, despite the degeneracies noted previously in the MCMC chains between M_*/L and M_{200}. An obvious future step, therefore, will be to implement gradients of M_*/L into the JAM models in some manner. An approach to this was recently demonstrated in Mitzkus et al. (2017), in which photometry of the ETG NGC 5102 was multiplied through by a M_*/L slope derived from stellar population modelling with a MGE model then computed subsequently. Mitzkus et al. (2017) found this to produce significantly improved fits to data over their JAM models with uniform M_*/L values. It would be interesting, therefore, to attempt a similar analysis on my sample ETGs as future work.

The use of a M_*/L gradient as a free parameter is not likely feasible in this case, due to inevitable degeneracies between dark and visible galaxy components that would result. Yıldırım et al. (2016), for instance, attempt to use a M_*/L gradient in their dynamical models of the compact ETG NGC 1281; they generally obtain positive M_*/L gradients along with a substantial dark matter component, despite such gradients not being supported by the galaxy's colour profile. Yıldırım et al. (2016) argue this to reflect a need for much dark mass in that galaxy. As such, it appears necessary to make use of stellar population modelling when investigating the M_*/L gradients of ETGs, as done for instance in Mitzkus et al. (2017) who include a M_*/L gradient as a fixed input for some of their JAM models, as opposed to employing dynamical models alone.

4.5 Summary

In this chapter, I presented results from Jeans dynamical modelling for my sample of ETGs, demonstrating the power of wide-field IFU data for investigating the properties of galaxies' dark and visible properties. I found that the Jeans models supported low dark matter fractions within $1R_e$ for most of the galaxies, along with total mass (dark plus stellar) density profiles that are approximately isothermal in most cases. My dark matter results are similar to those obtained from Jeans models of ATLAS^{3D} data, while my finding of near-isothermal total density profiles is in good agreement with a number of previous studies. Such profiles are not a generic prediction of ΛCDM cosmology, and so provide constraints for galaxy simulations.

For most of my galaxies, I obtain good consistency between the M_*/L of the galaxies inferred from the JAM models with that inferred from stellar population modelling, with the JAM value most commonly resembling those calculated from stellar population models of spectra beyond $1R_e$. The agreement that I find between stellar and dynamical modelling approaches is encouraging, and I therefore suggest the use of M_*/L gradients in dynamical models as a future step in my work.

In the following chapter, I will present a Schwarzschild modelling analysis of the galaxy NGC 3998, in order to compare and contrast the results presented this chapter and to study the orbital anisotropy of this galaxy to much greater depth.

5

Schwarzschild modelling of NGC 3998

In this chapter, I present results of Schwarzshild dynamical modelling of the galaxy NGC 3998 from my ETG sample, using the code and methods presented in van den Bosch et al. (2008). I model the galaxy's line-of-sight velocity distribution (LOSVD) up to the 4th Gauss-Hermite moment, enabling a detailed investigation of the galaxy's mass distribution as well as its orbital anisotropy as a function of position. I then discuss what the dynamical modelling implies in terms of NGC 3998's evolution history.

Schwarzschild models make use of the orbit superposition method first introduced in Schwarzschild (1979). Here, a luminous galaxy is modelled as a numerical superposition of individual stellar orbits, each of which contribute to the observed photometry and to the observed stellar kinematics. Schwarzschild models make no prior assumptions regarding a galaxy's orbital anisotropy; rather, a library of stellar orbits is fitted directly to observational data. Schwarzschild models therefore allow one to study the deprojected dynamics of a galaxy in detail, enabling direct comparison with galaxies in simulations; this is something that is not possible when using the Jeans Anisotropic Modelling (JAM; Cappellari, 2008) approach presented in Chapter 4 of this thesis.

The work presented in this chapter is heavily based on Boardman et al. (2016) and makes use of Mitchell data from that paper; the data was subsequently re-reduced prior to the preparation of this thesis.

5.1 Data

My aim in this work was to construct detailed dynamical models of the lenticular galaxy NGC 3998. It was therefore necessary to make use of kinematic data for this galaxy as well as photometric data, as was the case for the models presented in the previous Chapter 4. I summarise the kinematics used for this chapter in Section 5.1.1 and I then describe the photometric data I employed in Section 5.1.2. I describe the calculation of the kinematics' Point Spread Function (PSF) in Section 5.1.3.

5.1.1 Kinematics

I obtained kinematics for NGC 3998 using the Mitchell Spectrograph IFU observations of this galaxy along with SAURON IFU observations taken as part of the ATLAS^{3D} survey (Cappellari et al., 2011a). The reduction of Mitchell observations and subsequent kinematic extraction is presented in Boardman et al. (2016), and used a similar set of procedures to those presented in Chapter 2 of this thesis. In brief, I Voronoi-binned the spectra to a target S/N of 40 per spectral FWHM, and then extracted a line-of-sight velocity distribution (LOSVD) up to the 4th Gauss-Hermite moment using the pPXF routine of Cappellari & Emsellem (2004) with ELODIE stars as inputs; I sky-subtracted the Mitchell spectra prior to fitting with pPXF. I also re-extracted the SAURON kinematics up to the 4th Gauss-Hermite moment, using ELODIE stars for maximum consistency with the Mitchell Spectrograph observations. Errors were obtained by first running 100 Monte-Carlo resimulations of each individual measurement with Gaussian noise added to the spectra; I also obtained systematic error terms by comparing kinematics obtained with ELODIE stars to kinematics obtained using the MILES library of observed stars, and I added these terms in quadrature with the original random errors. I masked all individual kinematic data-points with large offsets between the MILES and ELODIE values.

In Figure 5.1, I present the Mitchell Spectrograph kinematics to be used in this chapter. I also present the re-extracted SAURON kinematics in Figure 5.2.

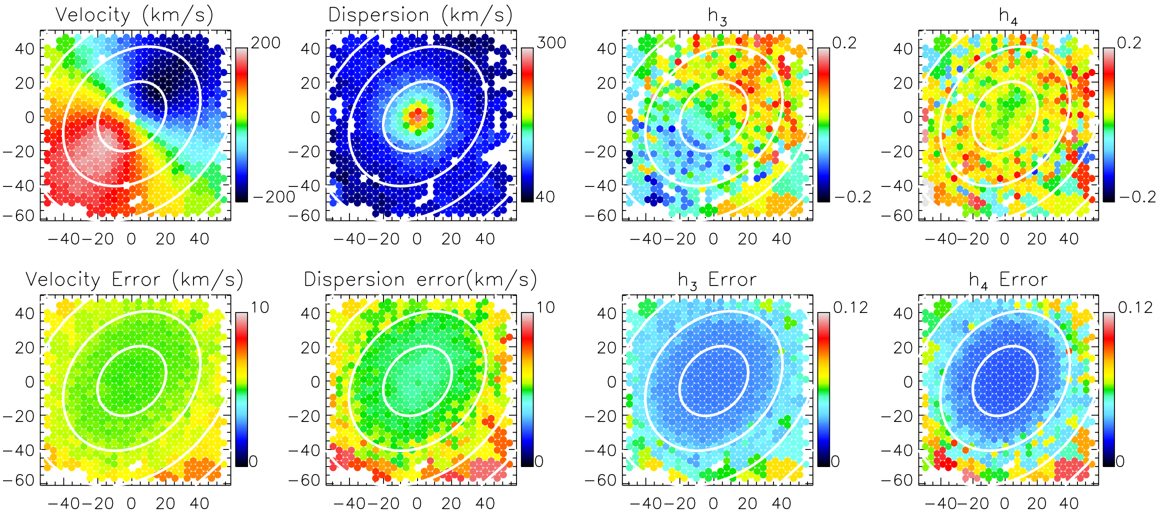

Figure 5.1: LOSVD and error maps measured for four moments from Mitchell Spectrograph observations of NGC 3998. The white contours are spaced in units of effective radii. White regions show bins/fibres that were excluded, as discussed in the text.

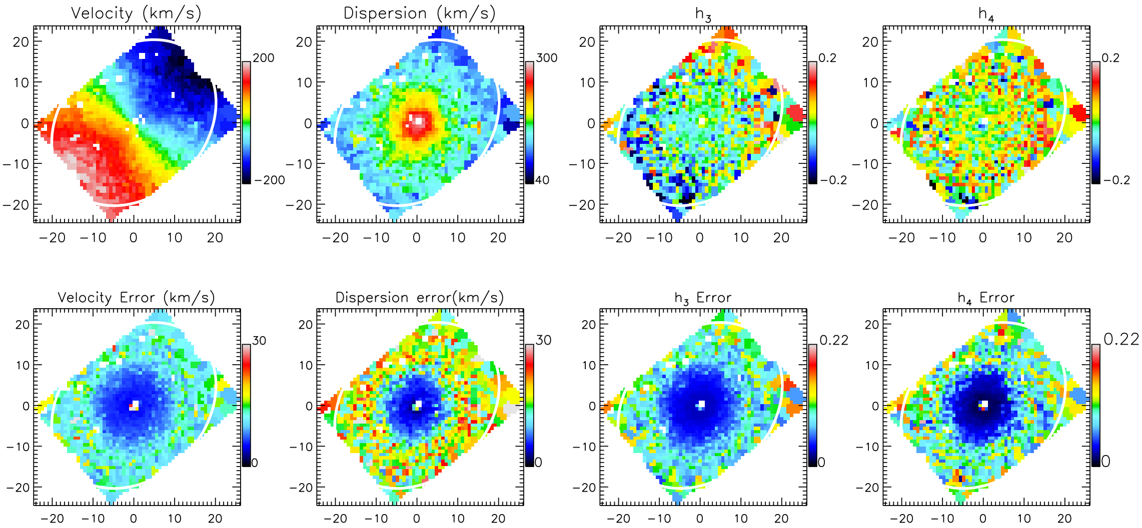

Figure 5.2: LOSVD and error maps extracted from SAURON data for NGC 3998, with the ELODIE library employed instead of the MILES library used in ATLAS^{3D}. The white ellipse shows the region enclosed by the innermost effective radius. Excluded datapoints are shown as white spaces.

5.1.2 Surface brightness model

I parametrized the surface brightness of NGC 3998 using the I-band Multi-Gaussian Expansion (MGE; see Chapter 4 of this thesis) model presented in Walsh et al. (2012). This model was constructed from a combination of wide-field WIRCAM imaging from the CFHT along with *HST* Wide-Field-Camera 2 (WFC2) imaging of NGC 3998's centre. This MGE model has a minimum σ value of $0.017''$, making it well-resolved in the centre and so well-suited for studying the high-spatial-resolution kinematics from the SAURON instrument; the MGE model also extends to well beyond $3R_e$, making it excellent for exploiting the large field of view (FOV) offered by the Mitchell observations. I note that this MGE model has a photometric position angle of 138.5°; this is slightly misalligned with the kinematic PA of 136° I derived in Chapter 3 of this thesis for NGC 3998. Mild triaxiality is a possible cause of such an offset; therefore, I do not force the photometric and kinematic PA to match when performing the Schwarzschild model fits.

5.1.3 Determination of point spread function for kinematics

The PSF of the Mitchell kinematics is not trivial to determine, both due to the high number of combined exposures as well as the larger individual optical fibres. I therefore decided to use the method described in Krajnović et al. (2009), in which a model surface brightness distribution is convolved with a proposed PSF and then compared to an observed flux map, in order to optimise both the PSF and the galaxy central position. This calculation was first discussed in Boardman et al. (2016), and I reproduce that discussion here.

The models of van den Bosch et al. (2008) code parametrize the PSF as the sum of one or more Gaussian PSF components. I experimented with including multiple Gaussian components in the fit to the Mitchell PSF, but found all but one of the components to produce a negligible contribution; as such, I ultimately allowed for a single Gaussian PSF component in the model of the Mitchell PSF. I allowed the right ascension (RA) and declination (DEC) position of the galaxy center to vary, and allowed for a non-zero sky brightness to account for any residual sky contamination; this resulted in there being four free parameters overall. I varied these parameters to determine the best-fitting spatial PSF and galaxy center, in each case convolving the Walsh et al. (2012) MGE model with a given PSF Gaussian; this yielded a best-fit PSF for the Mitchell observations of $\sigma = 1.4''$.

I also fitted a two-component PSF to the SAURON datacube for NGC 3998, after finding both components to be non-negligible. I first allowed the RA and DEC positions of the galaxy vary as before, finding the best-fitting values of both to be $< 0.1''$ away from the stated numbers; as such, I performed a second fit in which the RA and DEC positions were held to their starting values, leaving the two PSF Gaussian widths as the only three parameters. The resulting best-fit PSF Gaussians have dispersions of $\sigma = 0.49''$ and $\sigma = 1.04''$ with relative weights of 0.7 and 0.3.

5.2 Schwarzschild modelling

I used the method and code of van den Bosch et al. (2008), which allows for triaxial galaxy geometries and which has been previously shown to be capable of reproducing simulated ETGs (van de Ven et al., 2008; van den Bosch & van de Ven, 2009). I explain the method itself in Section 5.2.1, and I discuss my specific implementation of it in Section 5.2.2.

5.2.1 Method

The code of van den Bosch et al. (2008) parametrises the surface brightness of a galaxy using the MGE formalism; as such, the first step to constructing a Schwarzschild model is to deproject a supplied MGE model according to a given viewing angle and (if needed) adding a dark halo component; for simplicity, this discussion will ignore the dark halo component. The viewing angle of a galaxy is defined using the angles ϑ, φ and ψ. The angles (ϑ, φ) are standard spherical coordinates and define the orientation of the line of sight with regards to the galaxy's short axis; $(0°, 0°)$ corresponds to a view down the short axis, while $(90°, 0°)$ and $(90°, 90°)$ are views down the long and intermediate axes respectively. ψ, meanwhile, defines a rotation around the line of sight and parametrises the misallignment in the sky between the short axis of a galaxy's surface brightness and the projection of that galaxy's intrinsic short axis; in the case of an axisymmetric galaxy, no such misallignment exists and $\psi = 90°$ (van den Bosch et al., 2008).

The viewing angle is parametrised in terms of the three triaxial shape parameters (q, p, u), which quantify the intrinsic shape of the *flattest* MGE component (in this case, the component with projected axis ratio $q' = 0.756$). q represents the short-to-long axis ratio, p the intermediate-to-long axis ratio, and u the ratio between the projected and intrinsic MGE Gaussian widths along the galaxy major axis; in the case of an axisymmetric galaxy, p and u will both be equal to unity. These three shape parameters may be related to the viewing angles $(\vartheta, \varphi, \psi)$ using equation (10) in van den Bosch et al. (2008):

$$\begin{aligned}
\cos^2\vartheta &= \frac{(u^2-q^2)(q'^2_{\min}u^2-q^2)}{(1-q^2)(p^2-q^2)} \\
\tan^2\varphi &= \frac{(u^2-p^2)(p^2-q'^2_{\min}u^2)(1-q^2)}{(1-u^2)(1-q'^2_{\min}u^2)(p^2-q^2)} \\
\tan^2\psi &= \frac{(1-q'^2_{\min}u^2)(p^2-q'^2_{\min}u^2)(u^2-q^2)}{(1-u^2)(u^2-p^2)(q'^2_{\min}u^2-q^2)}
\end{aligned} \tag{5.1}$$

where $q'_{\min}$ represents the axis ratio of the *flattest* (projected) MGE Gaussian. These equations are valid for $q \leq p \leq 1$, $q \leq q'$ and $\max(q/q', p) \leq u \leq \min(p/q', 1)$. These equations have eight possible solutions; four of these are unphysical while the remaining four represent the same intrinsic shape, meaning that only one of the four physical solutions needs to be modelled. Afterwards, we may obtain a deprojected shape (q_j, p_j, u_j) for each MGE Gaussian component using Equations 7-9 from van den Bosch et al. (2008):

$$\begin{aligned}
1-q_j^2 &= \frac{\delta'_j(2\cos2\psi+\sin2\psi(\sec\vartheta\cot\varphi-\cos\vartheta\tan\varphi))}{2\sin^2\vartheta\left(\delta'_j\cos\psi(\cos\psi+\cot\varphi\sec\vartheta\sin\psi)-1\right)} \\
p_j^2-q_j^2 &= \frac{\delta'_j(2\cos2\psi+\sin2\psi(\cot\vartheta\cot\varphi-\sec\vartheta\tan\varphi))}{2\sin^2\vartheta\left(\delta'_j\cos\psi(\cos\psi+\cot\varphi\sec\vartheta\sin\psi)-1\right)} \\
u_j^2 &= \frac{1}{q'_j}\sqrt{p_j^2\cos^2\vartheta+q_j^2\sin^2\vartheta(p_j^2\cos^2\varphi+\sin^2\varphi)}
\end{aligned} \tag{5.2}$$

where $\delta'_j = 1-q'^2_j$ and in which I have implicitly assumed that the MGE model contains no isophotal twists. This gives rise to a three-dimensional MGE mass-density of the following form:

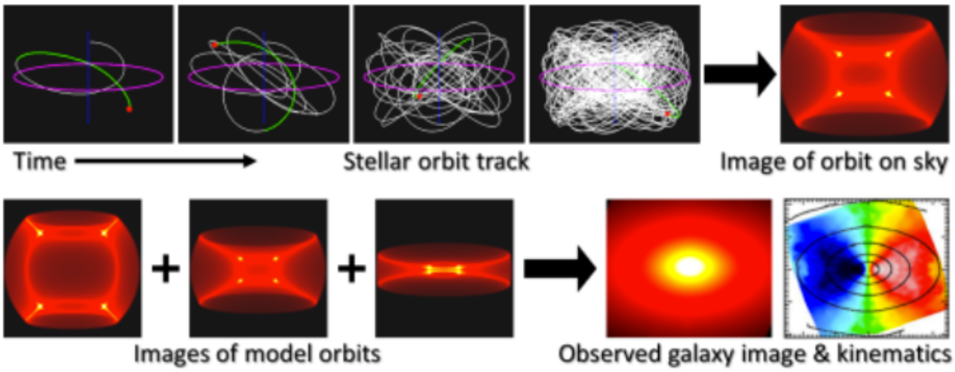

Figure 5.3: Creation of a Scwarzschild model. A series of model orbits are simulated, each of which contribute to the photometry and kinematics of their host galaxy. Afterwards, a superposition of orbits is constructed so as to best-fit the photometric and kinematic data for a target galaxy. From Figure 3 of Cappellari (2015), top and middle row.

$$\rho(x,y,z) = \sum_{j=1}^{N} (M_*/L) \frac{L_j}{(\sigma_j \sqrt{2\pi})^3 p_j q_j} \times \exp\left[-\frac{1}{2\sigma_j^2} \left(x^2 + \frac{y^2}{p_j^2} + \frac{z^2}{q_j^2} \right) \right] \tag{5.3}$$

where (x, y, z) is a Cartesian coordinate system centred on the galaxy and aligned with the principle axis of the MGE Gaussians (e.g. Cappellari, 2002). N is the total number of Gaussian components of the MGE model M_*/L describes the stellar mass-to-light ratio of a galaxy, which here will be assumed to be constant across the FOV; L_j describes the total luminosity of a given MGE Gaussian, while σ_j is the standard deviation of that Gaussian.

Following the MGE model's deprojection, a Schwarzschild model is calculated in the manner summarised in Figure 5.3. A library of likely stellar orbits is generated based on the three-dimensional mass distribution, and is designed to include both tube orbits (orbits with net rotation) and box orbits (oscillatory orbits with no net rotation); each of these orbits makes a separate contribution to the projected photometry and kinematics of the Schwarzschild model. Afterwards, the best-fitting superposition of orbits is determined so as to best match the observed photometry and kinematics of a target galaxy, using a quadratic programming solver (Gould et al., 2003) to solve the least squares problem. The size and shape of Voronoi bins is taken into account during this process, as is the effect of the PSF.

5.2.2 Implementation

I generated a series of Schwarzschild models in order to constrain the viewing angle of NGC 3998 (and so its deprojected triaxial shape), its stellar mass-to-light ratio M_*/L and the distribution of its dark matter. I used an NFW dark halo parametrisation (Navarro et al., 1996) to model the galaxy's dark matter component, parametrised in terms of concentration parameter c and halo mass M_{200}. I assumed a black hole mass of $8.1 \times 10^8 M_\odot$ throughout my analysis, from the best-fit Schwarzschild model of Walsh et al. (2012), as my kinematics are not of sufficient spatial resolution to constrain this term.

I constructed an orbit library for a given Schwarzschild model as follows. First, I sampled orbits along 21 equipotential shells, with the orbit energy implicitly sampled via a logarithmic grid in radius between $0.5''$ and $294''$; for each radius, an energy is obtained by calculating the potential at that radius along the galaxy major axis. I sampled over 7 radial directions and 7 angular directions for each shell. By construction, the resulting library consists mostly of tube orbits and contains few box orbits. To ensure that the final library contained enough box orbits over NGC 3998's outer regions, I then calculated an additional set of orbits by dropping stars from the same 21 equipotential shells, sampling over 7×7 directions spaced evenly in terms of angles. I bundled 3^3 orbits with adjacent starting positions in all cases. Each orbit library therefore contains 18520 orbits in total.

I used kinematics from both the Mitchell Spectrograph and SAURON as inputs to the models. I masked Mitchell fibres with centres less than $8''$ from the galaxy centre and I masked SAURON pixels greater than $10''$; this allows me to take advantage of the high spatial resolution of the central SAURON data while also making use of the wide FOV offered by the Mitchell data. I brought the central values of the velocity and h_3 terms to zero using the methods of Krajnović et al. (2006) and van den Bosch & de Zeeuw (2010) respectively, which both calculate corrections to galaxies' adopted systemic velocities as part of their routines. I then determined the superposition of orbits that best-fitted the supplied kinematics, with the intrinsic and projected model masses constrained to be within 2% of the supplied MGE model throughout the procedure. Afterwards, I parametrised the quality of the fit using the χ^2 statistic, which in this case is given by

$$\chi^2 = \sum_{i=1}^{N} \left(\frac{D_{mod,i} - D_i}{\Delta D_i} \right)^2 \tag{5.4}$$

where D signifies the values for each kinematic moment (velocity V, dispersion σ, h_3 and h_4) in turn, ΔD the corresponding error values and D_{mod} the values from a given model. N signifies the total number of observables being used to constrain the model parameters, and corresponds to datapoints for all four kinematic moments individually. By calculating the χ^2 over a range of Schwarzschild models, I could then proceed to constrain all free parameters of interest.

I obtained confidence intervals on all free parameters using the standard deviation of the χ^2 statistic, following the reasoning outlined in the previous Chapter of this thesis. This approach was first introduced for Schwarzschild modelling in van den Bosch et al. (2008) and has since been validated in both van de Ven et al. (2008) and van den Bosch & van de Ven (2009). The standard deviation is of χ^2 is given by $\sqrt{2(N_{obs} - N_{par})}$, where N_{obs} is the number of unmasked datapoints and N_{par} the number of free parameters. In this case, $N_{obs} = 3866$ and so I approximate the standard deviation to be equal to $\sqrt{2(N_{obs})}$; in turn, this means I define the confidence intervals using $\Delta\chi^2 = 87.9$.

5.2.3 Results

My aim in this study was to constrain the viewing angle of NGC 3998 as well as the distribution of its dark and visible mass components. Such an aim involves many free parameters that are computationally expensive to fit simultaneously, due to the relatively high computational cost of generating a given Schwarzschild model. I therefore set out to limit the number of free parameters as much as possible, for the sake of efficiency.

First, I generated a set of Schwarzschild models aimed purely at constraining the galaxy viewing angle, in which the dark halo parameters were held fixed. I estimated a reasonable set of parameters for the dark matter halo as follows. First, I used the best-fit I-band stellar mass-to-light ratio (M_*/L) of Walsh et al. (2012) to derive a total stellar mass for NGC 3998 of $7 \times 10^{10} M_\odot$ from their MGE model. I then estimated a dark-to-stellar mass fraction of 34.8, using the lowest-redshift fitting formula of Leauthaud et al. (2012). Lastly, I used the implied dark halo mass M_{200} of $2.434 \times 10^{12} M_\odot$ to estimate a halo concentration of $\log(c) = 0.867$, using the formula of Sánchez-Conde & Prada (2014).

This Schwarzschild model grid therefore had four free parameters: the shape parameters (q, p, u) and M_*/L. I sampled q down to a low minimum value of 0.06, motivated by the fast rotator shape results of Weijmans et al. (2014), and I sampled p down to a value of 0.92. I used all possible values of u for each given combination of q and p. I sampled 16 I-band M_*/L values evenly between 3.1 and 6.1 $M_\odot/L_\odot$. I found from this grid a galaxy shape of $(q, p, u) = (0.06^{+0.18}_{-0.00}, 0.98^{0.003}_{0.004}, 0.99^{+0.002}_{-0.001})$, where the lower bound on q corresponds to the lowest tested value and so is not a true lower limit. As such, my modelling favours a near-axisymmetric shape for NGC 3998. I note that I obtain very narrow bounds for p and u; this is likely due to the small misallignment between the photometric and kinematic PAs discussed previously, which produces a kinematic misallignment between models and data (and so a large increase in χ^2) unless p and u take very specific values. Motivated by this result, I fixed p and u to their best-fit values of 0.98 and 0.99 over the remainder of my analysis.

I then generated a second Schwarzschild model grid in which I fitted for the NFW dark halo mass, M_*/L and the axis ratio q. I used q values between 0.06 and 0.38,in steps of 0.08. I fixed the halo concentration c to the same value as before, due to the available FOV being smaller than the NFW scale radius for most realistic dark halo parameters, (see, e.g. Yıldırım et al., 2016, for a similar argument). I used a range of $\log_{10}(M_{200}/M_*)$ from 0.01 to 4.09, with models without dark matter also included, and I sampled the same M_*/L values as before. I specifically employ $\log_{10}(M_{200}/M_*)$ as a free parameter as opposed to M_{200} in isolation, in order to avoid having to recompute the Schwarzschild orbit libraries for each value of M_*/L.

The shape parameters (q, p, u) correspond to the *flattest* component of the input MGE model, making their physical meaning difficult to interpret. I therefore calculated the resulting shape of the overall model by first deprojecting it according to (q, p, u) and then fitting triaxial ellipsoids of constant luminosity density. Marginalising over other free parameters, I thus find a minor-to-major axis ratio at $1R_\mathrm{e}$ of $q_{R_\mathrm{e}} = 0.44^{+0.05}_{-0.00}$; I conclude from this that NGC 3998 is a flattened and near-oblate galaxy. If I consider the dark matter-free case only, I instead find $q_{R_\mathrm{e}} = 0.48^{+0.04}_{-0.04}$; thus, I find the q_{R_e} confidence region to show a slight dependence on the presence of dark matter.

I present the resulting $\Delta\chi^2$ from the latter model grid in terms of M_{200} and M_*/L in Figure 5.4, in which I have marginalised over galaxy shape. I present separate $\Delta\chi^2$ profiles for M_{200}, M/L and q_{R_e} in Figure 5.5. My best-fit model has a χ^2/DOF of 1.11. I find $M_*/L =$

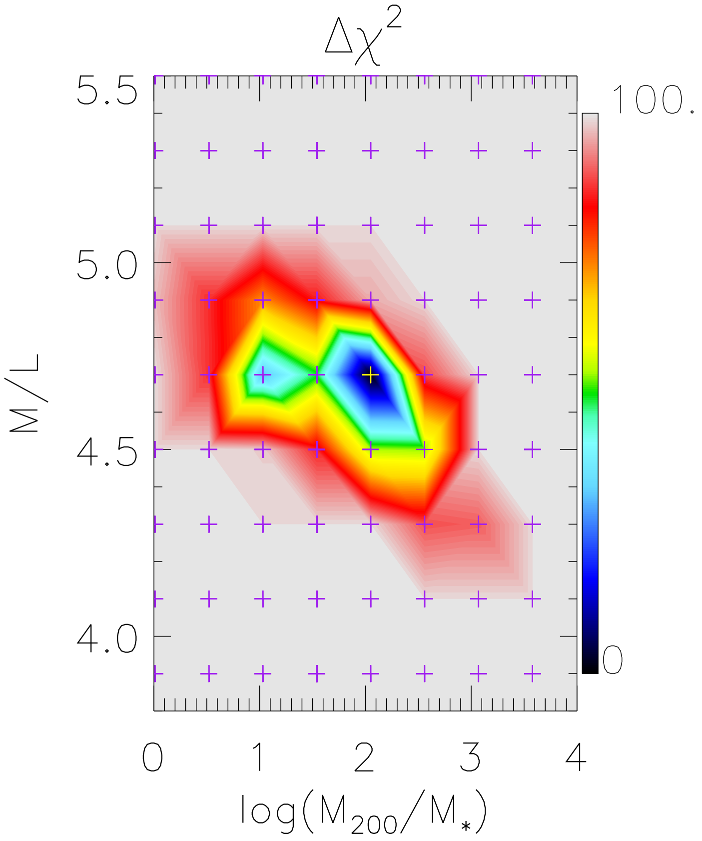

Figure 5.4: Map of $\Delta(\chi^2)$ from the Schwarzschild modelling in terms of the dark matter mass fraction and the stellar M/L, in units of $M_\odot/L_\odot$, with the galaxy shape marginalised over. The crosses show the locations of each Schwarzschild model in the parameter space, with the yellow cross representing the best-fitting model. The best-fit model has a χ^2/DOF of 1.11.

$4.7^{+0.32}_{-0.45}M_\odot/L_\odot$, and I find a dark halo mass of $\log_{10}(M_{200}/M_*) \leq 3.13$. I find no firm lower limit on the dark halo mass, as the best-fitting DM-free model falls within my χ^2 confidence limit.

In Figure 5.6 I plot the inferred best-fit dark matter fraction along with the associated confidence interval. I define the dark matter fraction as the fraction of dark mass within a sphere of given radius, using a circularised MGE surface brightness model as in Cappellari (2013). I find a best-fitting dark matter fraction of $(7.1^{+8.1}_{-7.1})$% within $1R_{\mathrm{e,circ}}$, where $R_{\mathrm{e,circ}}$ is the circularised effective radius of 23.99″ reported in table 1 of Cappellari et al. (2013b). Thus, I find that low central dark mass fractions are preferred by my models, in good agreement with the dark fraction of (15 ± 6)% at $1R_{\mathrm{e,circ}}$ reported in Cappellari et al. (2013a).

I computed the I-band M_*/L around a $1R_{\mathrm{e}}$ aperture using the SSP modelling described in Chapter 3 of this thesis, obtaining a value of $4.28 \pm 0.03 M_\odot/L_\odot$; as such, I find my SSP modelling results to be consistent with the M_*/L I infer from Schwarzschild modelling. Cap-

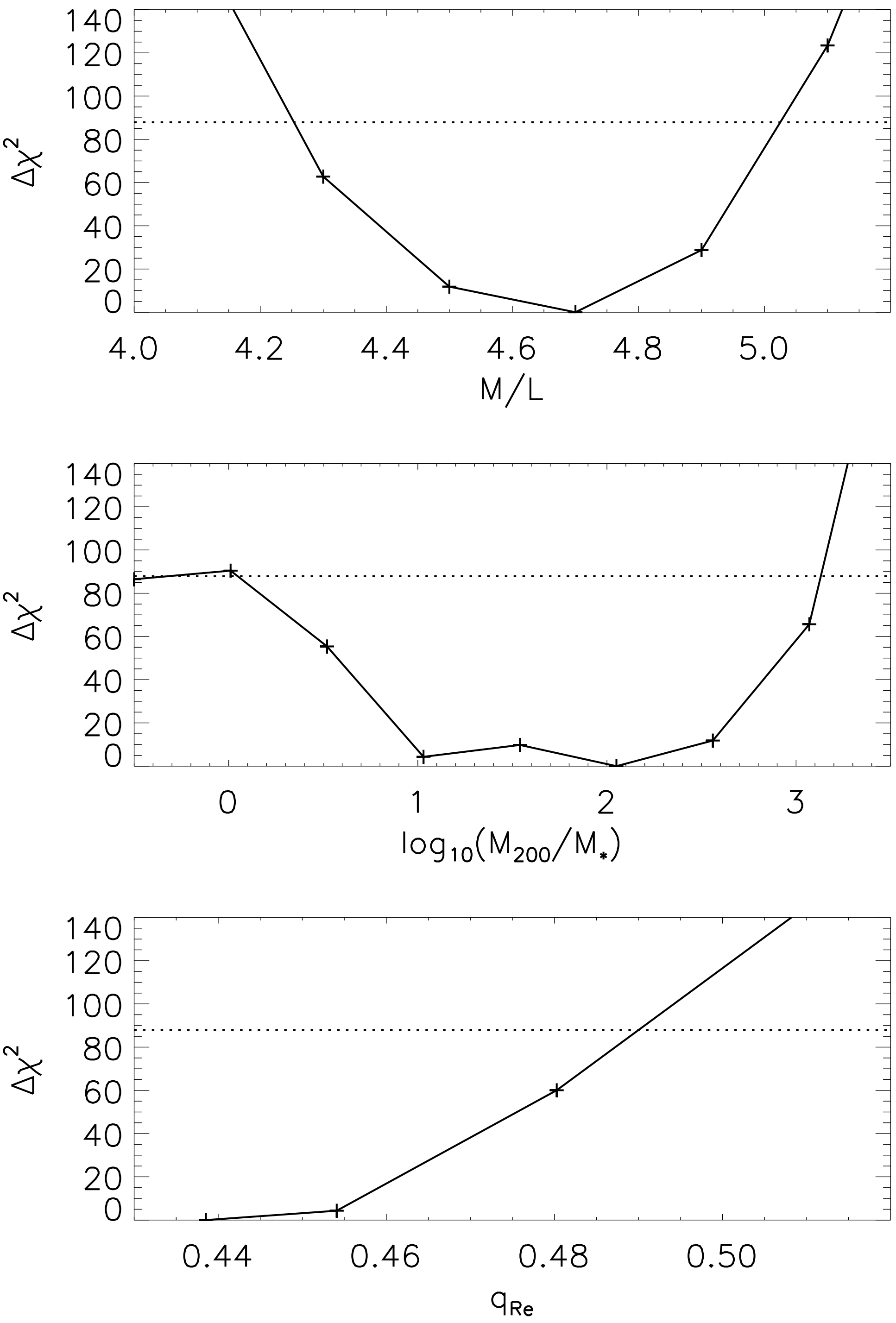

Figure 5.5: $\Delta\chi^2$ plotted as a function of the I-band M_*/L (top), the NFW dark halo mass (middle) and the axis ratio q_{R_e}, with all other parameters marginalised over in each case. The leftmost point on the middle window is for the DM-free case. The horizontal dashed line signifies $\Delta\chi^2 = 87.9$, which marks the bounds of the χ^2 confidence region which in turn is set by the standard deviation of the χ^2 statistic. I obtain relatively tight constraints on the stellar M/L, and I obtain tight upper limits on q_{R_e} and the dark halo mass.

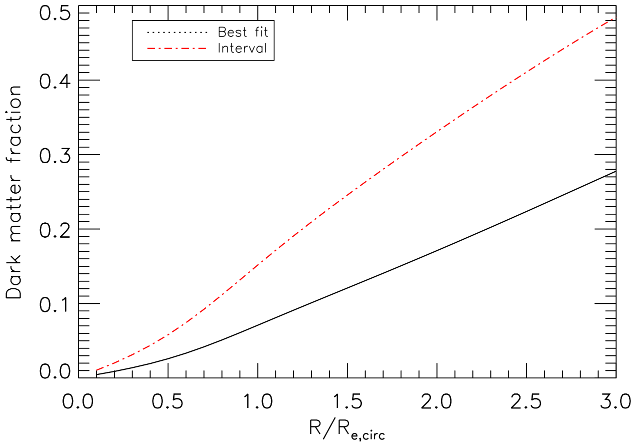

Figure 5.6: Profile of best-fit enclosed dark mass fraction out to $3R_{\text{e,circ}}$(black line), along with the upper limit (dash-dotted red line). I show no lower limit because the best-fit DM-free model falls within the χ^2 confidence limit. $R_{\text{e,circ}}$ is the circularised effective radius from Table 1 of Cappellari et al. (2013b). I find tight upper limits on the dark matter content, with the Schwarzschild modelling preferring little dark matter within $1R_{\text{e,circ}}$.

pellari et al. (2013a) report an r-band M_*/L of $6.58 \pm 0.39 M_\odot/L_\odot$ for this galaxy, from stellar population modelling of ATLAS$^{\text{3D}}$ data using a $1R_\text{e}$ aperture and assuming a Salpeter IMF slope; by comparison, I obtain an r-band value $6.19 \pm 0.06 M_\odot/L_\odot$ from my own SSP modelling. Assuming an identical ratio between M_*/L values in different bands, I infer an I-band M_*/L of $4.55 \pm 0.27 M_\odot/L_\odot$ from the ATLAS$^{\text{3D}}$ r-band result; as such, I find my Schwarzschild modelling to be in in excellent agreement with the stellar population modelling of Cappellari et al. (2013a). My results here suggest that the combination of Schwarzschild modelling and wide-field IFU data is sufficient to disentangle between dark and visible mass to at least some degree.

In Figure 5.7 and Figure 5.8, I compare the input Mitchell kinematics maps to three selected orbit models: the best-fit model, a dark matter heavy model and the best-fitting dark-matter-free model. I show the same comparisons for the SAURON data in Figure 5.9 and Figure 5.10. I summarise the properties of the selected models in Table 5.1. The DM-free model is within my χ^2 confidence criterion whereas the DM-heavy model is significantly beyond it ($\Delta\chi^2 = 164.1$). The DM-heavy model has velocity dispersions are generally somewhat higher in the outskirts than for the other two models (Figure 5.11); this is the main cause of the higher χ^2 that this model yields.

In Figure 5.12, I plot the total (dark plus stellar) mass density profiles of all allowed Schwarzchild models. I calculated these profiles in the same manner as in Chapter 4, approximating $p = u = 1$ due to the near-axisymmetric shape I inferred for this galaxy. I find

Model	q	M/L	$\log_{10}\left(\frac{M_{200}}{M_*}\right)$	$f_{DM}(R_{\mathrm{e,circ}})$
Best fit	0.06	4.7	2.05	7.1%
DM-heavy	0.06	4.1	3.58	20.2%
DM-free	0.22	4.9	N/A	0%

Table 5.1: Summary of the three models shown in Figures 13-16 and discussed in the text. $f_{DM}(R_{\mathrm{e,circ}})$ denotes the dark fraction within one effective radius.

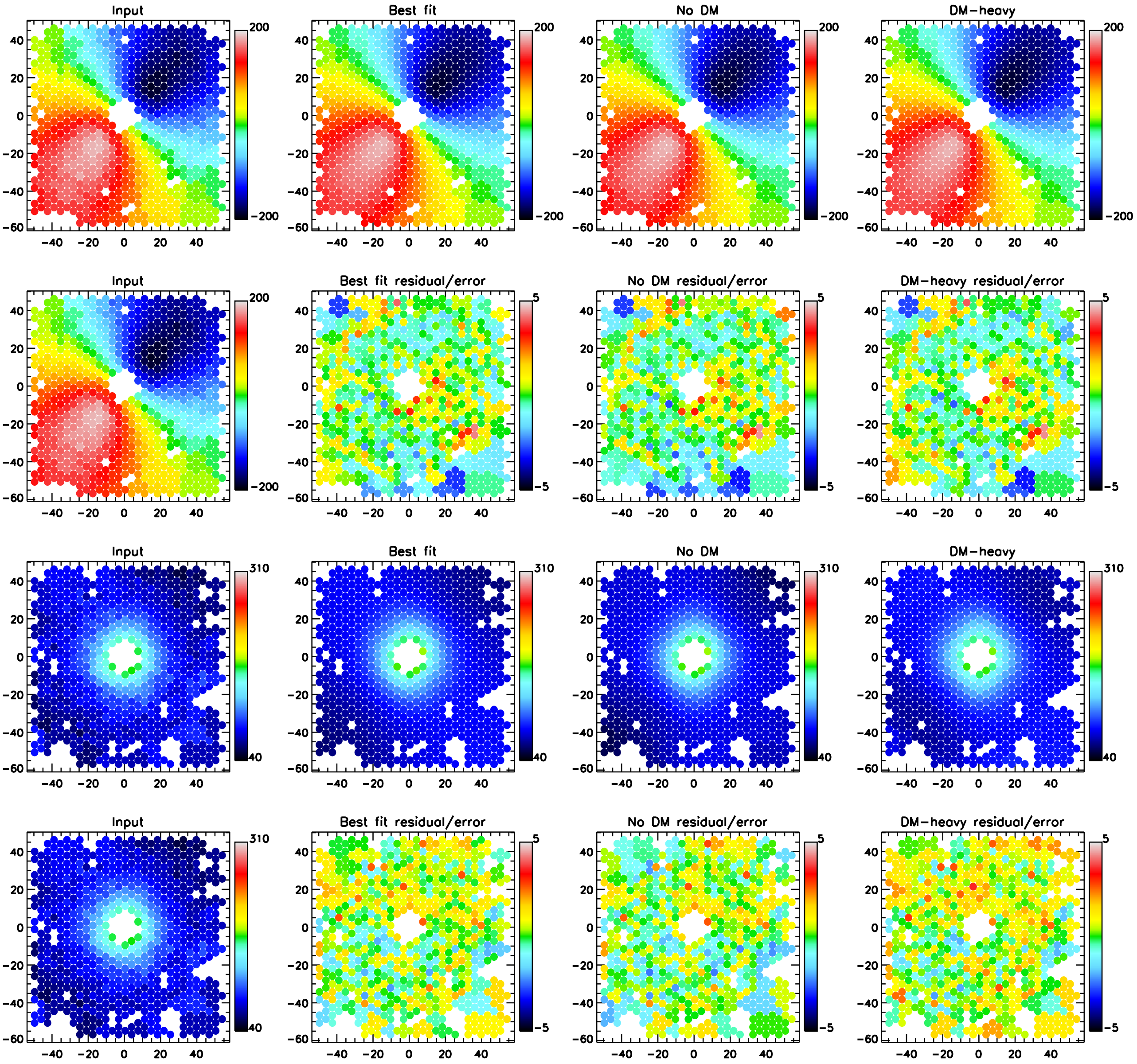

Figure 5.7: From top to bottom: input Mitchell velocity and model velocities in km/s, velocity residual/error of model velocities in units of σ, input and model dispersions in km/s, and residual/error of model dispersions in units of σ. I summarise the properties of the three selected models in Table 5.1. Only unmasked bins are shown.

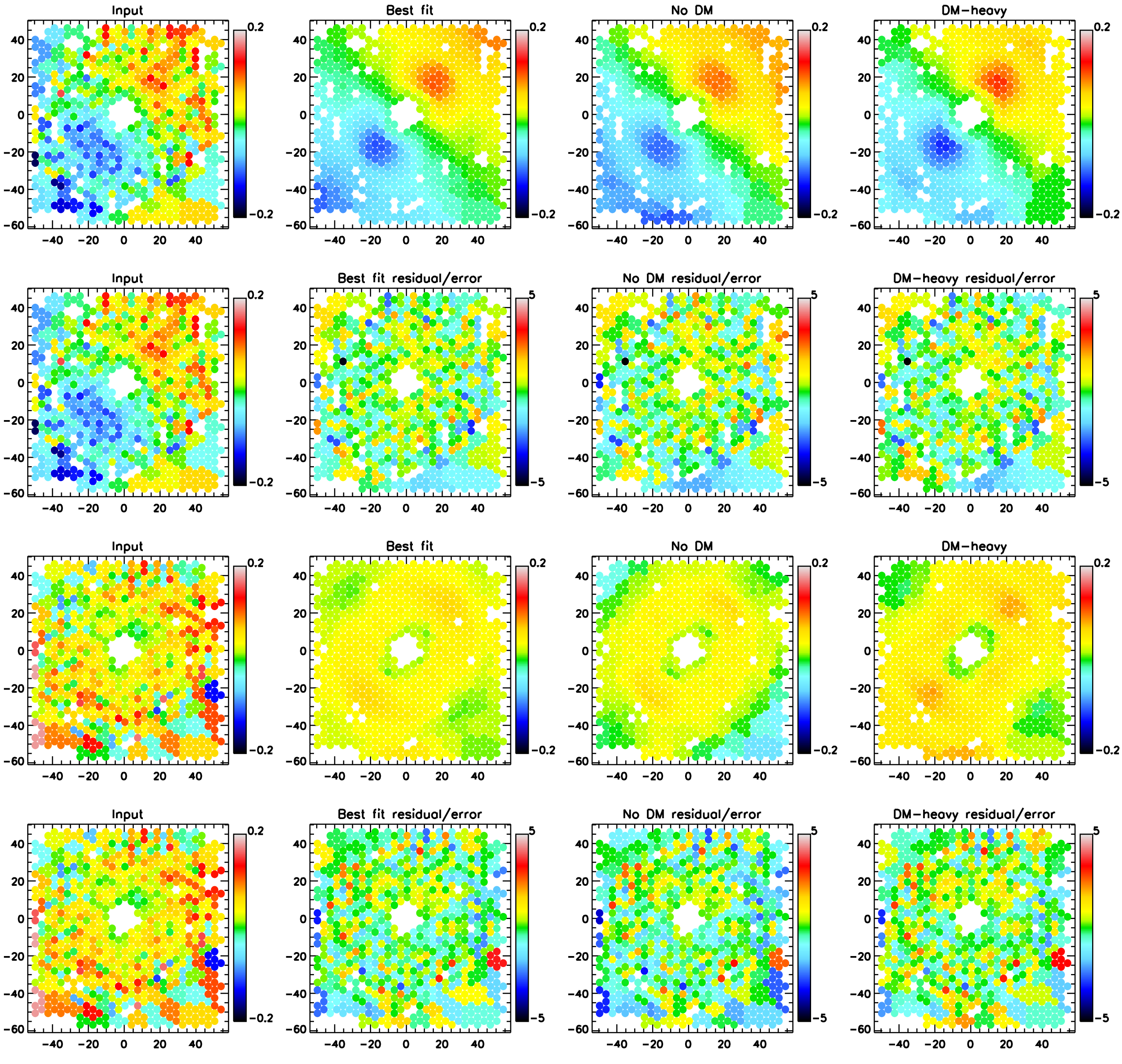

Figure 5.8: As in Figure 5.7, but for h_3 and h_4.

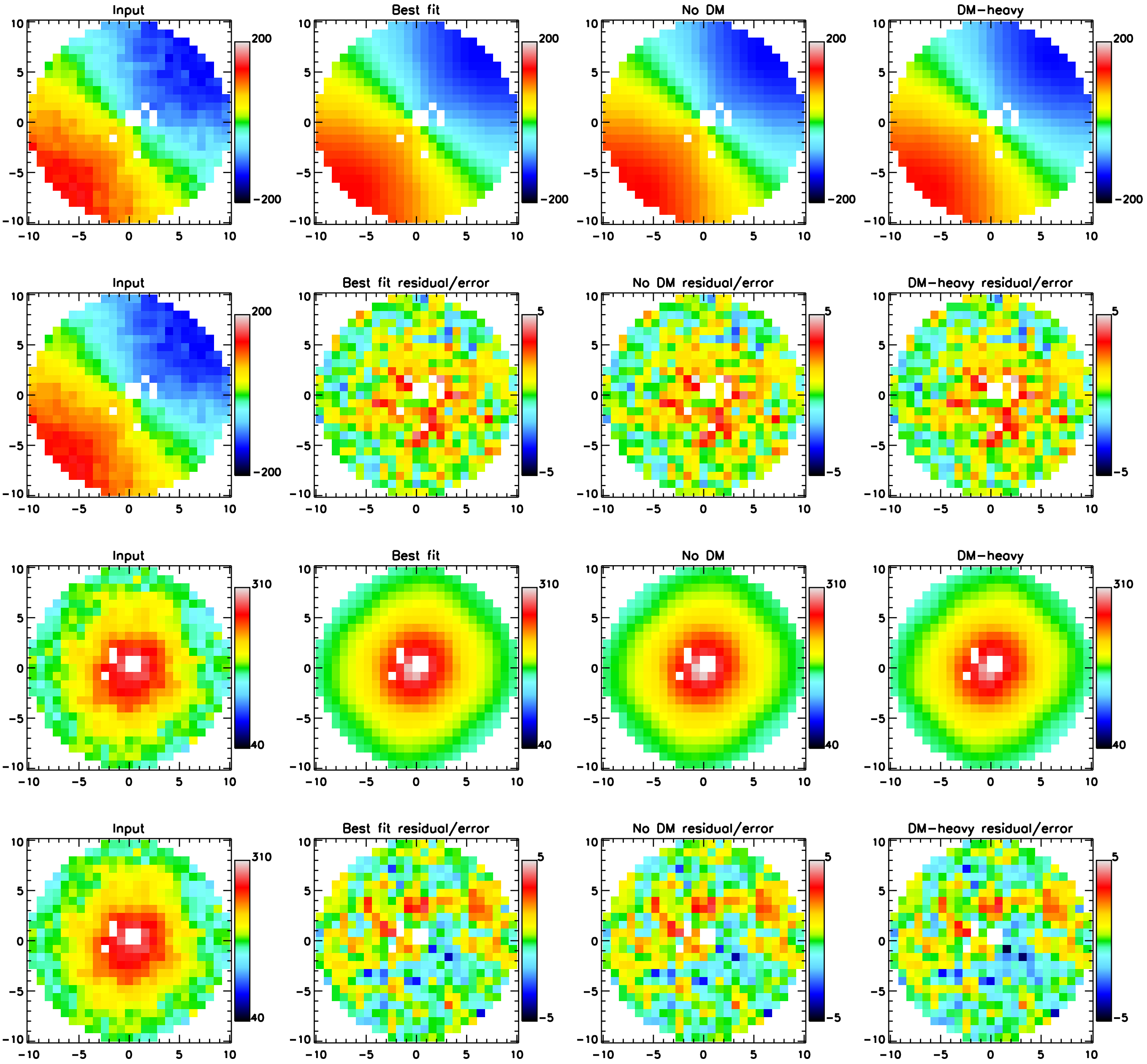

Input
Best fit
No DM
DM−heavy
Input
Best fit residual/error
No DM residual/error
DM−heavy residual/error
Input
Best fit
No DM
DM−heavy
Input
Best fit residual/error
No DM residual/error
DM−heavy residual/error

Figure 5.9: As in Figure 5.7, but for the SAURON data.

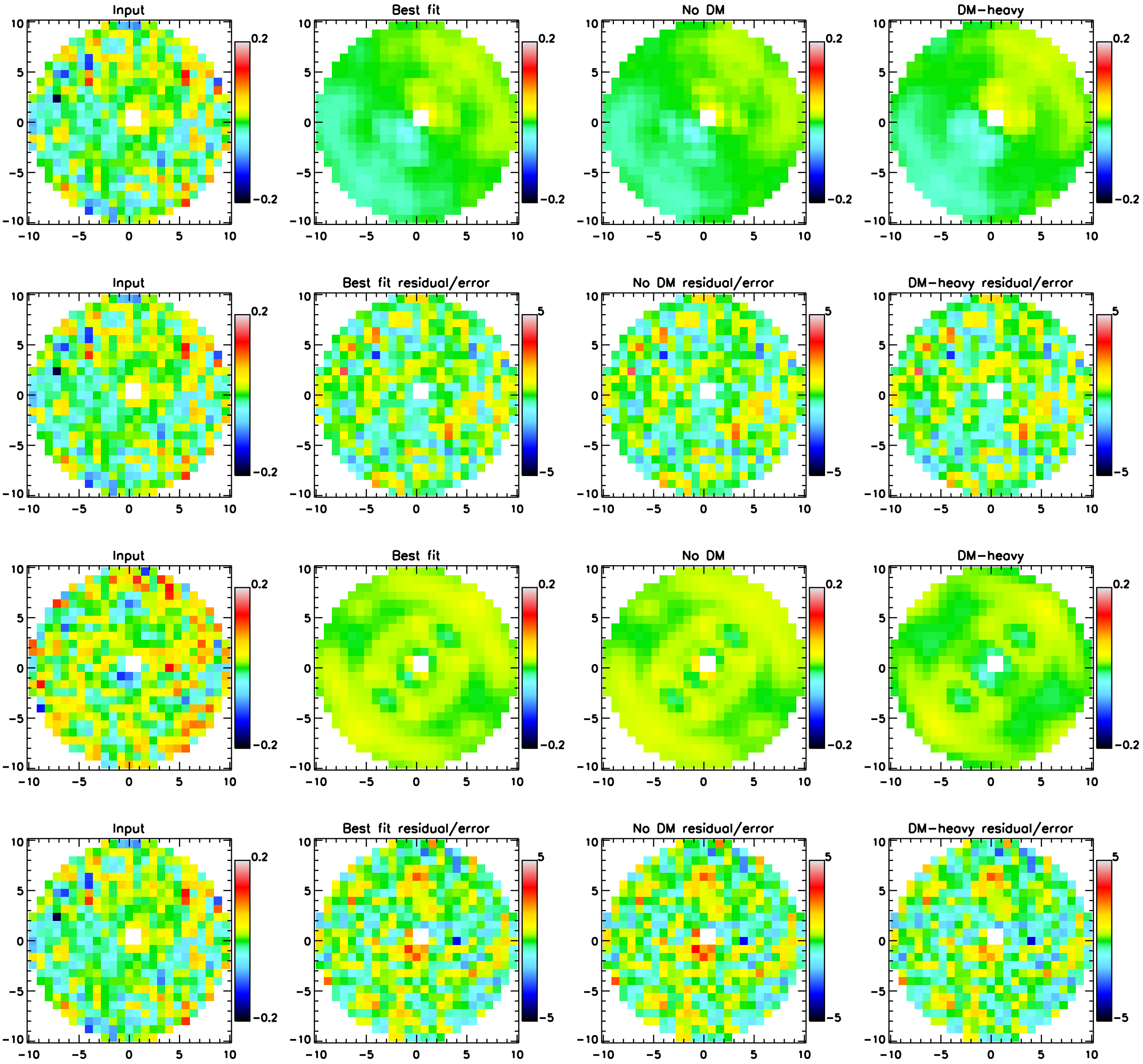

Input

Best fit

No DM

DM−heavy

Input

Best fit residual/error

No DM residual/error

DM−heavy residual/error

Input

Best fit

No DM

DM−heavy

Input

Best fit residual/error

No DM residual/error

DM−heavy residual/error

Figure 5.10: As in Figure 5.7, but for h_3 and h_4 from the SAURON data.

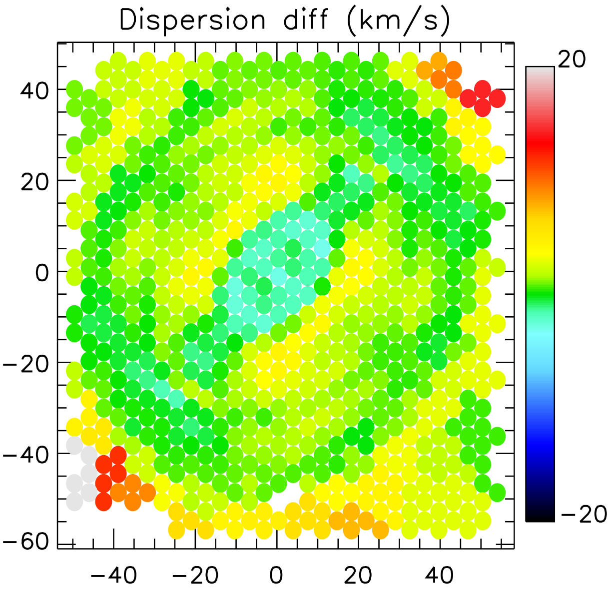

Figure 5.11: Difference in line of sight velocity dispersion between the selected DM-heavy model and the best-fit model, where a positive number indicates the former model being higher. The dispersion is somewhat higher over much of the FOV beyond $1R_{\rm e}$ as a result of the increased dark matter content, which is the main cause of the DM-heavy model's higher χ^2.

the models to follow near-isothermal profiles beyond the central effective radius; this in good agreement with the average logarithmic slope of 2.19 ± 0.03 reported from the JAM of Cappellari et al. (2015), as well as with the JAM modelling of my ETG sample presented in the previous chapter of this thesis.

In the top panel of Figure 5.13, I present the distribution of orbits in my best-fitting orbit model model as a function of spin parameter λ_z. The spin parameter is defined as $\lambda_z = \overline{J}_z / J_{max}$, where $\overline{J}_z$ is the time-averaged angular momentum along the galaxy short axis and J_{max} the angular momentum of a circular orbit of the same binding energy. I find evidence of both a slow-rotating bulge component (signified by the presence of non-rotating orbits, defined here as having $-0.2 < \lambda_z < 0.2$) and a fast-rotating disk ($\lambda_z > 0.2$), with the disk component dominating particularly beyond the central half-light radius. I also find a non-negligible counter-rotating component ($\lambda_z < -0.2$) within the central 10 arcseconds, which is not apparent from a visual inspection of the SAURON or Mitchell kinematics maps; as demonstrated in the bottom panel of Figure 5.13, this feature is present in all Schwarzschild models allowed by my χ^2 criterion.

In Figure 5.14, I plot the orbital anisotropy parameters $\beta_r = 1 - (\sigma_t/\sigma_r)^2$ and $\beta_z = 1-(\sigma_z/\sigma_R)^2$ as a function of radius, as inferred from all Schwarzschild models allowed by my chosen χ^2 criterion. The tangential velocity dispersion σ_t is defined as $\sigma_t^2 = (\sigma_\theta^2 + \sigma_\phi^2)/2$,

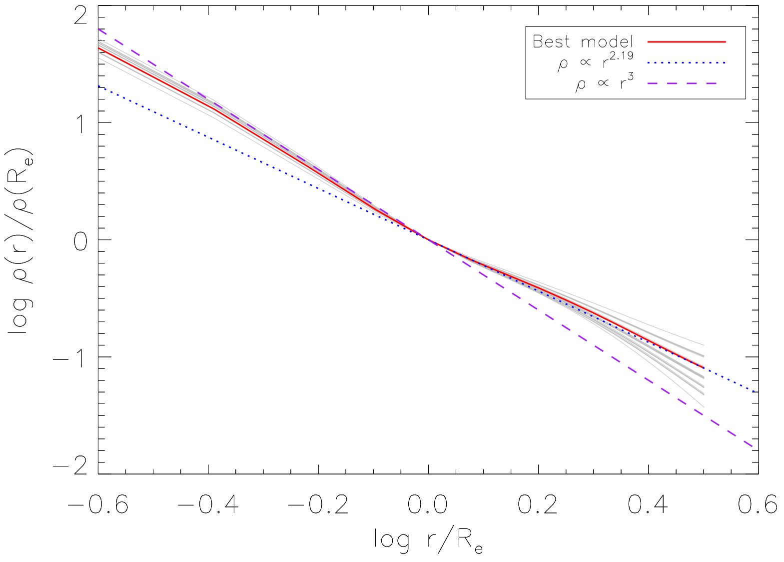

Figure 5.12: Total (dark plus baryonic) density profiles of all Schwarzschild models within the χ^2 confidence criterion, with lines for $\rho \propto r^{2.19}$ (Cappellari et al., 2015) and $\rho \propto r^3$ shown for comparison. I find the Schwarzschild modelling to favour near-isothermal behaviour beyond the central effective radius, with the density profile somewhat steeper at lower radii.

where (r,θ,ϕ) are the standard spherical coordinates centred on the galaxy. (R,z) are cylindrical coordinates, with σ_z therefore denoting the dispersion out of the plane of the disc. The best-fit model is radially anisotropic ($\beta_r > 0$) in the centre, similar to the results of Walsh et al. (2012), but is instead tangentially anisotropic further out; the rest of the allowed models behave similarly. I also find β_z to vary strongly as a function of position in a similar manner to β_r.

Given my findings on NGC 3998's mass distribution and anisotropy from Schwarzschild modelling, it is interesting to compare to the JAM models presented in Chapter 4 of this thesis. The "$2-\beta$" JAM models from that chapter are particularly suited to such a comparison, since they allow for anisotropy variations as well as variations in a galaxy's dark and visible mass distribution. To summarise, the 2-β JAM models allow for two anisotropy parameters $\beta_{z,in}$ and $\beta_{z,out}$ which parametrise the orbital anisotropy of luminous MGE Gaussians with standard deviations lower than or greater than $1R_{\rm e}$ respectively. I also allowed for an NFW dark matter halo in the models. Given the assumption of axisymmetry in JAM, these models have five free parameters: q_{min}, $\beta_{z,in}$, $\beta_{z,out}$, M_*/L and M_{200}; I note that the JAM models of this galaxy were carried out using g-band photometry, meaning that the M_*/L of the JAM models isn't directly comparable with the Schwarzschild models. I present the MCMC chain for the $2-\beta$

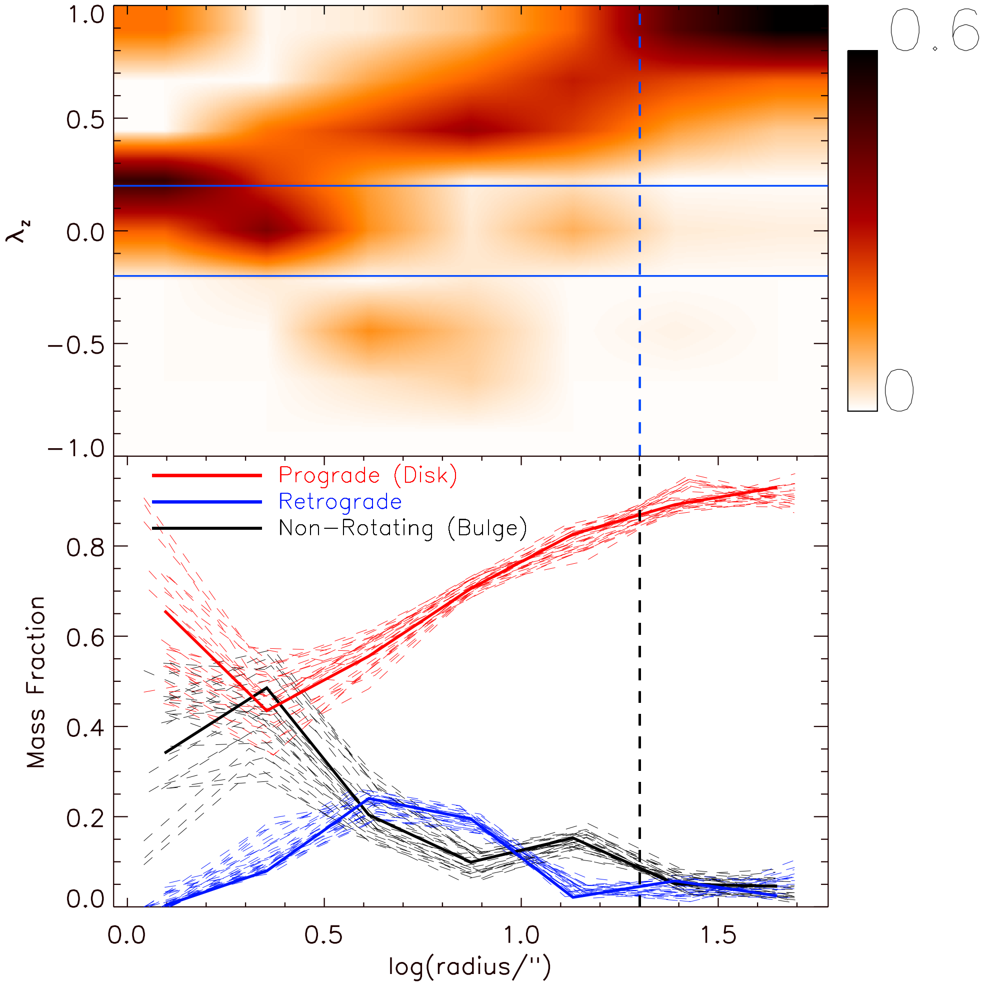

Figure 5.13: Top panel: mass distribution of orbits for the best-fitting Schwarzschild model, normalised per unit radius, plotted as a function of time-averaged radius and spin. Bottom panel: distributions of orbits plotted for all Schwarzschild models allowed by my χ^2 criterion, with the best-fit models shown as solid lines and all others shown as dashed lines. The vertical dashed lines mark 1 R_e. A bulge-disk separation is evident, with the disk coming to dominate in the outer observed regions for all allowed models. I also find the allowed Schwarzschild models to contain a non-negligible counter-rotating component.

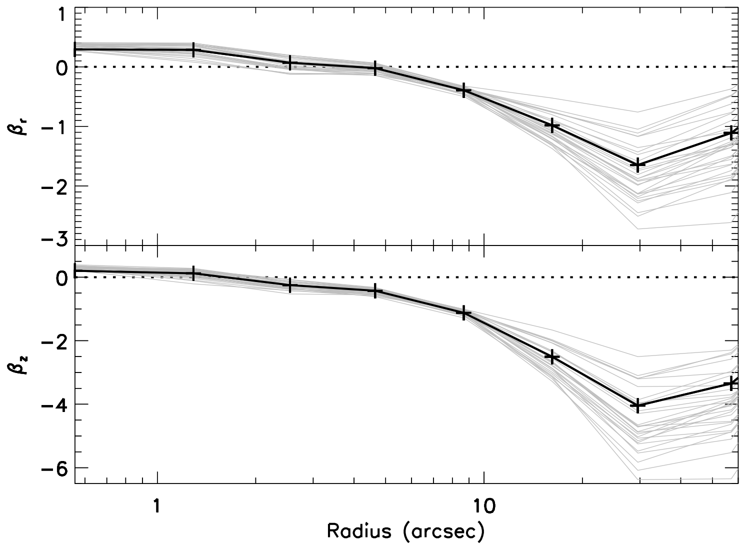

Figure 5.14: Orbital anisotropy parameters β_r (top) and β_z (bottom) for the best-fitting model (black line with black crosses) along with all other allowed models (grey lines), plotted as a function of radius along the galaxy major axis. The dotted lines represent isotropy. I find the orbital anistropy to vary signficantly as a function of position, with the model becoming tangentially anisotropic away from NGC 3998's centre.

JAM models of NGC 3998 in Figure 5.15, and I present maps and histograms of this chain in Figure 5.16; these chains are constructed after scaling the errors on the kinematics, as explained in Chapter 4.

As in Chapter 4, I estimate parameter confidence ranges on the MCMC chains by taking the median and standard deviation of the MCMC chain in terms of each parameter in turn; I also convert q_{min} and M_{200} to q_{Re} and $f_{dm,e}$ respectively. From these JAM models, I find $q_{Re} = 0.47^{+0.04}_{-0.04}$, $\beta_{z,in} = 0.09 \pm 0.29$, $\beta_{z,out} = -1.05 \pm 1.65$ and $f_{dm,e} = 0.006^{0.006}_{-0.003}$; thus, my shape results here are in excellent agreement with those from the Schwarzschild models, with the preference for low dark matter fractions also consistent with the Schwarzschild results. My results in terms of anisotropy are inconclusive, though I note that visual inspection of the chain suggests a preference of negative $\beta_{z,out}$. More edge-on galaxy inclinations are associated with more tangential anisotropies in the MCMC chains, as was previously noted in Chapter 4 for the base JAM models. Overall, my JAM modelling favours $\beta_{z,out}$ values somewhat less negative than would be predicted from the Schwarzschild modelling; one possible reason for this is that the Schwarzschild modelling makes use of additional kinematic data (h_3 and h_4) with respect to the JAM modelling. As with some of the base JAM chains presented in Chapter 4, visual inspection of this chain also reveals undesired structure, particularly in terms of $\beta_{z,out}$; I will investigate methods of removing this structure as part of my future work.

5.3 Discussion

In the preceding sections, I have constrained the dark and visible mass distribution of NGC 3998 using detailed Schwarzschild dynamical models, with the models also allowing me to investigate the galaxy's deprojected dynamics. I find NGC 3998 to be a near-oblate face-on fast-rotating galaxy, in agreement with the flattening for this galaxy inferred in Cappellari et al. (2013b). Notably, I find the Schwarzschild modelling to be sufficient to obtain tight constraints on the galaxy's intrinsic shape; this was not the case in Walsh et al. (2012), in which the kinematics were entirely within the inner effective radius, and so demonstrates the potential of wide-field IFU data in studying ETGs' mass structure.

I obtained an I-band M_*/L of $4.7^{+0.32}_{-0.45} M_\odot/L_\odot$ from the Schwarzschild modelling, and found this to be consistent with my own stellar population modelling as well as that reported in Cappellari et al. (2013a). This suggests that the combination of Schwarzchild modelling and

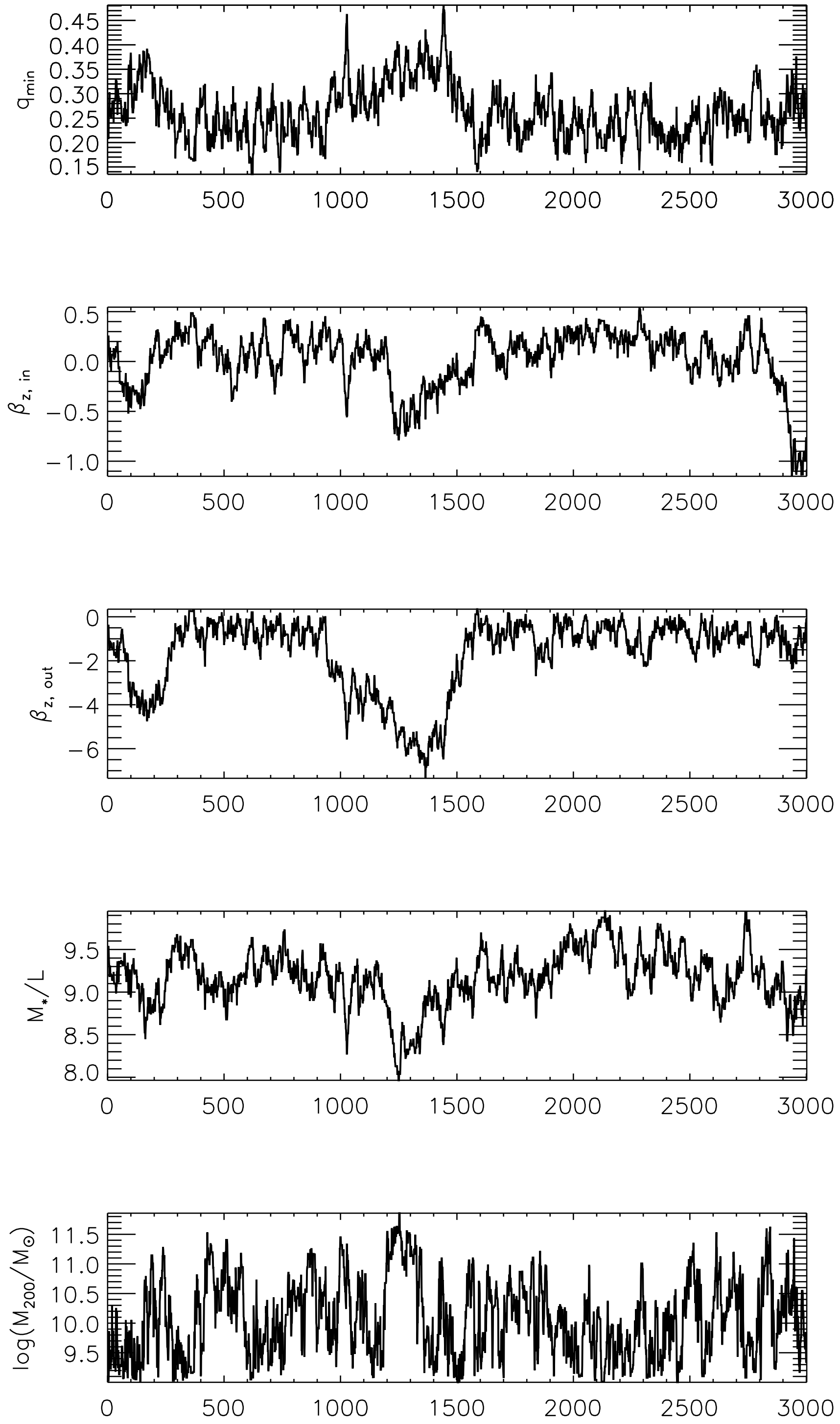

Figure 5.15: MCMC chain for the 2-β JAM models of NGC 3998, plotted in terms of each free parameter in turn.

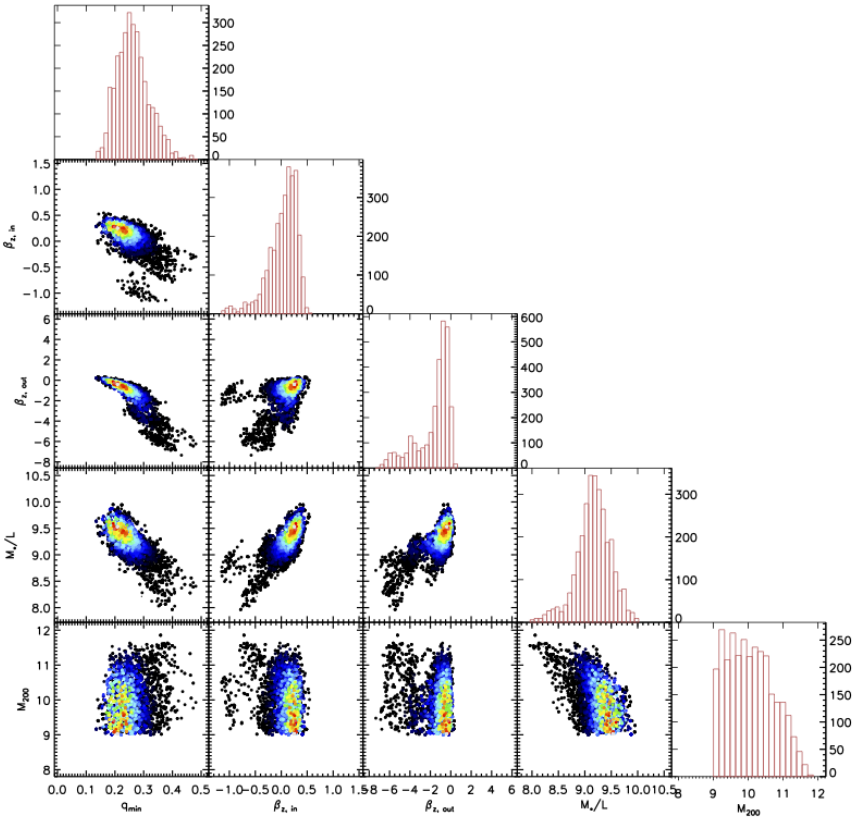

Figure 5.16: MCMC chain of the 2-β JAM models of NGC 3998. The color-coding corresponds to the likelihood of a given JAM model, with black points corresponding to models disfavoured by 1σ or greater after re-scaling the errors.

wide-field IFU data is sufficient to disentangle a galaxy's dark and visible mass structure to at least some degree. As with the JAM models in Chapter 4 of this thesis, a logical next step here would be to make use of M_*/L gradients in Schwarzschild models. Such a gradient most likely would not be plausible as a free parameter, due to degeneracies with galaxies' stellar components (e.g. Yıldırım et al., 2016), but could be a fixed input into a dynamical model based on the results of stellar population modelling (e.g. Mitzkus et al., 2017).

My modelling implies NGC 3998 to be disc-dominated over much of the Mitchell FOV with only a small proportion of radial orbits in the outskirts; furthermore, I find both Jeans and Schwarzschild modelling to favour tangential anisotropy over much of my FOV. Tangential anisotropy in simulations is associated with large fractions of in-situ- formed stars (Wu et al., 2014), possibly as a result of a recent (redshift $z < 2$) dissipational event (Röttgers et al., 2014), whereas significant late-time accretion of stars is expected from simulations to produce an excess of radial orbits beyond the central effective radius (e.g. Oser et al., 2010; Wu et al., 2014). My inferred galaxy shape of $q_{R_e} = 0.44^{+0.05}_{-0.00}$ is also consistent with a past dissipational event, from comparisons with the cosmological simulations of Naab et al. (2014). As such, I find dynamical modelling of NGC 3998 provide a picture of its evolution which is both consistent and complimentary with the stellar population modelling discussed in chapter 3 of this thesis.

5.4 Summary

In this chapter, I presented detailed Schwarzschild modelling of the galaxy NGC 3998. My modelling implies NGC 3998 to be a near-oblate and flattened galaxy, consistent with the inclination reported in Cappellari et al. (2013b), and favours a low dark fraction within the galaxy's central effective radius.

I find from Schwarzschild modelling a dark matter fraction of $(7.1^{+8.1}_{-7.1})\%$ within $1R_e$. At the same time, I obtain from the Schwarzschild models an I-band M_*/L of $4.7^{+0.32}_{-0.45} M_\odot/L_\odot$, which I find to be in good agreement with stellar population modelling of this galaxy; this agreement adds weight to the idea of a low central dark matter fraction, as it implies that a degeneracy between dark and visible mass is not an adequate explanation for the results I find.

I find NGC 3998 to be disc-dominated in its outer regions, with the dynamical models favouring strong tangential anisotropy beyond $1R_e$. From comparisons to simulations, I argue that my modelling of NGC 3998 is consistent with it having experienced some past dissipational event. My dynamical modelling therefore presents a consistent picture with respect to the stellar population modelling presented in Chapter 3 of this thesis, demonstrating the complimentary nature of the two approaches.

6

Summary of conclusions and future work

Lenticular and elliptical galaxies, collectively referred to as "Early-type galaxies" (ETGs), are commonly thought to represent the end-points of galaxy evolution. These galaxies are therefore integral to our understanding of the Universe, and their evolutionary paths continue to be of great interest. Much progress in understanding these galaxies has been made through integral-field unit (IFU) spectroscopy, with the SAURON (de Zeeuw et al., 2002) and ATLAS^{3D} (Cappellari et al., 2011a) surveys in particular serving to greatly increase our knowledge of these galaxies. Fast-rotating ETGs have been shown to lie on a parallel morphological sequence with respect to spiral galaxies (Cappellari et al., 2011b), with the evolution of fast-rotating ETGs appearing to be linked closely to the growth of their central bulge (Cappellari et al., 2013b); these findings suggest a connection between ETGs and spiral galaxies.

However, the exact nature of this ETG-spiral connection remains unclear. One possibility is that fast-rotating ETGs result from the passive fading of high-redshift spiral galaxies (e.g. Dressler et al., 1997; Peng et al., 2015); this is supported by measurements of galaxies' total luminosity and disk scale length, which are larger for Sa-type spiral galaxies than for Lenticular systems (Vaghmare et al., 2015). However, IFU spectroscopy from the CALIFA survey has demonstrated that ETGs have lower stellar angular momentum for a given concentration with respect to spiral galaxies (Falcón-Barroso et al., 2015); this is inconsistent with passive fading scenarios, but appears to be consistent with simulations of major mergers (Querejeta et al., 2015). The presence of significant star-gas misallignments in roughly half of nearby ETGs (e.g. Sarzi et al., 2006; Davis et al., 2011; Serra et al., 2014) likewise suggests that some kind of interaction event must have occurred in many of these objects. Wide-field IFU observations hold the potential to increase our understanding of ETGs' evolution further, by allowing detailed study of their contents beyond the central effective radius.

I used the Mitchell Spectrograph to obtain integral-field spectroscopic data for twelve nearby early-type galaxies, with the observations extending beyond two half-light radii (or effective radii, R_e) in most cases. Such a wide field of view (FOV) remains rare for ETG studies, making this work different from most such studies to date; previous studies of this type include the SLUGGs survey (Brodie et al., 2014) and the Greene et al. (2013) Mitchell Spectrograph study of massive ETGs. These galaxies have been detected in H I by the Westerbork Synthesis Radio Telescope (Serra et al., 2012), with ten of the twelve containing regularly-rotating H I discs; H I kinematics for these galaxies have been presented in Serra et al. (2014). I extracted stellar and gaseous kinematics for the galaxies from the Mitchell Spectrograph data, inferred the properties of their stellar populations via spectral modelling, and made use of multiple dynamical modelling approaches in order to investigate their three-dimensional mass structure. I summarise the key results of my study in the proceeding subsections.

6.1 Stellar kinematics and populations of early-type galaxies with the Mitchell Spectrograph

In Chapter 3, I presented stellar and gaseous kinematics for the ETGs along with line strength measurements and stellar population constraints from spectral modelling. I found no abrupt changes in the kinematic behaviour of the galaxies' stars: ETGs that are fast-rotating at one half-light radius remain fast-rotating throughout the FOV, while slow-rotating galaxies likewise remain slow-rotating. As such, I found that fast/slow rotator classification proposed in (Emsellem et al., 2007) - based largely on IFU data confined to $1R_e$ - seems to characterise the kinematics of most ETGs even much beyond the central effective radius. My result here is very similar to what Raskutti et al. (2014) find from their Mitchell Spectrograph spectra of massive ETGs, though my result is different from Arnold et al. (2014) in that they find a handful of centrally fast-rotating ETGs to slow drops in rotation. I argued this difference to be a result of differences between my sample and that of Arnold et al. (2014): the Arnold et al. (2014) sample contains a much greater proportion of elliptical galaxies, including elliptical galaxies with signs of embedded stellar discs within the innermost effective radius.

I found negative metallicity gradients for most of the galaxies which persisted beyond the central effective radius, along with negative gradients in stellar mass-to-light ratio M_*/L for those objects in line with previous studies. I found my stellar population models to imply the existence of multiple distinct stellar populations in the galaxies NGC 3626 and NGC 6798, separated by age; given the presence of gas in these galaxies, I argued these features to be signs of star formation triggered by gaseous interactions.

I compared my galaxies' stellar kinematics to results from previous simulations (Naab et al., 2014; Röttgers et al., 2014) noting the similarity between the kinematics of my fast-rotating ETGs to simulated ETGs with gas-rich histories; given the presence of H I in my sample galaxies, such a similarity is encouraging. My metalicity gradients disfavour late major mergers, due to both the steepness of the gradients and an apparent lack of a break beyond the central effective radius, but are consistent with one or more minor mergers having occurred. As such, I find that the stellar kinematics and populations of these ETGs paint a consistent evolutionary picture, in which one or more gaseous interaction events served to shape these galaxies into their present forms; such a picture is also consistent with previous optical observations of these objects, which show signs of faint substructure in several cases (Duc et al., 2015).

6.2 Jeans dynamical modelling of early-type galaxies

In Chapter 4 of this thesis, I reported results of Jeans dynamical modelling of my ETG sample obtained using the Jeans Anisotropic Modelling (JAM) method of (Cappellari, 2008) to model the galaxies' second velocity moments. The JAM method predicts the observed true second velocity moment of a galaxy from a Multi Gaussian Expansion (MGE; Cappellari, 2002) mass model, based on an input viewing angle and an assumed orbital anisotropy; this allows one to constrain a galaxy's dark and visible mass distribution by comparing the JAM predictions to observational data.

First, I generated a "base" set of models in which the orbital anisotropy parameter β_z was assumed to be constant across the galaxy; I treated this as a free parameter along with the galaxy minor-to-major axis ratio, the stellar mass-to-light ratio M_*/L and the dark halo mass M_{200}. I modelled the dark matter components of the galaxies using the Navarro et al. (1996) parametrization. I generated three sets of JAM models. I also generated a set of "2-β" models, in which I used a pair of β_z parameters to model galaxies' inner and outer components separately; with these, I verified that the chosen treatment of β_z did *not* significantly affect the derived values of M_*/L or M_{200}. Lastly, I generated a set of dark matter-free models, which allowed for two β_z components but no dark halo, in order to compare the quality of those models with models which included dark matter. In all cases, I used a Markov Chain Monte Carlo (MCMC) method in order to constrain the galaxies' three-dimensional dark and visible mass structures for a given set of JAM models.

I found the JAM method to provide good fits to the galaxies' kinematics, with the base models providing fits of comparable quality to the 2-β models. I found my modelling to support low dark matter fractions within one effective radius for most of the galaxies, with a mean fraction of just 11 per cent derived from the MCMC chains; in addition, I noted three galaxies for which JAM models without dark matter provided fits that were formally better than achieved by the base models. When considering the dark and visible galaxy mass together, I found my modelling to favour near-isothermal total mass density profiles for the majority of sample galaxies. Such profiles are not generic predictions of ΛCDM cosmology, and so provide important constraints on the physics of galaxy formation.

I inferred M_*/L values from the JAM models that were generally in good consistency with the values I obtained from stellar population modelling. I argue from this that the wide FOV of the Mitchell spectrograph is sufficient for dynamical models to disentangle between dark and visible mass to at least some degree; based on this, and based on the work presented in Chapter 3, I suggested the use of M_*/L gradients in future studies of this kind.

6.3 Schwarzschild modelling of NGC 3998

In Chapter 5 I presented results from detailed Schwarzschild (1979) dynamical modelling of the galaxy NGC 3998, using the code and method of van den Bosch et al. (2008). I modelled the galaxy's stellar kinematics up to the fourth Gauss-Hermite moment, using kinematics from both the SAURON and Mitchell Spectrograph IFU instruments. In Schwarzschild's method, a galaxy is modelled as a superposition of individual stellar orbits. Unlike the JAM method employed in Chapter 4, no assumptions are made in Schwarzschild models concerning the behaviour of a galaxy's orbital anisotropy. Schwarzschild models can thus used to study a galaxy's deprojected dynamics in detail, providing valuable comparisons to computer simulations, as well as to constrain the structure of that galaxy's mass.

I generated a series of Schwarzschild models of the galaxy in order to obtain constraints on its three-dimensional shape, its stellar mass-to-light ratio and its dark halo mass; I also studied the three-dimensional dynamics of Schwarzschild models which I found to provide good fits to the kinematic data, which I defined as being all those models with a $\Delta\chi^2$ value lower than the standard deviation of the χ^2 statistic.

I found from the Schwarzschild models a dark matter fraction within one effective radius of $(7.1^{+8.1}_{-7.1})\%$, with models without dark matter providing acceptable fits to the data; this is consistent with the JAM modelling I carried out for this galaxy, in which the dark matter free models provided lower-χ^2 fits than the base models while containing the same number of free parameters. I also found the Schwarzschild models to favour near-isothermal total mass density profiles beyond the central half light radius, which is again consistent with my results from JAM modelling.

I found all good Schwarzschild models to display tangential anisotropy in the stellar kinematics over much of the studied FOV; such a result supports a past gas-rich interaction, based on comparisons with simulations (Röttgers et al., 2014), and so is consistent with the discussion provided in Chapter 3 of this thesis. My inferred minor-to-major axis ratio at one half-light radius, $q_{R_e} = 0.44^{+0.05}_{-0.00}$, is likewise consistent with the shapes reported in the cosmological simulation results of Naab et al. (2014) for galaxies with gas-rich histories. I note that I obtain a tight constraint on the minor-to-major axis ratio; such constraints were not obtained in Walsh et al. (2012), who conducted a Schwarzschild study of this object using data confined to the central half-light radius, which again highlights the power of wide field IFU data for investigating ETGs' structure.

6.4 Future work

A key feature of my galaxy sample is that all galaxies have been detected in H I, with ten out the twelve galaxies containing large-scale regularly rotating H I discs. As such, this sample is likely *not* representative of *all* ETGs within the covered mass range. It would be illuminating, then, expand this Mitchell ETG sample to include ETGs of similar mass that lack detectable quantities of gas. By studying their stellar populations and dynamics in the manner described in this thesis, one could gain a significantly more complete view of how intermediate-mass ETGs evolve. Such work would also be greatly complementary with respect to current large-scale IFU surveys such as MaNGA (Bundy et al., 2015), which encompass large numbers of ETGs but which generally achieve FOVs less than $2R_e$ for individual galaxies.

There are a number of aspects of the presented work that I intend to expand upon in the more immediate future, particularly with regards to dynamical modelling of the sample ETGs. Most immediately, I intend to expand my Schwarzschild modelling work to other galaxies in my ETG sample, with particular attention paid to the galaxies' orbital anisotropy and to comparisons with simulations. Where necessary, I will improve my modelling of the galaxies' surface photometry by using available short exposures with the Canada-France-Hawaii Telescope (CFHT) to better-model the galaxies' central regions. In addition to obtaining robust constraints on my galaxies' mass contents from this work, I will learn much about my galaxies' stellar dynamics; this in turn will allow me to better-understand the processes that shaped these galaxies into their present forms, based on comparisons with computer simulations and with results on these galaxies from stellar population modelling.

Following this Schwarzschild work, I plan to further expand my dynamical modelling work in multiple ways. Firstly, I intend to study the use of mass-to-light ratio gradients in my dynamical models, motivated by the detection of such gradients in Chapter 3 of this thesis. Most likely, it will not be feasible to treat such a gradient as a free parameter, owing to degeneracies between galaxies' dark and visible components (e.g. Yıldırım et al., 2016); however, a valid approach would be to instead derive gradients from stellar population modelling and then to use these gradients as fixed inputs to dynamical models (e.g. Mitzkus et al., 2017). This work will allow me to gain greater insight into the visible mass structure of galaxies,as well as into the stucture of those galaxies' dark matter contents, by reducing the degeneracy between dark and visible mass in dynamical models.

In addition, I plan to enhance my dynamical modelling by taking advantage of the H I data available for these galaxies. Most of the galaxies in my sample contain regularly-rotating H I discs, with data extending well beyond the FOV of the Mitchell Spectrograph IFU observations; such discs represent an ideal opportunity to study these galaxies' dark matter halos in a way that is independent of the galaxies' stars. My work here would involve the fitting of H I rotation curves in parallel with Jeans and Schwarzschild dynamical models, which would serve to lift the degeneracy between dark and visible mass for these galaxies. This work would allow me to learn much about the structure of ETG dark halos, as it would allow me to determine both the mass and concentration of dark halos in a non-degenerate way.

Bibliography

Adams, J. J. et al. 2011, The Astrophysical Journal Supplement Series, 192, 5

Adams, J. J., Gebhardt, K., Blanc, G. A., Fabricius, M. H., Hill, G. J., Murphy, J. D., van den Bosch, R. C. E., & van de Ven, G. 2012, ApJ, 745, 92, 1110.5951

Ahn, C. P., Alexandroff, R., Allende Prieto, C., Anders, F., Anderson, S. F., Anderton, T., Andrews, B. H., & et al. 2014, ApJS, 211, 17, 1307.7735

Arnold, J. A. et al. 2014, ApJ, 791, 80, 1310.2607

Auger, M. W., Treu, T., Bolton, A. S., Gavazzi, R., Koopmans, L. V. E., Marshall, P. J., Moustakas, L. A., & Burles, S. 2010, ApJ, 724, 511, 1007.2880

Bacon, R. et al. 2001, MNRAS, 326, 23, astro-ph/0103451

Bahcall, J. N., & Casertano, S. 1985, ApJ Letters, 293, L7

Barnabè, M., Auger, M. W., Treu, T., Koopmans, L. V. E., Bolton, A. S., Czoske, O., & Gavazzi, R. 2010, MNRAS, 406, 2339, 1002.1083

Barnabè, M., Czoske, O., Koopmans, L. V. E., Treu, T., & Bolton, A. S. 2011, MNRAS, 415, 2215, 1102.2261

Beers, T. C., Flynn, K., & Gebhardt, K. 1990, AJ, 100, 32

Bellstedt, S., Forbes, D. A., Foster, C., Romanowsky, A. J., Brodie, J. P., Pastorello, N., Alabi, A., & Villaume, A. 2017, MNRAS, 467, 4540, 1702.05099

Bendinelli, O. 1991, ApJ, 366, 599

Binney, J., & Merrifield, M. 1998, Galactic Astronomy

Blanc, G. A., Heiderman, A., Gebhardt, K., Evans, II, N. J., & Adams, J. 2009, ApJ, 704, 842, 0908.2810

Blanc, G. A. et al. 2013, AJ, 145, 138, 1303.1552

Blumenthal, G. R., Faber, S. M., Primack, J. R., & Rees, M. J. 1984, Nature, 311, 517

Boardman, N. F. et al. 2017, ArXiv e-prints, 1707.05735

——. 2016, MNRAS, 460, 3029, 1605.04795

Bolton, A. S., Burles, S., Koopmans, L. V. E., Treu, T., & Moustakas, L. A. 2006, ApJ, 638, 703, astro-ph/0511453

Bosma, A. 1978, PhD thesis, Groningen Univ.

Boylan-Kolchin, M., Bullock, J. S., & Kaplinghat, M. 2011, MNRAS, 415, L40, 1103.0007

Brodie, J. P. et al. 2014, ApJ, 796, 52, 1405.2079

Bullock, J. S., Kolatt, T. S., Sigad, Y., Somerville, R. S., Kravtsov, A. V., Klypin, A. A., Primack, J. R., & Dekel, A. 2001, MNRAS, 321, 559, astro-ph/9908159

Bundy, K. et al. 2015, ApJ, 798, 7, 1412.1482

Burstein, D. 1979, ApJ, 234, 435

Cappellari, M. 2002, MNRAS, 333, 400, astro-ph/0201430

Cappellari, M. 2008, MNRAS, 390, 71, 0806.0042

Cappellari, M. 2013, ApJ Letters, 778, L2, 1309.1136

Cappellari, M. 2015, in IAU Symposium, Vol. 311, Galaxy Masses as Constraints of Formation Models, ed. M. Cappellari & S. Courteau, 20–30, 1410.7329

——. 2017, MNRAS, 466, 798, 1607.08538

Cappellari, M. et al. 2006, MNRAS, 366, 1126, astro-ph/0505042

Cappellari, M., & Copin, Y. 2003, MNRAS, 342, 345, astro-ph/0302262

Cappellari, M., & Emsellem, E. 2004, PASP, 116, 138, astro-ph/0312201

Cappellari, M. et al. 2011a, MNRAS, 413, 813

——. 2011b, MNRAS, 416, 1680

——. 2013a, MNRAS, 432, 1862, 1208.3523

——. 2015, ApJ Letters, 804, L21, 1504.00075

——. 2013b, MNRAS, 432, 1709, 1208.3522

Cimatti, A., Nipoti, C., & Cassata, P. 2012, MNRAS, 422, L62, 1202.5403

Coccato, L., Gerhard, O., & Arnaboldi, M. 2010, MNRAS, 407, L26, 1006.2382

Davies, R. L., Sadler, E. M., & Peletier, R. F. 1993, MNRAS, 262, 650

Davis, T. A. et al. 2011, MNRAS, 417, 882, 1107.0002

de Lorenzi, F. et al. 2009, MNRAS, 395, 76, 0804.3350

de Lorenzi, F., Gerhard, O., Saglia, R. P., Sambhus, N., Debattista, V. P., Pannella, M., & Méndez, R. H. 2008, MNRAS, 385, 1729, 0802.1726 de Zeeuw, P. T. et al. 2002, MNRAS, 329, 513, astro-ph/0109511

Dekel, A., Stoehr, F., Mamon, G. A., Cox, T. J., Novak, G. S., & Primack, J. R. 2005, Nature, 437, 707, astro-ph/0501622

Douglas, N. G. et al. 2007, ApJ, 664, 257, astro-ph/0703047

Draper, H. 1877, Nature, 15, 218

Dressler, A. 1980, ApJ, 236, 351

Dressler, A. et al. 1997, ApJ, 490, 577, astro-ph/9707232

Duc, P.-A. et al. 2015, MNRAS, 446, 120, 1410.0981

Dutton, A. A., & Treu, T. 2014, MNRAS, 438, 3594, 1303.4389

Efstathiou, G., Sutherland, W. J., & Maddox, S. J. 1990, Nature, 348, 705

Emsellem, E. et al. 2011, MNRAS, 414, 888, 1102.4444

——. 2007, MNRAS, 379, 401, astro-ph/0703531

Emsellem, E., Monnet, G., & Bacon, R. 1994, A& A, 285, 723

Faber, S. M., & Jackson, R. E. 1976, ApJ, 204, 668

Falcón-Barroso, J., Lyubenova, M., & van de Ven, G. 2015, in IAU Symposium, Vol. 311, Galaxy Masses as Constraints of Formation Models, ed. M. Cappellari & S. Courteau, 78–81, 1409.7786

Falcón-Barroso, J., Sánchez-Blázquez, P., Vazdekis, A., Ricciardelli, E., Cardiel, N., Cenarro, A. J., Gorgas, J., & Peletier, R. F. 2011, A& A, 532, A95, 1107.2303

Foster, C. et al. 2016, MNRAS, 457, 147, 1512.06130

Frieman, J. A., Turner, M. S., & Huterer, D. 2008, ARA& A, 46, 385, 0803.0982

Gott, III, J. R., & Thuan, T. X. 1976, ApJ, 204, 649

Gould, N. I. M., Orban, D., & Toint, P. L. 2003, ACM Trans. Math. Softw., 29, 353

Governato, F. et al. 2012, MNRAS, 422, 1231, 1202.0554

Greene, J. E., Janish, R., Ma, C.-P., McConnell, N. J., Blakeslee, J. P., Thomas, J., & Murphy, J. D. 2015, ApJ, 807, 11, 1504.02483

Greene, J. E., Murphy, J. D., Comerford, J. M., Gebhardt, K., & Adams, J. J. 2012, ApJ, 750, 32, 1202.4464

Greene, J. E., Murphy, J. D., Graves, G. J., Gunn, J. E., Raskutti, S., Comerford, J. M., & Gebhardt, K. 2013, ApJ, 776, 64, 1308.2682

Grossi, M. et al. 2009, A& A, 498, 407, 0903.0602

Gunn, J. E., & Gott, III, J. R. 1972, ApJ, 176, 1

Herschel, W. 1800a, Philosophical Transactions of the Royal Society of London Series I, 90, 284

——. 1800b, Philosophical Transactions of the Royal Society of London Series I, 90, 255

Hill, G. J., Gebhardt, K., Komatsu, E., & MacQueen, P. J. 2004, in American Institute of Physics Conference Series, Vol. 743, The New Cosmology: Conference on Strings and Cosmology, ed. R. E. Allen, D. V. Nanopoulos, & C. N. Pope, 224–233

Hill, G. J. et al. 2008, in Astronomical Telescopes and Instrumentation: Synergies Between Ground and Space, International Society for Optics and Photonics, 701470–701470

Hirschmann, M., Naab, T., Ostriker, J. P., Forbes, D. A., Duc, P.-A., Davé, R., Oser, L., & Karabal, E. 2015, MNRAS, 449, 528, 1410.2244

Hoffman, L., Cox, T. J., Dutta, S., & Hernquist, L. 2010, ApJ, 723, 818, 1001.0799

Hopkins, P. F., Cox, T. J., Dutta, S. N., Hernquist, L., Kormendy, J., & Lauer, T. R. 2009, ApJS, 181, 135, 0805.3533

Hubble, E. P. 1929, ApJ, 69

——. 1936, Realm of the Nebulae

Jablonka, P., Gorgas, J., & Goudfrooij, P. 2007, A& A, 474, 763, 0707.0561

Jeans, J. H. 1922, MNRAS, 82, 122

Kapteyn, J. C. 1922, ApJ, 55, 302

Kapteyn, J. C., & van Rhijn, P. J. 1920, ApJ, 52, 23

Katkov, I. Y., Kniazev, A. Y., & Sil'chenko, O. K. 2015, AJ, 150, 24, 1505.01386

Kelson, D. D. 2003, Publications of the Astronomical Society of the Pacific, 115, 688

Kelson, D. D., Illingworth, G. D., Franx, M., & van Dokkum, P. G. 2006, ApJ, 653, 159, astro-ph/0606642

Kirchhoff, G. 1860, Annalen der Physik, 185, 148

Klypin, A., Kravtsov, A. V., Valenzuela, O., & Prada, F. 1999, ApJ, 522, 82, astro-ph/9901240

Knapp, G. R., Turner, E. L., & Cunniffe, P. E. 1985, AJ, 90, 454

Kobayashi, C. 2004, MNRAS, 347, 740, astro-ph/0310160

Kochanek, C. S. 2003, ApJ, 583, 49, astro-ph/0206006

Kormendy, J., & Bender, R. 1996, ApJ Letters, 464, L119

Kormendy, J., & Freeman, K. C. 2004, in IAU Symposium, Vol. 220, Dark Matter in Galaxies, ed. S. Ryder, D. Pisano, M. Walker, & K. Freeman, 377, astro-ph/0407321

Krajnović, D., Cappellari, M., de Zeeuw, P. T., & Copin, Y. 2006, MNRAS, 366, 787, astro-ph/0512200

Krajnović, D. et al. 2011, MNRAS, 414, 2923, 1102.3801

Krajnović, D., McDermid, R. M., Cappellari, M., & Davies, R. L. 2009, MNRAS, 399, 1839, 0907.3748

Lablanche, P.-Y. et al. 2012, MNRAS, 424, 1495, 1206.0291

Larson, R. B., Tinsley, B. M., & Caldwell, C. N. 1980, ApJ, 237, 692

Leauthaud, A. et al. 2012, ApJ, 744, 159, 1104.0928

Ma, C.-P., Greene, J. E., McConnell, N., Janish, R., Blakeslee, J. P., Thomas, J., & Murphy, J. D. 2014, ApJ, 795, 158, 1407.1054

Maddox, S. J., Efstathiou, G., Sutherland, W. J., & Loveday, J. 1990, MNRAS, 242, 43P

Mandelbaum, R., Seljak, U., & Hirata, C. M. 2008, JCAP, 8, 006, 0805.2552

McDermid, R. M. et al. 2015, MNRAS, 448, 3484, 1501.03723

Milgrom, M. 1983, ApJ, 270, 365

Mitzkus, M., Cappellari, M., & Walcher, C. J. 2017, MNRAS, 464, 4789, 1610.04516

Molaeinezhad, A., Falcón-Barroso, J., Martínez-Valpuesta, I., Khosroshahi, H. G., Vazdekis, A., La Barbera, F., Peletier, R. F., & Balcells, M. 2017, MNRAS, 1701.03466

Monnet, G., Bacon, R., & Emsellem, E. 1992, A& A, 253, 366

Moore, B., Quinn, T., Governato, F., Stadel, J., & Lake, G. 1999, MNRAS, 310, 1147, astro-ph/9903164

Murphy, J. D., Gebhardt, K., & Adams, J. J. 2011, The Astrophysical Journal, 729, 129

Naab, T. et al. 2014, MNRAS, 444, 3357, 1311.0284

Napolitano, N. R. 2012, Memorie della Societa Astronomica Italiana Supplementi, 19, 222

Navarro, J. F., Frenk, C. S., & White, S. D. M. 1996, ApJ, 462, 563, astro-ph/9508025

Oort, J. H. 1932, Bull. Astron. Inst. Neth., 6, 249

Oser, L., Naab, T., Ostriker, J. P., & Johansson, P. H. 2012, ApJ, 744, 63, 1106.5490

Oser, L., Ostriker, J. P., Naab, T., Johansson, P. H., & Burkert, A. 2010, ApJ, 725, 2312, 1010.1381

Pastorello, N., Forbes, D. A., Foster, C., Brodie, J. P., Usher, C., Romanowsky, A. J., Strader, J., & Arnold, J. A. 2014, MNRAS, 442, 1003, 1405.2338

Pastorello, N. et al. 2016, Publ. Astron. Soc. Aust., 33, e035, 1607.05799

Paturel, G., Petit, C., Prugniel, P., Theureau, G., Rousseau, J., Brouty, M., Dubois, P., & Cambrésy, L. 2003, A& A, 412, 45

Peng, Y., Maiolino, R., & Cochrane, R. 2015, Nature, 521, 192, 1505.03143

Poci, A., Cappellari, M., & McDermid, R. M. 2017, MNRAS, 1612.05805

Prugniel, P., & Soubiran, C. 2001, A& A, 369, 1048, astro-ph/0101378

Querejeta, M. et al. 2015, A& A, 579, L2, 1506.00640

Raskutti, S., Greene, J. E., & Murphy, J. D. 2014, ApJ, 786, 23, 1403.4627

Rawle, T. D., Smith, R. J., Lucey, J. R., & Swinbank, A. M. 2008, MNRAS, 389, 1891, 0807.3545

Remus, R.-S., Burkert, A., Dolag, K., Johansson, P. H., Naab, T., Oser, L., & Thomas, J. 2013, ApJ, 766, 71, 1211.3420

Romanowsky, A. J., Douglas, N. G., Arnaboldi, M., Kuijken, K., Merrifield, M. R., Napolitano, N. R., Capaccioli, M., & Freeman, K. C. 2003, Science, 301, 1696, astro-ph/0308518

Röttgers, B., Naab, T., & Oser, L. 2014, MNRAS, 445, 1065, 1406.6696

Rubin, V. C., & Ford, Jr., W. K. 1970, ApJ, 159, 379

Rubin, V. C., Ford, Jr., W. K., & Thonnard, N. 1980, ApJ, 238, 471

Sánchez-Blázquez, P. et al. 2006, MNRAS, 371, 703, astro-ph/0607009

Sánchez-Conde, M. A., & Prada, F. 2014, MNRAS, 442, 2271, 1312.1729

Sandage, A., Freeman, K. C., & Stokes, N. R. 1970, ApJ, 160, 831

Sandage, A., & Visvanathan, N. 1978, ApJ, 225, 742

Sarzi, M. et al. 2006, MNRAS, 366, 1151, astro-ph/0511307

Scheiner, J. 1899, ApJ, 9

Schiavon, R. P. 2007, ApJS, 171, 146, astro-ph/0611464

Schlafly, E. F., & Finkbeiner, D. P. 2011, ApJ, 737, 103, 1012.4804

Schwarzschild, M. 1979, ApJ, 232, 236

Scott, N. et al. 2013, MNRAS, 432, 1894, 1211.4615

Serra, P. et al. 2012, MNRAS, 422, 1835, 1111.4241

——. 2014, MNRAS, 444, 3388, 1401.3180

Smoot, G. F. et al. 1992, ApJ Letters, 396, L1

Somerville, R. S., & Davé, R. 2015, ARA& A, 53, 51, 1412.2712

Springel, V. et al. 2005, Nature, 435, 629, astro-ph/0504097

Thomas, D., Maraston, C., Bender, R., & Mendes de Oliveira, C. 2005, ApJ, 621, 673, astro-ph/0410209

Tortora, C., Napolitano, N. R., Romanowsky, A. J., Jetzer, P., Cardone, V. F., & Capaccioli, M. 2011, MNRAS, 418, 1557, 1107.2918

Trujillo, I. et al. 2006, ApJ, 650, 18, astro-ph/0504225

Vaghmare, K., Barway, S., Mathur, S., & Kembhavi, A. K. 2015, MNRAS, 450, 873, 1503.07635

van Albada, T. S., & Sancisi, R. 1986, Philosophical Transactions of the Royal Society of London Series A, 320, 447

van de Ven, G., de Zeeuw, P. T., & van den Bosch, R. C. E. 2008, MNRAS, 385, 614, 0712.0309

van de Voort, F., Davis, T. A., Kereš, D., Quataert, E., Faucher-Giguère, C.-A., & Hopkins, P. F. 2015, MNRAS, 451, 3269, 1504.03685

van den Bosch, R. C. E., & de Zeeuw, P. T. 2010, MNRAS, 401, 1770, 0910.0844

van den Bosch, R. C. E., & van de Ven, G. 2009, MNRAS, 398, 1117, 0811.3474

van den Bosch, R. C. E., van de Ven, G., Verolme, E. K., Cappellari, M., & de Zeeuw, P. T. 2008, MNRAS, 385, 647, 0712.0113

van Dokkum, P. G. et al. 2013, ApJ Letters, 771, L35, 1304.2391

——. 2010, ApJ, 709, 1018, 0912.0514

Vazdekis, A. et al. 2015, MNRAS, 449, 1177, 1504.08032

Vazdekis, A., Ricciardelli, E., Cenarro, A. J., Rivero-González, J. G., Díaz-García, L. A., & Falcón-Barroso, J. 2012, MNRAS, 424, 157, 1205.5496

Vazdekis, A., Sánchez-Blázquez, P., Falcón-Barroso, J., Cenarro, A. J., Beasley, M. A., Cardiel, N., Gorgas, J., & Peletier, R. F. 2010, MNRAS, 404, 1639, 1004.4439

Walsh, J. L., van den Bosch, R. C. E., Barth, A. J., & Sarzi, M. 2012, ApJ, 753, 79, 1205.0816

Wardle, M., & Knapp, G. R. 1986, AJ, 91, 23

Weijmans, A.-M. et al. 2009, MNRAS, 398, 561, 0906.0018

——. 2014, MNRAS, 444, 3340, 1408.1099

Wilkinson, D. M. et al. 2015, MNRAS, 449, 328, 1503.01124

Wollaston, W. H. 1802, Philosophical Transactions of the Royal Society of London, 92, 365, http://rstl.royalsocietypublishing.org/content/92/365.full.pdf+html

Worthey, G., Faber, S. M., Gonzalez, J. J., & Burstein, D. 1994, ApJS, 94, 687

Wu, X., Gerhard, O., Naab, T., Oser, L., Martinez-Valpuesta, I., Hilz, M., Churazov, E., & Lyskova, N. 2014, MNRAS, 438, 2701, 1209.3741

Yıldırım, A. et al. 2016, MNRAS, 456, 538, 1511.03131

Yıldırım, A., van den Bosch, R. C. E., van de Ven, G., Husemann, B., Lyubenova, M., Walsh, J. L., Gebhardt, K., & Gültekin, K. 2015, MNRAS, 452, 1792, 1506.06762

Yoachim, P., Roškar, R., & Debattista, V. P. 2010, ApJ Letters, 716, L4, 1005.0851

Zhu, L. et al. 2016, MNRAS, 462, 4001, 1608.08238

Zwicky, F. 1933, Helvetica Physica Acta, 6, 110

——. 1937, ApJ, 86, 217